PACIFIC EARTHQUAKE ENGINEERING RESEARCH CENTER

Seismic Behavior of Bridge Columns Subjected to Various Loading Patterns

Asadollah Esmaeily-Gh.
Kansas State University

and

Yan Xiao
University of Southern California

PEER 2002/15
DEC. 2002

Seismic Behavior of Bridge Columns Subjected to Various Loading Patterns

Asadollah Esmaeily-Gh.
Assistant Professor
Department of Civil Engineering
Kansas State University

and

Yan Xiao
Associate Professor of Civil Engineering
Department of Civil and Environmental Engineering
University of Southern California

PEER Report 2002/15
Pacific Earthquake Engineering Research Center
College of Engineering
University of California, Berkeley

December 2002

ABSTRACT

As a part of an experimental program investigating the effects of a variable axial load on the seismic behavior of bridge piers, six scaled reinforced concrete bridge columns with circular sections were tested at the Structural Laboratory of the University of Southern California (USC). The primary experimental parameters were the axial load and loading pattern. The loading program included a combination of a constant, proportionally or nonproportionally variable axial load and a monotonic or cyclic lateral displacement. The objectives were to study the effects of different loads and the displacement paths for both the axial and lateral loading directions, to provide the benchmark data for dynamic and large-scale tests, and to evaluate existing material models and analytical methods.

The effects of the axial load and loading pattern were observed to be significant in the flexural strength capacity, the failure pattern, and the ductility and deformation of the columns. The plastic hinge formation was significantly different in the case of a variable axial load, requiring a modification of the existing plastic hinge models. The conventional analytical methods underestimated the flexural strength for high compressive axial loads in a monotonic analysis. Based on the experimental observations, several models for steel and concrete stress-strain behavior and two plastic hinge methods were developed and then employed in a computer program developed to address the analytical needs of the research.

Chapters 1 to 5 cover the preparation and phases of the experimental studies. Problem areas, research objectives, previous research on the subject, the development of experimental methods, the method developed and implemented in this research, the experimental program, and results are discussed. Chapters 6 to 9 discuss different material models and various analytical methods, and the models and methods developed in the research. The main features of USC_RC, the application developed to address the analytical needs of this research, are discussed, and the experimental results are compared with the analytical evaluations.

The experimental and analytical studies and conclusions are summarized in Chapter 10. Test results are included in terms of different graphs in Appendix 1. The computer code written in FORTRAN 95 and used in the aforesaid application is included as Appendix 2. Appendix 3 explains the simple multispring model developed to simulate a circular reinforced concrete section for a nonlinear degrading hysteretic moment-curvature analysis.

ACKNOWLEDGMENTS

This final project report is based on the dissertation presented by the first author under the supervision of Professor Yan Xiao, submitted to the Faculty of the Graduate School of the University of Southern California in partial fulfillment of the requirements for the degree of Doctor of Philosophy in Civil Engineering. The dissertation committee also includes Professors L. C. Wellford, J. C. Anderson, and N. Meshakati, of the Department of Civil Engineering, and Professor B. Yang of the Department of Mechanical Engineering.

Our special thanks go to Mr. Robert Bueche, previous manager of the USC Civil Engineering Laboratory, and to Mr. Lance Hill, current manager, for their technical support during the experimental phase of the research, and to Mr. Hui Wu for his kind assistance in performing the large-scale tests at various stages of this research program.

The research described in the report was funded by the Pacific Earthquake Engineering Research Center (PEER) and the National Science Foundation (NSF) for a three-year research project. The Pacific Earthquake Engineering Research Center is supported by the Earthquake Engineering Research Centers Program of the National Science Foundation under Award Number EEC-9701568.

CONTENTS

LIST OF FIGURES

LIST OF TABLES

1 Introduction

Compared to steel and other building materials, many factors make the response of reinforced concrete complicated: cracking and crushing of concrete, yielding, strain hardening of reinforcing steel, bond between steel and concrete, buckling and rupture of the reinforcement, confinement, creep, and shrinkage of concrete. Understanding the inelastic cyclic behavior of reinforced concrete (RC) structures subjected to different loading conditions has been the main subject of extensive research, and this research has led to significant improvements in the design practice.

Columns are the most essential and important structural elements in buildings and bridges. Structural columns are subjected not only to vertical loading effects due to gravity, but also to combined variable axial forces, moment, and shear due to actions such as earthquake loading. Owing to the "overturning moment," columns or piers in multi-column bents are subjected to variable axial forces corresponding to the direction of, and typically proportional to, the lateral forces. In a seismic event, the columns in a bridge are also subjected to vertical ground motions, which are nonproportional to the horizontal loading. It has been shown that in some cases, particularly for near-fault situations, vertical ground motions cannot be ignored (Bozorgnia, 1995). The effects of vertical ground motions are equally important for the design of buildings and bridge piers.

1.1 PROBLEM AREAS

A comprehensive research program was carried out at the University of Southern California, as part of a collaborative project with UCB, UCSD, UCI, and the Pacific Earthquake Engineering Research Center (PEER). The central focus of the research was to experimentally and analytically address the problems associated with the capacity assessment and performance of bridge piers. The main problem areas addressed by the team at USC are related to:

1. Insufficient testing data on bridge piers subjected to various nonsequential types of loading paths: Such data are needed to provide a more realistic characterization of performance of bridge piers. This characterization is important in development of the design guidelines, considering the effect of different loading paths, and in the validation and refinement of analytical models and tools. The response of bridge piers, subjected to pulse type loading, is quite different as compared with the response in typical sequential loading tests. Additionally, the behavior of columns in the "C"-type bents, frequently used in the construction of several bridge types, behave completely different depending on the direction and sequence of the horizontal displacement input.
2. Variable axial loads: Owing to the overturning moment, columns in multiple-column bents experience variable vertical forces corresponding to the direction of, and typically proportional to, the horizontal forces. Columns are also subjected to the vertical components of ground motion, which is nonproportional to the horizontal loading. Past earthquake records have shown that in some cases, vertical ground motions cannot be ignored, particularly for near-fault situations. For example, the lateral displacement ductility in a column, designed based on constant axial load, with a relatively low axial load ratio, can become unsatisfactory when the actual axial load due to the overturning effects or the vertical ground motion exceeds the balance axial load. The problem becomes even more significant when shear design is considered. The increase of axial load from the design level (typically 5% to 10% axial load ratio) to the level of the balance axial load results in the increase of column flexural capacity, thus increasing shear demand. On the other hand, changes of axial load from compression to tension can result in significant decreases in column shear strength.
3. In terms of capacity, both the strength and deformation of columns is dependent on the magnitude and direction of axial load. The loading path of the axial force also has significant effects on the hysteretic behavior.
4. Design implementation of the effects of various loading paths: The above effects need to be considered in the design of bridge piers. This is not only important for the design of new bridges, but also for the retrofitting of existing deficient structures.

1.2 RESEARCH OBJECTIVES

The overall objective of this research project is to investigate the seismic performance of RC bridge columns with circular sections, subjected to different loading conditions.

The experimental tasks are:

- to study the effects of different, quasi-statically loaded displacement paths.
- to study the effects of combined, nonproportional cyclic loading inputs for both the axial and lateral directions of columns.

From the analytical perspective, the experimental results are essential for

- the assessment of the adequacy and the calibration of the existing analytical tools.
- the evaluation of analytical methods. For example, the plastic hinge method in calculating the flexural deflection of an RC column is suspect for its adequacy for columns subjected to variable axial load.
- the assessment of various material models for their effectiveness in predicting moment-curvature or force-displacement responses.

2 Review of Experimental Research

Columns with circular sections reinforced transversally by spiral steel, which enhances the strength and ductility of concrete, have been used both in bridges and high-rise buildings. However experimental data on the performance of this type of section under different loading conditions are insufficient, specifically, on bridge piers subjected to nonsequential types of loading paths. The role of the axial load is very important in the ductility, strength, and stiffness, and energy dissipation. Most of the previous works in this regard has been limited to the effects of constant axial load on the flexural behavior of the RC members. The effects of a variable axial load on the general performance of RC structures has not been studied enough in comparison.

In terms of the type of the axial load, experimental works may be organized into two main categories: (1) all the works considering a constant axial load and (2) cases with a proportionally or nonproportionally variable axial load. The second category may be divided into two sub-categories, namely, cases with proportionally variable axial load and those with nonproportionally variable axial load.

2.1 CONSTANT AXIAL LOAD

Wong, Paulay, and Priestley (1993) studied the response of circular RC columns under multi-directional seismic forces. Sixteen circular RC column models with an aspect ratio of 2 and different spiral reinforcement were tested to investigate the sensitivity of the strength and stiffness of shear-resisting mechanisms to various displacement patterns and axial compression load intensities. Shear deformations were expected to be significant for these columns, particularly under low axial compression. The hysteretic performance and displacement ductility capacity of the columns were improved by increased spiral steel content or by increased axial compression. In comparison with uniaxial displacement paths, biaxial displacement patterns have led to more severe degradation of strength and stiffness. However, the displacement ductility capacity has not been observed to be sensitive to the type of biaxial displacement pattern. Simple orthogonal displacement patterns have been found to be sufficient to represent horizontal two-dimensional seismic effects. Current code provisions were found to underestimate the shear strength of circular columns. The authors propose a shear design procedure that enables the shear-strength displacement-ductility relationship to be estimated, while also including the effects of displacement history.

Priestley and Park (1987) through a review of a wide-ranging research project aimed at improving understanding of seismic performance of bridge substructures, have shown that current methods for predicting flexural strength invariably underestimate the true flexural strength by a substantial margin, particularly when axial load levels are high. They proposed a new design method for predicting the flexural strength and ductility of confined bridge columns.

Lehman and Moehle (1998) conducted an experimental study at the University of California, Berkeley, to explore the issues of actual column performance and the adequacy of available analytical methods, but their emphasis was mainly on the effect of the reinforcement ratio on column response. Their specimens were subjected to a constant axial load and a reversed cyclic lateral load. They concluded that variation of the longitudinal reinforcement ratio alters the column response. In particular, increased pinching was noted in the response of columns with low levels of longitudinal reinforcement ratios (0.75%). The displacement capacity was noted to decrease with a decrease in quantity of the longitudinal reinforcement. The largest ductility in their three tests on the scaled specimens occurred at a reinforcement ratio of 1.5% with a slight decrease in ductility capacity with a positive or negative deviation. They also concluded that assuming that the displacement capacity is limited by the compressive strain capacity of the confined core inaccurately predicts a trend of increasing displacement capacity with a decrease in the longitudinal reinforcement.

El-Bahy et al. (1999), in experimental studies on the cumulative seismic damage of circular bridge columns under earthquake excitation, showed two potential failure modes: low-cycle fatigue of the longitudinal reinforcing bars, and confinement failure due to rupture of confining spirals. They developed a fatigue life expression that they claim may be used in the damage-based seismic design of circular, flexural bridge columns.

Jaradat et al. (1998) studied the performance of existing bridge columns under cyclic loading with a constant axial load. The flexural and shear performance of older columns for purposes of seismic assessment and retrofit design particularly has been studied with regard to assessing the residual strengths present in degraded hinge regions. Their test variables included column aspect ratio, longitudinal reinforcing ratio, lap splice length, and retrofitting detail. Shear failures were observed both outside and within the plastic hinge regions. In the specimens failing in flexure, plastic hinge regions with poor confinement and lap splices experienced rapid flexural strength degradation. However, the degraded spliced region continued to carry the shear and axial loads applied through the column. They concluded that increasing amounts of longitudinal reinforcement resulted in a shear failure in the shorter specimens due to the increase in shear demand. In the specimens that had flexural-dominated failures, larger amounts of longitudinal reinforcement resulted in lesser pinching in the hysteretic curves but a higher rate of moment degradation. A smaller shear span-to-depth ratio caused an increase in the column shear demand. The specimens with larger span-to-depth ratios dissipated more energy and experienced less pinching in the hysteretic curves. Increasing the splice length at the column base resulted in a slight increase in column strength and a delay in the onset of splice degradation. On the basis of the presented experimental results of their study and comparisons of performance with the existing and proposed shear and flexural strength models, they concluded that the Priestley and Seible flexural strength model closely predicts the peak moment strength of the column plastic-hinge region with poor confinement and no lap splice. The model proposed by Priestley and Seible also underestimates the point of moment degradation due to bar buckling. This model also closely predicts the moment capacity, onset point and rate of degradation, and the eventual residual moment strength at large displacement levels for the column plastic-hinge region incorporating the poorly confined 20d and 35d lap splices.

Saatcioglu and Baingo (1999) experimentally studied the behavior of high-strength concrete columns with concrete strengths of up to 90 MPa. Large-scale columns were tested under different levels of constant axial compression and incrementally increasing lateral deformation reversals. The columns had a circular cross section and circular transverse reinforcement. Different volumetric ratios and grades of steel were used to confine the core concrete. Their results indicate that the deformability of high-strength concrete columns can be improved significantly through confinement. The inelastic drift capacity of columns can be improved to levels well beyond those usually expected during strong earthquakes.

Jaradat, McLean, and Marsh (1988) conducted a study to investigate the flexural and shear performance of existing columns for purposes of seismic assessment and retrofit design. The test variables included column aspect ratio, longitudinal reinforcing ratio, lap splice length, and retrofitting detail.

Numerous other studies relate to different aspects of piers, with either a circular section or other sections, under a constant axial load, and mostly subjected to a quasi-statically variable lateral load. Kowalsky, Priestley, and Seible (1999*)* conducted research on the shear and flexural behavior of lightweight concrete bridge columns in seismic regions; Priestley and Benzoni (1996*)* focused on the seismic performance of circular columns with low longitudinal reinforcement ratios; and Nadim, Saiidi, and Sanders (1999) studied the performance of rectangular piers with moderate confinement. Since the main framework of these studies has already been introduced, no further description will be presented except when necessary for details regarding a specific study.

2.2 VARIABLE AXIAL LOAD (PROPORTIONAL AND NONPROPORTIONAL)

Sheikh and Toklucu (1993*)* studied the behavior of RC columns confined by circular spirals and hoops. Their research has mainly focused on investigating the effect of the type, amount, and also the configuration of the lateral reinforcement on the behavior of the column under a monotonically varying axial load. No lateral force was applied, and the main concept has been directly related to the confinement effects.

Few analytical works have been done considering the effects of a variable axial load proportional to the moment of the lateral force on the response of RC structures. Benzoni et al. (1996) conducted research on the seismic performance of RC columns under varying axial load by studying the behavior of four circular RC bridge columns with different axial load regimes. The four columns were 0.46m (18 in.) in diameter and 1.83m (72 in.) high, tested in double bending. They were 0.4:1 scale models of 1.15m (45 in.) diameter bridge columns with 2.5 % and 5% longitudinal steel ratio. The specimens were tested under cyclic inelastic lateral displacements with axial loads either constant or varying as a function of the horizontal forces.

Gilbertsen and Moehle (1980), Abrams (1987), Emori and Schnobrich (1978), and Keshavarzian and Schnobrich (1984) considered the variation of axial load in their studies. Krenger and Linbeck (1986) are among the few researchers who have considered uncoupled variation of axial and lateral loads. Sadeghvaziri, Icriegh, and Fouch (1988, 1990) conducted analytical work investigating the effects of independently variable axial and lateral loads on the behavior of RC members. In *Behavior of RC Columns under Non-proportionally Varying Axial Load,* they developed a uniaxial flexural model in which the columns are represented with an assemblage of plane-stress and bar elements to model the concrete and the reinforcing steel. They have shown that nonproportional fluctuations in the axial force have a significant effect on the post-elastic cyclic response of RC columns. The results show that the hysteresis loops are not of the conventional type. Considering the lateral shear versus lateral displacement, the hysteresis loops demonstrate anomalies such as negative energy-dissipation capacity. The causes of these abnormal behavioral characteristics are explained in light of axial deformation and axial hysteresis energy. Furthermore, as a result of phasing, the hysteresis loops do not follow a unique pattern. Thus, the current discrete models are not adequate for the analysis of RC structures under uncoupled variations in axial and lateral loads.

Those properties of RC columns that are affected by such a loading condition are very important factors for seismic performance. They showed that as a result of this, the response of RC structures is significantly altered under biaxial earthquake motions. They concluded that there is a great need for further analytical and experimental studies on this subject especially considering other parameters. The effects of different degrees of concrete confinement must be investigated. The importance of this parameter on the flexural behavior of RC columns under zero or constant axial force is well established. They anticipated that it will have an even more pronounced effect under nonproportional variation of the axial force. The bond stress-slip relationship is significantly affected by cyclic loading. Under fluctuating axial force, considerably more alternate yielding in tension and compression will occur compared to the case of constant axial force. The effects of these and other parameters, such as the biaxial state of stress, must be investigated. Furthermore, they concluded that discrete analytical models must be developed that can account for the effects of changes in axial rigidity on flexural behavior.

3 Development of Experimental Methods

This chapter discusses existing methods used to test columns under simulated seismic loads. In particular the treatment of P-delta effects is specifically discussed. A large-scale testing facility developed at the USC Structural Laboratory was upgraded for testing columns subjected to variable axial load.

3.1 LATERAL LOADING UNDER CONSTANT AXIAL LOAD

Most of the research on the behavior of RC columns has been restricted to cyclic lateral loading with a constant axial load, as described in the previous chapter. However, different testing configurations are adopted depending on the nature of the equipment available.

3.1.1 Direct Axial Loading

Application of a direct axial load by an actuator or hydraulic testing machine is the first straightforward method. The key point in this method is that the axial load is perpendicular to the critical section under investigation; for example, the lateral load is applied to a point between the top and bottom of a specimen by an actuator (or a jack), while the top and bottom are fixed. Figure 3.1 shows the test setup used for testing high-strength concrete columns under simulated earthquake loading by Byrak and Sheikh (1997). The axial load is applied directly on the specimen, which is hinged at the two ends, where no lateral displacement is allowed. The point of application of the lateral load (or displacement) is between the two ends.

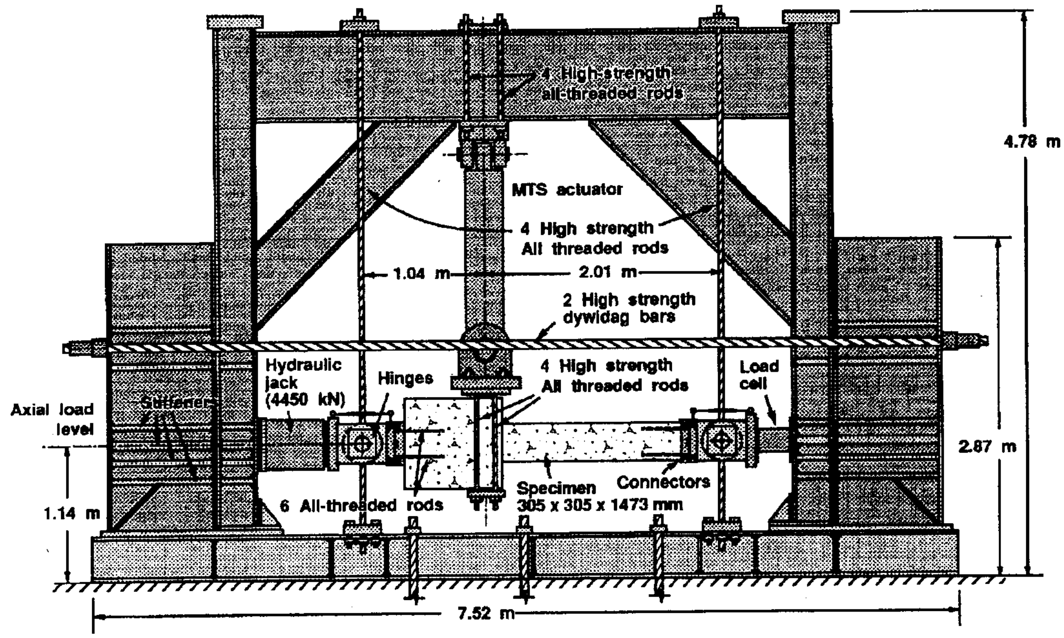

Figure 3.1 Schematic of Byrak and Sheikh (1997) test setup for direct axial loading

Figure 3.2 shows the loading arrangement by Park (Park and Joen, 1990) and others in tests on prestressed concrete piles. The two ends are pinned and the axial load is applied on one end while its direction is always kept vertical. Figure 3.3 shows the setup at the University of Canterbury for direct axial loading.

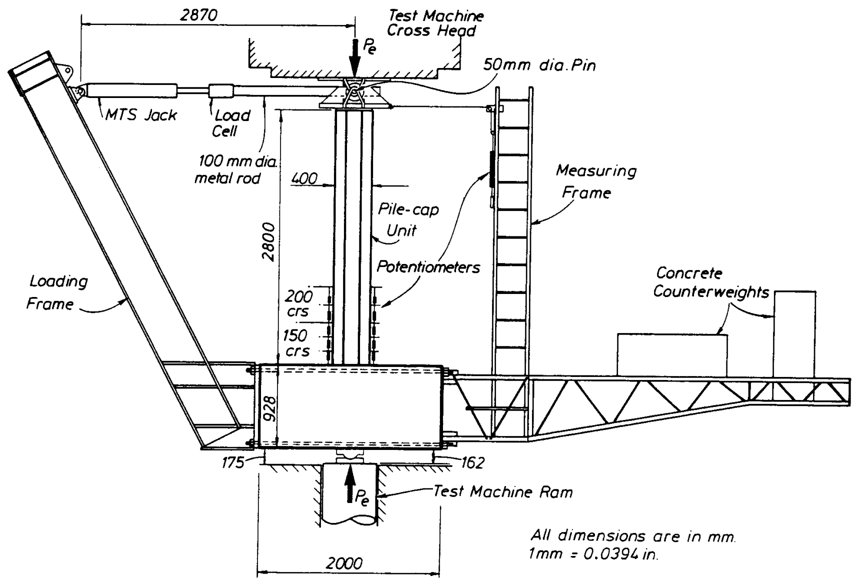

Figure 3.2 Loading arrangements by Park et al. (1990) for direct axial loading in their simulated seismic load tests on prestressed concrete piles

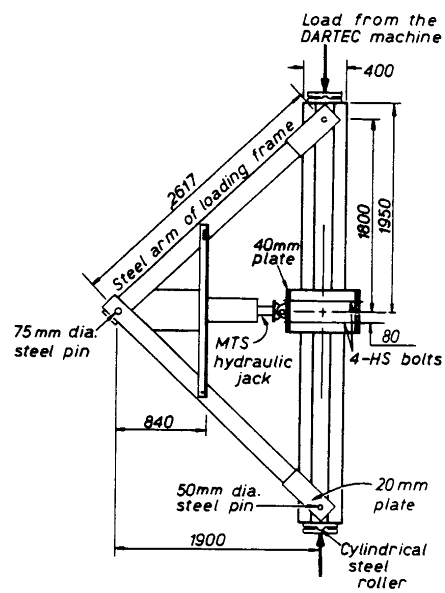

Figure 3.3 Direct axial loading arrangement used at the University of Canterbury

3.1.2 Post-tensioning

Another widely used method is to test a column in a cantilever configuration and to apply the axial load by the post-tensioning method. In this method, leftmost in Figure 3.4, an axial load is applied by a jack, which provides a post-tensioning force to the bars. The bars are hinged to the strong floor or frame at one end and to the jack at the other. The direction of this force follows the direction of the post-tensioning bar and varies according to the lateral displacement. Depending on the horizontal displacement and the corresponding angle, the load can be decomposed into the horizontal and vertical components, and the resulting P-Δ effect can be calculated at any point, namely the column interface with its footing.

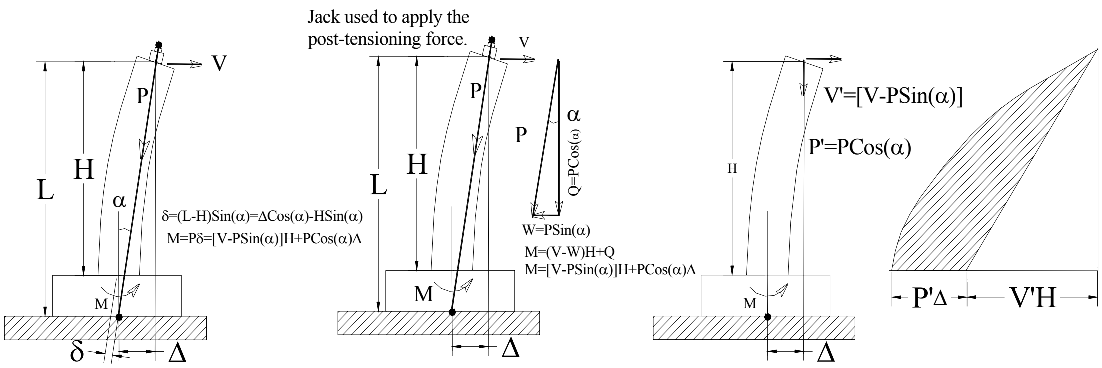

Figure 3.4 Effects of P-Δ in the conventional setup, as discussed here

A detailed discussion is provided here on the method used by Mander (Dutta, Mander, and Kokorina, 1999), where a complicated test configuration compared to the aforesaid post-tensioning method was employed to apply a vertical axial load so that the possible P-Δ error is avoided.

3.1.3 Mander et al.: Method and Discussions

Mander (Dutta, Mander, and Kokorina, 1999) proposed that then-existing test methods did not correctly model the P-Δ effects. Figure 3.5 shows the effects of axial loading on the specimen and contrasts them with how the tests should be conducted to properly reflect the true P-Δ effects.

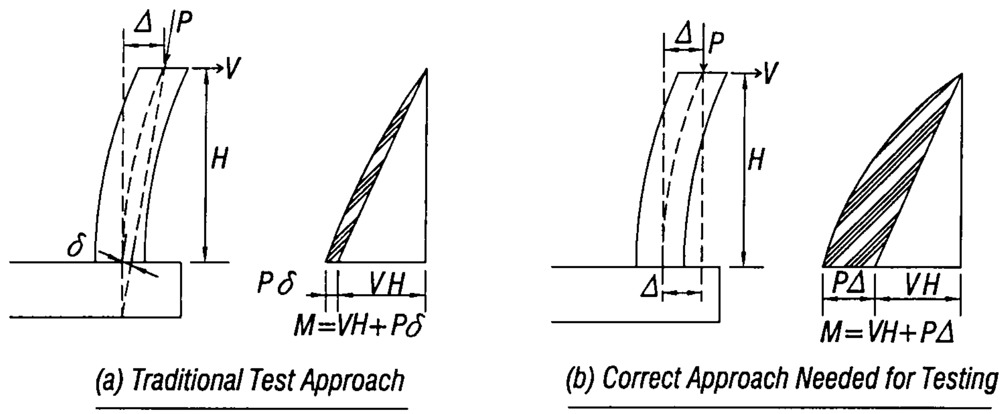

Figure 3.5 Effects of P-Δ in the conventional and modified setup, as discussed by Mander

From Figure 3.5 it is evident that at the base of the column where the bending moments are the largest when under lateral load, there is an additional secondary moment due to the column's lateral deflected shape. This secondary moment is equal to P-Δ that arises from the deviation in the axial force vector from the bent column axis. The experimental P-δ moment is less than the correct P-Δ moment, where P should always be aligned vertically.

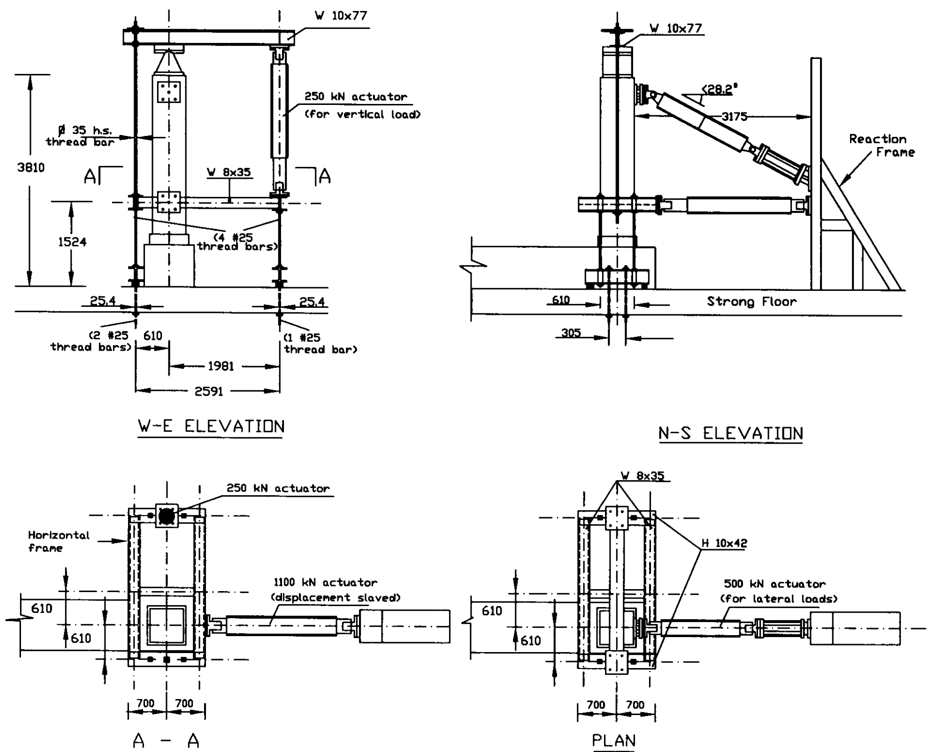

Figure 3.6 Modifications in test setup, proposed by Mander, for the application of the axial load

To rectify the experimental deficiency in the secondary P-Δ moments, it is necessary to ensure that the experimental axial load (as applied by an actuator system) be truly vertical. To this end a strong-floor-based column testing rig at the State University of New York, Buffalo, was modified as shown in Figure 3.6. The vertical load is applied by a lever beam system connected to a secondary frame. This frame is connected to a second (lower) actuator. The displacements of this actuator are slaved to the top actuator that is the primary driver in the experiment. The axial load is controlled by a vertical servo-hydraulic actuator (250 kN) mounted on the secondary frame at the eastern end and a 35 mm diameter high-strength threadbar at the western end via a lever beam mounted on top of the column. The frame is supported by two 32 mm diameter high-strength threadbars at the western end and two 25.4 mm diameter bars of the same variety at the eastern end. These bars in turn pass through specially constructed I-beams with oversized tubular gaps along the web and anchored at the bottom via washers and locking nuts. The I-beams were supported on elastomeric bearings and prestressed to the laboratory strong floor. The lateral load was applied to the specimen by a 500 kN capacity ±127 mm stroke MTS servo-hydraulic actuator at a height of 2712 mm from the top of the foundation beam. One end of the actuator was attached to the specimen through the actuator end plate and another end of the actuator was bolted to the extension and connected to the reaction frame. The angle of inclination of this top actuator was varied from 0 degrees in the variable amplitude testing to 26.2 degrees in the random seismic input testing. This was deliberately done to model the effect of uplift forces that arise from a combination of the framing action and vertical motion. A second "horizontal" actuator with a load capacity of 1100 kN and ±102 mm displacement capacity was attached to the horizontal frame and traced the same displacement pattern (displacement "slaved") as the top actuator. This automatically ensured that the line of application of the axial load was kept vertical at all times, thereby eliminating any possibilities of P-Δ error. To prevent sliding of the specimen under lateral load, the foundation beam was anchored to the laboratory's 457 mm thick strong floor by applying prestress of 250 kN to each of the 25 mm diameter high-strength threadbars. These threadbars passed through 76 mm steel pipes that were cast in the foundation beam, giving a total hold-down prestress of 1000 kN. Therefore, by assuming a conservative value for the coefficient of friction of about 0.5 between the concrete specimen and the concrete strong floor, the dependable resistance against sliding is 500 kN. This was considerably greater than the lateral load capacity expected for this class of specimen.

3.1.4 Discussion and Comments

The P-Δ effect, the primary issue discussed by Mander et al., can be viewed from a different perspective. The P-Δ errors in a conventional test setup with post-tensioning bars can be corrected by properly interpreting the data. There is no difference between the patterns of force application in Figure 3.4 and Figure 3.7, while the $P-\Delta$ effect may be considered as shown in Figure 3.7, where $M = VH + P\Delta$, and δ is as indicated in the figure. Now, even if the same δ is used as in Figure 3.4, as shown in the figure:

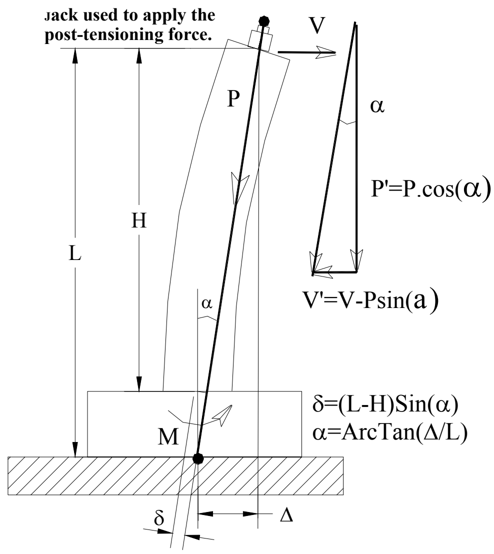

Figure 3.7 $P-\Delta$ effect as in Figure 3.4

$$\delta = (L-H)\sin(\alpha) = (L-H)\left(\frac{\Delta}{\sqrt{\Delta^2+L^2}}\right) \tag{3.1}$$

and the corresponding moment at the column base is:

$$P\delta = P(L-H)\left(\frac{\Delta}{\sqrt{\Delta^2+L^2}}\right) = P\left(\frac{L}{\sqrt{\Delta^2+L^2}}\right)\Delta - P\left(\frac{\Delta}{\sqrt{\Delta^2+L^2}}\right)H \tag{3.2}$$

or

$$P\delta = P\cos(\alpha)\Delta - P\sin(\alpha)\Delta H \tag{3.3}$$

Now, considering the moment at the column interface with the footing:

$$\begin{aligned} M &= VH + P\delta = VH + PCos(\alpha)\Delta - PSin(\alpha)\Delta H = \\ &[V - PSin(\alpha)]H + PCos(\alpha)\Delta \end{aligned} \tag{3.4}$$

Let $V^{'} = [V - PSin(\alpha)]$ and $P^{'} = PCos(\alpha)$, therefore:

$$M = V^{'}H + P^{'}\Delta \tag{3.5}$$

In the above equation, *P.sin(α)* is the restoring force of the post-tensioning bar, and *P.cos(α)* is the vertical load. As shown in Figure 3.5(b), it is clear that the true lateral force to the column is:

$$V^{'} = V - P\sin(\alpha) \tag{3.6}$$

and the vertical load is:

$$P' = P\cos(\alpha) \tag{3.7}$$

Note that $P' \approx P$, since α is typically small. It can be concluded that the conventional method of post-tensioning is valid without any deficiency so long as the true forces are used in data analysis.

3.1.5 Method Developed at USC Structural Lab

A system that enables testing of concrete columns in a large-scale model has been developed at the University of Southern California (Xiao and Henry, 2002). As shown in Figure 3.8, the testing system utilizes two actuators with 1,334 kN (300 kips) capacity for cyclic loading in both the lateral and axial directions of the column specimen. An axial force as large as 6,000 kN (about 1,300 kips) can be loaded through a specially designed lever arm that amplifies the force output of one of the actuators by six times. Figure 3.9 schematically illustrates the concepts of the lever arm system for axial loading. By setting the distance between the axis of vertical connectors and the column axis to be l/5 of the distance between the vertical actuator and the column axis, a force of 5 times the actuator force can be generated in the vertical connectors. By considering the vertical equilibrium condition of the lever arm, one can easily understand that the axial load applied to the column specimen is 6 times the vertical actuator force. As also shown in Figure 3.9, if a lateral displacement Δ is induced, the applied axial load becomes inclined, and thus the true vertical load subjected to the column is the vertical component of the applied axial load. It can be shown that for a small deformation (Δ <5%*h*), the true vertical load and the applied axial load can be considered approximately the same. On the other hand, the inclination of the applied axial load corresponding to Δ has a horizontal component (V1 and V2, Figure 3.10). Because this horizontal component is not negligible compared with the lateral load capacity of the column, it must be subtracted from the applied lateral load to obtain the true lateral force carried by the column specimen.

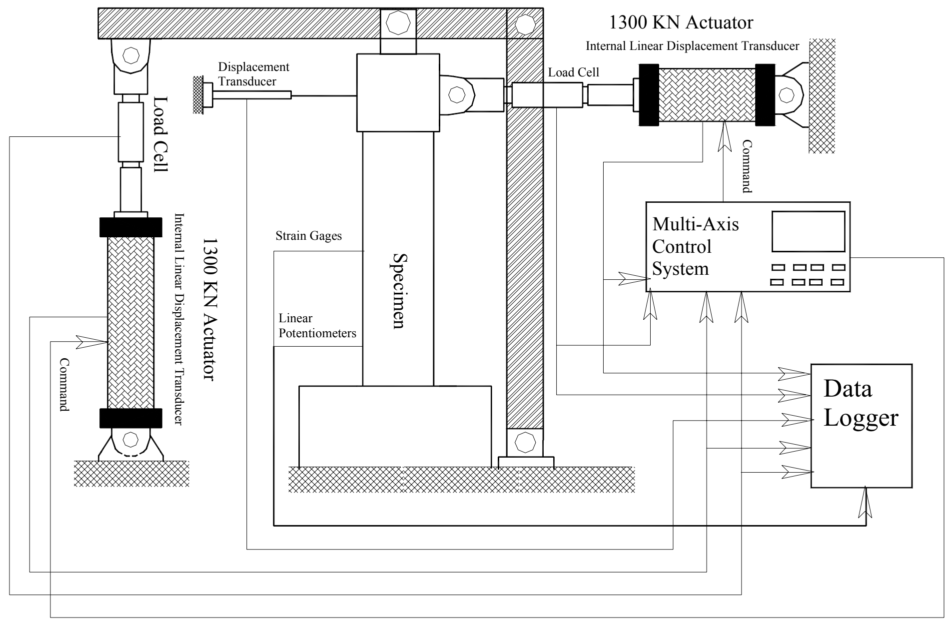

Figure 3.8 Outline of test setup for application of lateral force (displacement) and a constant, proportionally variable, or nonproportionally variable axial load

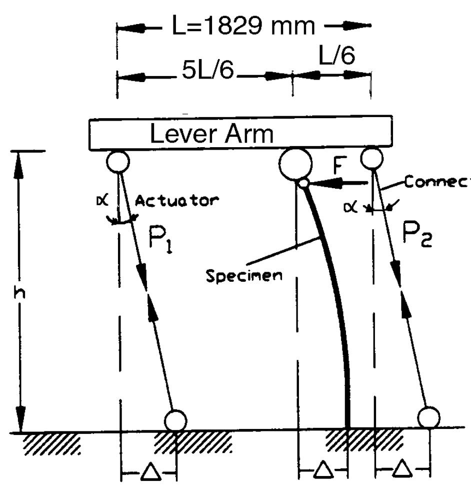

Figure 3.9 Lever arm system for axial loading

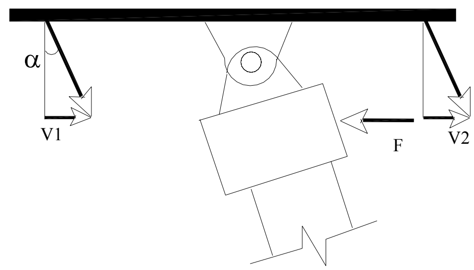

Figure 3.10 Restoring forces resulting from inclination

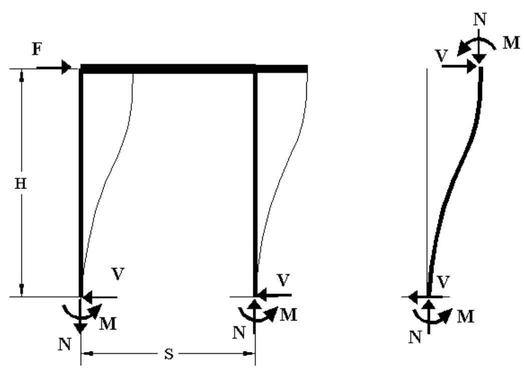

Figure 3.11 Overturning moment and resulting axial load

3.2 PROPORTIONALLY VARIABLE AXIAL LOADING

In a multicolumn bent, as a consequence of the overturning moment, *F.H*, axial forces, which are proportional to the lateral force, are imposed in the outermost columns (Figure 3.11). If the horizontal member is assumed to be rigid enough, the resulting reactions are as shown in the figure, in which

$N = FH/2S$ and $M = FH/4$

Therefore to simulate the aforesaid loading case, for a lateral force V applied on the column, we should apply an axial load proportional to the lateral force so that

$N/V = H/S$

where N is the axial force. Such a condition can be simulated by controlling the applied forces following the proportion (Figure 3.8). This proportionality can also be realized through an inclined force, where the angle of inclination is determined based on the actual structure to be simulated. The angle of inclination θ, has a tangent equal to the height/span ratio of *H/S*. The inclination angle of the actuator determines the coefficient of proportionality, which is approximately constant for small deflections.

For a case in which *H=2S*, the angle is $tan^{-1}(2)=63.43$ *degrees* and for a case in which *H=S*, the angle is $tan^{-1}(1)=45$ *degrees*. Figure 3.12 shows the setup configuration used for a proportionally variable axial load in the current study. The angle is 47.3 degrees, which is used as an angle close to 45 degrees due to instrument limitations.

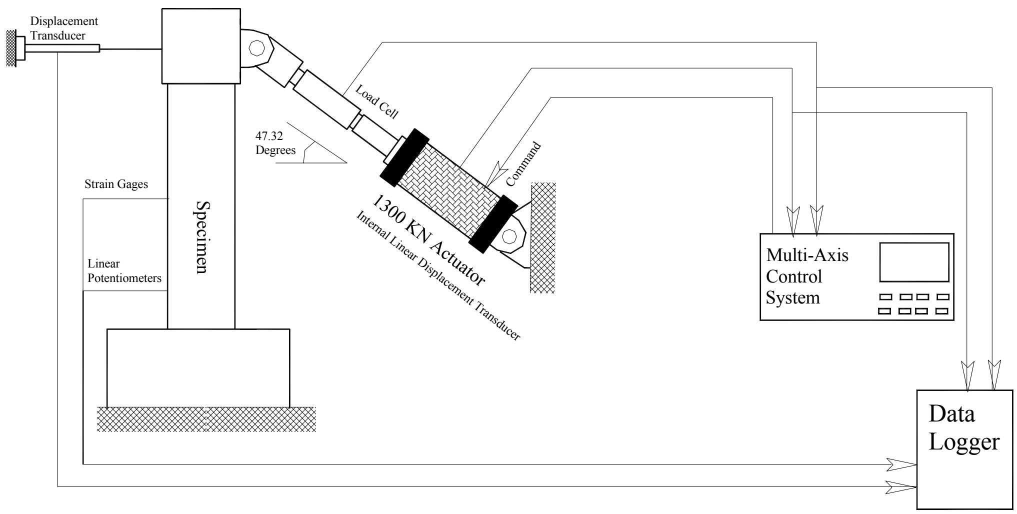

Figure 3.12 Setup configuration for a proportionally variable axial load

3.3 NONPROPORTIONALLY VARIABLE AXIAL LOADING

Besides the overturning effect where an axial load proportional to the lateral force is imposed, as discussed previously, columns are also subjected to axial loads that are nonproportional to horizontal loading due to the vertical ground motions. It has been shown that in some cases particularly for near-fault situations, the vertical ground motions cannot be neglected. The effects of vertical motions are equally important to the design of bridge piers. In this study, the large-scale testing facility at the USC Structural Lab was upgraded to simulate loading conditions with cyclic lateral forces and nonproportionally variable axial loads. As shown in Figure 3.8, the axial load applied by the vertical actuator and the horizontal force applied by the horizontal actuator were controlled to follow a predetermined path. To simulate a certain loading pattern, the effect of the restoring forces should be considered and implemented in the process of loading control.

3.3.1 Multi-Axis Loading Control System

The objectives of the overall research program required testing several specimens under specific loading patterns, in addition to the cases with a constant axial load and a proportionally variable axial load. To achieve a predetermined loading pattern in a test, a control system was developed. A brief description is presented here of the requirements for a simple case of the load or displacement control pattern, for which the actuators can be programmed through an interface with a computer.

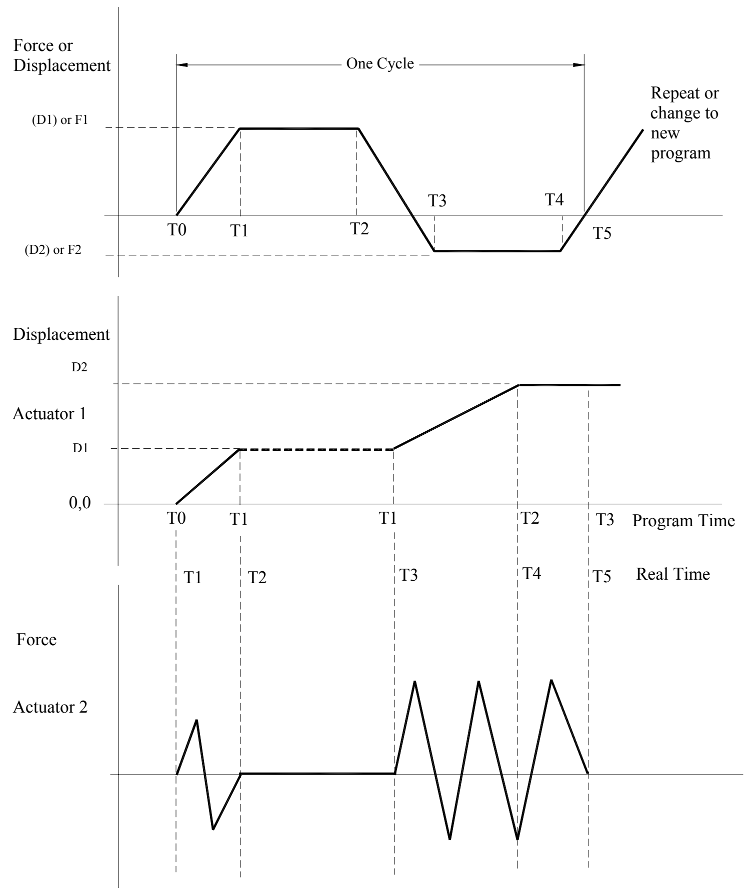

Figure 3.13 Requirement for the control system, and a sample of two axis controls (displacement and force)

General Requirements

Force Control

Control Input Parameters:

1. Target Force, F_1, (can be tension, compression, or zero)

2. Loading rate to reach F_1; or T1, time required to reach F_1
3. Time: T2 or (T2-T1); i.e., the duration for maintaining F_1
4. Target Force, F_2 (can be tension, compression, or zero)
5. Loading rate to reach, F_2 or T4
6. T5 or (T5-T4), i.e., the duration for maintaining F_2
7. Number of Repeating Cycles
8. Termination Command (the choice of terminating the process, if necessary, at any time.)

Displacement Control

Same as (1 to 8) above, except for target displacement Δ_1 and Δ_2 (instead of F_1 and F_2). Note that the two actuators may be used at the same time with different control parameters (force and displacement) and patterns. Figure 3.13 shows the requirements as stated above, and a sample application in which the first actuator is displacement control and the second one is force control.

Devices

The system, implemented at the USC Structural Lab for conducting tests with a nonproportionally variable axial load, consists of two actuators, the PMC-6270 Motion Control Box, and a PC (or a terminal). This system is used to operate the two existing actuators with predetermined load or displacement patterns. Each actuator can be in either force or displacement control mode, independently and simultaneously. This section provides a brief description of the system. The system has different features and capabilities that may be utilized based on the needs.

Actuators

The horizontal actuator has a stroke of 18 inches, with a valve that requires a voltage of 24 DC-V and a current of 2 amps for operation, and a servo (that drives the valve) which in turn is commanded by a command voltage of –10 Volts to +10 Volts, in the two different directions. The voltage and current required for valve operation are independent of the command voltage. It means that the current or voltage to control the valve comes from the control box and is programmed based on test requirements. This current or voltage directs the movement of the actuator and its rate, while the current and voltage for valve operation provides the energy for the operation and can be supplied by any other reliable source. The vertical actuator has a stroke of 9 inches, with a valve that does not require an external voltage and current for operation.

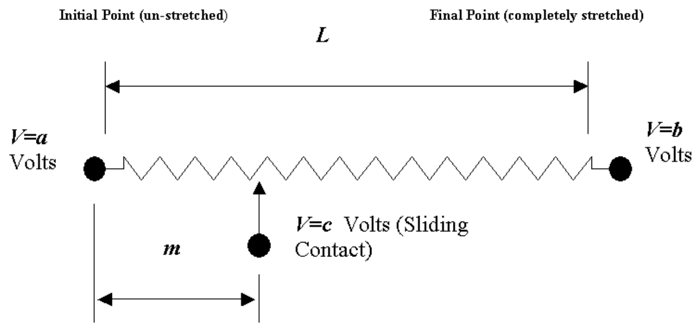

Figure 3.14 Internal linear displacement transducer

Both actuators have an internal LDT (Linear Displacement Transducer) which is actually a resistor installed along the longitudinal direction of the actuator. When a constant base voltage is applied to the resistor (e.g., *constant voltage=b-a*, as in Figure 3.14), the position of the actuator can be detected by the return voltage (feedback voltage) from the actuator, which comes from a sliding contact on the resistor. As an example, suppose that the total stroke of an actuator is L inches and that the LDT (actually the resistor) exactly covers this stroke length. It means that when the actuator is not stretched, the sliding contact is at the beginning, resulting in zero resistance between the initial point and the contact point; and when it is completely stretched (maximum stroke) the sliding contact is at the end of the resistor, resulting in the maximum possible resistance which is equal to the total resistance of the LDT resistor. Also assume that the actuator has been stretched for m inches from the completely unstretched condition. Since there is a linear relation between the resistance, current, and voltage ($V=IR$, where V=Voltage, I=Current, R=Resistance), the actuator position (amount of stretch) can easily be detected by the feedback voltage from the sliding contact.

$$m = (\frac{c}{b-a})L \tag{3.8}$$

This feedback is used by the control box to determine the command, considering the commanded position, the required velocity, and other parameters.

A homemade load cell is installed on each actuator, which can be used as a feedback device, for the applied force by the actuator when the actuator is used in the force control mode.

By using the base voltage and the load factor of the load cell, the coefficient to convert the feedback voltage to force can easily be obtained.

Each actuator has three main sets of wires. The first set includes 3 wires coming from the internal LDT, which are connected to the initial, sliding contact, and final points. The second set has 2 wires for the command, one (red wire) for the positive (+) command line, the other (black) for the negative (–). The third set includes the two outputs of the homemade load cell consisting of 16 electrical resistant strain gauges configured in two full-bridge circuits. The two outputs of the load cell can be used independently for measurement of the applied load by the corresponding actuator, or as a feedback for the force control mode cases, when a proper base voltage is used. The horizontal actuator has one more set of wires, used solely to provide the voltage and current required for the valve operation.

Control Box (PMC-6270)

The control box is a stand-alone, two axis motion controller. It does not need any computational device, like a PC, except as a terminal. This box provides sophisticated two axis control of any servo system driven by a voltage (from –10 to +10 volts) or a current (at different levels). The box implements a dual processor approach, comprising a microprocessor for executing high-level motion programs, and a digital signal processor (DSP) for high-speed, sophisticated servo control. The box can handle three different types of feedback: linear displacement transducers (LDTs), incremental encoder, or analog inputs (with the ANI option installed, as for the box). It should be mentioned that the internal LDTs of the existing actuators fall in the third group, which provide an analog signal feedback, while the external LDTs are usually digital, or pulse-based.

The control box has its own programming language. The user has the option of inputting a direct command. The single command issued by the user will only be executed and the process will stop until the next command. The commands can also be grouped as a program that can be saved either in the box or on the connected computer. In this case when the program is loaded, the commands within it will be executed in turn like any other procedural program on a computer. When using programs, special care should be given to the process and to the way the actuators are interrelated in terms of the movement or force in the program. It is always a good idea to interrelate the axes in the program so that failure of either one stops the whole process.

This guarantees that the test either proceeds on the proper path or, otherwise, stops. Support software for the Microsoft Windows and DOS operating environments is a standard provision with the 6270.

The features of the box may be summarized as follows:

- 1 or 2 axes of control for current-driven or voltage-driven servo systems; feedback from linear displacement transducer (LDT) or incremental encoder feedback (or voltage feedback with ANI option, as is the case for the system used in current study)
- Controls electric servo drives in the velocity or torque mode
- Digital signal processor (DSP) for servo control (digital proportional, integral, and velocity feedback, plus acceleration and velocity feedforward-PIV&F)
- DOS support disk
- Motion Architect for Windows
- Windows-based visual data gathering and tuning aid available when using the Motion Architect Servo Tuner option (can be ordered for an easier operational interface)
- 40,000 bytes of nonvolatile memory for storing programs; 150,000 bytes are available with the -M option (optional)
- Capability to interrupt program execution on error conditions
- Multi-axis teaching mode
- S-curve motion profiling
- 2-axis linear interpolation
- Ratio following, position following, advance and retard variable storage, conditional branching, and math capability
- Program debug tools, *single-step* and *trace* modes, breakpoints, and simulation of I/O
- Internal universal power supply
- Direct interface to RP240 remote operator panel (optional)
- Operates stand-alone or interfaces to PCs & PLCs
- 3-wire, RS-232C interface to PC or dumb terminal

- I/O capabilities (all I/O are optically isolated):
    - ±10V analog control output (both axes)
    - Shutdown output when there is no feedback or signals are contradictory (both axes)
    - Drive fault input (both axes)
    - LDT input (both axes)
    - Incremental encoder input (axis 1 only)
    - CW & CCW end-of-travel limit inputs (both axes)
    - Home limit input (both axes)
    - 38-bit analog inputs for joystick control and variable input (0.0V–2.5V)
    - 2 (trigger) inputs—used for hardware position latch
    - 24 programmable inputs (Opto-22™ compatible)
    - 24 programmable outputs (Opto-22™ compatible)
    - 2 auxiliary programmable outputs that can be configured for accurate output on position
- 6270-AM Option offers two ±10V, 14-bit analog inputs; can be used for position feedback (currently installed in the box)

The control box has several ports. Some are always used, while others are for advanced applications.. The ports DRIVE1 and DRIVE2 are used for axes commands and feedback. The AUX port is used for connecting the terminal or computer to the box. These three ports are the main ones needed in a test. The LDT1 and LDT2 ports can provide zero to 15, or –15 to +15 DC V, respectively, as a reliable constant DC base voltage for the LDTs (or load cells).

Computer

The computer serves mainly as a terminal but when loaded with the Motion Architect Software, may also be used to implement functions such as storing programs and manipulating output data. The computer should have the proper port for connection with the box. Although a standard 25-node-port can be used, a 9-node-port is preferable.

4 Experimental Program

Throughout the experimental program, six one-quarter-scale model columns were constructed and tested under the following loading conditions:

1. Constant axial load, with a displacement-controlled cyclic quasi-static lateral force
2. An axial load proportional to the displacement-controlled cyclic quasi-static lateral force simulating the actual loading of the columns, considering the overturning moment
3. A monotonic displacement-controlled lateral force with a constant axial load
4. A monotonic displacement-controlled lateral force without any axial load
5. A monotonic displacement-controlled lateral force, with a nonproportionally variable axial load
6. Same as case 5, with a difference in the pattern of the axial load.

The objective of the research was to study the overall performance of the RC columns with circular sections transversally reinforced by spiral under different loading conditions. The experimental data were also used to verify the analytical models and methods.

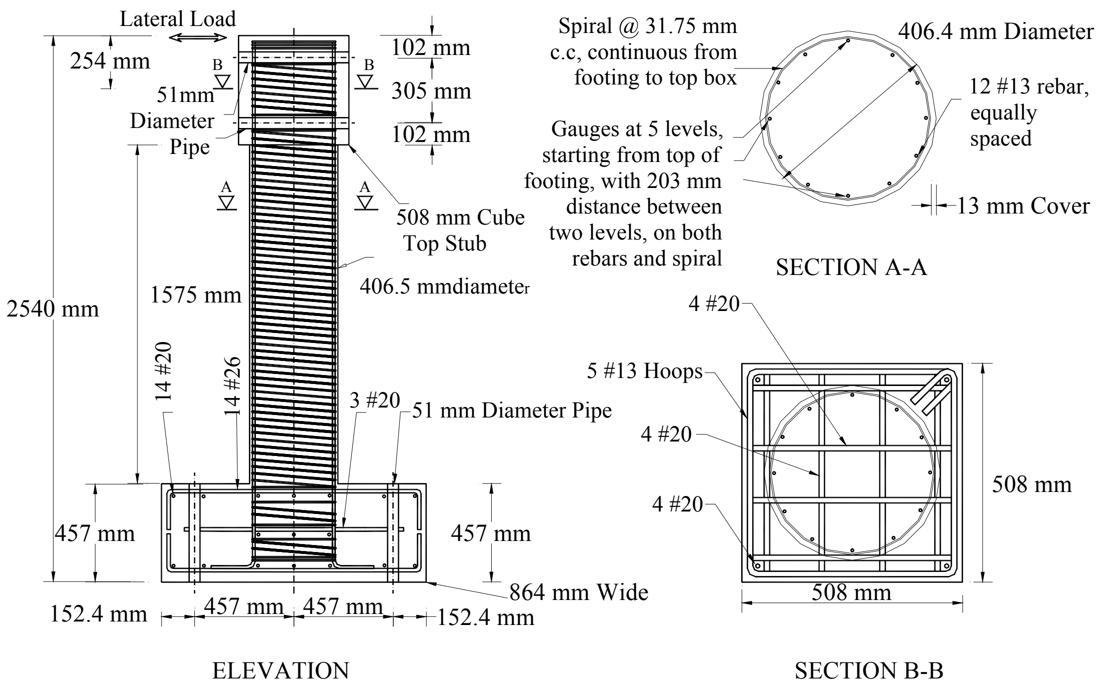

Figure 4.1 Details of the specimens

4.1 MODEL COLUMN

Five of the model columns had a circular section with a diameter of 406.4 mm (16 in.), and a total height of 2082.8 mm (82 in.) above the top of the footing. The effective length of the column was 1828.8 mm (72 in.) from the top of the footing to the application point of the lateral force. The footing was 863.6 mm (34 in.) wide, 1219.2 mm (48 in.) long with a thickness of 457.2 mm (18 in.). The longitudinal reinforcement consisted of 12 #13 (#4 English) Grade 60 bars equally distributed around the section. The confinement was a W2.5 Grade 60 spiral, spaced at 31.75 mm (1.25 in). The clear cover to the spiral was 12.7 mm (0.5 in.). For the sixth specimen, the diameter of the column was 432 mm (17 in.) with all other specifications the same as for the other five specimens. Details are shown in Figure 4.1 and tabulated in Table 4.1.

Table 4.1 Reinforcement details of specimens

Specimen Name	Grade	Reinforcement		Steel Ratio(%)		Concrete Type	Lateral Force	Axial Load
		Longitudinal	Transverse	Longitudinal	Transverse			
PEER-Column #1	G60	12#4	W2.5 @1.25" Spiral	1.17	0.52	1	Cyclic	$30\% A_g f'_c$
PEER-Column #2	G60	12#4	W2.5 @1.25" Spiral	1.17	0.52	1	Cyclic	$\tan(47.32^0)$ $LateralForce$
PEER-Column #3	G60	12#4	W2.9 @1.25" Spiral	1.17	0.52	2	Monotonic	$30\% A_g f'_c$
PEER-Column #4	G60	12#4	W2.9 @1.25" Spiral	1.17	0.52	2	Monotonic	None
PEER-Column #5	G60	12#4	W2.5 @1.25" Spiral	1.17	0.52	2	Monotonic	Non-Proportionally Variable
PEER-Column #6	G60	12#4	W2.5 @1.25" Spiral	1.17	0.52	2	Monotonic	Non-Proportionally Variable

Note: 1 inch = 25.4 mm, bar #4 = #13 in SI.

Table 4.2 Experimental material properties

Specimen	Grade	Nominal Yield Strength (ksi)	Nominal Modulus of Elasticity (ksi)	Actual Yield Strength (ksi)	Actual Ultimate Strength (ksi)	Modulus of Elasticity (10^3 ksi)
				Average	Average	Average
Rebar, #4	G60	60	29000	71	84	20
Spiral, W2.5	G60	60	29000	68	107	23.8
Spiral, W2.5	G60	60	29000	68	107	23.8
Concrete-Type1	NS	N/A	N/A	N/A	7.3	N/A
Concrete-Type2	NS	N/A	N/A	N/A	7.15	N/A

Note: 1 ksi = 6.9 MPa

4.2 MATERIAL PROPERTIES

The material properties are summarized in Table 4.2. The steel grade was G60 with a nominal yield stress of 414 MPa (60 ksi). The steel was tested at the USC Structural Lab. The actual yield strength, ultimate strength, and the modulus of elasticity of the rebar and the spiral are summarized in Table 4.2. The normal-strength concrete was obtained from a local ready-mix plant. The concrete strength was tested to be 49.34 MPa (7.15 ksi), using 6 cylindrical specimens for the first two specimens (tested on the first phase of testing) and 50.37 MPa (7.3 ksi) for the other four specimens (tested in the second phase).

4.3 CONSTRUCTION

The specimens were constructed in the Structural Lab at USC. The strain gages were applied at the predetermined locations of selected rebars and then the steel cages were made, including the longitudinal and transverse reinforcement. The columns were fixed at the center of the footing cage, as the footing cages were constructed. Casting using ready-mix concrete was done in two steps: first the footings and then the column with the top stub. Before casting the column and top stub concrete, the strain gages were applied at the proper locations on the spiral.

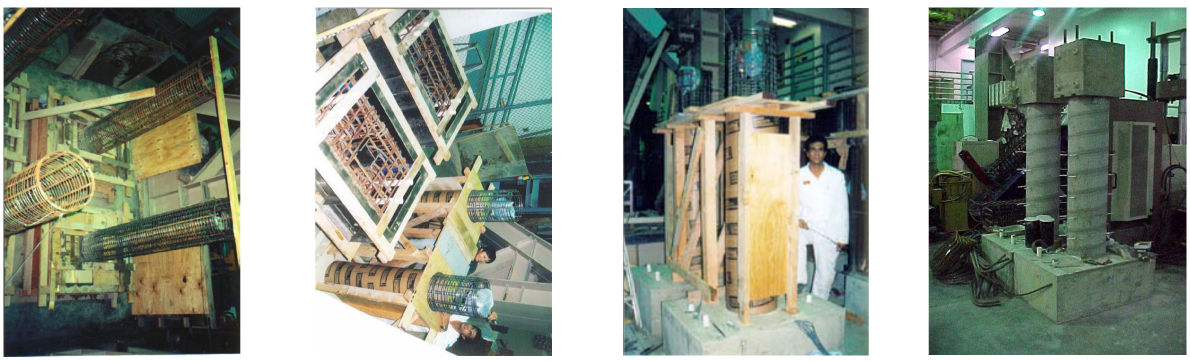

Figure 4.2 Construction of specimens

The top stub was constructed as a 508 by 508 mm (20 in. by 20 in.) cube centered at a height of 1829 mm (72 in.) with respect to the footing top surface. Four threaded bars were placed in the top stub to be used for connections required when a variable axial load was applied. Figure 4.2 shows the columns during construction, before casting concrete, and after the footing was completed, before casting concrete for the main column and the top stub.

4.4 INSTRUMENTATION

The applied forces were measured using calibrated load cells. The horizontal displacement was detected using a linear potentiometer with a travel stroke of 457 mm (18 in.). Two other linear potentiometers were used to measure the axial deformation of the columns during the test. In order to have a good understanding of the behavior of the column and the section, it is important to have enough experimental data to study the flexural deformation, curvature at different levels, and strain distribution over the cross section at different levels. To achieve this goal, 5 levels equally spaced at 8 inches apart, starting on the top of the footing were determined as shown in

Figure 4.3, and 3 strain gages were applied on the spiral at three locations at each level. At each level, 3 longitudinal bars were also gaged. The total number of the gages adds up to 30. Besides the strain gages, 10 linear sensors were installed on two opposite sides of the column, shown in Figure 4.3. The curvature of the sections at different levels can be calculated both by using the data from the linear sensors at two opposite sides, and by the strain gages applied at the same positions on the rebars. The first is an average of a certain length of the column, while the second is the curvature at a specific level provided the strain gage data are within a reliable range.

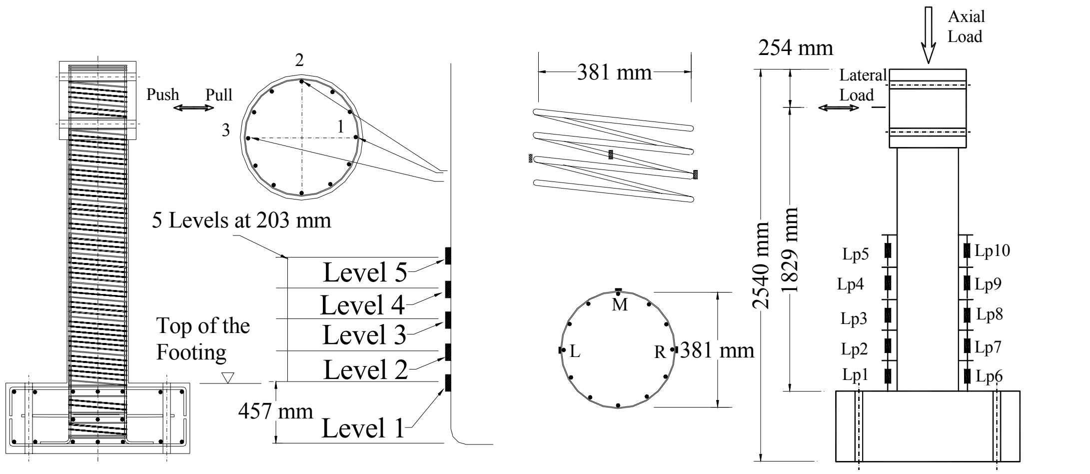

Figure 4.3 Location of strain gages, and linear potentiometers on the specimens

4.5 TEST SETUP

Two different testing configurations were designed for the six specimens. For the first test, a constant axial load equal to 30% of the $A_g f'_c$ was applied during the test. The test setup is shown in Figure 4.4. The axial load was applied by a vertical actuator, which was force controlled, so that a constant axial force was applied. The horizontal or lateral quasi-static cyclic load was applied by the horizontal actuator as shown in the figure. For the second column, the axial load was variable and proportional to the cyclic lateral load. The test setup for the second column is shown in Figure 4.5 in which an inclined actuator force was applied to produce an axial force proportional to the horizontal lateral force, simulating the actual case of lateral load with the overturning moment. The loading condition for the columns is schematically shown in Figure 4.6 (left and right).

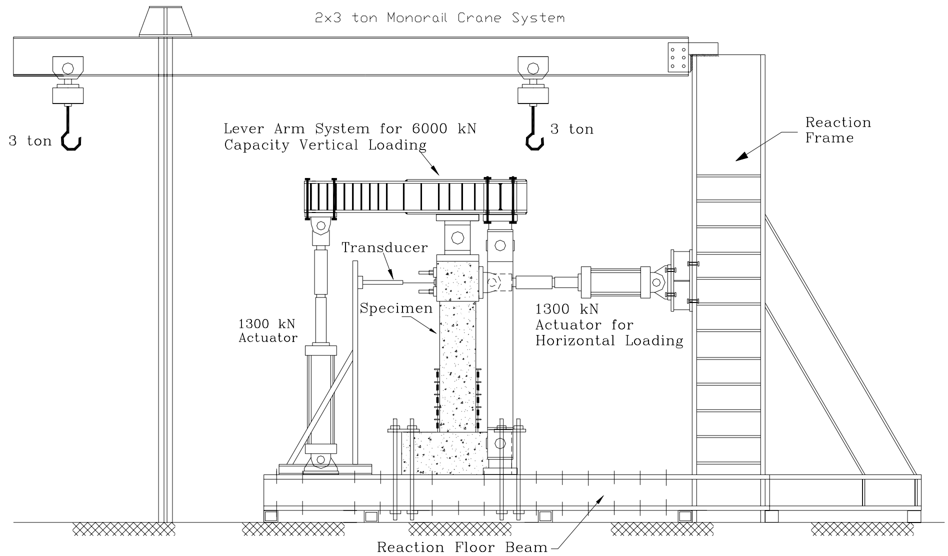

Figure 4.4 Test setup for tests 1, 3, 4, 5, and 6

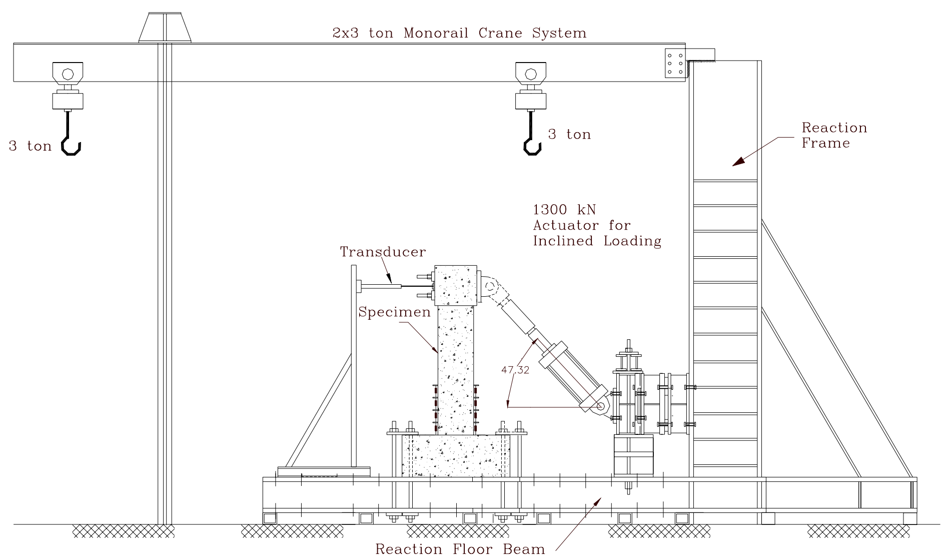

Figure 4.5 Test setup and configuration for test 2

4.6 LOADING PROGRAM

As shown in Figure 4.7 (a), the standard lateral loading procedure used for the first two tests was based on the lateral drift ratio, Δ/H, defined as the ratio of the lateral displacement divided by column height. Displacement reversals in the push and pull directions were symmetric. One loading cycle applied corresponded to an increment of 0.25% drift ratio until Δ/H=1% was reached. Three cycles were attempted thereafter for each of the peak drift ratios, Δ/H=1%, 1.5%, 2%, 3%, 4%, 6%, etc. The vertical loads were different in the first two cases. For the first specimen, a constant axial load, equal to 30% of $A_g f'_c$ was applied. For the second specimen the axial load was proportional to the lateral force.

The third specimen was tested under a constant axial load of 30% of $A_g f'_c$ and a monotonically increasing lateral displacement controlled load up to the failure of the specimen. The loading condition for the fourth specimen was like that of the third except for the axial load, which was zero. The fifth test was carried out under a monotonically increasing lateral displacement controlled force, while the axial load was nonproportionally variable, fluctuating between +30% and –10% of $A_g f'_c$. The loading condition for the sixth test was like that of the fifth test except for the pattern of the axial load. Figure 4.7 shows the general loading conditions for tests one through six.

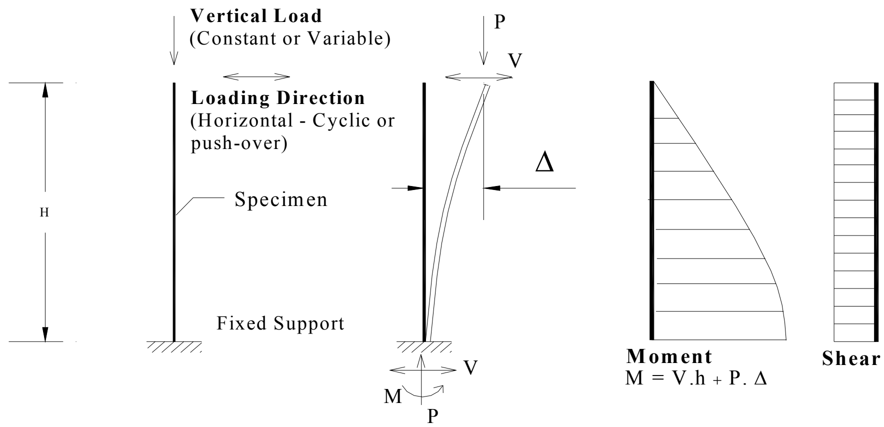

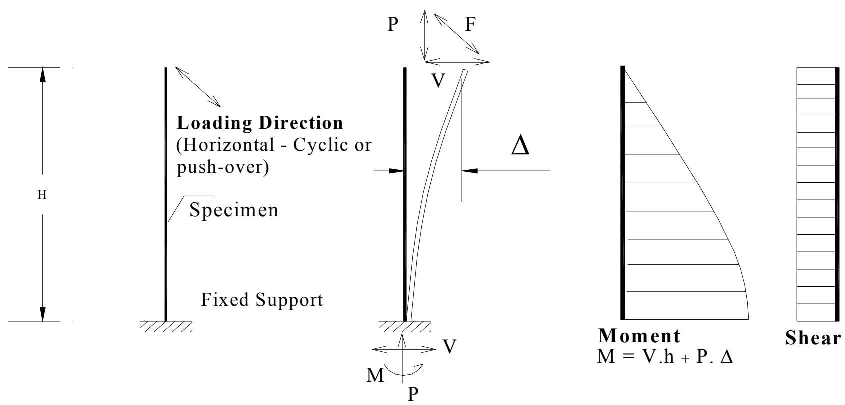

Figure 4.6 Loading condition for specimens 1,3,4 (without axial load P), 5, 6 (top), and specimen 2 (bottom)

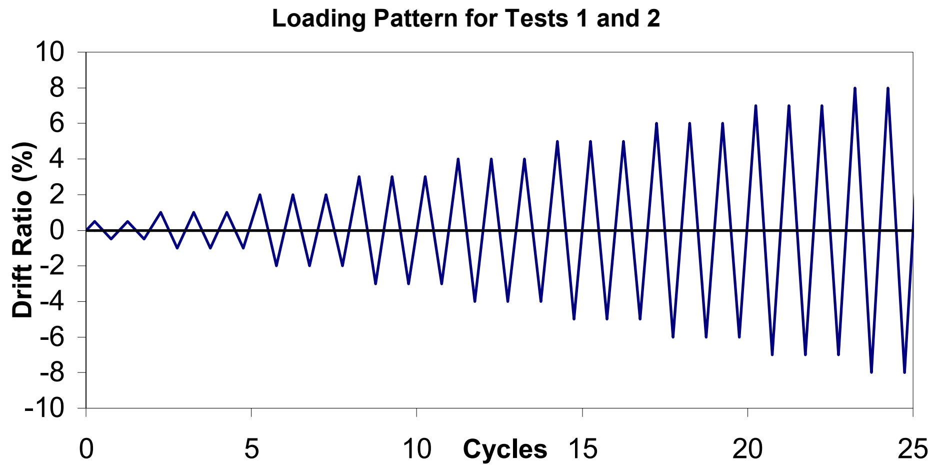

(a)

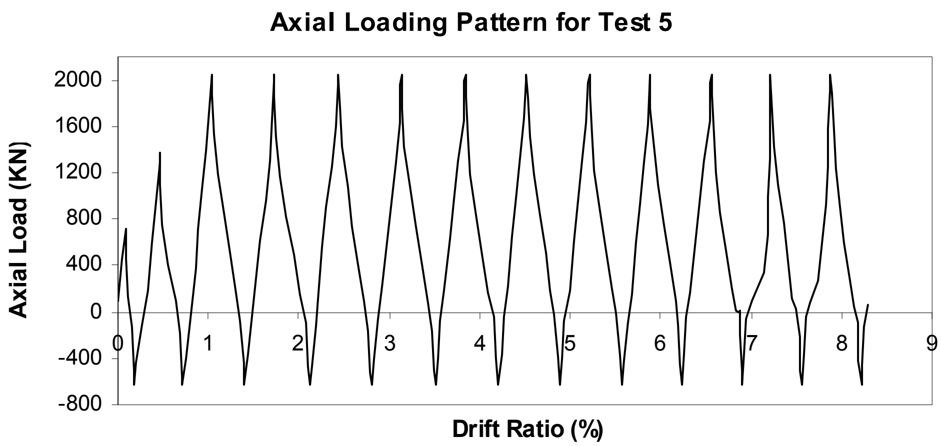

(b)

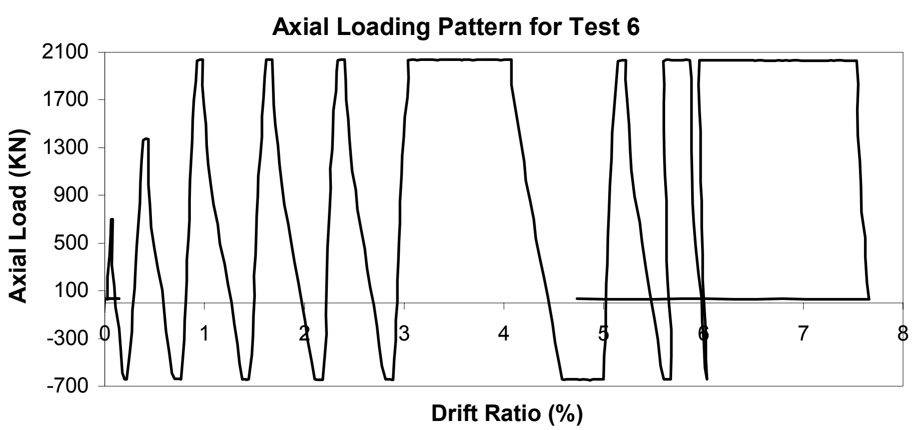

(c)

Figure 4.7 Loading condition for tests 1 and 2(a), 5(b), and 6(c)

4.7 PRELIMINARY ANALYSIS

Before the two tests, the yield strength corresponding to the first yield of the critical section and the maximum flexural strength and corresponding deflections were estimated for the specimens using the computer program USC_RC that was developed to analyze the behavior of RC members with different sections subjected to various quasi-static loading conditions. USC_RC is a user-friendly Windows-based application capable of working in either the SI (Système International) or English Units system. The program can handle RC columns with different cross sections and axial loads. The analysis can be done both for monotonic and cyclic (employing the hysteretic behavior of the material) cases, and the hysteretic response of the member can be predicted. The analysis is based on the fiber model, in which the section is divided into infinitesimal elements, which in turn replaces the member with longitudinal fibers.

For the first specimen, due to the high axial load the crushing of the concrete proceeded the yielding of the longitudinal bars, and was predicted to be at a force of 129 kN (28.75 kips) and a displacement of 15.11 mm (0.595 in.), corresponding to a drift ratio of 0.82%. All the predicted values are summarized in Table 4.3 for the first test. These predictions were compared to the experimental results to investigate the analytical tools used in the prediction, especially in cases of cyclic loading and to consider the hysteretic response of the material.

Table 4.3 Analytical predictions (by USC_RC) for the first test

Analytical Predictions	Displacement mm (In)	Drift ratio (%)	Horizontal Force kN (Kips)	Axial Load kN (Kips)
First Yield	15.11 (0.595)	0.82	129 (28.75)	1917 (431)
Maximum Strength	24.13 (0.95)	1.32	171.2 (38.5)	1917n(431)
Failure	53.44 (2.1)	3	169 (38)	1917n(431)

An estimate of the maximum horizontal force and corresponding displacements in the two different directions for the second specimen, where the axial load varies proportionally with the horizontal force, can be made manually as follows. First, the moment-axial force interaction curve for the section is calculated when the strain in the outermost concrete fiber is equal to the strain of confined concrete at maximum strength. Based on the test setup, the relationship between the moment and axial force, ignoring the geometrical nonlinearity and also small angle variations imposed by the deflection, is derived as follows:

$$F_h = F\cos(\alpha) \tag{4.1}$$

$$N = F\sin(\alpha) \tag{4.2}$$

where F is the inclined applied force, F_h is the horizontal force and N is the proportional axial load.

$$M = L'F_h \tag{4.3}$$

where M is the moment at critical section. Therefore :

$$N = \frac{1}{L'}\tan(\alpha)M \tag{4.4}$$

If a constant initial axial load is present, then:

$$N = \frac{1}{L'}\tan(\alpha)M + P^0 \tag{4.5}$$

where P^0 is the initial axial force. In our case, the initial axial load was zero. By using the proper values, the interaction curve and moment axial force relationship curves could be plotted and the intersection points predicted as the maximum lateral force and corresponding axial force in the two opposite directions. For the case of the test, the predictions were made by USC_RC, which can handle cases with proportionally variable axial loads. The predictions for this test are summarized in Table 4.4.

Table 4.4 Analytical predictions for the test with proportionally variable axial load

Analytical Predictions	Push Direction (Negative Axia Load)				Pull Direction (Positive Axial Load)			
	Displacement mm(In)	Drift Ratio(%)	Horizontal Force kN (Kips)	Axial Load kN (Kips)	Displacement	Drift Ratio(%)	Horizontal Force	Axial Load
First Yield	10.36 (0.408)	0.57	37 (8.33)	-40 (-9)	-10.72 (-0.422)	-.58	-43.4 (-9.75)	46.7(10.53)
Maximum	120.4 (4.78)	6.63	73.7 (16.56)	-79.6 (-17.9)	-111.5 (-4.39)	-6.1	-89.34 (-19.63)	94.33(21.2)
Failure	147.1 (5.79)	8	71.7 (16.1)	-77.34(-17.4)	-138.43 (-5.45)	-7.6	-86.5 (-19.4)	93.4 (21)

During the test, the angle changes as the horizontal deflection is imposed, but the effect is relatively small and is ignored. Analytical predictions for the third test are similar to those predicted for the first test, as shown in the Table 4.3. The results of the analytical predictions for test 4 with zero axial load are summarized in Table 4.5.

For tests 5 and 6, the analytical predictions were made by analyzing the response under a monotonically increasing lateral displacement subjected to a predetermined axial load pattern. The results of the analysis will be discussed when the experimental results are compared with analytical predictions.

Table 4.5 Analytical predictions by USC_RC for the fourth test

Analytical Predictions	Displacement mm (In)	Drift ratio (%)	Horizontal Force kN (Kips)	Axial Load kN (Kips)
First Yield	10.5 (0.415)	0.58	40 (8.9)	0.
Maximum Strength	117.3 (4.62)	6.4	80 (18)	0.
Failure	149. (5.86)	8.1	78 (17.5)	0.

The computer program developed and used to address the analytical needs and the material models and analytical methods developed and used during the analytical phase of this research are discussed in detail in the analytical part of this report.

5 Experimental Results

5.1 OBSERVATIONS

5.1.1 Specimen One

The displacement in the first step of loading cycles was approximately 25% more than the predicted displacement at the first yield. Concrete crushing proceeded the yielding of the longitudinal reinforcement due to the high level of axial load. So at the first step, with a drift ratio of 0.5%, slightly visible cracks formed near the footing. At a drift ratio of 1% (1.8 mm deflection) the cracks widened more and spread to a height of 81 mm above the footing surface. As the displacement reached a drift ratio of 2% (3.66 mm), slight crushing was observed due to spalling of the cover concrete within a height of 200 mm above the footing. At a drift ratio of 3%, the spalling spread up to a height of 400 mm, but no flexural failure due to compressive failure of the confined concrete was observed. At this stage, the cover concrete of the footing near the column was partially removed. The rupture of the spiral at 2 consecutive levels near the footing, followed by buckling of the furthermost rebar, occurred at the first cycle of a drift ratio equal to 4% (73 mm), causing crushing of the concrete near the footing and a severe degradation in strength. The total length of the crushed concrete was about 400 mm near the footing surface, implying formation of a plastic hinge near the footing. The test was continued for the 2 consecutive cycles, when the column failed in flexural mode. During all the tests, no damage was observed for the column portion above a length of 810 mm. From the ductility standpoint, assuming the first yield of the longitudinal steel as the yield point, corresponding to a drift ratio of 0.72%, the column achieved a ductility of slightly more than 6 before the flexural failure. Figure 5.1 shows different stages during the first test, and Figure 5.2 shows the failure pattern of the specimen. As was observed during the test, the concrete has crushed over the same height at the two opposite sides of the column, as expected, due to a constant axial load.

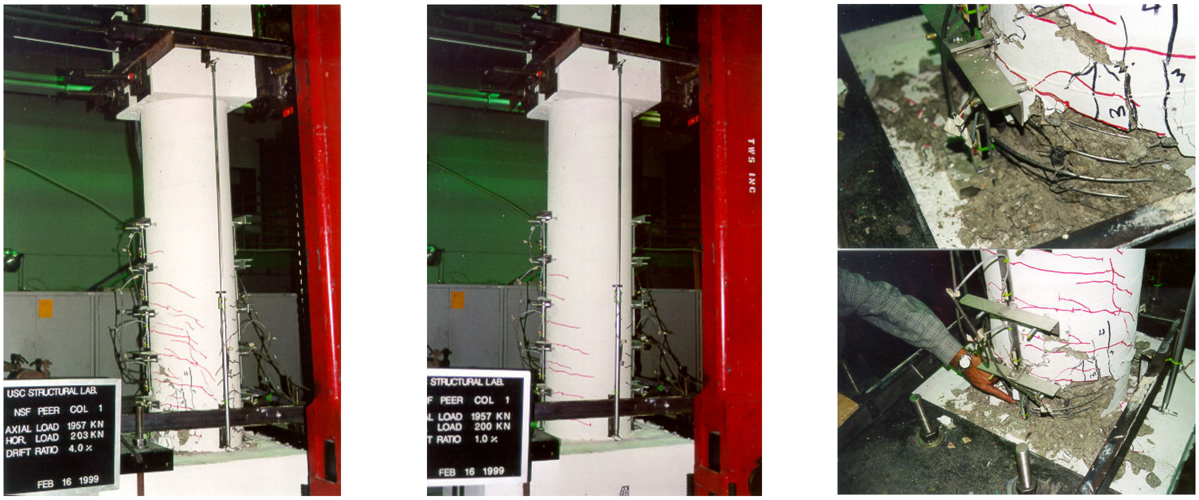

Figure 5.1 **Specimen one at drift ratios of 1%, 2%, and 4%. Expansion of the confined concrete near the footing is visible at a drift ratio of 4%(d).**

Figure 5.2 **Failure pattern of specimen one. Expansion of the confined concrete, rupture of spiral, and buckling of the main bars. Specimen failed in the flexural mode under a relatively high axial load.**

5.1.2 Specimen Two

The axial force in the push and pull directions for test 2 was small enough for the steel to yield first. This occurred at a horizontal displacement of about 9 mm (0.5 % drift ratio) in the push direction and at a horizontal displacement of 9.7 mm (0.53 % drift ratio) in the pull direction. In the first step of the displacement control load, the applied displacement was approximately around the first yield displacement (0.5% drift ratio) in the push and pull directions. After the third cycle of the first step the cracks were visible all the way up to the top of the column, which distinguishes this test from the first one because of the tensile axial load in the push direction. At the first cycle of a drift ratio of 3%, minor concrete crushing occurred at the interface of the column and footing, on the pull side, where the axial load is compressive; in the following cycles of this step, no further crushing of the concrete was observed. At a drift ratio of 4% the concrete crushed within a height of about 100 mm on the pull side while the height of the crushed concrete was around 70 mm on the push side. At the first cycle of 6% drift ratio, the concrete crushed more over a length of approximately 178 mm near the column bottom in the pull direction, and about 130 mm in the push direction. Apparently, the differences in direction and magnitude of the axial load caused significantly different damage patterns in the column. At the second cycle of 6% drift ratio, the furthermost rebar on the push side buckled and when the load was reversed, straightened leaving a gap between the rebar and the spiral. The same behavior was observed on the other side when the reversal load was applied. At the third cycle of 6% drift ratio, two adjacent spirals ruptured followed by the buckling of the nearby rebars. At this stage, even if the crushing of the concrete was considerable in a relatively small region near the footing, compared with the first column, no spalling was observed. The test was continued for the next step at a drift ratio of 8%, at which the two buckled rebars ruptured, followed by a severe degradation in the horizontal load capacity. The specimen failed in the flexural mode. Figure 5.3 shows different stages of the test, and Figure 5.4 the failure pattern of the column. As observed during the test, the difference in the length of the crushed concrete at opposite sides of the column was slightly visible. The figure shows the first crushing on the pull side, whereas no crushing was observed on the push side.

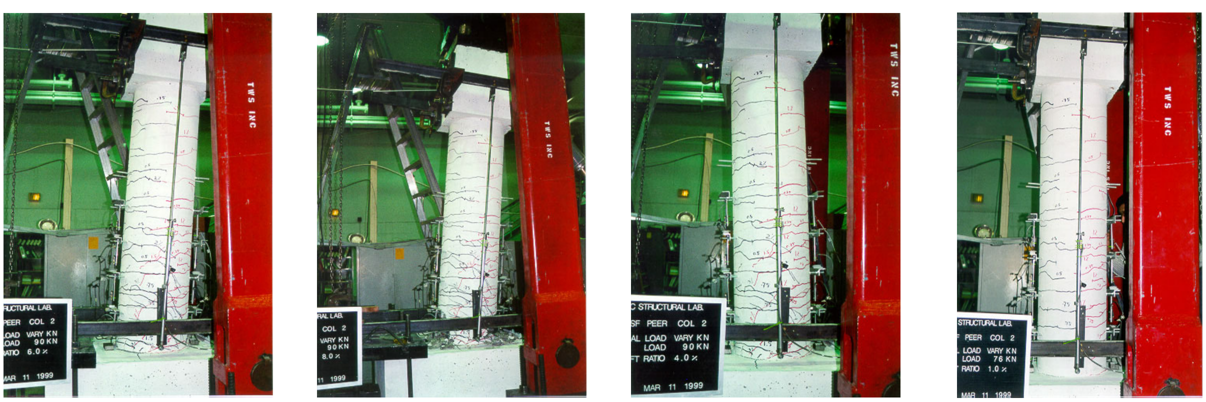

Figure 5.3 Specimen two at drift ratio of (a) 1% (b) 4%, (c) 6%, and (d) 8%

Figure 5.4 Failure pattern of specimen two. Buckling of the main bar and straightening in reversal at a drift ratio of (a and b) 6%, (c) different crush pattern on the two opposite sides of the column and, (d) rupture of the main bars at a drift ratio of 8%.

5.1.3 Specimen Three

This specimen was subjected to a monotonic lateral displacement and a constant axial load of 30% $A_g f'_c$. At a displacement of 14.7 mm (0.58 in.) corresponding to a drift ratio of 0.8%, the first flexural cracks were formed. As stated, the high level of the axial load was the reason for the concrete to start crushing before yielding of the longitudinal bars. The onset of crushing was at a drift ratio of 2% and spread upward from the column-footing interface as the drift ratio was increased to 3% and consequently 4%. Right after the occurrence of the 4% drift ratio, the first rupture of the spiral close to the column-footing interface occurred, which caused a loss in the horizontal force. At drift ratios of 5% to 6% more transverse reinforcement rupture occurred and at a drift ratio close to 6%, the longitudinal rebars buckled at two locations near the footing. Then a reversal displacement was applied up to the point where the lateral load vanished. The test was concluded at this point.

5.1.4 Specimen Four

This test was done without any axial load, and with a monotonically increasing lateral displacement. The displacement was increased up to a drift ratio of 10%, where the limit of the horizontal actuator was reached and a reversal displacement was applied up to –10% drift ratio, and then back to zero, forming one full cycle. At a drift ratio of 0.5% the first flexural cracks were formed. This value was close to the predicted yield displacement. The onset of crushing of the concrete near the column-footing area was observed between the drift ratios of 2% and 3%.

As the displacement was increased to 7% drift ratio, more crushing of the concrete occurred at the front face of the column where the concrete was under compression. No failure was detected up to the drift ratio of 10%, which was the limit imposed by the testing equipment. The test was continued by applying a reversal displacement up to –10% drift ratio, during which the same behavior was observed as in the push direction. Then the displacement was pushed back to zero at the end of the test.

Figure 5.5 Different instances from test 3: onset of spalling, buckling of the rebars, rupture of spiral, and complete failure

5.1.5 Specimen Five

In this test the specimen was subjected to a monotonically increasing lateral displacement and a nonproportionally variable axial load, changing from between +30% and –10% of $A_gf'_c$. The rate of change of the axial load with respect to the lateral displacement was so that at least one whole cycle of axial loading was completed within the first yield of the section. The first yield was analytically chosen to be the least value of the yield displacements at the column with the axial load changing between +30% and –10% of $A_gf'_c$. Fulfilling this condition and following the exact path of the predetermined loading pattern was achieved by using the newly developed multi-axis loading control system. The actual pattern of the axial load is shown in Figure 3.7(b), which is plotted based on the experimental data. The axial load of +20% $A_gf'_c$ at the beginning of the test was reduced to –10% $A_gf'_c$ at the same displacement and then increased to +20% $A_gf'_c$, while the displacement was increased to 0.1% drift ratio. When the axial load was decreased to –10%

$A_g f'_c$, slightly visible cracks were observed. The first crushing was observed at 2% drift ratio and increased as the drift ratio increased at the peak levels of the axial load. Despite the tests under a constant or proportionally variable axial load, the analytical strength of the column under a corresponding axial load in a case of constant axial load with the same level was not reached. This issue encouraged the researchers to plan a different pattern of axial load so that the effect of the axial loading pattern could be investigated more. At drift ratios close to but more than 3%, a sudden increase in crushing of the concrete within the vicinity of the column-footing interface was observed, and some inclined cracks were formed. The rupture of the spiral steel occurred at a drift ratio close to 6%, and the second was observed at a drift ratio of slightly more than 8%. The test was continued up to a drift ratio of 8.5%.

5.1.6 Specimen Six

The lateral displacement and level of axial load for this test were similar to those of the previous test except for the pattern of the axial load. This difference caused a significant change in the response of the specimen. At drift ratios of 0.5% cracking was visible on the push side of the column. Crushing of the concrete near the column-footing interface started at a drift ratio close to 1.5%. At a drift ratio of 2% slight inclined cracks were formed. There were more cracks and crushing of the concrete as the lateral displacement was increased under the variable axial load. Rupture of the spiral occurred at a drift ratio of 6.5%. The test was continued up to a drift ratio of close to 8% and then the displacement was decreased to zero under zero axial load. The test was continued with the same pattern in the pull direction for close to 4 cycles of axial load change, then the displacement was brought back to zero at the end of testing. Figure 5.6 shows different instances of tests 5 and 6.

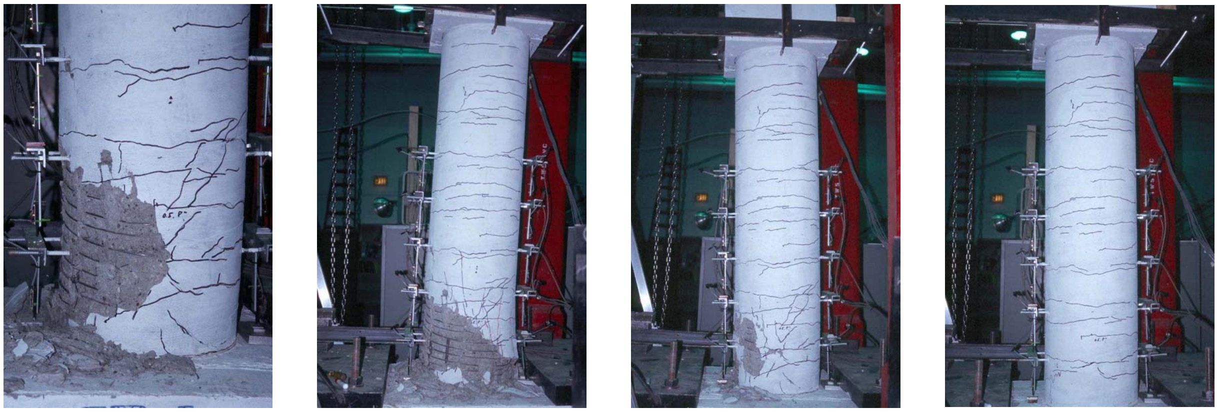

Figure 5.6 Different instances from tests 5 and 6: Initial cracking at tensile axial load all over the column; spalling, crushing, and rupture of spiral

5.2 HORIZONTAL-FORCE DRIFT-DEFORMATION RESPONSE

The curves showing the hysteretic behavior of the columns are plotted based on the drift defined as:

$$d(\%) = 100\frac{\delta}{L} \tag{5.1}$$

where δ is the total horizontal deflection and L is the effective height of the column, from the top of the footing to the force application point. The ductility factor is defined as:

$$\mu = \frac{\delta}{\delta_y} \tag{5.2}$$

where δ is the total horizontal deflection and δ_y is the horizontal deflection at the first yield of the tensile steel or crushing of concrete at the critical section of the column. The first experimental yield point was determined when the tensile strain at the furthermost rebar of the section at the interface of the footing and column reaches the yield strain of steel. For the horizontal-force drift ratio hysteretic curves, the horizontal axis is the drift, and the vertical axis is the horizontal force in kN. The dotted line is the analytical prediction considering confinement and the effect of the axial load.

5.2.1 Specimen One

Figure 5.7 shows the horizontal-force drift-ratio hysteretic relationship resulting from test one. Compared with the test results on a similar specimen with zero axial load, the flexural strength has increased as the axial force has increased, but with a decrease in ductility. That is because the failure of the concrete precedes the failure or even yield of the rebars, due to a high level of axial load.

Increasing the confinement both in strength and amount leads to an increase in ductility, which is most important for seismic design. At a horizontal force of about 170 kN and a drift of 0.73%, the column reached the first yield, and at a drift ratio of 2.5% achieved its maximum capacity, which was about 220 kN. The maximum ductility achieved was around 6, and the maximum drift was 4%, corresponding to a deflection of 73 mm. The dotted lines show the predicted capacity for the specimen considering the effects of confinement and axial force. The prediction is conservative compared with the experimental results.

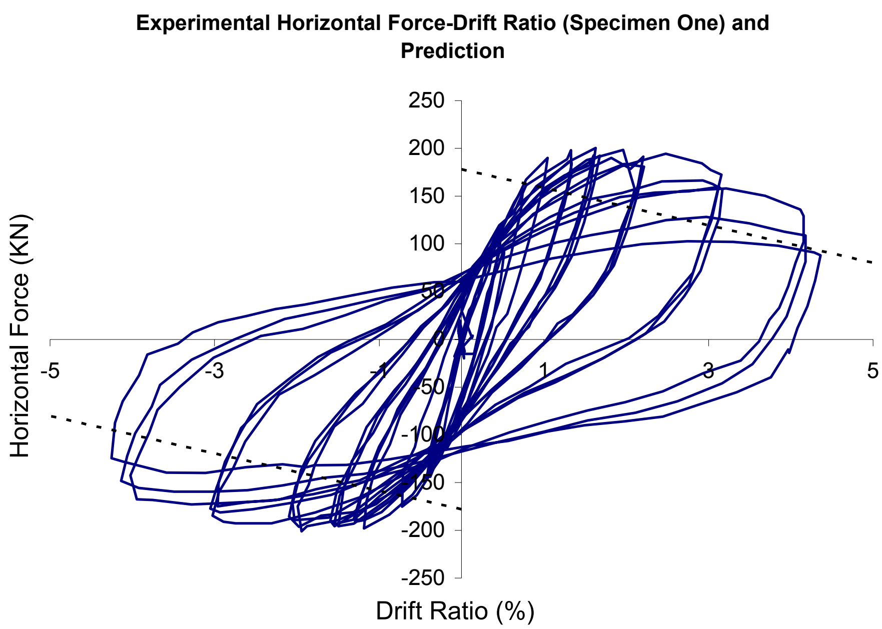

Figure 5.7 Horizontal force vs. drift ratio for specimen one

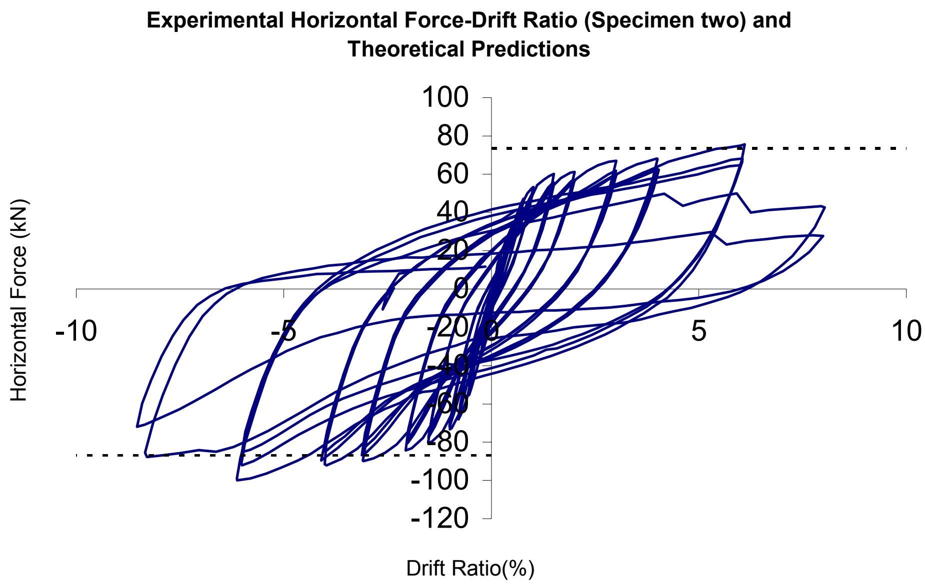

Figure 5.8 Horizontal force vs. drift ratio for specimen two

5.2.2 Specimen Two

Figure 5.8, shows the hysteretic response for test two. Since the axial force was proportional to the horizontal force and its value has opposite signs in two opposite directions, the behavior of the column was different in the pull and push directions, as expected from the analytical prediction. In the push direction, where there was a tensile axial load, the first yield occurred at a drift ratio of 0.49% and a horizontal force of 25.3 kN, while in the pull direction with a compressive axial load, it was at a drift ratio of 0.53% corresponding to a horizontal force of 44.3 kN. In the push direction, the capacity was 60.5 kN at a drift of 6.11%, while in the pull direction the capacity increased to 80 kN at a drift of 6.12%. The dotted lines show the estimated capacities in the two directions. The estimation was based on the predicted capacity and the corresponding axial load. As shown in the figure, in the push direction where the axial force is tensile, the capacity is well estimated, while in the opposite direction with a compressive axial load, it has been underestimated. The column achieved a ductility of about 11 in the push direction and 15 in the pull direction during the test. The column failed at a drift ratio of 6% (137 mm) in the push and at 8% (183 mm) in the pull direction.

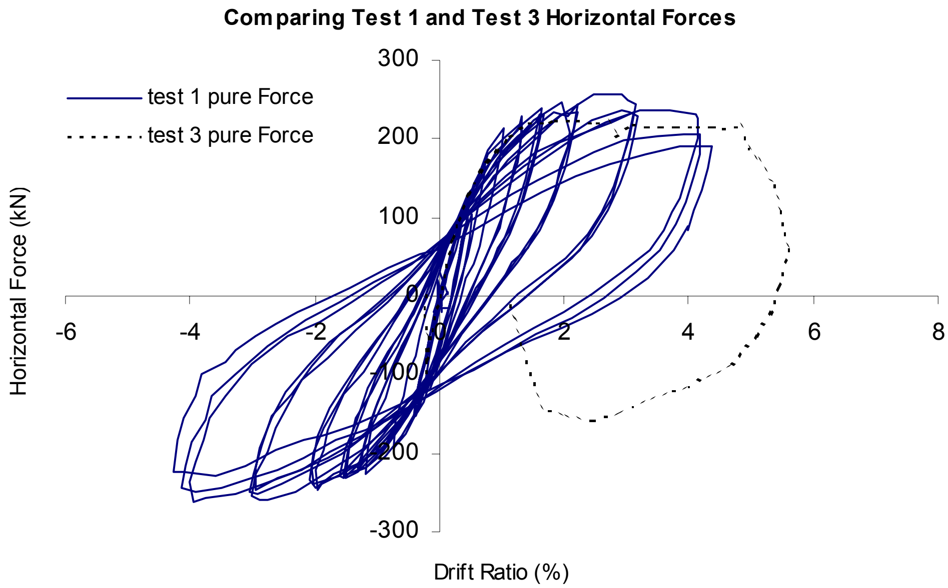

Figure 5.9 Comparison of lateral forces in tests one and three

5.2.3 Specimen Three

This specimen was under a monotonically increasing lateral displacement and a constant axial load equal to 30% $A_g f'_c$. The observed peak strength of the column in this case was less than for specimen one, which was under the same level of axial load but a cyclic lateral displacement. In Figure 5.9 the results of the two tests are compared. The displacement capacity for this column was slightly more than for the first specimen, while it reached its maximum capacity in a smaller drift ratio compared to test one. Figure 5.10 shows the experimental horizontal force versus drift ratio and the expected analytical capacity.

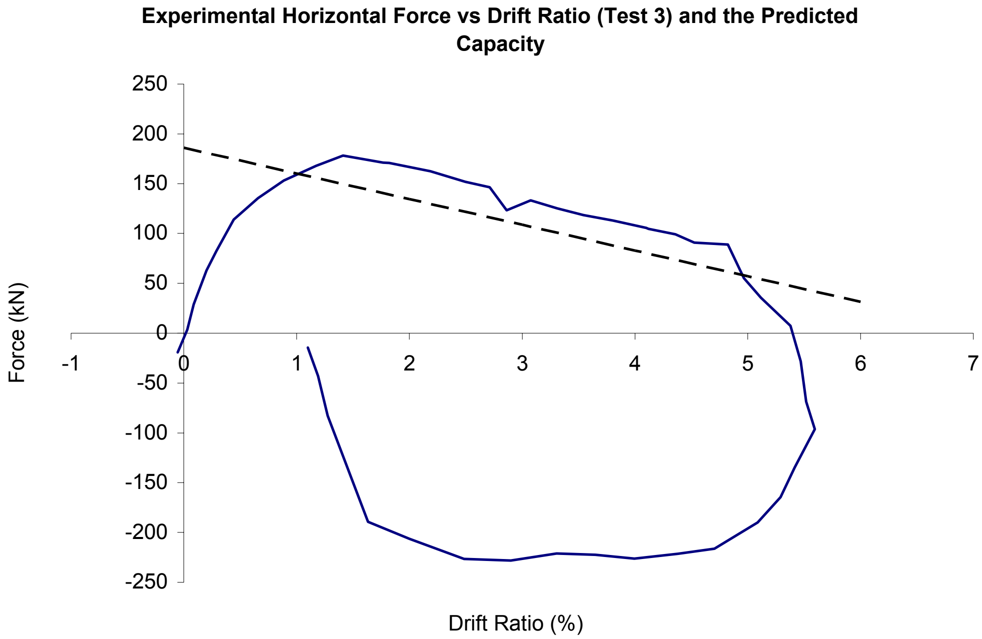

Figure 5.10 Horizontal force vs. drift ratio, specimen three

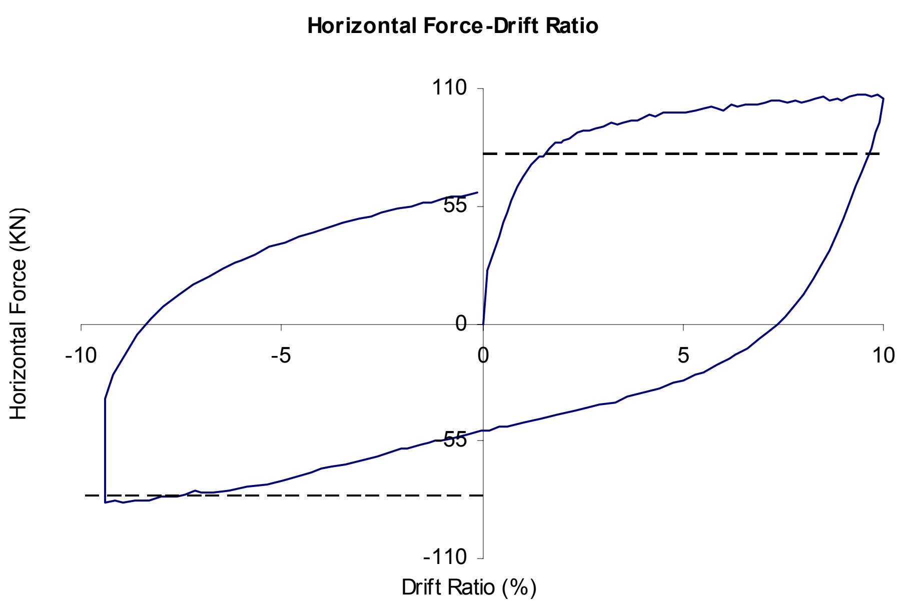

Figure 5.11 Horizontal force vs. drift ratio, specimen four

The analytical capacity is evaluated for the column under axial load, and the dotted line is plotted considering the effect of axial load. The capacity is underestimated, as in the first test where a similar axial load was applied.

5.2.4 Specimen Four

Specimen 4 was applied with monotonic lateral loading without any axial force. The first yield of the longitudinal steel occurred at a drift ratio of 0.5%. Its experimental strength was beyond the predicted analytical strength and the drift ratio reached 10%, more than the analytically predicted drift ratio at failure, when the reversal displacement was applied due to the stroke limit of the actuator. The specimen did not fail at this drift ratio, and the strength increased without any degradation up to the maximum practical stroke. In the pull direction, while the drift ratio was applied up to the end of the stroke limit of the actuator, the strength was close to that analytically predicted but less than the strength in the push direction. This was because of the degradation imposed while the push drift was applied. Figure 5.11 shows the horizontal force versus drift ratio for this specimen.

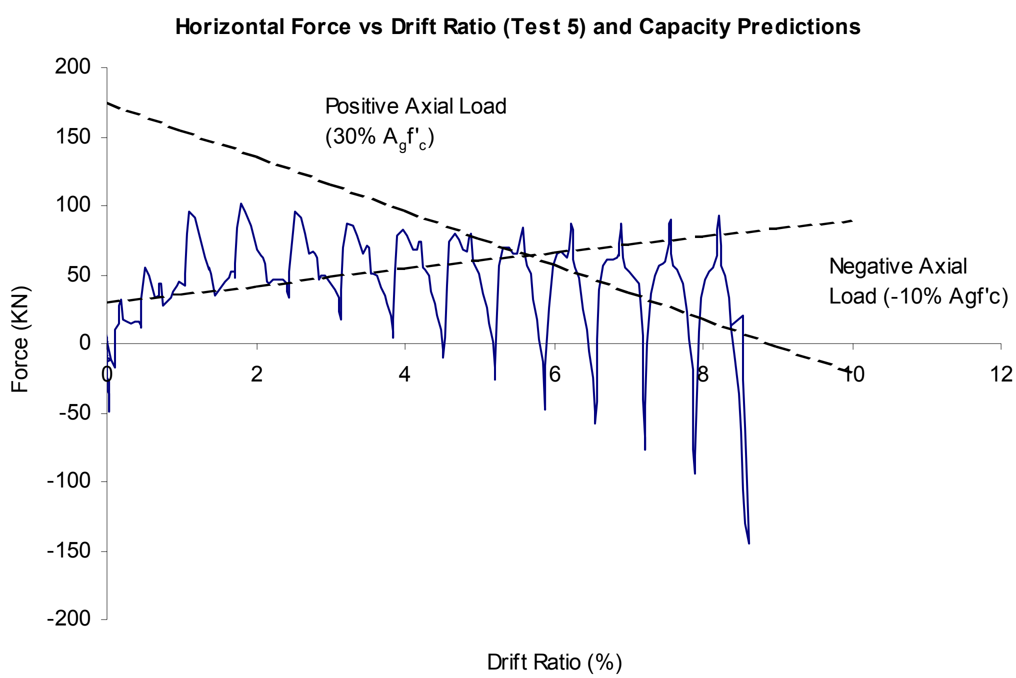

Figure 5.12 Horizontal force vs. drift ratio, specimen five

5.2.5 Specimen Five

Figure 5.12 shows the lateral-force drift-ratio response of specimen five. The horizontal force fluctuation follows the axial load variation. Since the P-Δ effect when the level of axial load reaches its maximum or minimum peaks is significantly large, its effect on the horizontal force is considerable. The horizontal force depends on the level of axial load from the perspective of strength , the amount of the lateral displacement to reach its proper value for a certain level of strength, and the level of the P-Δ effect. These are the facts that can justify the appearance of the horizontal force response curve. Figure 5.13 shows the curves with and without the P-Δ effect, and the scaled axial load for comparison purposes. The figure is self-explanatory and the effect of axial load on increasing the strength and the P-Δ effect is obvious.

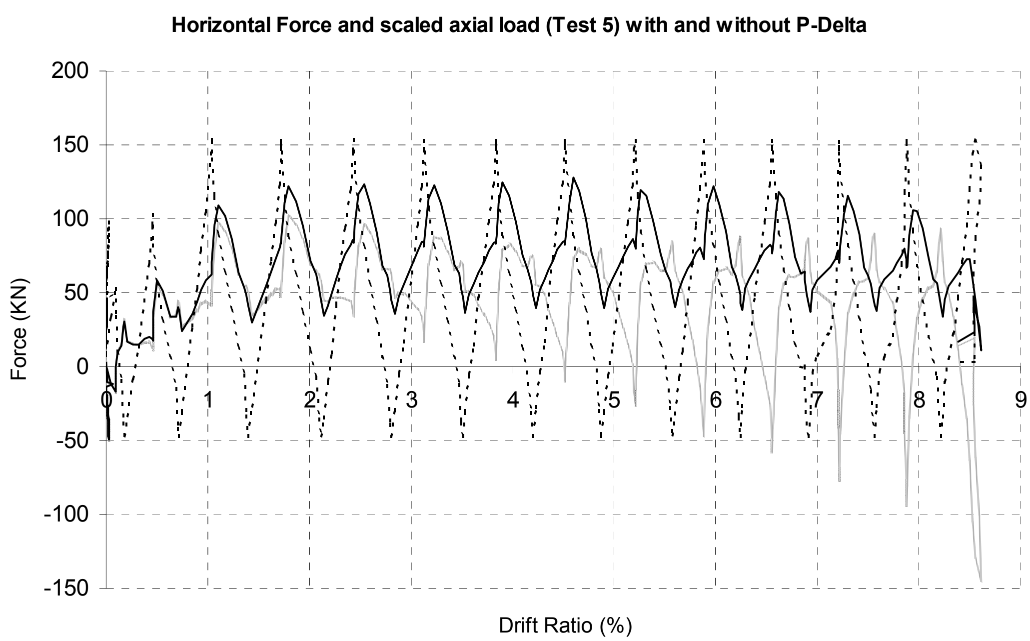

Figure 5.13 Horizontal force with and without (solid) P-Δ effect, and the scaled axial load (dotted) vs. drift ratio, specimen five

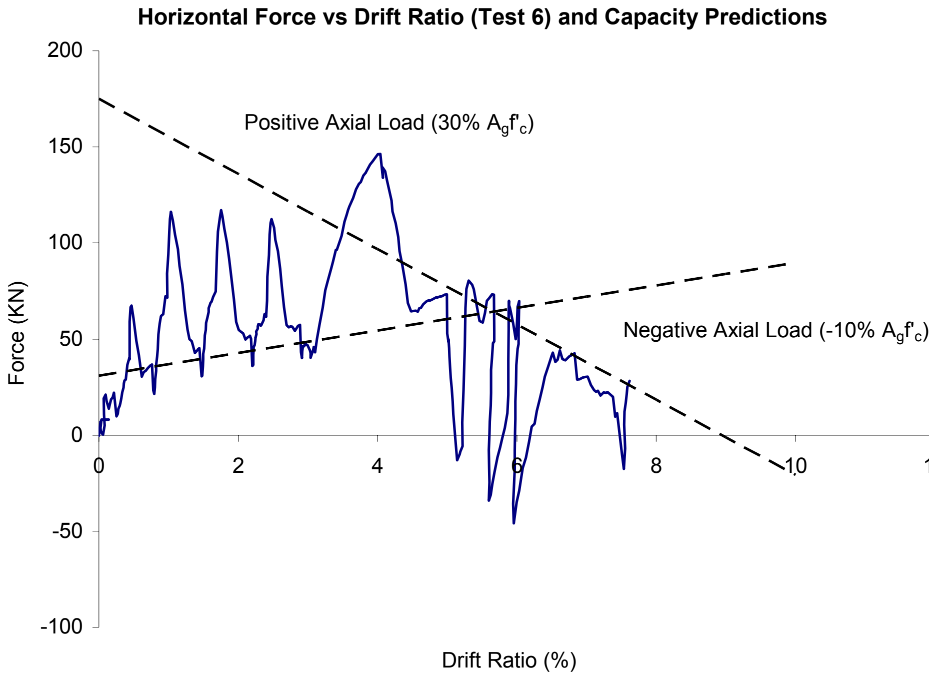

Figure 5.14 Horizontal force vs. drift ratio, specimen six

5.2.6 Specimen Six

The loading pattern for the axial load was different from the previous specimen considering the cycle and duration, while all other parameters, such as the peak values, are the same. All the aforesaid observations are also true for this case. The main difference in this case is that the lateral load had enough space in terms of lateral displacement under a certain level of axial load to reach its maximum value. In other words, when the axial load is reversed from its negative value and increased to its positive value, while the lateral displacement is increasing independently, the horizontal force increases, but for a certain level of the axial load, it cannot reach its peak value, except for the cases when the axial load is kept constant at that level while the lateral displacement is increased until the peak value is reached. Figure 5.14 shows the horizontal force versus drift ratio, and Figure 5.15 compares the horizontal force, with and without the P-Δ effect, and the scaled axial load.

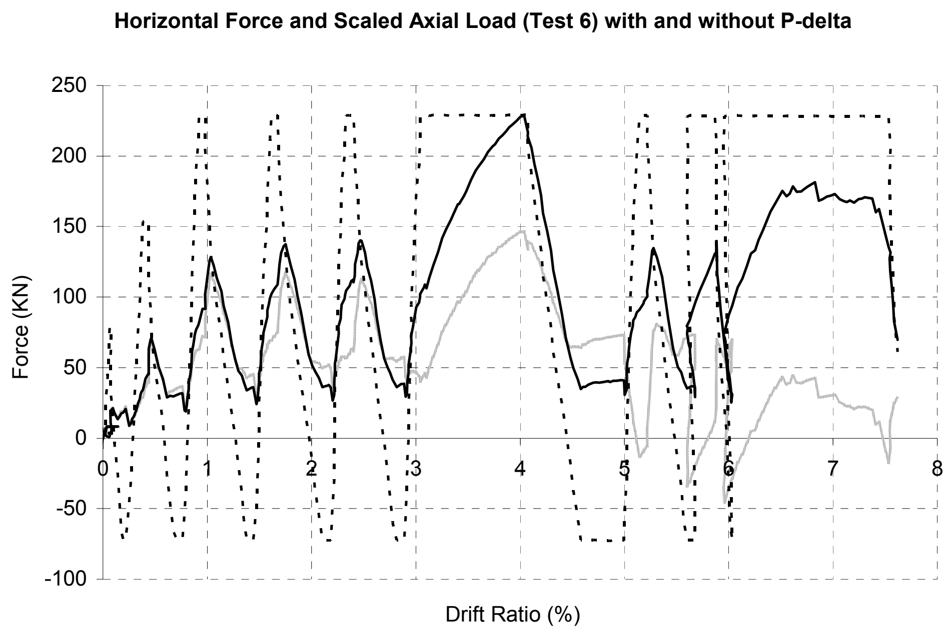

Figure 5.15 Horizontal force with and without P-Δ effect (solid), and the scaled axial load (dotted) vs. drift ratio, specimen six

5.3 EFFECTS OF VARIABLE AXIAL LOAD

Figure 5.16 shows the critical moment versus drift ratio for column two. Owing to the proportionality of the axial load with the horizontal force, in the push direction the axial force is tensile, in the pull direction compressive. The variation of the axial load resulted in different responses in the push and pull directions. The experimental values corresponding to the first yield of the longitudinal rebar, and the peak flexural strength of the specimen are summarized in Table 5.1 The first yield of the longitudinal bar occurred at a drift ratio of 0.4677% corresponding to a horizontal force of 31.22 kN (7.02 kips) in the push direction when the axial load was –27.28 kN (-6.13 kips), while in the pull direction, the first yield of the longitudinal bar was at a drift ratio of –0.53% corresponding to a horizontal force of –55.43 kN (-12.46 kips) when the axial load was 47.91 kN (10.77 kips). Experimentally, there was a difference of 24.21 kN between the yield forces in the two opposite directions. The difference between the corresponding displacements was around 1.14 mm (0.045 in.) due to the variation of the axial load between the values stated above. The specimen reached its maximum capacity at a drift ratio of 6.11% corresponding to a horizontal force of 75.65 kN (17.0 kips) with an axial load of

–70.45 kN (-15.84 kips) in the push direction. The maximum capacity of the specimen in the pull direction was reached at a drift ratio of –6.17%, corresponding to a horizontal force of –100 kN (-22.48 kips) under an axial load of 81.52 kN (18.32 kips). The variation of the axial load caused this difference between the capacities in the two opposite directions. The difference between the displacements, as for the yield point, is not significant, and the experimentally detected difference was around 1.09 mm (0.043 in.). The ductility of the specimen in the two opposite directions was slightly different. In the push direction the ductility, defined as the ultimate displacement divided by the yield displacement was 13, in the pull direction 11.6. The increase in the axial load led to a decrease in ductility.

Table 5.1 Experimental forces and displacements in opposite directions, test 2

Experimental Data Test 2	Push Direction (Negative Axial Load)				Pull Direction (Positive Axial Load)			
	Displacement mm(In)	Drift Ratio(%)	Horizontal Force kN (Kips)	Axial Load kN (Kips)	Displacement	Drift Ratio(%)	Horizontal Force	Axial Load
First Yield	8.55 (0.336)	0.4677	31.22 (7.02)	-27.28(-6.13)	-9.69(-0.3816)	-.53	-55.43 (-12.46)	47.91(10.77)
Maximum	111.74 (5.39)	6.11	75.65 (17.0)	-70.45(-15.84)	-112.84 (-4.44)	-6.17	-100. (-22.48)	81.52 (18.32)

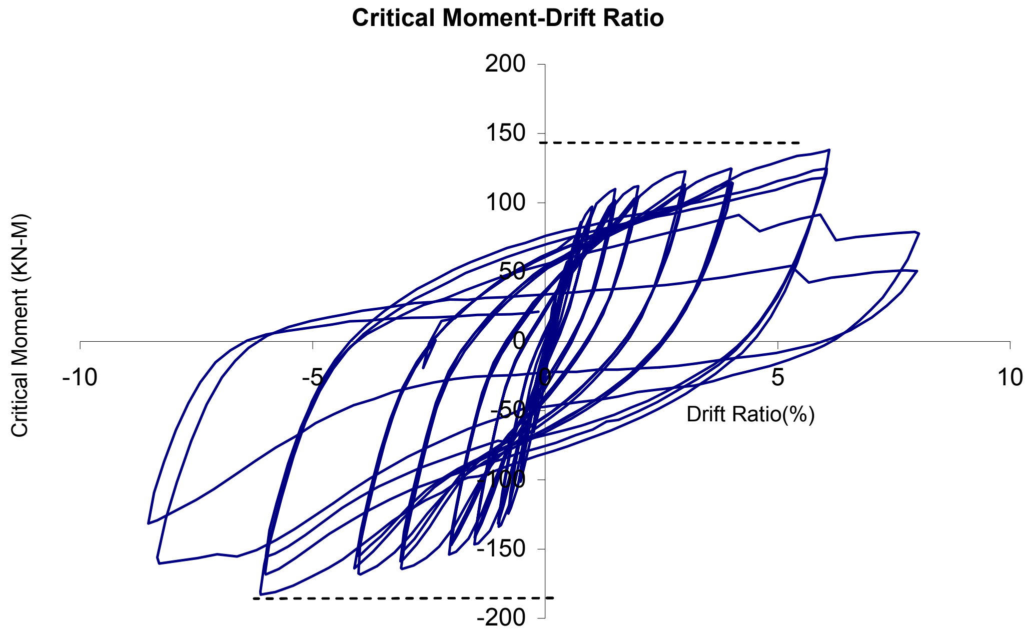

Figure 5.16 Critical moment vs. drift ratio, specimen two

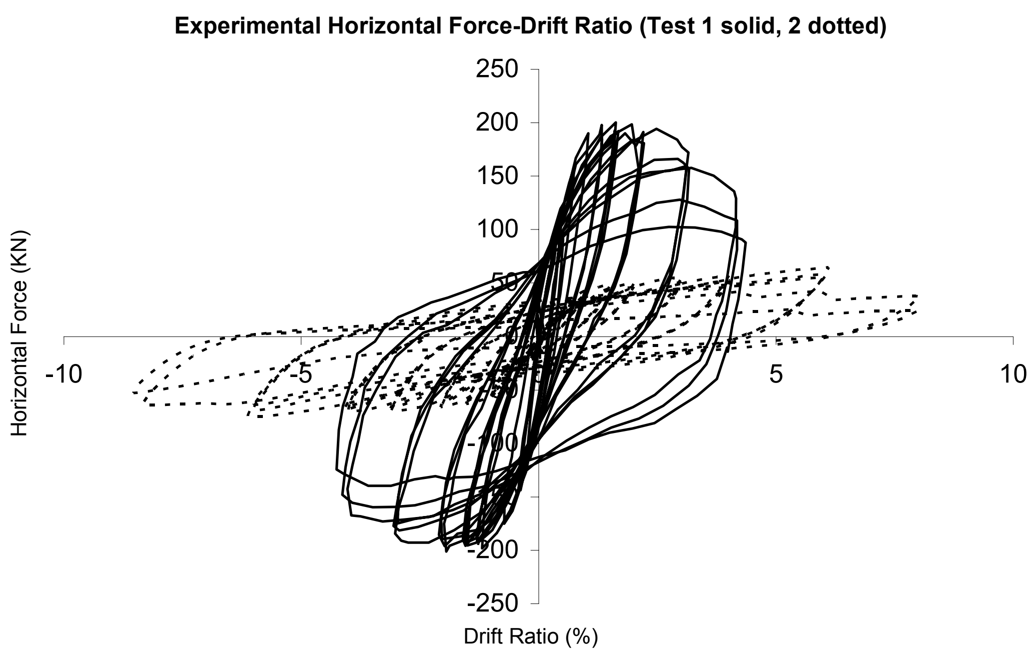

Figure 5.17 Comparison of tests one and two

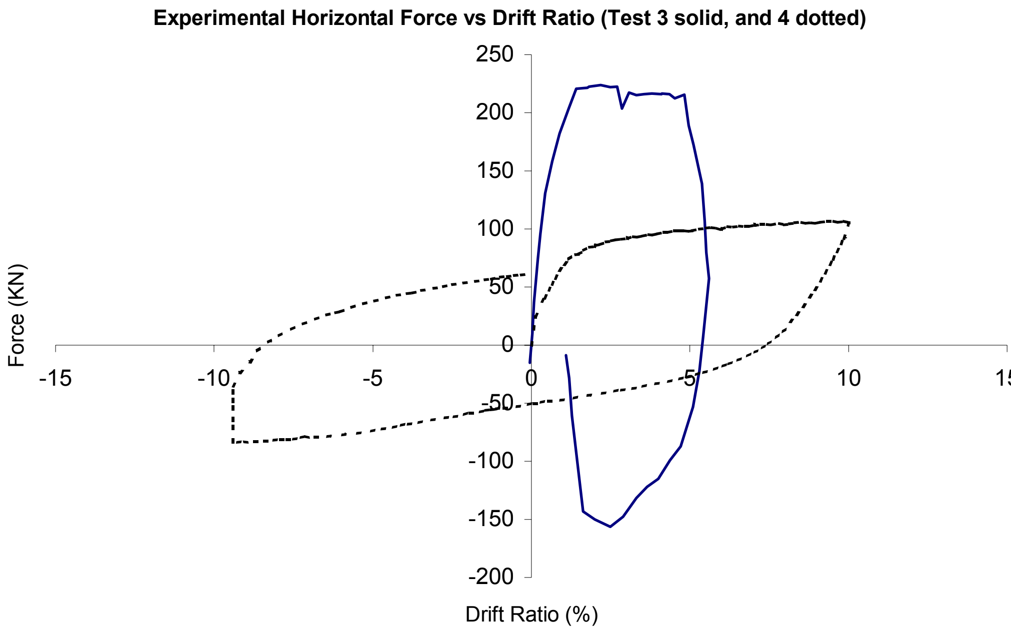

Figure 5.18 Comparison of tests three and four

In general the test results show that the compressive axial load in the pull direction led to an increase in the capacity, and that the tensile axial load in the push direction reduced the capacity.

Figure 5.17 compares the horizontal force of tests one and two, and Figure 5.18 compares the same values for specimens 3 and 4. The effect of the axial load on the flexural strength and ductility of the column is clearly visible. The significant increase in strength costs a significant decrease in ductility. This effect can also be seen in Figure 5.13 and Figure 5.15, where the horizontal force has been plotted for tests 5 and 6, respectively, compared to the scaled value of the axial load. If we correct the P-Δ effect, the effect of the axial load is explicitly shown in the figures. The other important issue is the effect of the pattern of axial load.

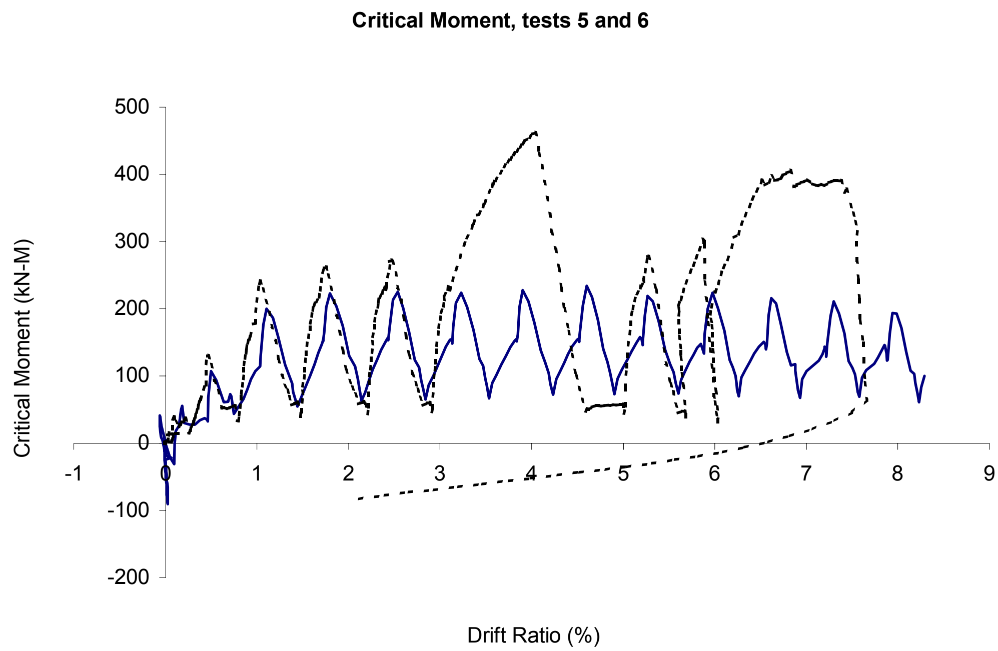

Figure 5.19 Comparison of tests five and six

Figure 5.19 compares the critical moments for tests 5 and 6. In Figure 5.20 the variation of the axial load with respect to the drift ratio is compared for tests five and six. The level of peak values for the axial load remained the same for both tests, the only difference being the pattern of loading. As shown, the pattern of the axial load with respect to the lateral displacement had a significant effect on the strength of the member. The reversal strain and strain hardening of steel, the compressed concrete, and the utilization of confining the steel are the main issues in this regard that should be addressed in this case. In general the effect of the axial load on the overall response of the column is significant, especially when the amount of the force is large and may not be ignored. The pattern of loading affects the response of the member.

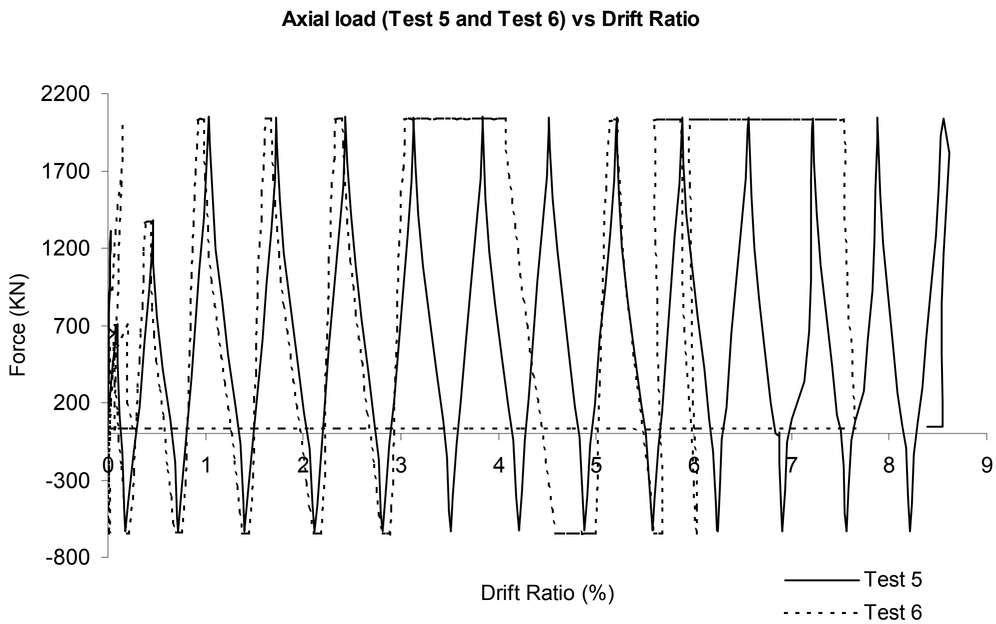

Figure 5.20 Comparison of variation of axial load in tests 5 and 6 with respect to drift ratio

5.4 RECORDED MOMENT-CURVATURE RESPONSE

The evaluation of the moment-curvature at different heights along the column can be carried out through two different methods. In the first method, an average curvature of a segment of the column is obtained using the longitudinal deformations measured by a pair of linear potentiometers, as shown in Figure 3.3. The average curvature can be expressed as:

$$\varphi_{ave} = \frac{(\Delta_1 - \Delta_2)}{D'.l_1} \tag{5.3}$$

where φ_{ave} is the average curvature over the specified length, Δ_1 and Δ_2 are the measured longitudinal deformations on two sides, *D'* and l_1 are the distance of the linear potentiometers and the length of the segment, respectively. The corresponding moment is calculated at the middle height of the segment, using the recorded values for the horizontal force and axial load, and the relative horizontal deflection at the corresponding step. In the second method, the curvature at a certain height level is evaluated. Here, the recorded strain at the two opposite longitudinal reinforcements at that level are employed and the curvature is evaluated as follows:

$$\varphi_{ave} = \frac{(\varepsilon_2 - \varepsilon_1)}{(D - 2c)} \qquad (5.4)$$

where ε_1 and ε_2 are the recorded strains at the two strain gages installed at the opposite sides of the column on the rebars, *D* is the column diameter, and *c* is the cover concrete thickness. The moment is calculated at the same level, using the recorded values for the horizontal force and axial load, and the relative horizontal deflection at the specific step. This method is reliable only within the elastic range of the strain, otherwise the residual strains when the reversal load is applied will be included in the measurements. In this report, the first method is used in evaluating the average curvature over a segment, and the second method is used solely to ensure the consistency of the data.

Figure 5.21 shows the moment-curvature response of the first specimen at segment one. This specimen was under a relatively high compressive axial load, and as a result, the maximum curvature achieved in the average section in segment one was about 0.0032 (1/in.). The section tolerated a moment of 3920 kip/in., corresponding to a lateral force of 57.5 kips.

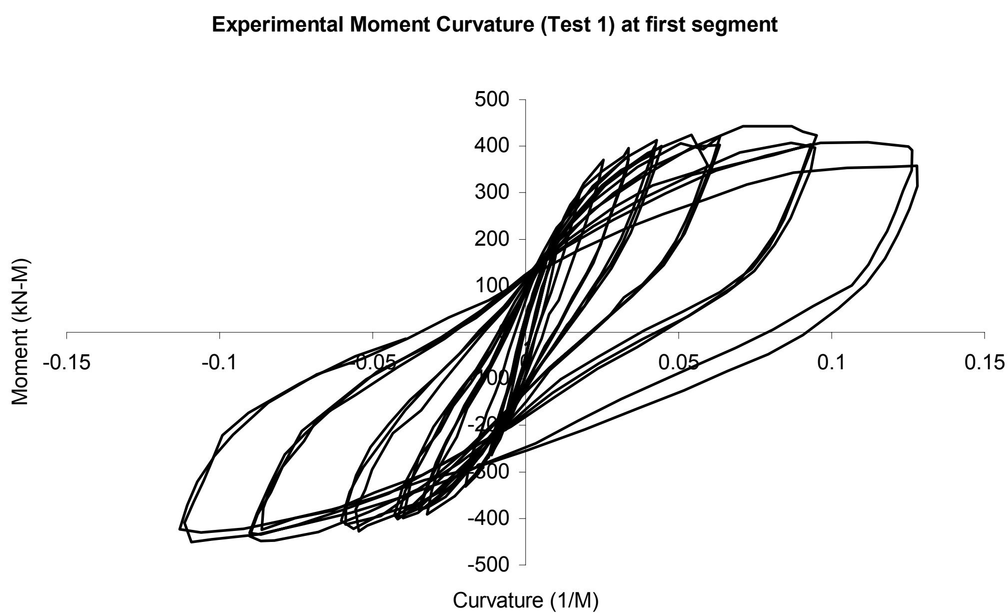

Figure 5.21 Experimental moment curvature of specimen one

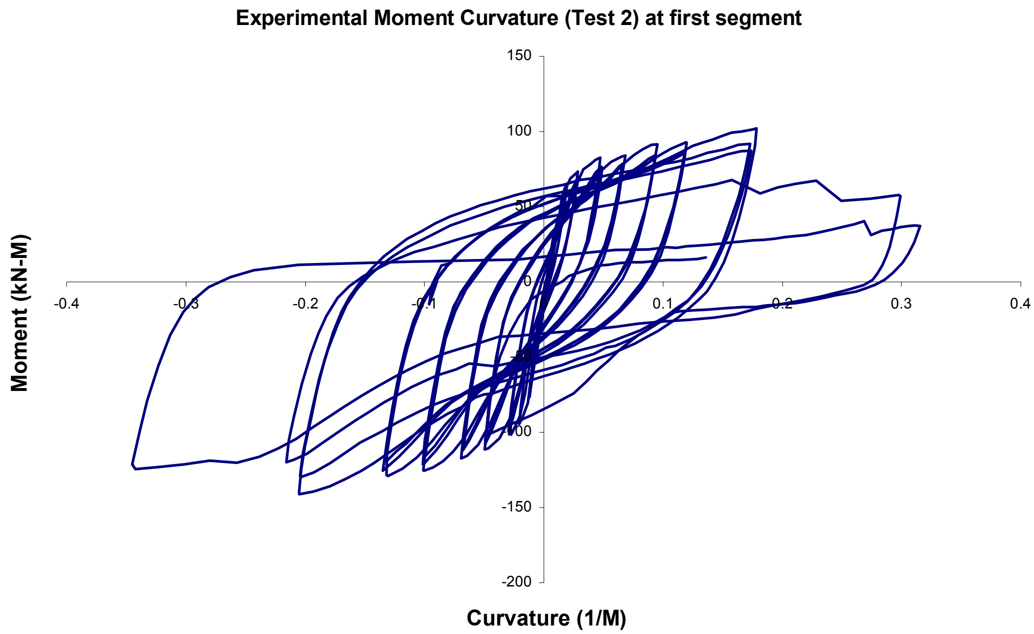

Figure 5.22 Experimental moment curvature of specimen two

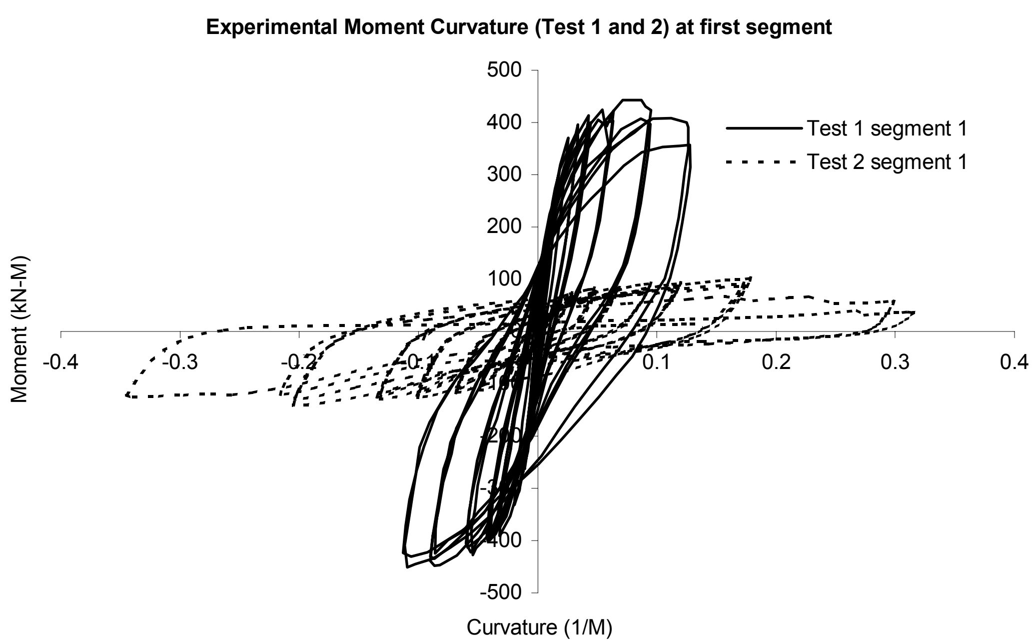

Figure 5.23 Comparison of the moment-curvature response at the first segment for tests one and two

In Figure 5.22 the experimental moment-curvature curve at the first segment for test two is plotted. In this test the axial load was proportionally variable with respect to the lateral force with a proportionality or $\tan(-43^{\circ}) = -0.9325$, so that in the push direction, where the lateral force was positive, the column experienced a negative axial load approximately equal to the lateral force in terms of magnitude, and in the pull direction, where the lateral force was negative, the exerted axial load on the column was positive. The ratio of the bending moment to the axial load at the critical section was –66.67, while at a section in the middle of the first segment (at a height of 100 mm [4.0 in.] above the critical section) this ratio was –63.

In Figure 5.23 the moment-curvature responses of the average section on segment one for tests one and two are compared. For test one, the high level of axial load caused an increase in the moment capacity of the section, while the ultimate curvature was limited to 0.0032 1/in. On the other hand, specimen two under a relatively low level of axial load could utilize its flexural ductility in terms of curvature at the mid-section on the first segment, while the moment capacity was lower than in the first test. As was observed for the horizontal-force drift-ratio hysteretic response of the columns, increasing the level of the axial load within a range, which is usually the balance point, increases the capacity in terms of the force or moment, while decreasing it in terms of displacement, curvature, or rotation.

Figure 5.24 shows the distribution of curvature along the column height at different drift ratios for specimens one and two. The horizontal axis is the curvature in terms of 1/m and the vertical axis is the column height in mm. The scale on the axes is chosen the same so that the curvature distribution can be compared for the two cases. The distribution of curvature along the height of the first specimen is symmetric for equivalent negative and positive drift ratios, as was expected due to a constant axial load. As shown in the figure, the distributions for the drift ratios of –4% and +4% have the same pattern. The effect of variation of the axial load in the push and pull directions on the curvature distribution for specimen two is shown in the figure.

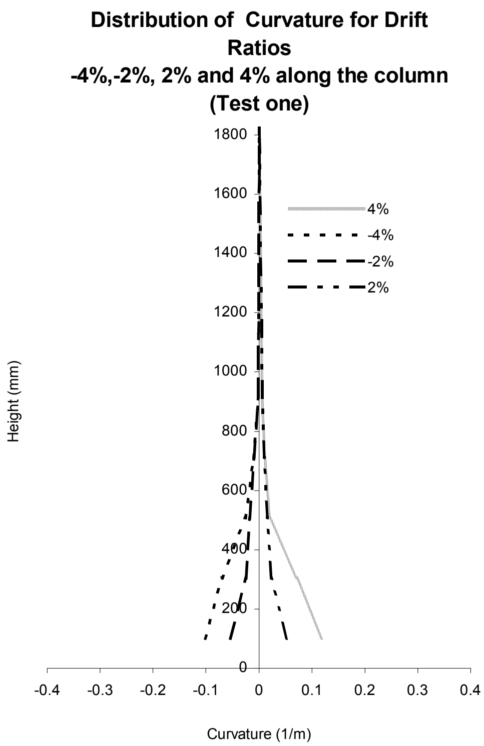

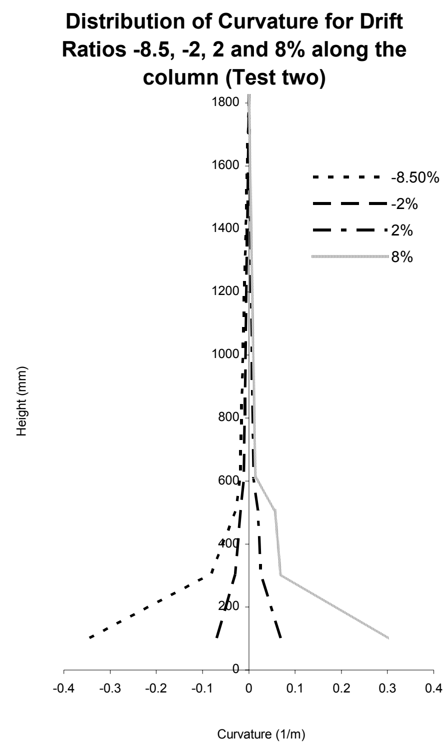

Figure 5.24 Distribution of curvature along the column at different drift ratios for test one and two

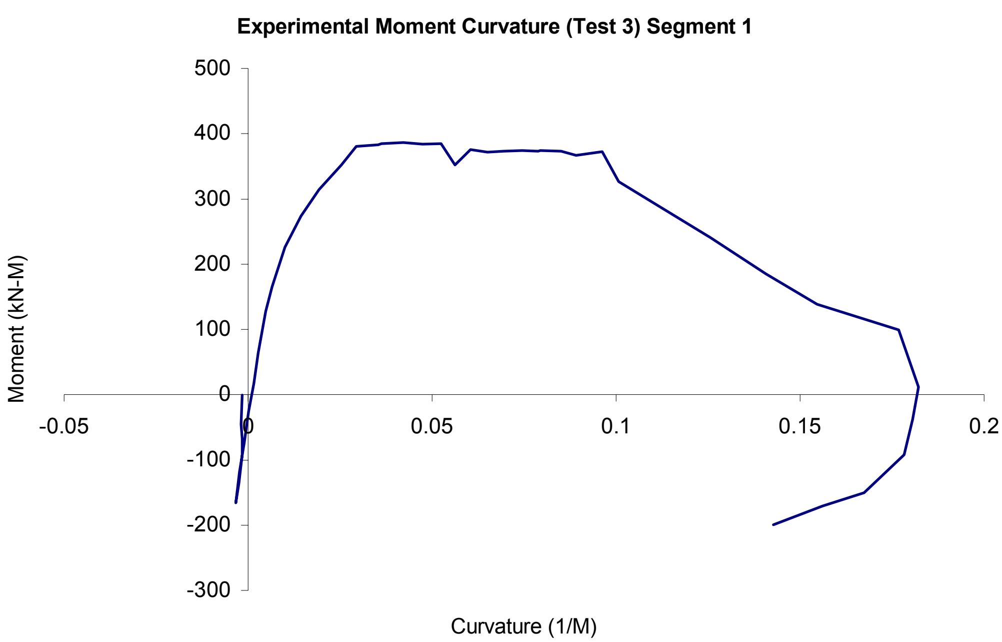

Figure 5.25 Experimental moment curvature of specimen three

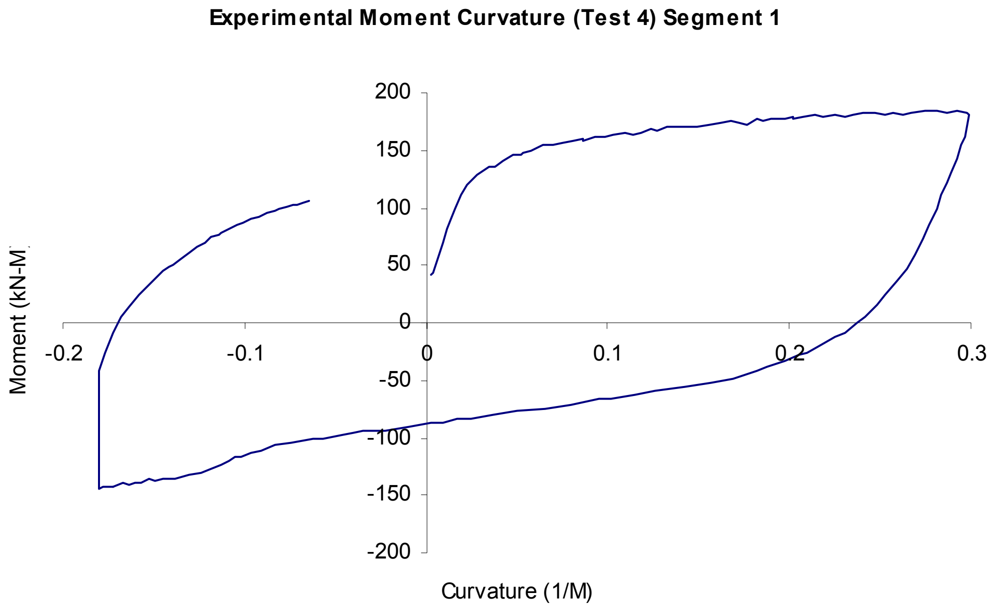

Figure 5.26 Experimental moment curvature of specimen four

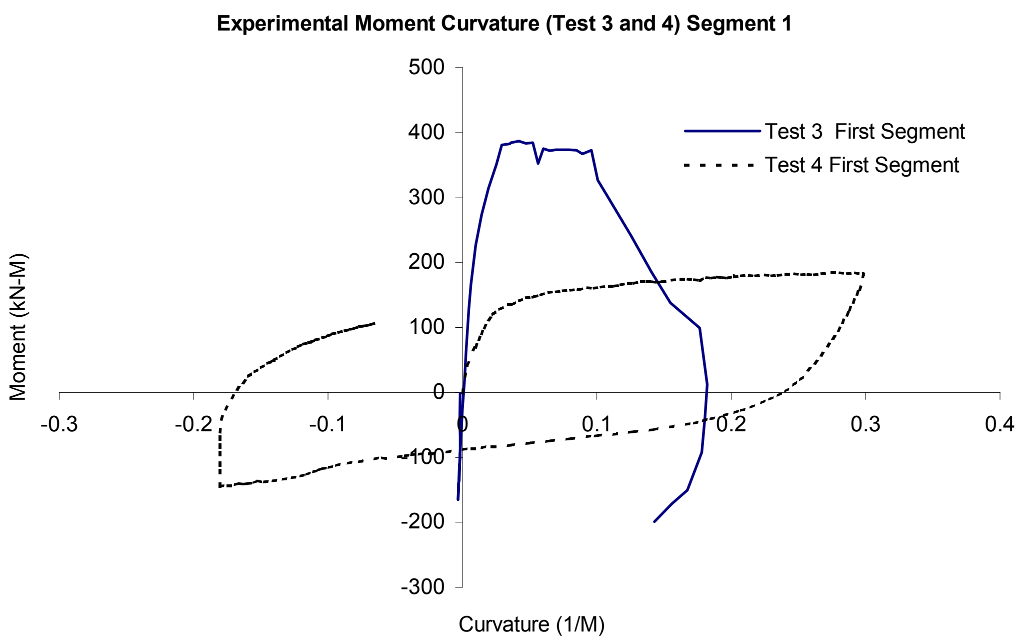

Figure 5.27 Comparison of the moment-curvature response at the first segment for tests three and four

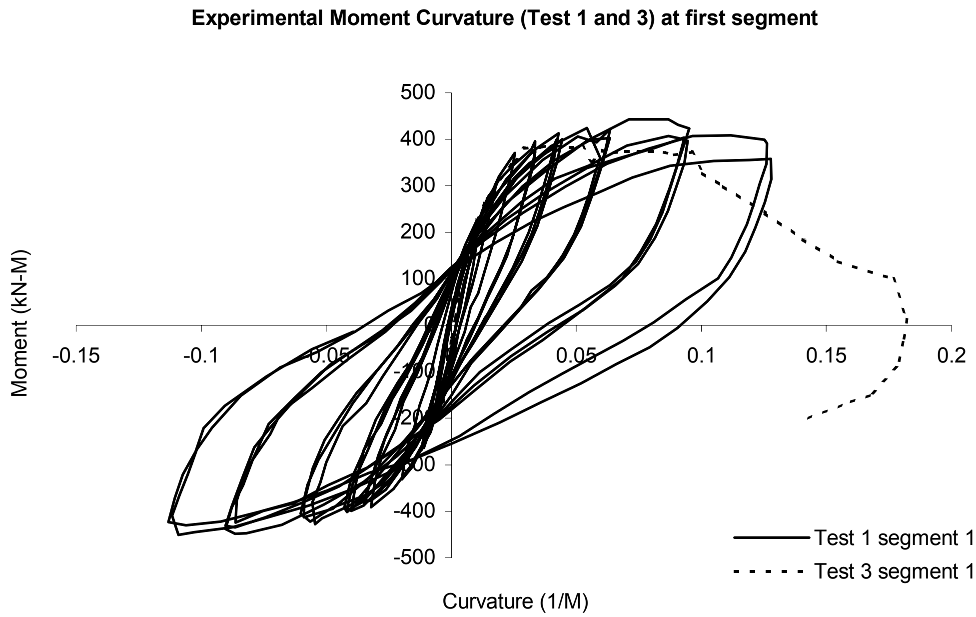

Figure 5.28 Comparison of moment-curvature response of the mid-section on segment one for specimens one and three

Figure 5.25 shows the moment-curvature response of specimen three at the first segment. This specimen was under a high level of axial load, identical to the first specimen and a monotonic lateral displacement. Figure 5.26 shows the moment-curvature response of specimen four at the first segment. In this case the monotonic lateral displacement was applied without any axial load.

Figure 5.27 compares the moment-curvature response of specimens three and four at an identical section. The same phenomenon is observed here as was for tests one and two. Test three was under a high axial load compared to test four under no axial load. The two tests are compared in terms of the moment curvature at the first segment as for tests one and two.

Figure 5.29 shows the distribution of curvature along the column height at different drift ratios for specimens three and four. The horizontal axis is the curvature in meter^{-1} (1/meter) and the vertical axis is the column height in millimeters. For specimen three, the curvature at the segment above the footing is less than the curvature at the next segment. This is because of the high level of axial load and the effect of footing in providing confining stresses for the segment in the vicinity of the column-footing interface. Specimen four was tested without axial load, and the pattern of curvature distribution for identical positive and negative drift ratios are fairly close.

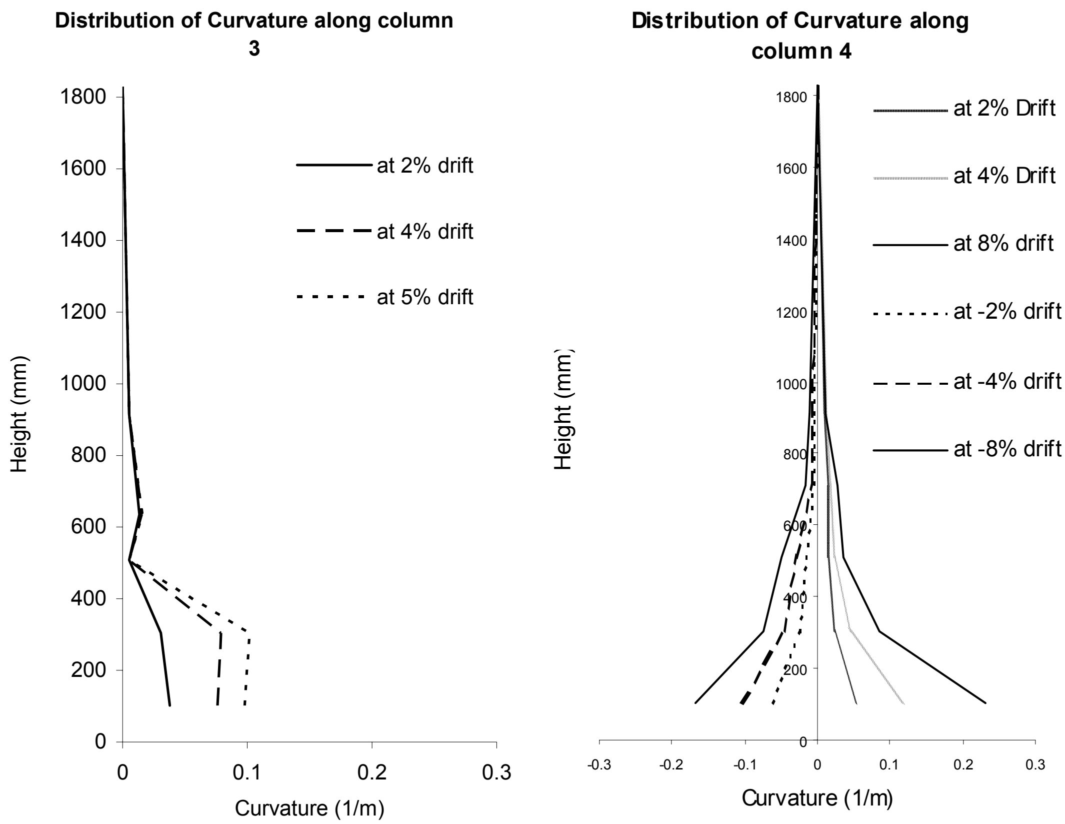

Figure 5.29 Distribution of curvature along the column at different drift ratios for tests three and four

The experimental moment-curvature responses of specimens five and six are shown in Figure 5.30 and Figure 5.31. The period of variation of the axial load in terms of curvature was 0.00045. In other words, one cycle of axial load variation between $-10\%A_g f_c^{'}$ and $+30\%A_g f_c^{'}$ was completed within a curvature variation of 0.00045 1/in. For test six, the same variation of axial load happened in a curvature range of 0.00062 1/in., but this difference was due to keeping the level or axial load at peak points constant for a short time. So, the slopes for both tests are the same and this difference is due to the aforesaid action. The rate of change of axial load with respect to curvature, or in other words, the period, was constant from zero up to a curvature of 0.0022. The rate was then changed at various instances. In Figure 5.32 the variation of the axial load with respect to curvature at the first segment for tests five and 6 is compared. Figure 5.33 compares the moment-curvature response of tests 5 and 6 at the first segment, and the significant effect of the pattern of the axial load is shown. Within a curvature of 0.002, the only difference between the two patterns of axial loads is the short pause of the axial load at peak points for test 6. This small difference caused a relatively significant difference in the moment-curvature response of the two tests within this range. Between curvatures 0.0022 and 0.0030, the level of the axial load was kept at the peak value in test 6, resulting in a very significant difference in the moment-curvature response.

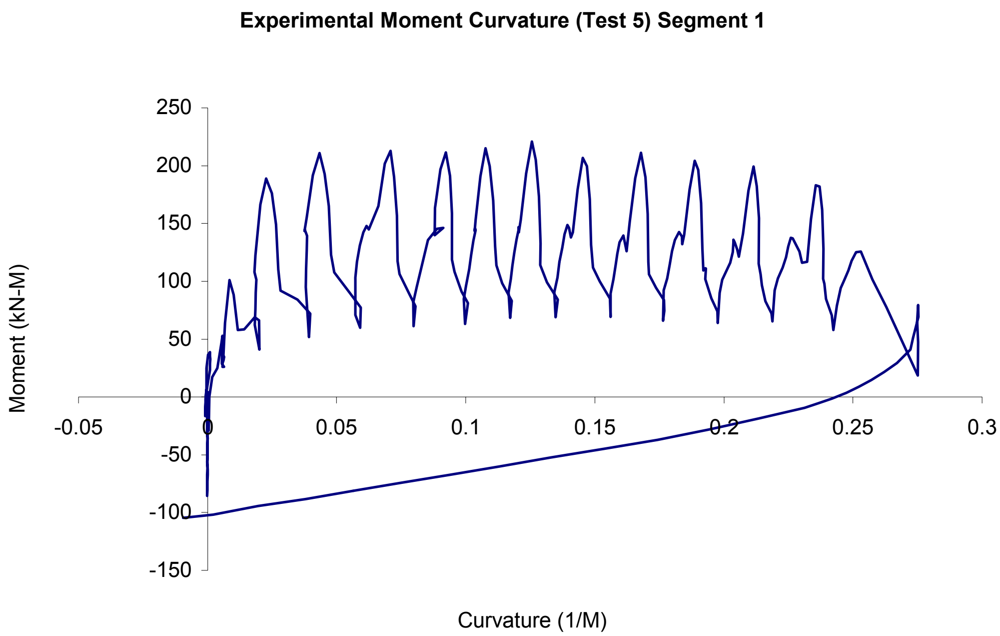

Figure 5.30 Experimental moment curvature of specimen five

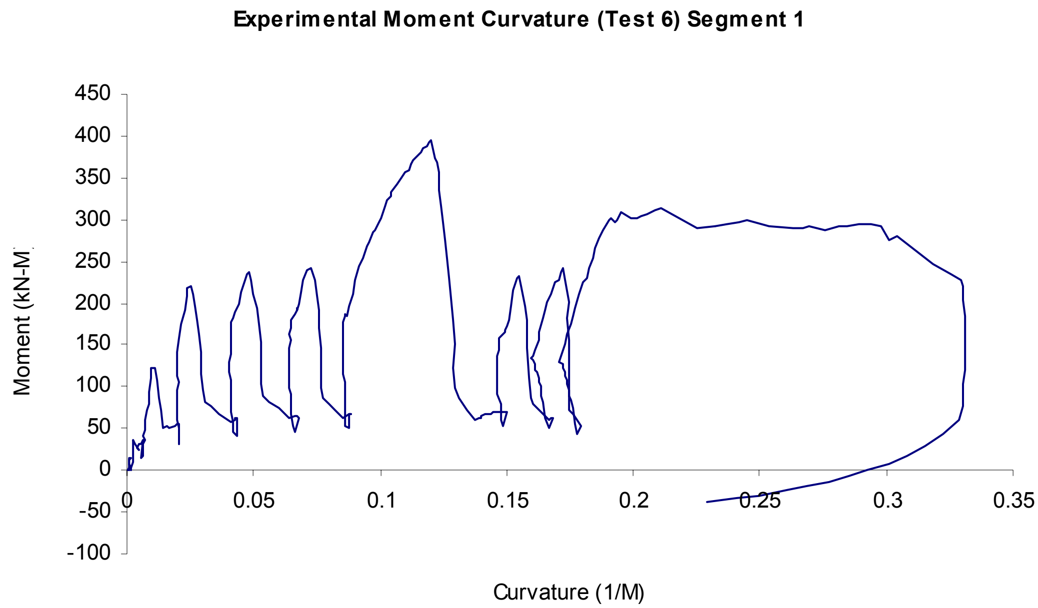

Figure 5.31 Experimental moment curvature of specimen six

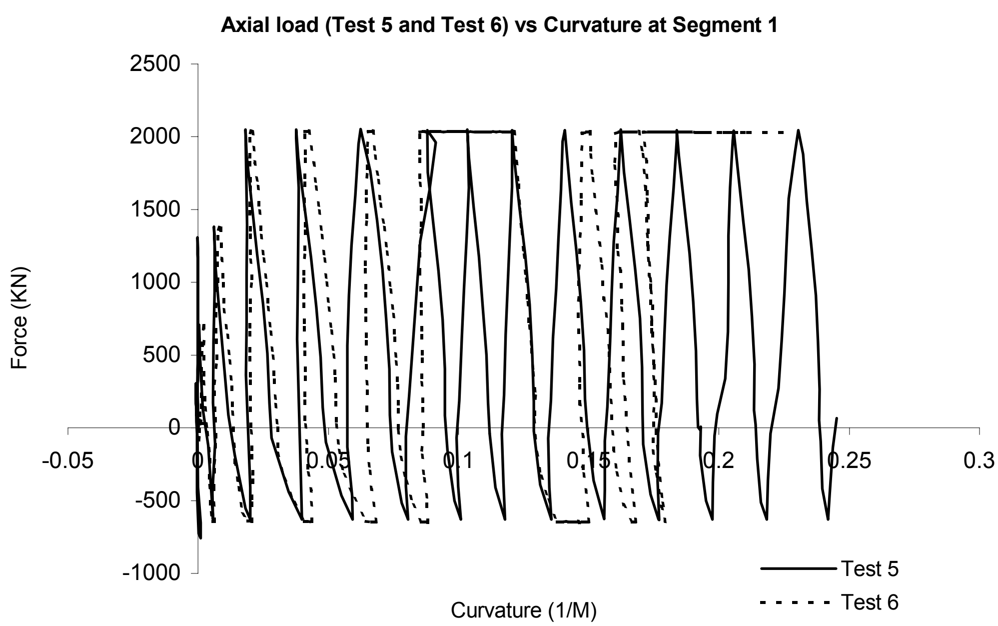

Figure 5.32 Comparing axial load for tests 5 and 6 considering curvature at first segment

After the curvature of 0.003, the pattern of variation of the axial load for the two tests with respect to curvature is different and at a curvature close to 0.004, the axial load level was fixed at the peak compressive value. Again, the difference in the response of the two tests is shown in Figure 5.33.

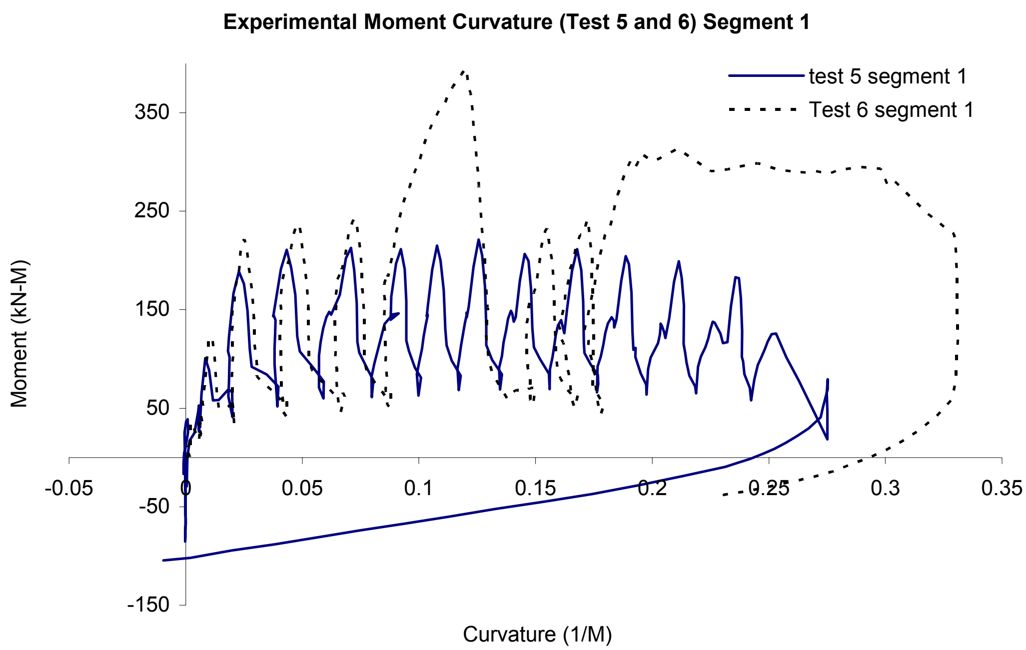

Figure 5.33 Comparison of moment-curvature response of tests 5 and 6 at the first segment

Figure 5.34 shows the distribution of curvature over the column height at different drift ratios and under various axial loads. The horizontal axis is the curvature (inch^{-1}) and the vertical axis is the column height. The figures show that for the same drift ratio, the pattern of curvature distribution along the column varies for different axial loads.

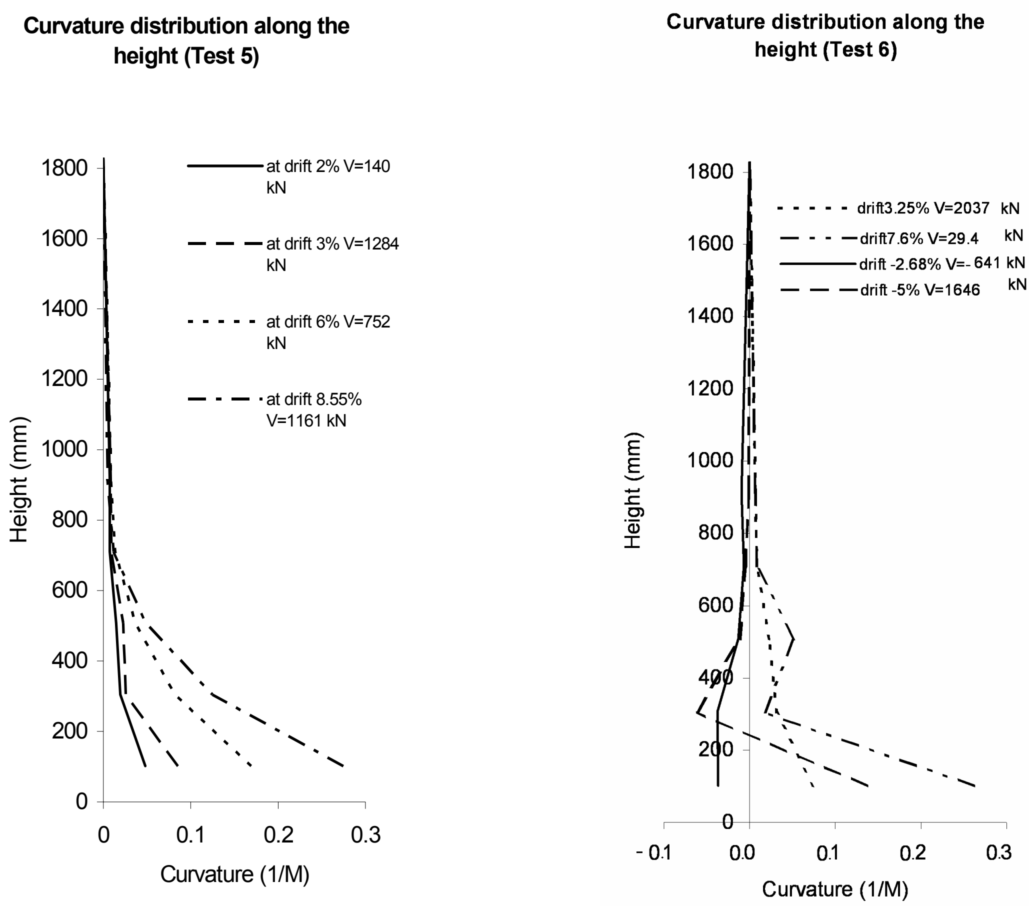

Figure 5.34 Distribution of curvature along the column at different drift ratios and axial forces for tests five and six

5.5 STEEL STRAIN RESPONSE

The steel strain response was determined from the results obtained from a total of 30 strain gages applied on the rebars and the spiral at 5 levels for specimen one, and from 24 gages for specimen two.

Figure 5.35 (a) shows the strain distribution on the spiral at the footing surface, a height of 8", and 16", for a drift ratio of -1.5% for specimen one.

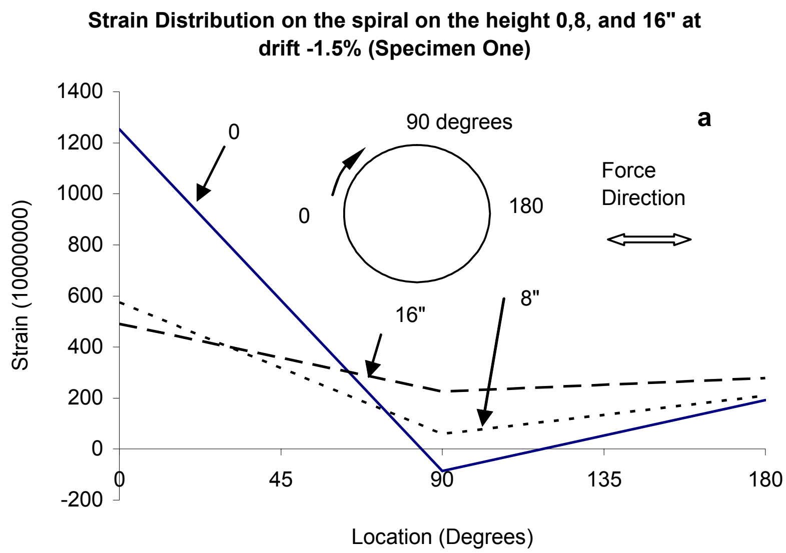

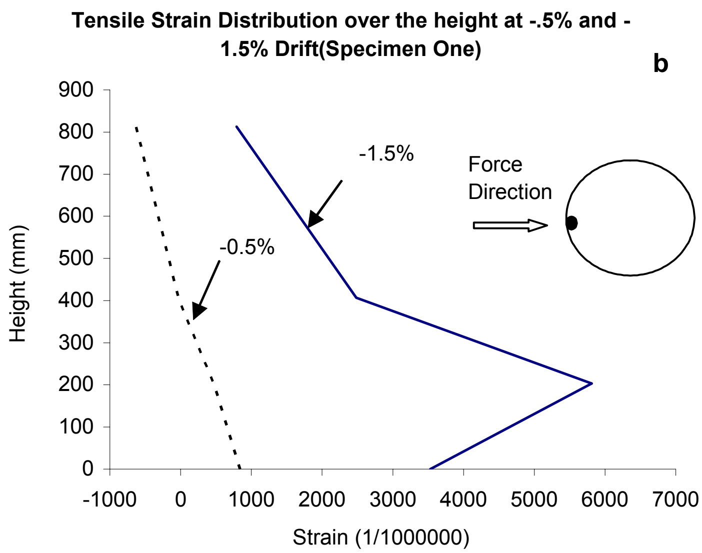

Figure 5.35 Specimen one

In Figure 5.35(b), the strain distribution along the column for drift ratios -0.5% and -1.5% on the tensile face is shown for the first specimen. At -0.5% drift, due to a high level of compressive axial load and relatively low moment, all the section is under compression at a height of 32 in. Figure 5.36(a) shows the strain distributions on the spiral and along the height for specimen two. In Figure 5.36(b), the strain distribution along the column for drift ratios of -1% and -1.5% is shown for a rebar on the tensile side. It should be noted that for both specimens the strain on the footing is shown to be less than at the next level, while the moment is greater and apparently a larger amount is expected. This is due to the plastic strain of the concrete and the total deformation in the section on the footing that results in a smaller portion of the moment carried by the steel compared to the section at a height of 203 mm (8 in.).

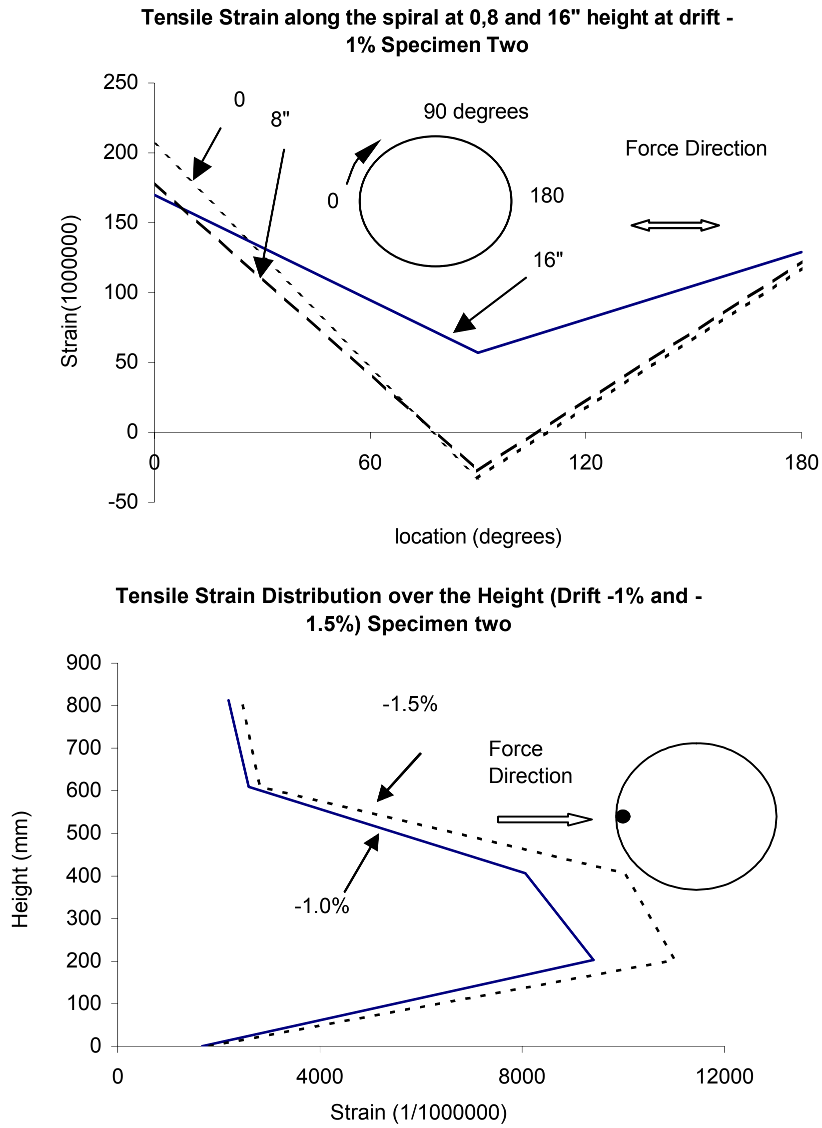

Figure 5.36 Specimen two

Figures 5.37 to 5.40 show the distribution of strain along the height of the column for the specimens at different drift ratios. The distribution of the tensile and compressive strain is completely different for different axial loading patterns. For the cases with a relatively high axial load, the strain at the location close to the column footing interface is less than the strain at the neighboring point above it on the column; while for the tests with zero, negative or a very low axial load level, this strain is more than at the neighboring point above, provided the rebar location on which the strain is recorded is in the compression side of the section. For tests 5 and 6, the distribution depends on the axial load level at the instance the data were captured and plotted. As shown, at different drift ratios the distribution from this perspective is different, corresponding to different levels of axial load. As an example of this phenomenon, the distribution of the strain on the compression side of specimen five is always such that the strain at the column-footing interface is less than at the location above it. In general, the strain at the column-footing interface is less when the location falls within the compression zone and is more when in the tensile zone, compared to the strain at the neighboring point above on the same rebar, but if the level of axial load is extremely high or low, the strain at the interface is lower or higher, respectively, throughout the section. The figures in Appendix I for each test show all the experimental responses of the specimens under the respective loading and displacement conditions.

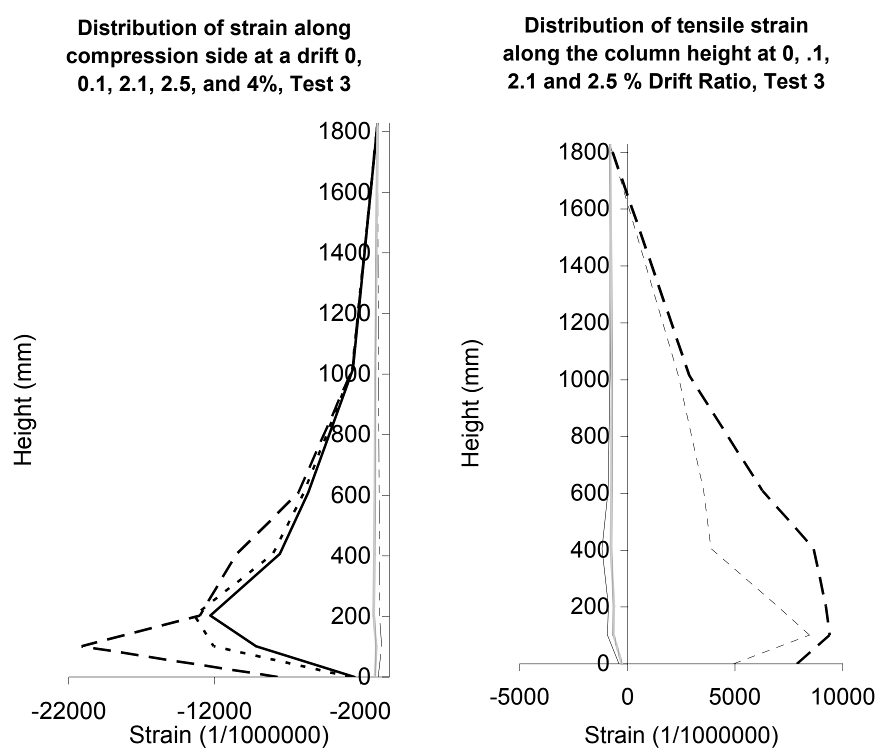

Figure 5.37 Strain distribution along the column height, specimen three

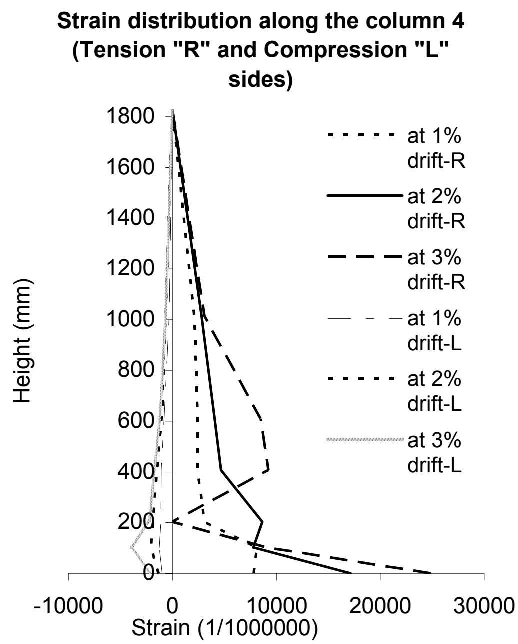

Figure 5.38 Strain distribution along column 4 (no axial load) at different drift ratios on compression and tension sides

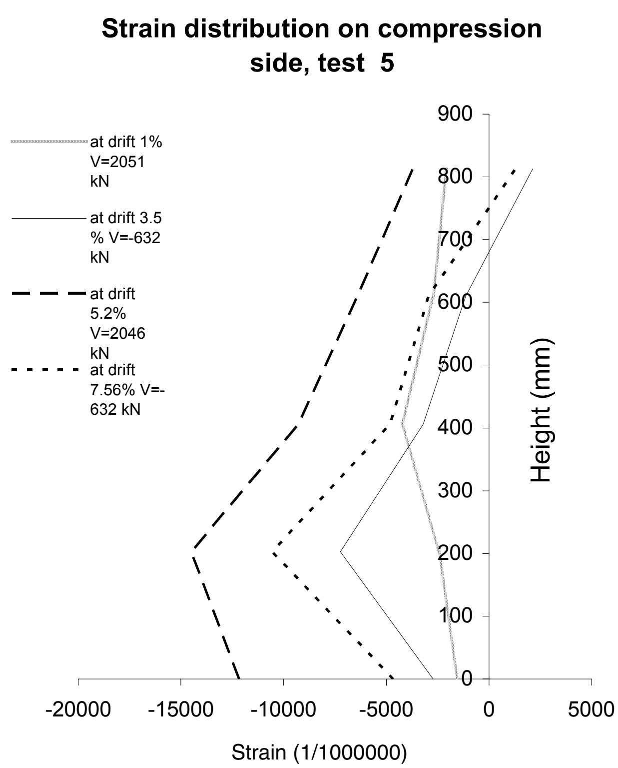

Figure 5.39 Strain distribution along column 5 at different drift ratios and various axial load levels

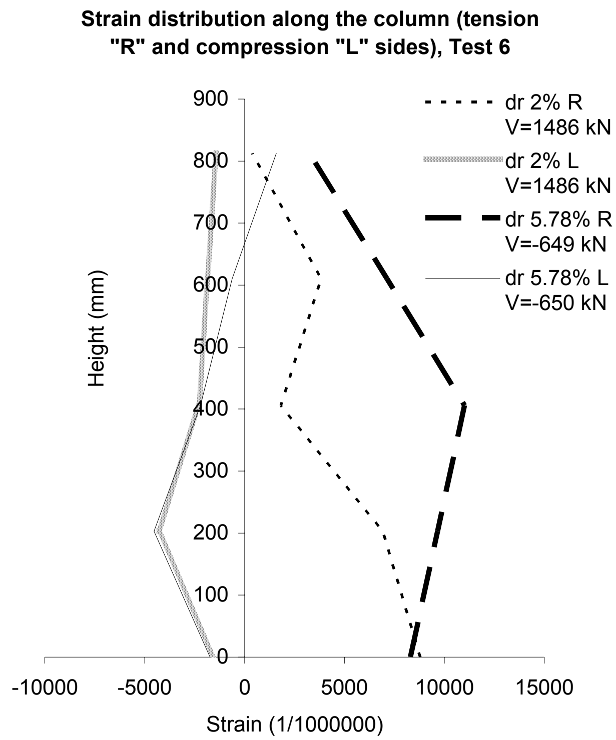

Figure 5.40 Strain distribution along column height, specimen 6, on compression and tension sides at different drift ratios and axial loads

6 Analytical Material Models

6.1 INTRODUCTION

The analysis of the behavior and the design of any RC structure or element, namely bridge substructures, the piles and columns of piers, requires analytical models and methods that accurately reflect the true nonlinear cyclic loading behavior of the element. Current analytical modeling techniques of structural elements use either a macro–modeling approach or a micro–finite element approach. It is evident that a coarse macro-approach, in which lumped plasticity within elements is used for the prediction of the response behavior, is too crude in many cases for investigating the detailed behavior of joints and plastic hinges. On the other hand, sophisticated finite element models may require a very fine mesh representation, prohibiting analysis of large- or even moderate-size bridges. Combining these two approaches has been considered the most appropriate compromise. This is also true for the analytical models for material behavior. While in some cases a simplified model for simulating the monotonic stress-strain relationship of a material in an approximate way may be adequate, in many other cases, where a detailed study of the response is expected, and especially in the case of a hysteretic response, more accurate and reliable models are required.

USC_RC, a tool developed to address the analytical needs of research on the seismic behavior of bridge piers, employs analytical models and methods that in some cases are the same as, or a revision of, existing conventional models and methods, and in others are specifically developed based on observations and experimental data.

The following reviews existing analytical models for material behavior, both monotonic and hysteretic response, and also models employed in the analytical part of the current research on the seismic behavior of bridge piers.

6.2 MATERIAL MODELS

Many different models have been proposed so far for the stress-strain relationship of the material used in an RC member. In general, for each material the model for the monotonic response of the material serves as the envelope curve for the hysteretic behavior model.

6.2.1 Monotonic Response

Typical monotonic stress-strain curves for steel and concrete have been obtained from steel bars loaded monotonically in tension, or concrete specimens loaded monotonically in compression.

6.2.1.1 Steel

Steel can be categorized into two major distinct groups in terms of its ductility. Figure 6.1 shows a typical stress-strain curve for cast iron that has a brittle nature, and a typical stress-strain curve for mild steel. Since the reinforcing steel used in RC structures and members is generally from the latter type, all the models discussed here fit this category.

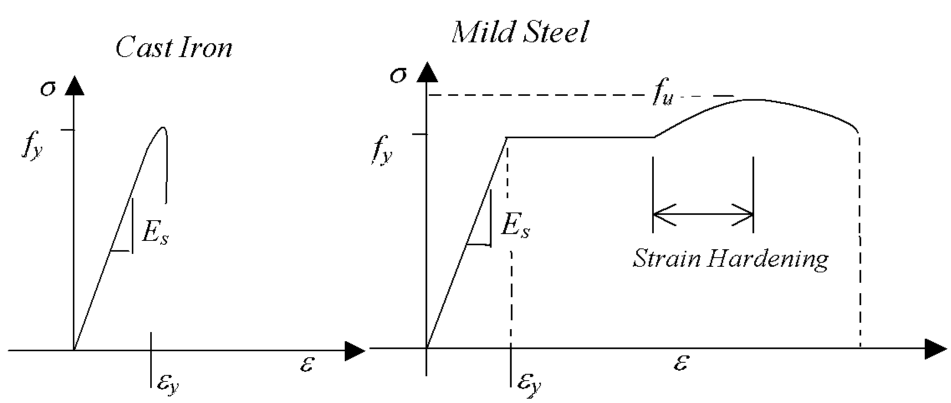

Figure 6.1 Typical stress-strain curves for cast iron and mild steel

Numerous tests have shown that the monotonic stress-strain curve for reinforcing steel can be described by three well-defined branches. This is generally the case for approximately all kinds of the reinforcing steel used in RC members. Different models are proposed for monotonic stress-strain response of steel. Some of these models are briefly discussed.

(a) Multilinear Model

A multilinear model has been used widely by researchers in analytical studies. In this model, several straight lines approximate the stress-strain curve. The slope of the first segment is equal to the modulus of elasticity of the steel, and the slope of the following segments are defined to be either a portion of the initial slope or zero, depending on the real observed stress-strain curve for which the approximation is applied. In most cases, two lines approximate the curve, the first segment having the modulus of elasticity of the steel as the slope, while the second has either a smaller slope or a slope equal to zero. Figure 6.2 shows two cases of a bilinear (A) and trilinear (B) modeling of the stress-strain behavior of steel. In most engineering cases, the former model has been used with results accurate enough for practical purposes.

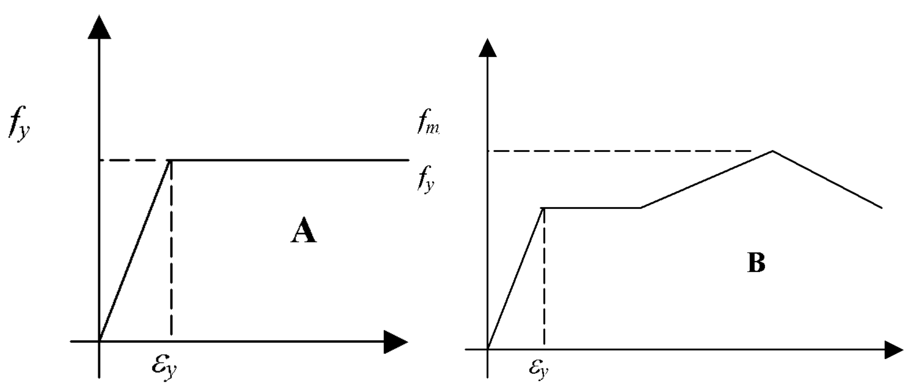

Figure 6.2 Typical multilinear stress-strain relationship curves used to model the stress-strain relationship of steel

(b) Park and Paulay Model

The actual stress-strain curve of steel, in its general shape, has been modeled by Park and Paulay (1975). The governing equations are as follows:

region AB $\quad f_s = \varepsilon_s E_s \quad$ (6.1)

region BC $\quad f_s = f_y \quad$ (6.2)

region CD $\quad f_s = f_y[\frac{m(\varepsilon_s - \varepsilon_{sh}) + 2}{60(\varepsilon_s - \varepsilon_{sh}) + 2} + \frac{(\varepsilon_s - \varepsilon_{sh})(60 - m)}{2(30r + 1)^2}] \quad$ (6.3) where $$m = \frac{(f_{su}/f_y)(30r+1)^2 - 60r - 1}{15r^2} \tag{6.4}$$

$$r = \varepsilon_{su} - \varepsilon_{sh} \tag{6.5}$$

(c) Mander Model

To have a better agreement with the actual behavior of mild steel, in some cases, the strain-hardening portion of the curve may be approximated by a curve. The following model is a sample that yields results close to real behavior when the proper parameters are used.

Mander et al. (1984) found that the strain-hardening region ($\varepsilon_{sh}<\varepsilon_s<\varepsilon_{su}$) in the stress-strain curve can be predicted with good accuracy by:

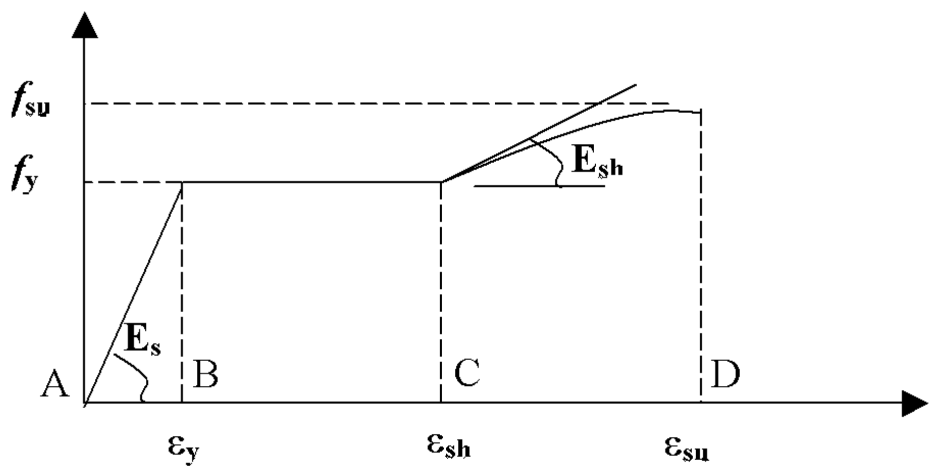

Figure 6.3 The proposed stress-strain curve for steel by Mander et al. (1984) and Park and Paulay (1975)

$$f_s = f_{su} - (f_{su} - f_y)\left(\frac{\varepsilon_{su} - \varepsilon_s}{\varepsilon_{su} - \varepsilon_{sh}}\right)^p \tag{6.6}$$

where ε_s is the steel strain; ε_{sh} is the steel strain at the commencement of strain hardening; ε_{su} is the steel strain at f_{su} ; f_s is the steel stress; f_{su} is the ultimate tensile strength of the steel; f_y is the yield strength of the steel; E_{sh} is the strain-hardening modulus of steel; and:

$$p = E_{sh}(\frac{\varepsilon_{su} - \varepsilon_{sh}}{f_{su} - f_y}) \tag{6.7}$$

(d) Model Developed and Used in the Analytical Program

The model developed and used in the analytical program in the second and third phases is different from the aforesaid models and yields results that comply well with the material test results. This model is flexible, and by adjustment of its parameters can be used to simulate the behavior of different types of steel, even if the main intension has been in simulating the mild steel cases. In this model, four parameters are used.

1. ***K_1*** is the ratio of the strain at the start of the strain hardening to the yield strain.
2. ***K_2*** is the ratio of the strain at the ultimate stress to the yield strain.
3. ***K_3*** is the ratio of the ultimate strain to the yield strain.
4. ***K_4*** is the ratio of the ultimate stress to the yield stress.

The curve is assumed to be linear up to the yield point, which is the case for approximately all kinds of steel, and to have a pure plastic deformation from the yield point up to a strain of ***K_1*** times the yield strain. The maximum strength is assumed to occur at a strain of ***K_2*** times the yield strain, and is equal to ***K_4*** times the yield stress, and steel rupture occurs at a strain of ***K_3*** times the yield strain. A quadratic curve joins the start of the strain-hardening point, the maximum strength point, and the rupture point. The parameters of the model employed in the analytical works of this study have been scaled so that the resulting curve is very close to the experimental curve resulting from the material tests on the sample bars and spiral used in the construction of columns. Figure 6.6 and Figure 6.7 show the experimental stress-strain curves for the longitudinal reinforcement and confining steel, respectively, resulting from the material tests conducted at the USC Structural Lab. Figure 6.4 shows the USC_RC monotonic stress-strain curve for steel. The four different parameters used to adjust the model to fit the experimental data are shown in the figure. By adjusting these parameters the experimental curves for either the longitudinal or transverse reinforcement can be successfully simulated. The mathematical formulation of the model is as follows:

- For $0 < \varepsilon < \varepsilon_y \Rightarrow \sigma = E_s \varepsilon$ where ε is the strain, ε_y is the yield strain of steel, σ is the stress, and E_s is the modulus of elasticity of steel.
- For $\varepsilon_y \leq \varepsilon < k_1 \Rightarrow \sigma = E_s \varepsilon_y$

- For $k_1\varepsilon \le \varepsilon < k_3\varepsilon \Rightarrow \quad \sigma = \dfrac{E_s(1-k_4)(\varepsilon^2 + 2k_2(k_4-1)E_s\left|\varepsilon\right| + E_s\varepsilon_y + k_1^{\,2}k_4 - 2k_1k_2k_4 + k_2^{\,2})\varepsilon}{\varepsilon_y\left|\varepsilon\right|(k_1^{\,2} - 2k_1k_2 + k_2^{\,2})}$

- For $\varepsilon > k_3\varepsilon_y \Rightarrow \sigma = 0.$

A flowchart for the monotonic stress-strain response of steel, as modeled in USC_RC is shown in Figure 6.5.

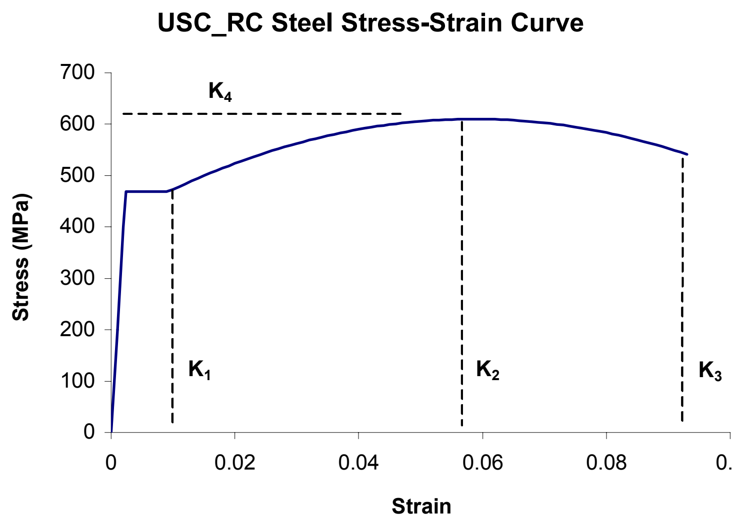

Figure 6.4 USC_RC model for monotonic stress-strain curve of steel

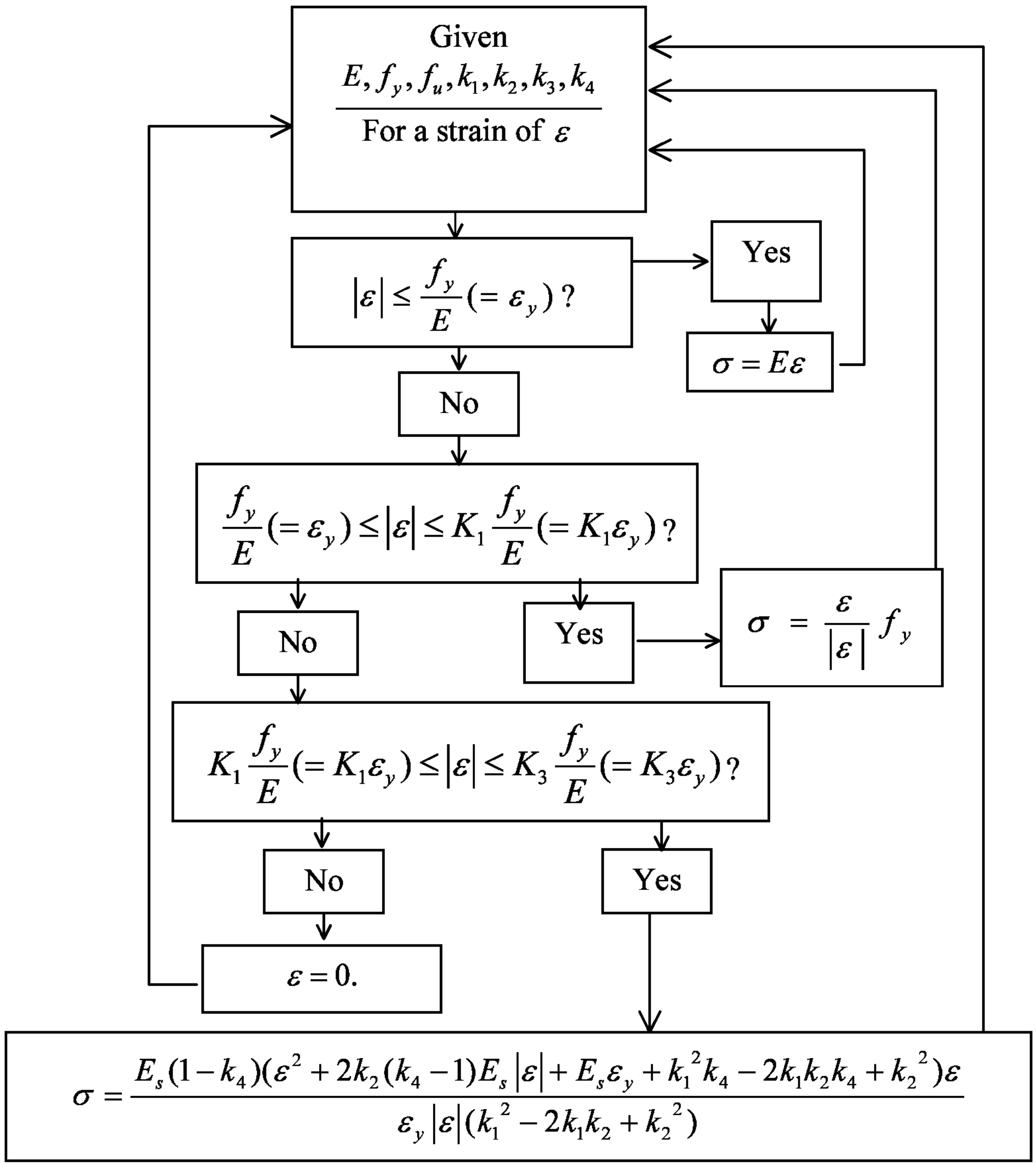

Figure 6.5 Flowchart for steel monotonic stress-strain response as modeled in USC_RC

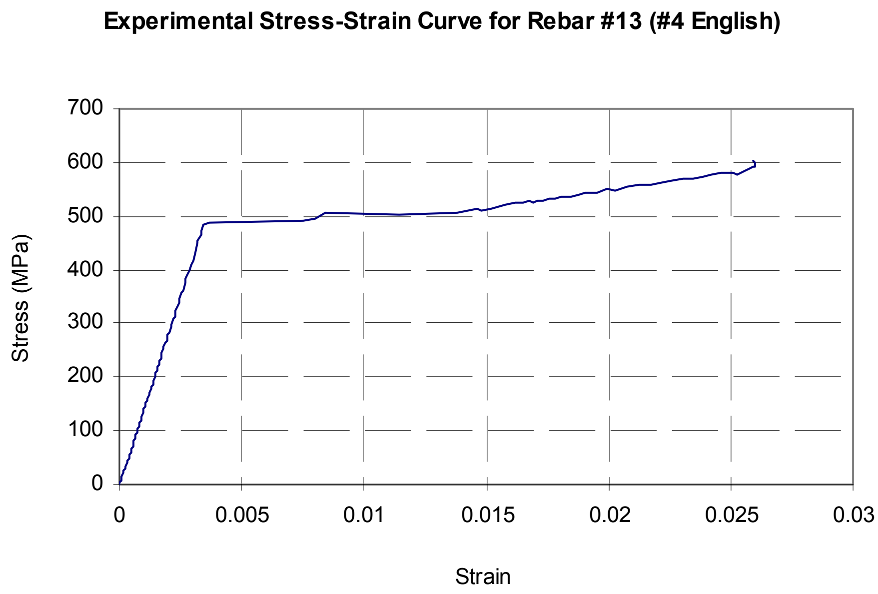

Figure 6.6 Experimental stress-strain curve for longitudinal bars

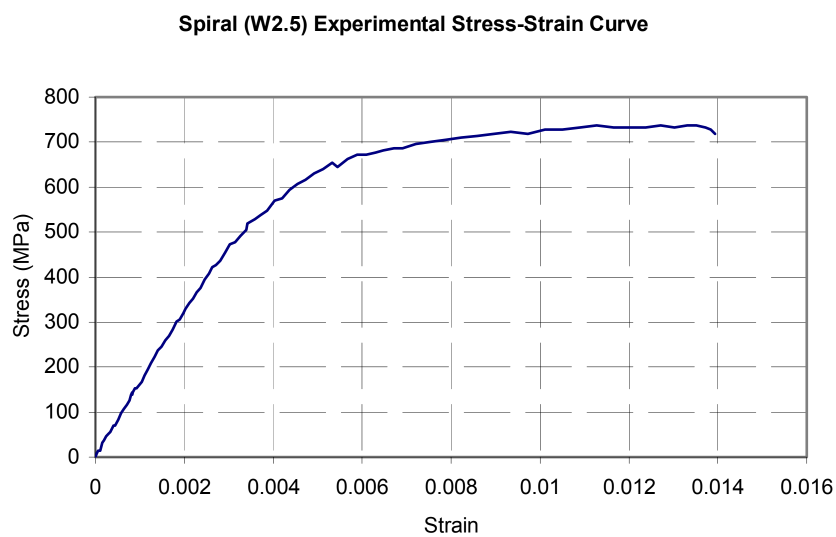

Figure 6.7 Experimental stress-strain curve for confining steel (spiral)

6.2.1.2 Concrete

Concrete is composed of two parts, confined concrete and cover concrete. Various models have been proposed to model the stress-strain relationship of confined and in turn unconfined concrete. The model employed in theoretical predictions plays a basic role in the compatibility of the data with the test results. Each model seems to have efficiency for a specific situation, while not for others. The following reviews the existing models, including the model employed in the first stage of the analytical works related to the tests.

(a) Richart Model

The pioneer work on the effect of transverse reinforcement on concrete compression behavior was conducted by Richart et al. (Richart, 1928). Based on the test results of 100 mm×200 mm (4 in.×8 in.) concrete cylinders subjected to different types of transverse pressure, he discovered that the strength and corresponding strain of concrete were increasingly proportional to the increase in transverse pressure, a phenomenon then that seems obvious nowadays. Based on those early studies, the compression strength of the concrete was expressed as:

$$f'_{cc} = f'_{co} + kf_r \tag{6.8}$$

where f'_{cc} is the compression strength of the concrete with transverse pressure; f'_{co} is the strength without pressure; f_r is the transverse pressure; and k is the experimental coefficient, which was proposed as being *4.1* by Richart et al. The peak strain, ε_{cc}, at the compression strength of confined concrete was expressed as:

$$\varepsilon_{cc} = \varepsilon_{co}\left[1 + 5\left(\frac{f'_{cc}}{f'_{co}} - 1\right)\right] \tag{6.9}$$

where ε_{co} is the peak strain at the strength of plain concrete cylinders. This equation, essentially represents the simplest form of the Mohr-Coulomb two-parameter criterion, which defines the shear stress as the function of the normal stress (Chen, 1982).

(b) Fafitis and Shah Model

Fafitis and Shah et al. (Fafitis and Shah, 1985) proposed a confinement model based on the results of their tests. The model was initially developed for circular columns confined with spiral reinforcement. They suggested that columns with square sections can be treated as circular columns with the core diameter equal to the side of the square core. The confinement index to estimate the effective confining pressure was defined as:

$$f_r = \frac{A_{sh}}{d_c}\frac{f_{yh}}{s} \tag{6.10}$$

where A_{sh} is the total section area of the transverse reinforcement in the vertical cross section within spacing s; d_c is the equivalent diameter for a square column section assuming it equals the side of the confined square concrete core; f_{yh} is the yield strength of the confinement steel. The complete stress-strain curve consists of two parts, ascending and descending branches. Both branches meet at the peak point with a zero slope, which avoids any discontinuity. The ascending branch in fact is a parabolic function with its extreme point coinciding with the peak of the stress-strain curve. The main parameters used in the ascending parts are the modulus of elasticity for unconfined concrete E_c, confined concrete strength f'_{cc}, and strain at confined strength ε_{cc}. The peak coordinates f'_{cc} and ε_{cc} are calculated based on the unconfined concrete cylinder strength f'_c and the confinement index f_r. The descending branch is an exponential curve asymptotically approaching zero, while the strain tends to infinity. The parameters used for calculating the descending branch are the same as for the ascending one, plus the modulus of elasticity of the unconfined concrete. The complete mathematical expressions describing Fafitis and Shah's model are:

$$f_c = f'_{cc}\left[1-\left(1-\frac{\varepsilon_c}{\varepsilon_{cc}}\right)^A\right]; \text{ for } \quad 0<\varepsilon_c \le \varepsilon_{cc} \tag{6.11}$$

$$f_c = f'_{cc}\exp\left[-k\left(\varepsilon_c-\varepsilon_{cc}\right)^{1.15}\right]; \quad \text{for} \quad \varepsilon_c > \varepsilon_{cc} \tag{6.12}$$

where

$$A = E_c \frac{\varepsilon_{cc}}{f'_{cc}} \tag{6.13}$$

$$k = 24.65 f'_c \exp\left(-0.01\frac{f_r}{\lambda_1}\right) \tag{6.14}$$

$$E_c = 33\omega^{1.5}\sqrt{f'_c}\ psi \tag{6.15}$$

$$\lambda_1 = 1 - 25\left(\frac{f_r}{f_c}\right)\left(1 - \exp\left(-3.24 f'_c\right)^9\right) \tag{6.16}$$

The factor λ_1 depends on the concrete strength and degree of the confinement. This model can easily be used for unconfined concrete by taking $f_r = 0$. The value of the parameter k equal to zero corresponds to perfectly brittle behavior, while an infinitely large k corresponds to perfectly plastic behavior of confined concrete.

(c) Sheikh and Uzumeri Model

The model of Sheikh and Uzumeri et al. (1982) is one of the earliest developed for the prediction of the stress-strain relationship of confined concrete in tied columns. The model was developed based on the experimental results from 24 tests conducted by them, as well from a number of tests conducted before 1982 by other researchers. The complete stress-strain curve consists of three main sections. The first section represents a parabolic curve with its center coordinates (f_{cc}, ε_{s1}), the second part is a horizontal line up to the strain ε_{s2}, and the third section represents an inclined line with a slope Z. It continues up to the point where the stress becomes $0.3f_{cc}$, after which it again continues horizontally. The f_{cc} is the strength of the confined concrete, and ε_{s1} and ε_{s2} are the minimum and maximum strains, respectively, corresponding to the maximum stress of the confined concrete. They are expressed as follows:

$$f_{cc} = K_s f'_{co} \tag{6.17}$$

$$\varepsilon_{s1} = 0.55 K_s f'_{co} \times 10^{-6} \tag{6.18}$$

f'_{co} is cylinder strength in *psi*.

$$\varepsilon_{s2} = \varepsilon_{co}\left[1 + \frac{0.81}{C}\left(1 - 5.0\left(\frac{s}{B}\right)^2\right)\frac{\rho_s f'_s}{\sqrt{f'_{co}}}\right] \tag{6.19}$$

Here all stresses are in *psi* and C is in inches. ε_{oo} is the strain corresponding to the maximum stress in a plain concrete specimen. The parameter K_s, which is called the strength gain factor, was determined from regression analysis based on tests of confined concrete columns:

$$K_s = 1.0 + \frac{2.73B^2}{P_{occ}}\left[\left(1 - \frac{nC^2}{5.5B^2}\right)\left(1 - \frac{s}{2B}\right)^2\right]\sqrt{\rho_s f'_s} \tag{6.20}$$

where f'_s is in *ksi* and P_{occ} is in *kips*. The slope Z for the third section of the stress-strain curve is expressed as:

$$Z = \frac{0.5}{\frac{3}{4}\rho_s\sqrt{\frac{B}{s}}} \tag{6.21}$$

The many parameters used in these equations depend mainly on the geometry of the specimen, amount of reinforcement, etc. Thus, s is the spacing of the transverse reinforcement; ρ_s is the volumetric ratio of transverse reinforcement; C is the center-to-center distance between longitudinal bars; and n is the number of curvatures between the longitudinal bars. This takes into account that some of the concrete at the surface of the core remains unconfined. For square columns n coincides with the number of the longitudinal bars. f'_s is the stress in the lateral reinforcement, which is recommended to take as the yield stress of the lateral reinforcement. P_{occ} is described by the following equation:

$$P_{occ} = f'_{co}(A_{co} - A_s) \tag{6.22}$$

where

$$A_{co} = B \times H \tag{6.23}$$

A_s is the total sectional area of the longitudinal steel bars; A_{co} is the area of the confined concrete core; B and H are the center-to-center distance of the perimeter hoop of the rectangular concrete core. According to Sheikh and Uzumeri et al. the maximum error in the predicted K_s value on the unsafe side is less than 4%, and the maximum conservative error is about 7%. They also proposed a parameter ε_{s85} for confined concrete strain corresponding to 85% of maximum concrete stress on the unloading branch of the stress-strain curve:

$$\varepsilon_{s85} = 0.225\rho_s\sqrt{\frac{B}{s}} + \varepsilon_{s2} \tag{6.24}$$

It is assumed as the ultimate strain of confined concrete.

(d) Mander, Priestley, and Park Model

Mander, Priestley, and Park (1988) and others have developed a general model for concrete confined by various types of transverse reinforcements (Mander, Priestley, and Park, 1988). The Mander model has been widely used in analyzing columns with both circular and rectangular cross sections (Xiao, Priestley and Seible, 1994; 1996). The load application can be either static or dynamic, applied monotonically or by load cycles. The transverse reinforcement can also be of different types: circular or spiral, rectangular hoops with or without cross ties. In this report only the stress-strain relationship for rectangular columns confined with rectangular hoops under monotonically applied load is considered. To develop the model, Mander conducted tests on full-scale confined RC columns, with a concrete strength of 30 MPa and steel yield strength of about 300 MPa. The main equation describing the monotonic stress-strain relationship for confined concrete is:

$$f_c = \frac{f'_{cc}xr}{r-1+x^r} \tag{6.25}$$

where x is the ratio of strain (ε_c) to the strain at peak stress (ε_{cc}), f'_{cc} is the peak stress for confined concrete; r is the ratio of the concrete's initial modulus to the difference of the initial and secant moduli of elasticity. These parameters and their components are mathematically expressed by:

$$x = \frac{\varepsilon_c}{\varepsilon_{cc}} \tag{6.26}$$

$$\varepsilon_{cc} = \left[R\left(\frac{f'_{cc}}{f'_{co}} - 1 \right) + 1 \right] \varepsilon_{co} \tag{6.27}$$

$$r = \frac{E_c}{E_c - E_{\sec}} \tag{6.28}$$

$$E_c = 5000\sqrt{f'_{co}} \ MPa \tag{6.29}$$

$$E_{\sec} = \frac{f'_{cc}}{\varepsilon_{cc}} \quad (6.30$$

In the above equations f'_{co} and ε_{co} are, respectively, the concrete cylinder strength and corresponding strain. The parameter R is an empirical value determined experimentally. According to Mander et al., it varies from 3 for high-strength concrete to 6 for normal-strength concrete. The main parameter figuring in the equations is the peak longitudinal compressive stress for confined concrete. It is expressed as:

$$f'_{cc} = f'_{co}\left(2.254\sqrt{1 + \frac{7.94 f'_l}{f'_{co}}} - \frac{2 f'_l}{f'_{co}} - 1.254 \right) \tag{6.31}$$

where f'_l is the effective lateral confining stress, defined as:

$$f'_l = \frac{1}{2} K_e \rho_s f_{yh} \tag{6.32}$$

The most important parameter in Mander's model is the confinement effectiveness coefficient K_e. It takes into account the efficiency of different types of transverse reinforcement. Mander et al. proposed different equations for K_e for different types of transverse reinforcement, particularly for circular sections and the spiral-shaped transverse reinforcement:

$$k_e = \frac{1-\frac{s'}{2d_s}}{1-\rho_{cc}} \tag{6.33}$$

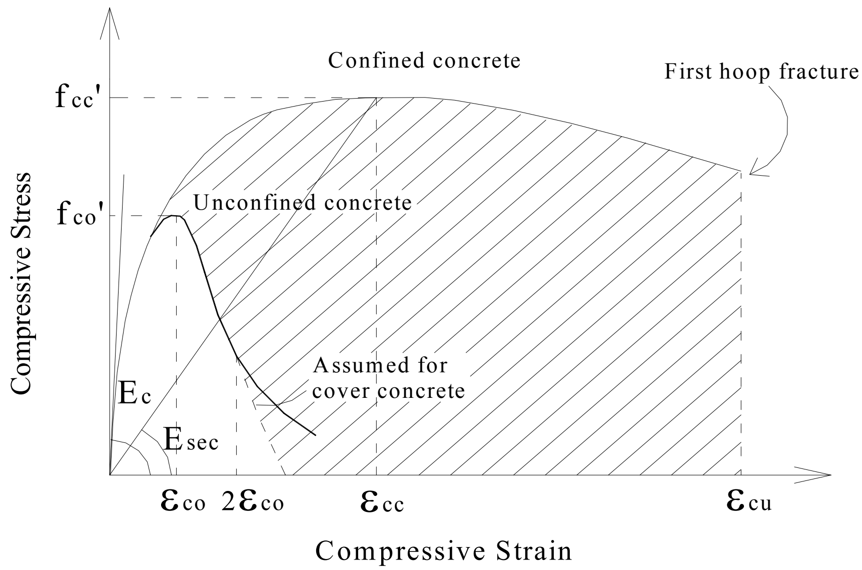

Figure 6.8 Mander et al. (1988) model for monotonic response of confined and unconfined concrete

Here ρ_{cc} is the ratio of the area of the longitudinal reinforcement to the area of the core section, and ρ_s is the ratio of the volume of the transverse confining steel to the volume of the confined concrete core. The expression f_{yh} is the yield strength of the transverse reinforcement. The model is valid only within a certain range of confinement steel; otherwise the results are not realistic and valid. Also there is a deficiency in the model regarding the descending part of the confined concrete stress-strain curve. The experimental results (Martirossian, 1996) show that some modifications as proposed by Martirossian and others are required to make it more realistic. Also, as already mentioned, the model may be applied only for a confinement range for which f'_l is between zero and about 2.3; otherwise the method will not yield realistic behavior.

(e) Li and Park Model

Li and Park et al. have conducted numerous tests on circular and square RC columns (Li and Park, 2001). Based on the test results, they modified Mander's model for predicting the performance of high-strength concrete columns with various types of reinforcement configurations. The Li and Park model can be used for the cases of both unconfined and confined concrete. Since their model is mainly for regarding the performance of high-strength concrete, it will not be explained here.

(f) Cusson and Paultre Model

Recent research projects conducted in the field of confined high-strength concrete include studies done by Cusson and Paultre (1993) on the development of a stress-strain model and its calibration against test results from 50 large-scale high-strength concrete tied columns tested under concentric loading. From those 50 test specimens, 30 high-strength concrete confined columns were experimented on by Cusson and Paultre, whereas the other 20 tests were conducted earlier by others. Since their work is mostly about the behavior of, and effect of confinement on high-strength concrete, the model will not be explained in further detail.

(g) Saatcioglu and Razvi Model

An interesting analytical model was proposed by Saatcioglu and Razvi. (Saatcioglu and Razvi, 1992) to construct a stress-strain relationship for confined concrete. The model consists of two parts: a parabolic ascending branch, followed by a linear descending branch. Lateral reinforcement in the sense of equivalent uniform lateral pressure in both circular and rectangular columns was used to develop the model characteristics for the strength and ductility of the confined concrete. The model has been compared with different types of column tests, including circular, square, and rectangular, as well as welded wire fabric. Spirals, rectilinear hoops, and cross ties have been used as lateral reinforcement in confined columns. Concentrating on the part of the model representing square columns, the confined concrete strength is calculated as:

$$f'_{cc} = f'_{co} + k_1 f_l \tag{6.34}$$

where f'_{cc} and f'_{co} are the confined and unconfined strengths of concrete in a member, respectively. Coefficient k_1 varies with different values of lateral pressure f_l. Based on the test data, a relationship between these two parameters has been established as:

$$k_1 = 6.7\left(f_l\right)^{-0.17} \tag{6.35}$$

where f_l is the uniform confining pressure in MPa.

Unconfined concrete strength f'_{co} is the plain concrete strength in a member under concentric loading. It might be different than the standard cylinder strength.

While the lateral confining pressure can easily be obtained from circular column tests, that is not the same for square and rectangular columns. Therefore, the term "effective lateral pressure" f_{le} has been proposed as:

$$f_{le} = k_2 f_l \tag{6.36}$$

and

$$f_l = \frac{\sum A_s f_{yt} \sin\alpha}{s b_c} \tag{6.37}$$

where k_2 is the 1.0 for circular columns and square columns with closely spaced lateral and laterally supported longitudinal reinforcement, α is the angle between the transverse reinforcement and b_c, and is equal to 90 degrees if they are perpendicular.

In general k_2 is expressed as:

$$k_2 = 0.26\sqrt{\left(\frac{b_c}{s}\right)\left(\frac{b_c}{s_l}\right)\left(\frac{1}{f_l}\right)} \le 1.0 \tag{6.38}$$

where pressure is in MPa. The strain corresponding to the peak stress of confined concrete (f'_{cc}) is denoted as ε_1 and is calculated as similar to that found by previous researchers (Balmer 1949; Mander et al. 1988):

$$\varepsilon_1 = \varepsilon_{01}\left(1+5K\right) \quad (6.39)$$

where

$$K = \frac{k_1 f_{le}}{f'_{co}} \quad (6.40)$$

In the above equations, ε_{01} is the strain corresponding to the peak stress of unconfined concrete, which should be determined under the same rate of loading used for the confined concrete. In the absence of experimental data the value 0.002 may be used. This concludes the first part of the model, i.e., the ascending branch of the stress-strain curve.

The descending branch of the curve is linear and connects the points (f'_{cc}, ε_1) and ($0.85 f'_{cc}, \varepsilon_{85}$) on the plane of the stress-strain curve. The value of strain corresponding to 85% of confined concrete strength is calculated as:

$$\varepsilon_{85} = 260\rho\varepsilon_1 + \varepsilon_{085} \quad (6.41)$$

where ρ is the volumetric ratio of transverse reinforcement and is expressed as:

$$\rho = \frac{\sum A_s}{s\left(b_{cx} + b_{cy}\right)} \quad (6.42)$$

and ε_{085} is the strain corresponding to 85% of the strength level beyond the peak stress of unconfined concrete. Again it should be determined under the same rate as for the confined concrete specimen. If no test data are available the value 0.0038 might be used.

Based on all the above-mentioned parameters, a stress-strain relationship for confined concrete has been proposed:

$$f_c = f'_{cc}\left[2\left(\frac{\varepsilon_c}{\varepsilon_1}\right) - \left(\frac{\varepsilon_c}{\varepsilon_1}\right)^2\right]^{\frac{1}{1+2K}} \le f'_{cc} \quad (6.43)$$

This is a parabolic relationship and is valid up to the peak stress point, after which the relationship is converted to a linear descending one.

(h) Sakino Model

Much research conducted in the field of confined concrete has been by Japanese researchers. This study will discuss research by Sakino et al. (1993). Many of these tests have been conducted on circular as well as rectangular confined RC columns under axial loading. Different types of transverse reinforcement have been used to obtain effective confinement for an RC column. The main stress-strain equation is represented as follows:

$$\sigma_c = {}_c\sigma_{cB} \frac{AX + (D-1)X^2}{1+(A-2)X + DX^2} \tag{6.44}$$

where ${}_c\sigma_{cB}$ is the confined concrete strength and is determined as:

$${}_c\sigma_{cB} = \sigma_p + \kappa\rho_h\sigma_{yh} \tag{6.45}$$

where σ_{yh} is the steel strength. The expression σ_p stands for plain concrete stress and is determined as:

$$\sigma_p = \mu_c\sigma_B \tag{6.46}$$

where ${}_c\sigma_B$ is the strength of a standard concrete cylinder, and μ is a coefficient which is equal to 0.8 for circular columns, and 1.0 for square columns. The coefficient κ is determined differently for circular and square columns. For square columns it is equal to:

$$\kappa = k_s\left(\frac{d''}{C}\right)\left(1-\frac{s}{2D_c}\right) \tag{6.47}$$

where $k_s = 11.5$; D_c is the center-to-center dimension of a steel hoop; and C is the transverse distance between any two anchored longitudinal bars.

Three parameters used in expressions *X*, *A*, and *K* are proposed as follows:

$$X = \frac{\varepsilon_c}{\varepsilon_{co}} \qquad A = \frac{E_c\varepsilon_{co}}{{}_c\sigma_{cB}} \qquad K = \frac{{}_c\sigma_{cB}}{\sigma_p} \tag{6.48}$$

ε_{co} is the strain corresponding to the peak stress of a confined concrete member and is determined as:

$$\varepsilon_{co} = \varepsilon_o \begin{cases} 1+4.7(K-1) & K \le 1.5 \\ 3.35+20(K-1.5) & K \ge 1.5 \end{cases} \tag{6.49}$$

ε_o is cylinder strain at peak stress:

$$\varepsilon_o = 0.5243\left({}_c\sigma_B\right)^{\frac{1}{4}} \times 10^{-3} \tag{6.50}$$

E_c is Young's modulus, which is calculated as:

$$E_c = 4k\left(\frac{{}_c\sigma_B}{1000}\right)^{\frac{1}{3}} \times 10^5 \times \left(\frac{\gamma}{2.4}\right)^2 \tag{6.51}$$

and k is an empirical coefficient expressed as follows, depending on the type of raw materials in the concrete mix.

$$k = \begin{cases} 1.0 \\ 1.2 \\ 0.9 \end{cases} \tag{6.52}$$

The variable D in the main stress-strain equation is calculated as:

$$D = \alpha + \beta\, {}_c\sigma_B + \gamma\sqrt{\frac{(K-1)\,{}_c\sigma_B}{23}} \tag{6.53}$$

where $\alpha = 1.5$; $\beta = -1.68 \times 10^{-3}$; and γ is equal to 0.75 for the steel tube and 0.50 for square hoops.

(i) Yong, Nour, and Nawy Model

This model was developed based on empirical results of a test program studying the effects of rectilinear confinement in high-strength concrete subjected to a monotonically increasing compressive axial load (Yong, Nour, and Nawy et al., 1988). Twenty-four columns of high-strength concrete were tested. The concrete strength ranged from 12,130 to 13,560 psi. The columns were rectilinearly confined with lateral ties and longitudinal rebars. All specimens failed in a single shear plane. #3 longitudinal steel bars were used with 61.5 ksi yield strength, 92.0 ksi ultimate stress, and 28,000 ksi Young's modulus. Since this model is closely related to the models already mentioned in detail, and is mostly for high-strength concrete, the model will not be explained here any further.

(j) Martirossian Model

Martirossian (1996) proposed a model for confined high-strength concrete that may be considered as a revised version of the aforementioned Mander's model for confined concrete. The revisions have been based on the results from extensive experimental tests on high-strength concrete columns at the USC Structural Lab. Since Martirossian's model is mainly for the behavior of high-strength concrete, no further discussion will follow.

(k) USC_RC Model

The model for the monotonic stress-strain relationship of confined and cover concrete employed in the USC_RC model for the analysis of the seismic behavior of bridge piers under different loading conditions is as proposed by Mander, Priestley, and Park, and is shown in Figure 6.8. Figure 6.9 shows a case of the confined and cover concrete envelope curves for the material strengths and section geometry for the column specimens. The ultimate strain for cover and confined concrete is determined based on the energy-based principle proposed by Mander (1988) By equating the ultimate strain energy capacity of the confining reinforcement per unit volume of concrete core (U_{sh}) to the difference in area between the confined (U_{cc}) and the unconfined (U_{co}) concrete stress-strain curves, plus additional energy required to maintain yield in the longitudinal steel in compression (U_{sc}), the longitudinal concrete compressive strain corresponding to hoop fracture can be calculated. Therefore:

$$U_{sh} = U_{cc} + U_{sc} - U_{co} \tag{6.54}$$

Substituting corresponding values in Equation (6.54) gives:

$$\rho_s A_{cc} \cdot \int_0^{\varepsilon_{sf}} f_s d\varepsilon_s = A_{cc} \cdot \int_0^{\varepsilon_{cu}} f_c d\varepsilon_c + \rho_{cc} A_{cc} \cdot \int_0^{\varepsilon_{cu}} f_{sl} d\varepsilon_c - A_{cc} \cdot \int_0^{\varepsilon_{sp}} f_c d\varepsilon_c \tag{6.55}$$

where ρ_s = ratio of volume of transverse reinforcement to volume of concrete core; A_{cc} = area of the concrete core; f_s and ε_s = stress and strain in transverse reinforcement; ε_{sf} = fracture strain of transverse reinforcement; f_c and ε_c = longitudinal compressive stress and strain in concrete; ε_{cu} = ultimate longitudinal concrete compressive strain; ρ_{cc} = ratio of volume of longitudinal reinforcement to volume of concrete core; f_{sl} = stress in longitudinal reinforcement; and ε_{sp} = spalling strain of unconfined concrete.

In the first term of the left-hand side of Equation (6.55), the expression:

$$\int_0^{\varepsilon_{sf}} f_s d\varepsilon_s = U_{sf} \tag{6.56}$$

is the total area under the stress-strain curve for the transverse reinforcement up to fracture strain ε_{sf}. Mander et al. concluded from several test results that the above value is independent of bar size or yield strength and could be considered accurate within 10% as:

$$U_{sf} = 110 MJ / m^3 \tag{6.57}$$

The area under the stress-strain curve for unconfined concrete may be approximated as:

$$\int_0^{\varepsilon_{sp}} f_c d\varepsilon_c = 0.017\sqrt{f'_{co}} MJ / m^3 \tag{6.58}$$

where f'_{co} =quasi-static compressive strength of concrete in MPa (1 MPa=145 psi). Thus Equation (6.56) simplifies to:

$$110\rho_s = \int_0^{\varepsilon_{cu}} f_c d\varepsilon_c + \rho_{cc} \int_0^{\varepsilon_{cu}} f_{sl} d\varepsilon_c - 0.017\sqrt{f'_{co}} MJ / m^3 \tag{6.59}$$

So, from the preliminary data, the ultimate confined concrete strain at the first rupture of transverse steel can be evaluated numerically. This method has been implemented in USC_RC to evaluate the ultimate confined concrete strain.

Figure 6.10 shows some of the models proposed for the confined concrete stress-strain curve, and Table 6.1 summarizes some of these models.

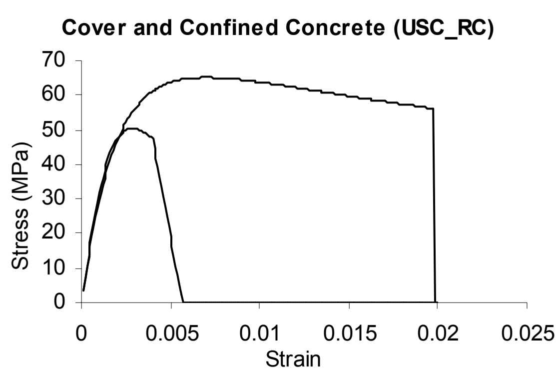

Figure 6.9 Confined and cover concrete envelope curves as used in USC_RC for analysis

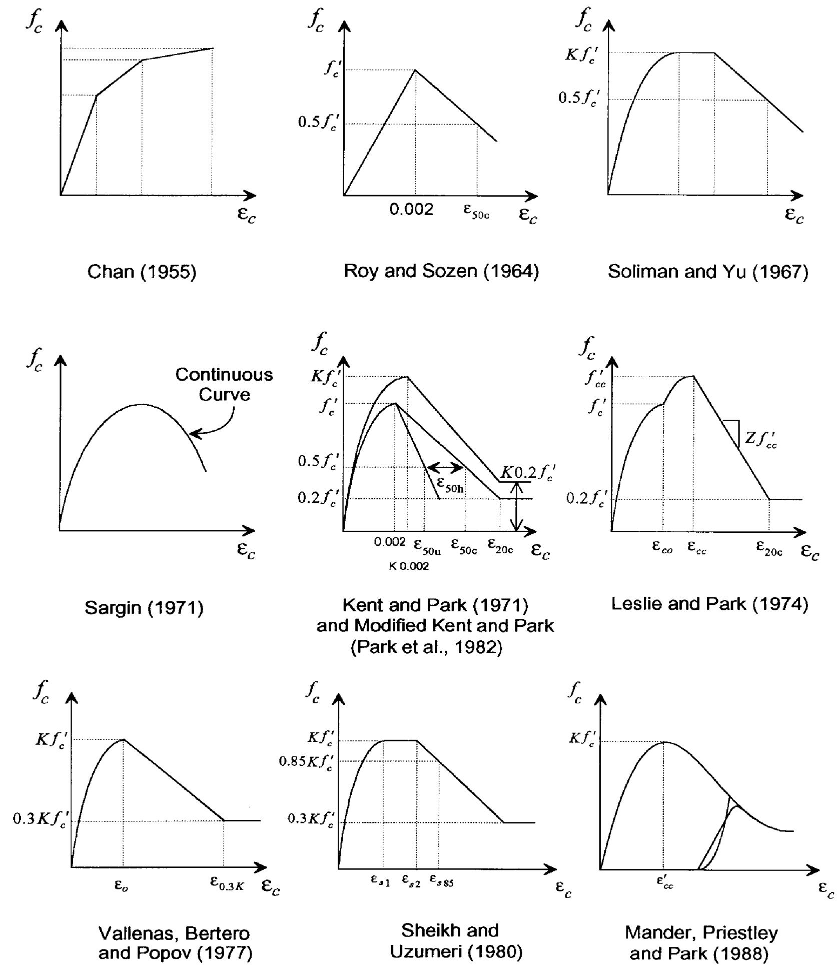

Figure 6.10 Stress-strain models proposed for confined concrete by different researchers

Table 6.1 Summary of several models for confined concrete response

Researcher	Confined Concrete Strength	Strain at Strength	Ultimate Strain
Richart	$f'_{cc} = f'_{co} + 4.1 f_r$	$\varepsilon_{cc} = \varepsilon_{co}\left[1 + 5\left(\frac{f'_{cc}}{f'_{co}} - 1\right)\right]$	
Sheikh and Uzumeri	$f_{cc} = K_s f_{co}$	$\varepsilon_{s1} = 0.55 K_s f'_{co} \times 10^{-6}$	$\varepsilon_{s85} = 0.225 \rho_s \sqrt{\frac{B}{s}} + \varepsilon_{s2}$
Mander, Priestley, and Park	$f'_{cc} = f'_{co}\left(2.254\sqrt{1 + \frac{7.94 f'_l}{f'_{co}}} - \frac{2 f'_l}{f'_{co}} - 1.254\right)$	$\varepsilon_{cc} = \left[R\left(\frac{f'_{cc}}{f'_{co}} - 1\right) + 1\right]\varepsilon_{co}$	Can numerically be evaluated using an energy based method.
Li and Park	$f'_{cc} = f'_{co}\left(1.413\sqrt{1 + \frac{11.4 f'_l}{f'_{co}}} - \frac{2 f'_l}{f'_{co}} - 0.413\right)$	$\varepsilon_{cc} = \varepsilon_{co}\left[-8.1 + 9.1\exp\left(\frac{f'_l}{f'_{co}}\right)\right]$	$\varepsilon_{cu} = \varepsilon_{co}\left[2 + \left(82.75 - 0.37 f'_{co}\right)\sqrt{\frac{f'_l}{f'_{co}}}\right]$
Cusson and Paultre	$\frac{f_{cc}}{f_{co}} = 1.0 + 2.1\left(\frac{f_{le}}{f_{co}}\right)^{0.7}$	$\varepsilon_{cc} = \varepsilon_{co} + 0.21\left(\frac{f_{le}}{f_{co}}\right)^{1.7}$	$\varepsilon_{c50c} = \varepsilon_{c50u} + 0.15\left(\frac{f_{le}}{f_{co}}\right)^{1.1}$
Saatcioglu and Razvi	$f'_{cc} = f'_{co} + k_1 f_l$	$\varepsilon_1 = \varepsilon_{01}\left(1 + 5K\right)$	$\varepsilon_{85} = 260 \rho \varepsilon_1 + \varepsilon_{085}$
Sakino	${}_c\sigma_{cB} = \sigma_p + \kappa \rho_h \sigma_{yh}$	$\varepsilon_{co} = \varepsilon_o \begin{cases} 1 + 4.7(K-1) & K \le 1.5 \\ 3.35 + 20(K-1.5) & K \ge 1.5 \end{cases}$	
Yong, Nour, and Nawy	$f_o = K f'_c$	$\varepsilon = 0.00265 + \frac{0.0035\left(1 - \frac{0.734 s}{h''}\right)\left(\rho'' f''_{yh}\right)^{\frac{2}{3}}}{\sqrt{f'_c}}$	
Martirossian Model	$f'_{cc} = f'_{co} + 3.68 \bar{f}_r$	$\varepsilon_{cc} = \varepsilon_{co}\left[1 + 5\left(\frac{f'_{cc}}{f'_{co}} - 1\right)\right]$	$\varepsilon_{cu} = 3\varepsilon_{co} + 1.1\varepsilon_{cc}$

6.2.2 Hysteretic Response

The hysteretic behavior of the reinforcing steel and concrete, especially the core concrete, has a remarkable effect on the hysteretic response of an RC member. Accurately modeling the hysteretic behavior is therefore crucial. General observations show that three basic components can be observed in the hysteretic response curve of any material or even of a structural member. These basic components may be described as follows.

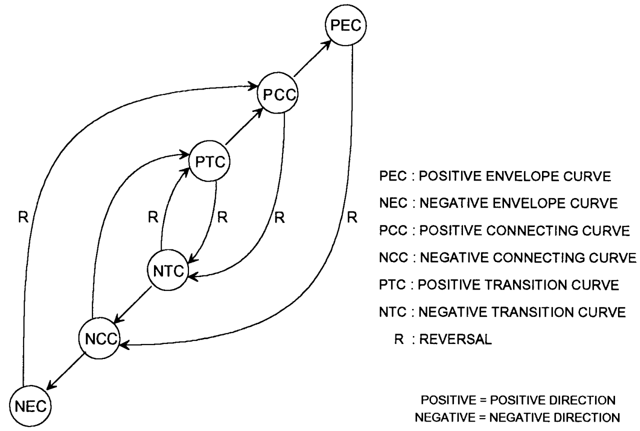

Figure 6.11 Relationship between curves in a rule-based hysteretic model

- Envelope curves can be fixed or re-locatable, or fixed or scalable. These curves are the backbones of the general hysteretic response. The degradation of material is usually simulated by shifting and scaling the envelope curves. The degradation can also be simulated by shifting the returning point. This means that the point of return to an envelope curve is different compared to the point where the last reversal occurred, a phenomenon that was observed during all the experiments discussed in this report.
- Connection curves are the connections between the envelope curves. There may be several points of inflation in these curves, as when used to represent pinching, and other softening and hardening phenomena within the material or structural element. Usually more than one equation should be employed to simulate these kinds of curves.
- Transition curves are those used when a reversal from a connecting curve takes place to make the transition to the connecting curve that goes in the opposite direction.

Different hysteretic models have been proposed both as a general hysteretic model, and as models to simulate the hysteretic response of steel or concrete.

Table 6.2 summarizes some general hysteretic models proposed by different researchers. These models cannot be regarded as both general and accurate. Each model may be applied in a specific case relatively successfully, while failing in others. As shown in the table, some models may be tuned to suit a particular case. Since in the current research the main goal is a detailed study of the seismic behavior of bridge columns, none of these models may be used to simulate the hysteretic response of a column. On the other hand, proper hysteretic models for materials, namely steel, confined concrete, and unconfined concrete are employed for a detailed analysis. The results show that this approach yields results that are closer to the experimental results, rather than simulating the hysteretic response of the whole column by using a tuned version of any general hysteretic model.

Table 6.2 Summarized specifications of some general hysteretic models

Model	Type	Controlled Parameters			Comparative Remarks			Sketch
		Stiffness Degradation	Pinching	Strength Deterioration	Additional *parameters	Overall Versatility	Overall Complexity	
Clough	S	N	N	N	0	L	L	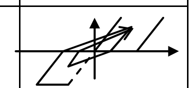
Fukada	S	Y	N	N	0	L	L	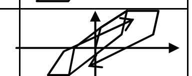
Aoyama	S	N	Y	Y	4	M	H	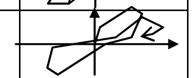
Kustu	S	N	Y	N	4	M	H	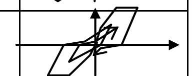
Tani	S	Y	N	N	2	H	M	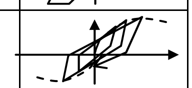
Takeda	S	Y	N	N	1	L	M	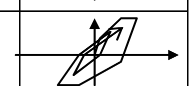
Park	C	Y	N	N	2	H	H	
Iwan	S	N	Y	N	1	L	M	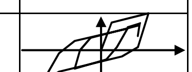
Takayanagi	S	Y	Y	Y	3	M	M	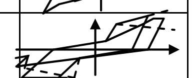
Muto	S	Y	N	N	0	L	L	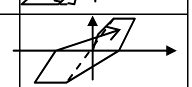
Atalay	C	Y	Y	N	4	L	H	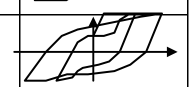
Nakata	C	Y	Y	Y	6	H	H	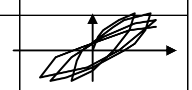
Blakeley	S	Y	N	Y	0	L	L	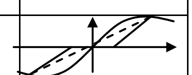
Mo	S	Y	Y	N	2	L	L	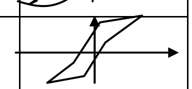
Pivot	S	Y	Y	N	0	M	L	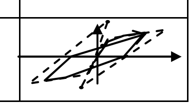

Notations: Y: Yes, N: No, S: Straight, C: Curved Line, L: Low, M:Medium, H: High,

6.2.2.1 Steel

(a) Simple Bilinear Hysteretic Model

Figure 6.12 shows a simple hysteretic model for steel. The envelope of this model is the bilinear stress-strain relationship of steel as described and shown in Figure 6.2 (A). Using this model in a hysteresis analysis provides results that are not as accurate as the results from a more realistic model. In this simple model, no degradation in strength or stiffness is considered and the strain-hardening effect is also ignored, as for the bilinear monotonic stress-strain curve.

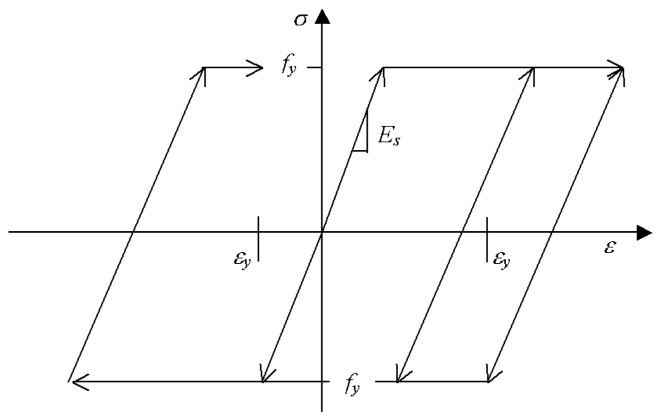

Figure 6.12 Simple bilinear hysteretic model for steel

(b) Ramberg-Osgood Model

Ramberg-Osgood (1943) equations can be used to get a reasonably good simulation for the hysteretic behavior of reinforcing steel. Figure 6.13 (Park and Paulay, 1975) shows this model compared with the experimental data on a sample with the same specifications in terms of yield, ultimate strength, and modulus of elasticity In fact f_{ch} and r in the following equation have been chosen empirically. The Ramberg-Osgood equation is as follows:

$$\varepsilon_s - \varepsilon_{si} = \frac{f_s}{E_s}\left(1 + \left|\frac{f_s}{f_{ch}}\right|^{r-1}\right) \tag{6.60}$$

where ε_s = steel strain, ε_{si} =steel strain at zero stress at the beginning of loading run, f_s = steel stress, E_s= modulus of elasticity of steel, f_{ch}= stress dependent on the yield strength and the plastic strain in the steel produced in the previous loading run, and r= parameter dependent on the loading run number.

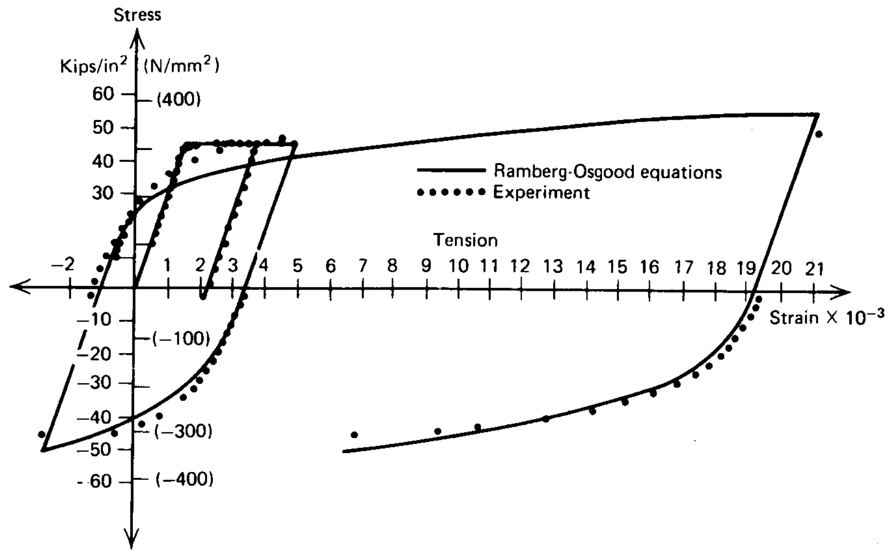

Figure 6.13 Hysteretic response of steel, based on Ramberg-Osgood equations

(c) Shibata Trilinear Model

Figure 6.14 shows the Shibata (1982) trilinear hysteretic curve for reinforcing steel. As shown in this figure, the yield strength in both the positive and negative (tension and compression) sides is assumed to be equal. The model is flexible in terms of the second and third level stiffness, and can be tuned to get close to a desired response. Kuramoto and Kabeyasawai (Kuramoto, Kabeyasawa, Shen, 1995), in their research on the influence of axial deformation on the ductility of high-strength RC columns under varying triaxial forces, took the post-yield stiffness,$E_{s3},$ and the reduced stiffness due to the Bauschinger effect, $E_{s2},$ as 1/200 and 1/10 of the elastic stiffness, E_{s1}, respectively. The incline of stiffness changing line C was taken as –1/200 of E_{s1}. The model used to simulate the hysteretic behavior of reinforcing steel in USC_RC is very similar to the Shibata model, but its flexibility is more comparable to this model, as will be discussed.

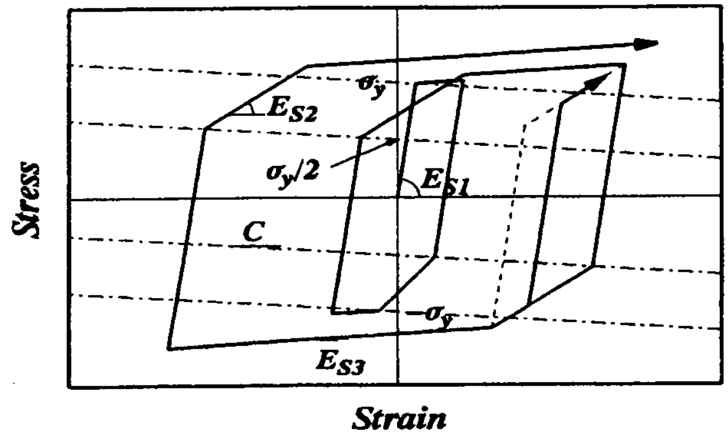

Figure 6.14 Shibata trilinear hysteretic curve for reinforcing steel

(d) Steel Hysteretic Model Developed and Used in USC_RC

The model developed and used in USC_RC is similar to the model proposed by Shibata (1982) but more flexible. The model has three major parts, common for any hysteretic model. Before any strain reversal, the stress and strain follow the monotonic stress-strain curve of steel as described in the USC_RC program and shown in Figure 6.4. At the turning point (strain reversal) the modulus of elasticity is assumed to be the same as the initial modulus of elasticity of steel. As shown in Figure 6.15 the same elasticity is assumed up to a stress after the sign of the transition of stress (after the stress sign changes from either positive to negative or vice versa) where the stress absolute value is a portion of the yield strength of the steel. This value can be tuned by a parameter, "P_1", and the value of this stress is "$P_1.f_y$", where "f_y" is the yield strength of steel. At this point the stiffness changes to a fraction of the initial stiffness. The value of the secondary rigidity can be tuned by changing parameter "P_2." In the model the secondary stiffness would be "$(P_1/P_2).E_s$", if in the first or third quarter of the coordinate plane, and "$(P_1/(2.P_2)).E_s$" if in the second and fourth quarter of the coordinate plane, where "E_s" is the modulus of the elasticity of steel. This change in stiffness is to consider a better effect for the strain hardening. Finally the stress-strain curve follows a linear path on a line lying on the same stress side that connects the point of ultimate strength and corresponding strain to the point with 1/9 times the yield strength of steel on the opposite strain side and at the ultimate strain. Figure 6.16 shows a sample curve of the steel hysteretic response as modeled in USC_RC. At the time just two parameters have been implemented in the model, but if necessary, increasing the number of parameters to four gives enough flexibility to tune the hysteretic response of the model to comply well with any desired hysteretic response for steel. The model can be mathematically explained by defining the stress and strain situation for the states where the initial (previous) stress-strain state is point 1, 2, or 3. Note that the behavior of the model is symmetric with respect to the origin because of assuming a symmetrical stress-strain curve for steel. Also, the direction of movement is shown in Figure 6.15.

- For point 1, provided no strain reversal has occurred previously for strains more than the yield strain in either the positive or negative (tension or compression) directions, the movement follows the monotonic stress-strain curve of steel. This curve is described in this chapter and shown in Figure 6.4.
- For point 2:

$$\text{If } \varepsilon > \varepsilon_p - \frac{\sigma_p + P_1 f_y}{E_s} \text{ then } \sigma = \sigma_p + E_s(\varepsilon - \varepsilon_p) \le f^{+line}(\varepsilon) \tag{6.61}$$

$$\text{If } \varepsilon \le \varepsilon_p - \frac{\sigma_p + P_1 f_y}{E_s} \text{ then :}$$

$$\sigma = P_1 f_y + (\frac{P_1}{2P_2} E_s(\varepsilon - \varepsilon_p + \frac{\sigma_p + P_1 f_y}{E_s}) \le f^{-line}(\varepsilon) \tag{6.62}$$

where:

$$f^{+line} = \left(\frac{f_u - \alpha f_y}{2\varepsilon_u}\right)\varepsilon + \frac{f_u + \alpha f_y}{2} \tag{6.63}$$

$$f^{-line} = \left(\frac{f_u - \alpha f_y}{2\varepsilon_u}\right)\varepsilon - \frac{f_u + \alpha f_y}{2} \tag{6.64}$$

where ε_p is the strain at the initial (previous) point, σ_p is the stress at the initial (previous) point, f_u is the ultimate strength of steel, f_y is the yield stress of steel, ε_u is the rupture strain of steel, and α is a parameter which can be tuned as desired. This parameter has been chosen as 0.9 in the model used in USC_RC for analysis.

- For point 3, the behavior is as explained for point 2 with the exception that:

$$\text{If } \varepsilon \le \varepsilon_p - \frac{\sigma_p + P_1 f_y}{E_s} \text{ then:}$$

$$\sigma = P_1 f_y + (\frac{P_1}{P_2} E_s (\varepsilon - \varepsilon_p + \frac{\sigma_p + P_1 f_y}{E_s}) \leq f^{-line}(\varepsilon) \qquad (6.65)$$

Note that the situation for point 2 moving in the other direction (increase in strain) is identical with a decrease in strain for point 3 and vice versa. In other words, the behavior is symmetric with respect to origin.

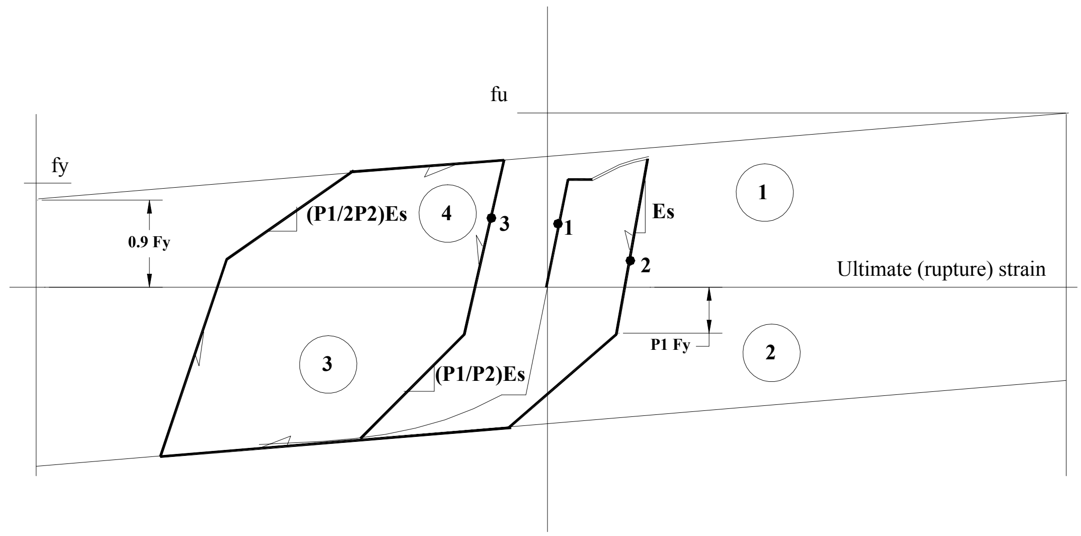

Figure 6.15 Steel hysteretic curve as modeled in USC_RC

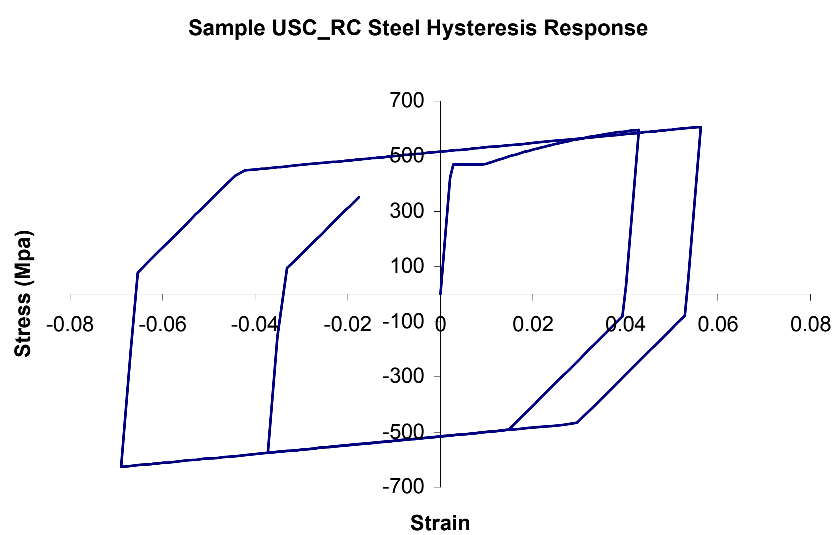

Figure 6.16 A sample hysteretic curve based on the USC_RC data

6.2.2.2 Concrete

Hysteretic models developed and proposed by different researchers are more comparable to the models proposed for the hysteretic behavior of steel. Each model has been developed based on the specific needs of the researcher. Most of the models are backed by empirical parameters and, in some cases, theoretical explanation. The following addresses some of the models and the method used in USC_RC.

(a) Park, Kent, and Sampson Model

A typical curve for the model proposed by Park, Kent, and Sampson (1972) is shown in Figure 6.17. The envelope curve for the compressive stress is represented by the relationship determined by Kent and Park (1969–1990) for concrete confined by hoops under monotonic loading. A linear stress-strain curve for concrete in tension may be assumed, having the same slope as the curve for compression at zero stress. The actual response of the concrete in this model, at the reversal of strain and stress, is approximated by a bilinear curve as demonstrated in the figure.

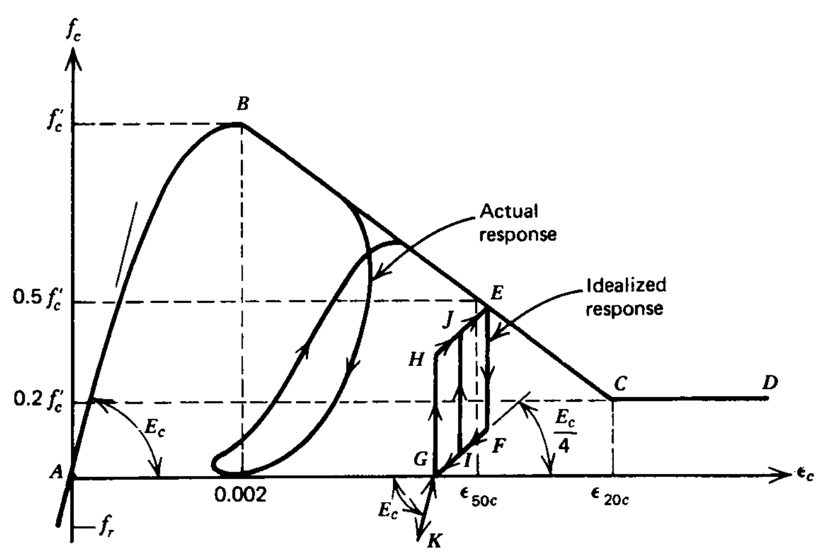

Figure 6.17 Hysteretic behavior of concrete as modeled by Park, Kent, and Sampson

(b) *Kuramoto and Kabeyasawa Model*

Figure 6.18 shows the hysteretic model for confined and cover concrete used by Kuramoto and Kabeyasawa (1991). Their hysteretic model is a divided linear model. As shown in the figure, σB is the cover concrete strength, *K* is the confinement coefficient, and E_{c1} is the initial stiffness of cover concrete, which is taken to be the same for confined concrete. All other parameters are self evident and their values can be tuned as needed, as was done by Kuramoto and Kabeyasawa.

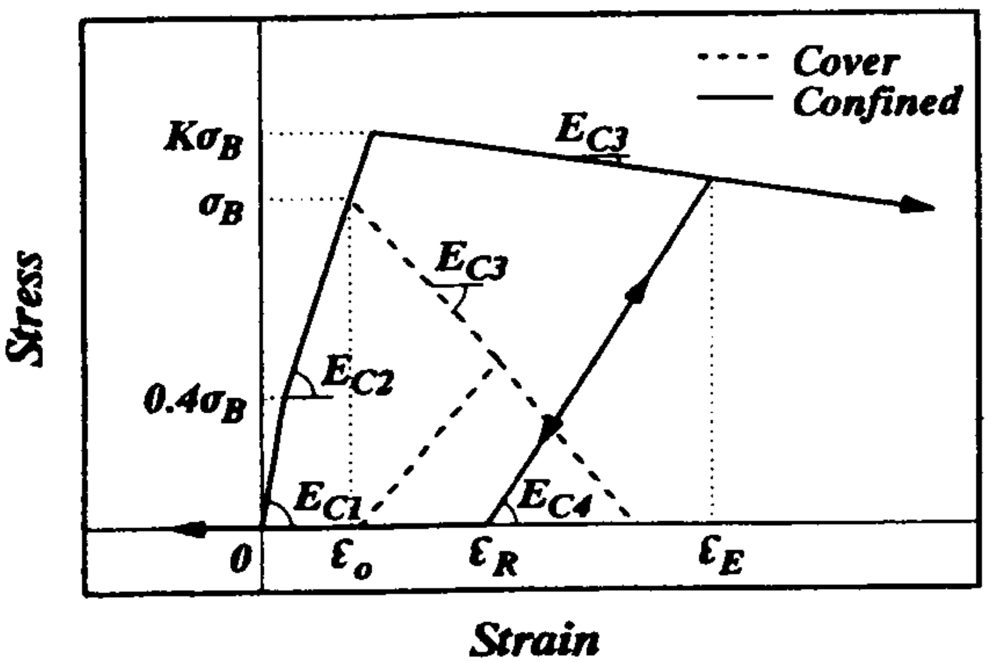

Figure 6.18 Kuramoto and Kabeyasawa model for hysteretic behavior of concrete

(c) *Mander et al. Model*

The procedure adopted by Mander et al. to simulate the hysteretic behavior of reinforced concrete is similar to the approach used by Takiguchi et al. (1976) but modified to be suitable for both unconfined and confined concrete. Figure 6.19 shows the model for the unloading branch and determination of plastic strain. In the figure .ε_{un} and f_{un} are the unloading strain and stress, respectively; ε_{pl} is the plastic strain. Mander et al. proposed a relatively complicated procedure to define the hysteretic curve.

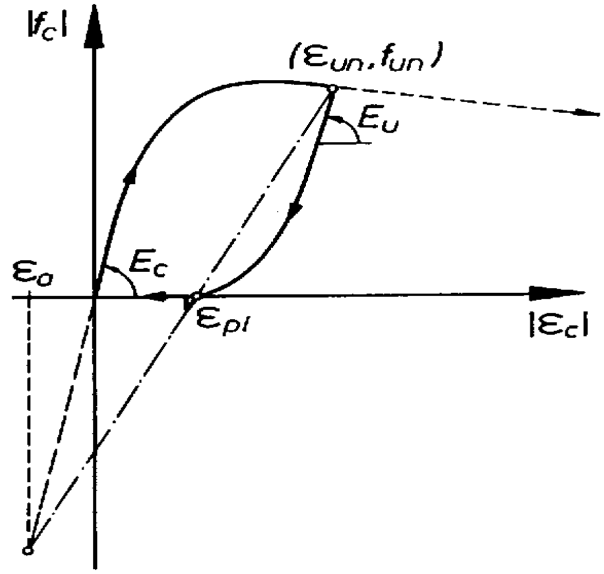

Figure 6.19 Stress-strain curves for unloading branch and determination of plastic strain as Mander model.

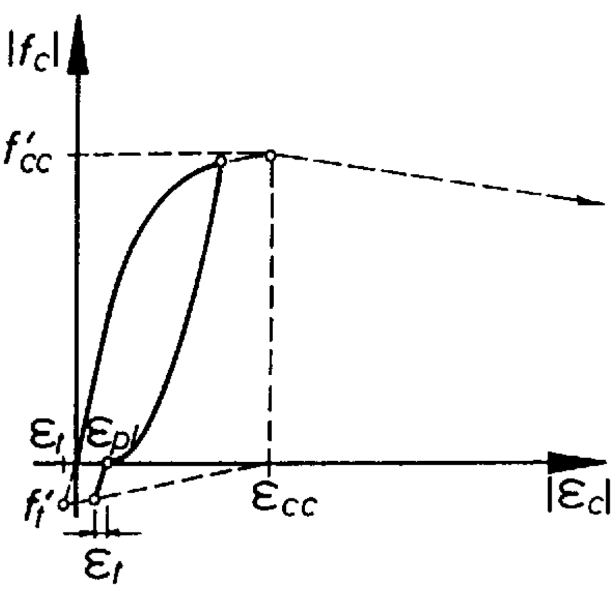

Figure 6.20 Assumed deterioration in tensile strength of concrete due to prior compression loading in the Mander model.

Figure 6.20 demonstrates the deterioration in the tensile strength of concrete due to prior compression loading.. In this figure ε_t is the tensile strain and f'_t is the initial tensile strength. The compressive strength of concrete is f'_{cc}.

Figure 6.21 shows a sample hysteretic stress-strain curve proposed by Mander et al. (1988) for the reloading curves in particular.

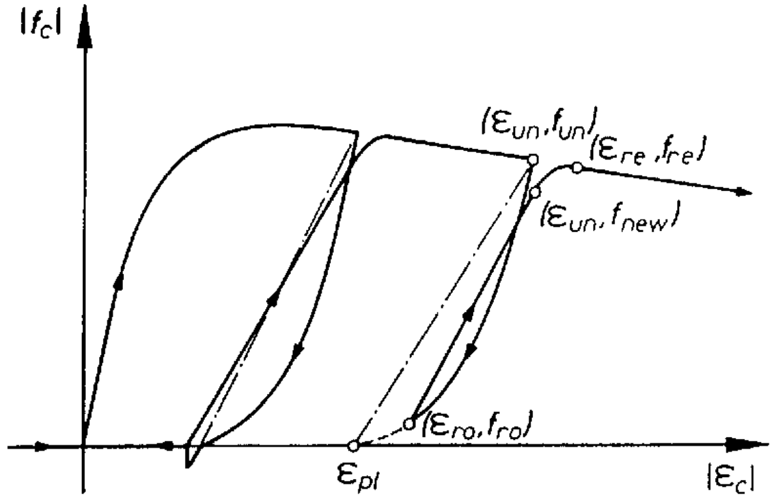

Figure 6.21 Stress-strain curves for reloading branch in the model proposed by Mander et al. (1988)

(d) Model Developed and Used in USC_RC

The envelope for the model is the monotonic stress-strain curve as shown in Figure 6.9, which is based on the model proposed by Mander et al. The response of the model is very similar to the model proposed by Mander et al. (1988), but requires much less computational effort. The USC_RC model can be very close to the Mander model by tuning the pertinent parameters. At a strain reversal the curve follows a parabolic path that is concave upward. The initial slope of the reversal curve is taken to be equal to the initial stiffness of the confined concrete. As the strain is decreased, the slope is gradually reduced and will be close to zero when the stress approaches zero. The stress remains zero for strains less than this value. At the second reversal of strain, the stress remains zero up to a strain where the stress had vanished in the first reversal, and then it grows with a slope equal to the initial stiffness of the confined concrete in the beginning. The slope decreases as the strain and corresponding stress increase. The stress increases up to the envelope curve and then follows that curve. It should be added that for the ascending and descending paths of the hysteretic curve, we may apply two different initial stiffnesses that in turn may be different from the initial stiffness of the confined concrete. In the analysis of the experimental results reported here and implemented by USC_RC, these values have been chosen to be identical. The model developed and used in USC_RC mathematically is as follows:

- For ascending and descending within the elastic range of the confined concrete response (defined here within a strain of 0.015 for confined concrete) the path follows the monotonic stress-strain curve as described earlier.
- For ascending from a point with a strain of ε_p and a stress of σ_p, as shown in Figure 6.22, the stress is evaluated as:

$$\sigma = -\frac{E_{c1}^{\ 2}}{4f_{cc}}\left(\varepsilon - \varepsilon_p + \frac{2f_{cc}}{E_{c1}} - \frac{2\sqrt{f_{cc}\left(f_{cc}-\sigma_p\right)}}{E_{c1}}\right)^2 + E_{c1}\left(\varepsilon - \varepsilon_p + \frac{2f_{cc}}{E_{c1}} - \frac{2\sqrt{f_{cc}\left(f_{cc}-\sigma_p\right)}}{E_{c1}}\right) \tag{6.66}$$

where $0 \le \sigma \le f^{con}\left(\varepsilon\right)$, E_{c1} is the slope when the stress is zero, f_{cc} is the confined concrete strength, ε is the new strain, and $f^{con}\left(\varepsilon\right)$ is the monotonic stress of the confined concrete at the new strain.

- For descending from a point with a strain of ε_p and a stress of σ_p as shown in Figure 6.23, the stress is evaluated as follows:

$$\text{For } \varepsilon > \varepsilon_p - \frac{2\sqrt{f_{cc}\sigma_p}}{E_{c2}}, \qquad \sigma = -\frac{E_{c1}^{\ 2}}{4f_{cc}}\left(\varepsilon - \varepsilon_p - \frac{2\sqrt{f_{cc}\sigma_p}}{E_{c2}}\right)^2 \le f^{con}\left(\varepsilon\right) \tag{6.67}$$

$$\text{For } \varepsilon \le \varepsilon_p - \frac{2\sqrt{f_{cc}\sigma_p}}{E_{c2}}, \qquad \sigma = 0. \tag{6.68}$$

In this model, E_{c1} and E_{c2} can be provided as is proper by the user. In USC_RC these values have been chosen to be the same as the initial stiffness of the confined concrete. Although the tensile stress of concrete has been ignored, it is not difficult to include in the model. Considering the tensile strength of concrete with the deterioration caused by the previous compressive loading, and replacing the ascending curve with a line, makes the model very close to what Mander et al. proposed for the hysteretic behavior of concrete. Another model similar to this but with a linear path for the descending and ascending branches was developed for the very preliminary testing of the code. Since this preliminary simple hysteretic model is not used in USC_RC, it will not be discussed.

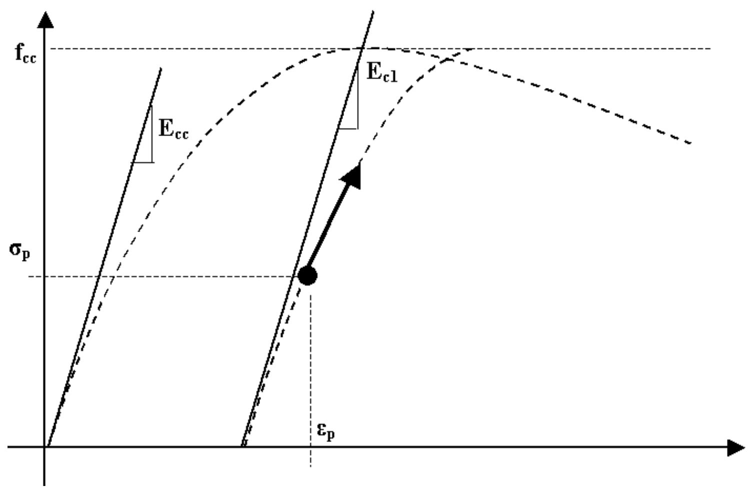

Figure 6.22 USC_RC confined concrete hysteretic model, ascending path

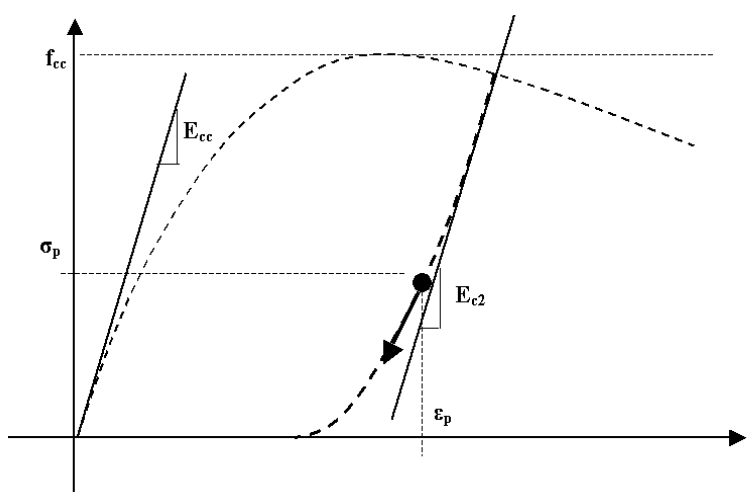

Figure 6.23 USC_RC confined concrete hysteretic model, descending path

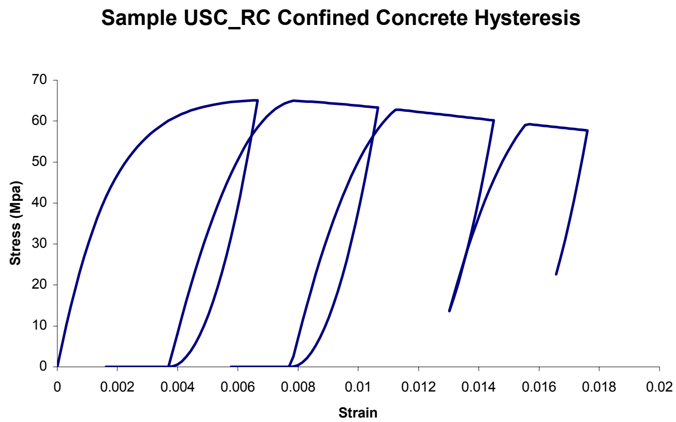

Figure 6.24 Confined concrete hysteretic behavior curve: a sample based on the data from USC_RC

(e) USC_RC Cover Concrete

The hysteretic model for cover concrete is, in general, similar to the model used for confined concrete. The differences are the envelope curve, and initial stiffness, and ultimate strength. The envelope for the cover concrete is also based on the model proposed by Mander et al. In this model, if the confinement coefficient is taken to be zero, the resulting curve can be used to simulate the envelope for the cover concrete stress-strain curve, with the exception that the tail of the curve at strains beyond 0.004 is replaced by a straight line. Figure 6.25 shows a sample of the hysteretic response of the model used for cover concrete in USC_RC.

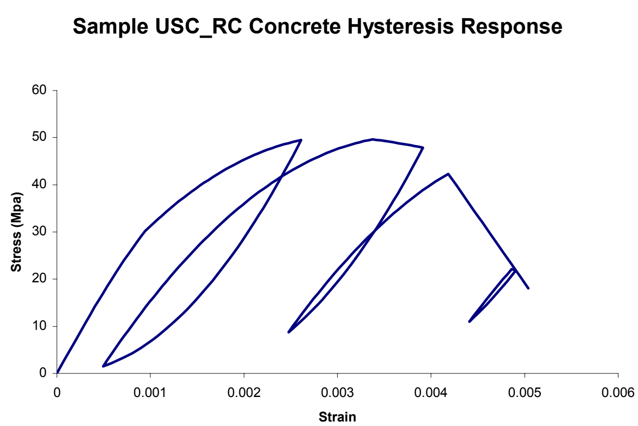

Figure 6.25 Cover concrete hysteretic behavior as modeled in USC_RC

7 Analytical Methods

In general the number of analytical methods developed for treating different cases is not limited, and based on the nature of the problem each researcher has developed an analytical tool and proposed a method to predict the behavior of a member or structure. These kinds of methods or tools may not be considered as the main standard tools, even if the predictions made using them were successful for some experiments. A method for treating a problem may be considered reliable if supported efficiently by a theoretical background, while yielding a good prediction for all the actual situations within the framework of the problem. However, all these mathematical models attempt to represent the gross structural response accurately. The aspects of methods dealing with the structural behavior of reinforced concrete can be classified into three categories: (a) modeling of material properties, (b) studies at the micro-structural level, and (c) studies at the macro-structural level. Considering the aforesaid, these models will be considered as analytical tools and some proposed methods will be reviewed for predicting the flexural strength and behavior of the members. The modeling of material properties was detailed in the previous chapter.

7.1 FINITE ELEMENT METHODS

The finite element method has been used under different assumptions and various methods as an analytical tool for RC members and structures. The shape of the element, number of nodes, linear or nonlinear approximations for displacement or strain within the element, as some basic assumptions, have led to many analytical methods within this category. As already mentioned, each individual method suits its corresponding application. The main concept, however, is dividing the member into elements small enough to yield the desired accuracy, with specified node number, proper displacement approximation, and finally, a suitable constitutive law.

Ngo and Scordelis (1967) developed a finite element model for reinforced concrete and carried out an analysis of beams with a predefined crack pattern. The first model included a cracking and bond simulation capability so that the stresses in the crack vicinity can be computed. This model was called the "discrete crack model." Since the publication of this pioneering work, the analysis of reinforced concrete has received great interest. Soon after the discrete crack model, a second approach was developed by Rashid (1968), who looked at the problem in a more global sense. This approach represented cracked concrete as an elastic orthotropic material with reduced elastic modulus in the direction normal to the crack plane. Within the finite element, the cracked concrete behavior was represented by the average stress-strain relation. It located zones of cracking and how crack development affected the overall response of the structure. This model was called "the smeared crack model."

Ignatakis et al. (1989) used this model (Figure 7.1) for RC columns under axial and shear loading. In this study, the concrete was represented by rectangular elements with smeared cracking, each one of which was subdivided by its diagonals into four simple triangular elements. The steel reinforcement was represented by separated one-dimensional elements. The interaction between concrete and steel was connected by a nonlinear spring linkage element for the bond-slip effect. It was reported that the model was capable of accounting for the complicated stress and strain distribution of a short column under axial and shear loading to failure, including the crack pattern. The advantages for this model are that the local behavior can be monitored and used for arbitrary shapes. The major disadvantages are the large amount of computation required and lack of capability for determining the behavior under cyclic loading. Furthermore, it is not obvious how the stress-strain relationship should be modified for biaxial loading.

In 1929, Wagner proposed the "diagonal tension field" for the post-buckling shear resistance of thin webbed metal beams. He assumed that the thin web could not resist compression after buckling, and that the shear would be carried by diagonal tension.

Mitchell and Collins (1991) applied Wagner's model to reinforced concrete assuming that concrete carries no tension after cracking and that the shear is carried by a field of diagonal compression. This model called the "diagonal compression field theory," was based on the smeared-crack concept, with equilibrium, compatibility, and stress-strain relationships formulated in terms of the average strains and average stresses. Uniform normal stress, shear stresses, and deformation are assumed in the elements. The basic assumptions are:

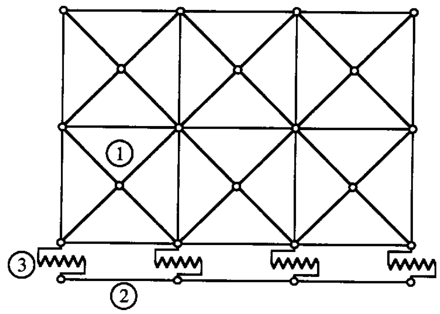

Figure 7.1 Finite element mesh: (1) concrete, (2) steel, (3) linkage elements

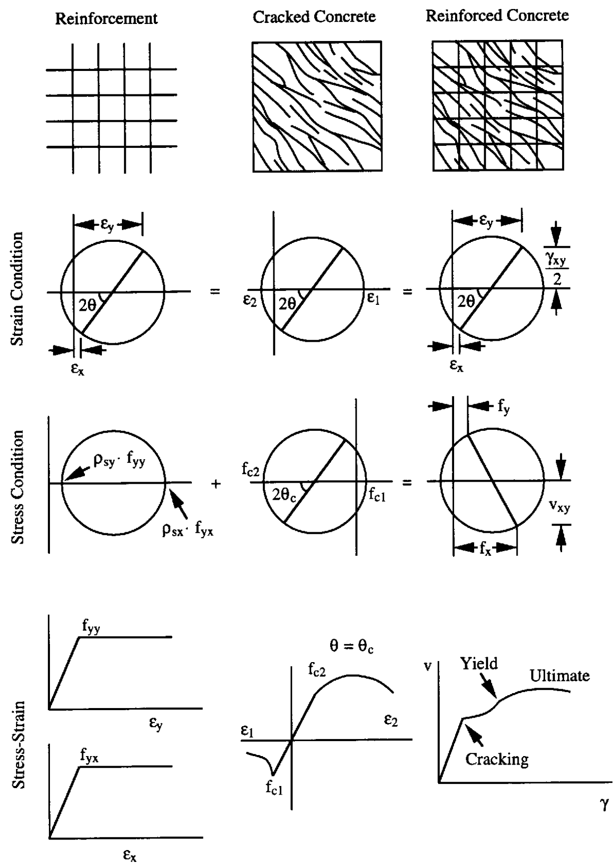

Figure 7.2 Compression field theory for reinforced concrete element

1. For each strain state there exists only one corresponding stress state.
2. Stresses and strains are considered in terms of average values over areas or distances large enough to include several cracks.
3. The average stress and strain can be expressed by using Mohr's circle.
4. Concrete and reinforcing bars are perfectly bonded together.
5. The longitudinal and transverse reinforcement are uniformly distributed.
6. Concrete and steel have the same average strain.

7. The cracked concrete has the same principal axes direction for stress and strain.
8. The deformation is assumed so that the edges remain straight and parallel.

The concept of this theory is to establish the relationship between the stress circle and the co-existing strain circle. The theory is schematically summarized in Figure 7.2, where:

$\varepsilon_x, \varepsilon_y, \gamma_{xy}$	=	plane strain components
f_x, f_y, v_{xy}	=	plane stress components
$\varepsilon_1, \varepsilon_2$	=	principal tensile and compressive strain in concrete
f_{c1}, f_{c2}	=	principal tensile and compressive stress in concrete
ρ_{sx}, ρ_{sy}	=	reinforcement ratio in x and y directions
f_{xy}, f_{yy}	=	yield stress of x and y reinforcement

Ghee et al. (1985) used this theory and subdivided a circular column section into a series of concrete laminate and reinforcement elements for ultimate strength analysis. Recently, Collins and Vecchio (1986) modified this by considering the average tensile stress in the cracked concrete, called "Modified Compression Field Theory" (MDCFT). Collins and others used this theory to study different loading in reinforced concrete, including reinforced concrete subjected to shear and cyclic loading. Seible and others also incorporated the MDCFT in developing an in-plane nonlinear finite element method for the modeling of a concrete and masonry system. The model can predict the structural behavior from the initial undamaged condition to the ultimate collapse, including simulation of cracking, yielding, and crushing. Good agreement was reported between the predicted response and observed tests. It was shown that the modified compression field theory is capable of predicting the response of reinforced concrete to in-plane shear, flexural, and axial stresses by considering equilibrium conditions, compatibility requirements, and average stress-strain relationships. Although this model is complex for the design of a single member, the procedure has the capability to provide a rational method for the analysis and design of members having unusual geometry or loading. The disadvantages of this model are the computational time and that the influence of intersecting cracks under biaxial loading have not been considered.

Zeris and Mahin (1991) proposed a kind of finite element model for the analysis of the nonlinear behavior of RC columns under biaxial excitation. The formulation accounts for most aspects of axial-flexural behavior. Their biaxial beam-column element models prismatic members with a straight longitudinal axis. The typical column is discretized into individual steel and concrete fibers located in sections monitored along the member. In their method, at least two sections must be defined. At the section level, the basic assumption of plane remaining plane is applied. Linear flexibility variation is assumed between monitored sections. So, even if the location of the interior section is arbitrary, it is dictated by the need for realism in establishing the flexibility distribution. In general, this method is very close to the fiber model, the only difference being the way strain variation or rotation of the section is approximated. In some cases a Hermitian approximation for the rotation has been properly applied. If the number of elements along the member is such that a linear approximation can be used for variation of rotation or curvature within the element, there is no difference between this method and the conventional fiber model, i.e., in other words, the fiber model may be regarded as a finite element method with its own approximations.

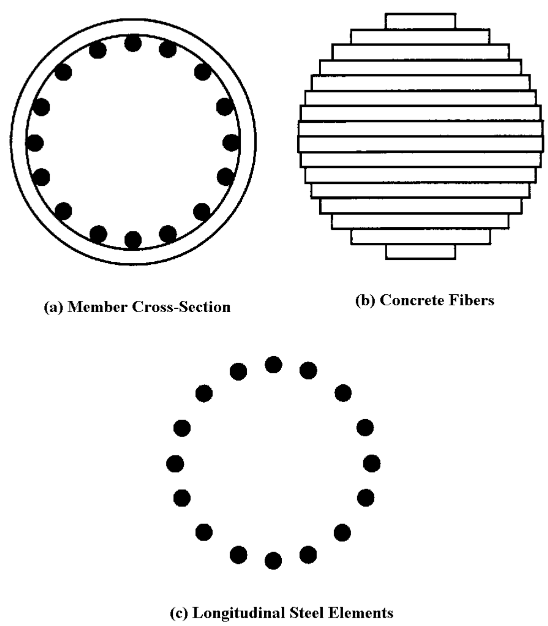

Figure 7.3 Discretization of circular member cross section into concrete laminate and longitudinal steel elements

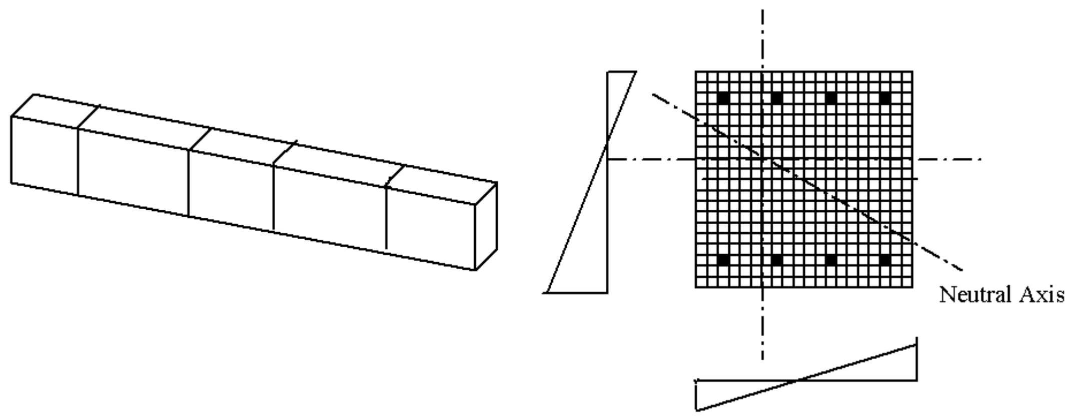

Figure 7.4 Element and section representation in the Zeris and Mahin method

Assa and Nishiyama (1998) presented an analytical method for the prediction of load-flexural deformation curve of RC columns subjected to simulated seismic loading. Their method is based on a finite element approach that allows for spreading of inelasticity along the member. The effect of the transverse reinforcement is considered in the uniaxial stress-strain relationship of the confined concrete. Their method is actually a kind of matrix analysis in which plastic hinges are also assumed at the proper nodes.

A constitutive model for RC finite element analysis, presented by Collins et al. (1991), may be implemented into a finite element formulation. The proposed approach works strictly in terms of the average stresses and average strains for both the concrete and the reinforcing steel. A result of the approach is that the proposed concrete tensile response must reflect the influence of the amount, distribution, and orientation of the reinforcement. For example, if the concrete is not reinforced, the average tension in the concrete must reduce rapidly to zero. On the other hand, if a large amount of well-distributed reinforcement is present, then considerable average tension should remain in the concrete after cracking.

Braga and Laterza (1998) proposed a new constitutive law that is valid for confined concrete. The transverse stresses induced by a hoop, either square or circular, in the cross section of axially loaded RC columns or beams are evaluated using Airy's functions relevant to plane strain states. The results for the square or circular hoops are then extended to hoops of polygonal shape, with or without bindings, and to a combination of hoops of different shapes. The formulation, valid for the cross section containing the hoop, is extended to the overall volume of the member through the interaction between hoops and longitudinal reinforcement.

Arya and Hegemier (1982) investigated a constitutive model for masonry concrete analysis. In this model, cracking and debonding were modeled by a double-node pair. It was reported that this model could rationally predict complex nonlinear behavior of concrete masonry assemblages such as shear walls and piers under both monotonic and cyclic loading.

Hegemier et al. (1986) introduced a "mixture model" to combine the concrete and steel nonlinear material properties for RC behavior, accounting for the steel-concrete interaction. The major advantage of this model is that the bond slip mechanism was integrated with a general nonlinear finite element from material properties, instead of introducing a special element. It should also be noted that the local behavior of the reinforced concrete could be monitored. This bond slip model has been successfully used to simulate the response of full-scale RC panels subjected to monotonic pull-out and tension tests and cyclic tension-compression loading. All the tests included debonding, slip, and concrete cracking. A major disadvantage of this constitutive model approach for practical application is the need for extensive computational power. It is also apparent that the application of this model to biaxial lateral force needs more investigation.

One of the finite element methods closely related to the analytical work done in this report is the method of evaluating the flexural deformation of an RC member by using a one-dimensional element, proposed by Golafshani et al. (2000). The scope of their research was to develop a one-dimensional element to demonstrate the nonlinear behavior of concrete filled tubes under cyclic as well as monotonic loads. Their one-dimensional element works in plane and extension to the three-dimensional case is claimed to be straightforward. In their method, a beam-column fiber element for the large displacement, inelastic strain analysis was implemented for the cyclic analysis of concrete-filled steel tubes (CFT). The method of displacement approximation was a total Lagrangian formulation. An eight-degree-of-freedom element with three nodes was chosen. The nodes at the ends have three degrees of freedom, while the node in the middle has two degrees of freedom. The quadratic Lagrangian shape functions for axial deformation and the cubic quadratic Hermitian shape function for the transverse direction were used. It was assumed that a perfect bond is maintained between the steel shell and concrete core. In formulating the problem, the following assumptions were proposed:

- Plane sections before and after banding remain plane.
- Shear deformations due to the size of the sections are negligible.
- During loading history the shell will not buckle. This assumption has had a negligible effect on the results for moderate and low ratios.

- Effects of confinement on the concrete and biaxial state of stress in the steel shell have been accounted for through the uniaxial models for confined concrete and employment of proper coefficients.
- Effects of creep and shrinkage have been neglected because of their small influence on the behavior of concrete-filled tubes.
- Effects of residual stresses have been neglected.

These assumptions make their method very close to a perfect fiber model analysis, and the only difference is the application of the finite element method through a one-dimensional element as a substitute for the plastic hinge assumption and method.

7.2 YIELD SURFACE MODEL

In 1976, Takizawa and Aoyama (1976) introduced a biaxial trilinear degrading model, using the plasticity theory. The model was developed with stress-strain corresponding to the member end-moment, *M*, and end-rotation, *θ*. The basic curve for this model is a trilinear curve, which was derived from sectional analysis and characterized by crack and yield points. The crack and yield conditions were postulated to be represented by ellipses in the moment space. In the biaxial moment space are two yield surfaces, an inner cracking surface and an outer yield surface. Figure 7.5 shows the yield surfaces in the stress space and the related trilinear skeleton curves for uniaxial flexure in the principal directions *X* and *Y*. Two yield functions were established to check the stress stage for the cracking surface:

$$f = \begin{bmatrix} M_x \\ M_y \end{bmatrix} \begin{bmatrix} \frac{1}{M_{Cx}^2} & 0 \\ 0 & \frac{1}{M_{Cy}^2} \end{bmatrix} \begin{bmatrix} M_x \\ M_y \end{bmatrix} \tag{7.1}$$

and for the yield surface:

$$g = \begin{bmatrix} M_x \\ M_y \end{bmatrix} \begin{bmatrix} \frac{1}{M_{Yx}^2} & 0 \\ 0 & \frac{1}{M_{Yy}^2} \end{bmatrix} \begin{bmatrix} M_x \\ M_y \end{bmatrix} \tag{7.2}$$

where:

M_x, M_y = current bending moments about the X and Y axes;

M_{Cx}, M_{Cy} = crack moments about the X and Y axes;

M_{Yx}, M_{Yy} = yield moments about the X and Y axes.

The following criteria of three-part plasticity were used for loading during biaxial flexure.

$$\begin{cases} f < 1 & \text{elastic range} \\ f \geq 1 \text{ and } g < 1 & \text{cracked and unyielded range} \\ f \geq 1 \text{ and } g \geq 1 & \text{yielding range} \end{cases} \qquad (7.3)$$

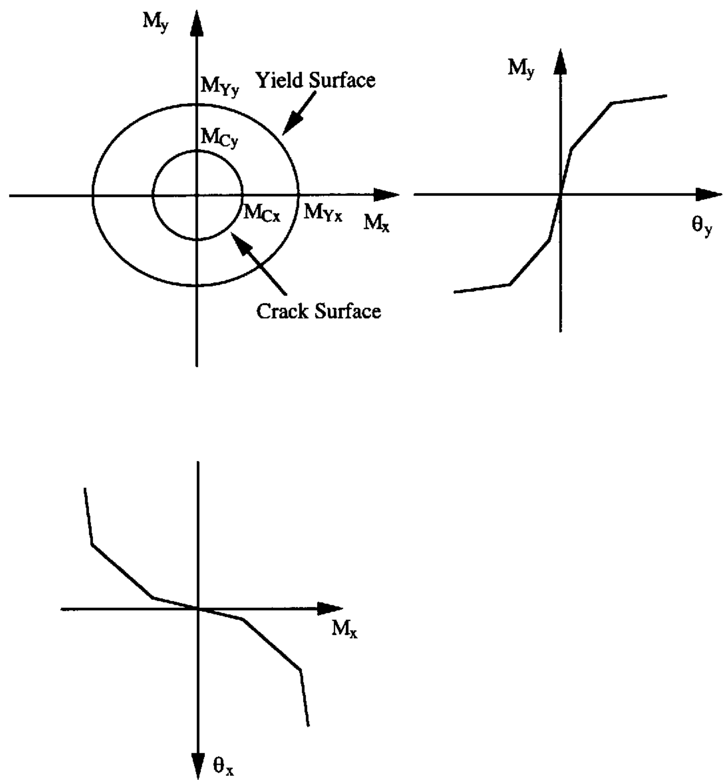

Figure 7.5 Skeleton curves and yield surfaces for yield surface model

Here, the elastic stiffness is modified once the cracking surface is reached, beyond which the cracking surface translates without changing shape. Upon reaching the yield surface, both the cracking and yielding surfaces are allowed to expand along the direction of yielding. Ziegler's hardening rule was used for the translation of the crack surface and the expansion for the crack and yield surfaces. Degradation is achieved by factoring the unloading stiffness with a degradation factor.

Chen and Powell (1986) continued the study of this model, using two approaches: (a) the distributed plasticity approach that assumes that yielding is distributed over the element. The element stiffness is determined by integrating along the member. The multidimensional action-deformation relationship must be specified for the cross section. (b) The lumped plasticity (plastic hinge) approach in which yield is assumed to take place only at the plastic hinge region of zero length, and the beam between the hinges is assumed to remain linearly elastic. In this approach, the multidimensional action-deformation relationship must be specified for the hinges.

Takizawa and Aoyama (1976), as well as Chen and Powell verified the lumped plasticity by comparison with the experimental data obtained by Takizawa and Aoyama at the University of Tokyo. The tests included uniaxial and biaxial bending. It has been shown that the lumped plasticity model was able to capture certain essential features of three-dimensional beam-column behavior. In addition to the lumped plasticity model, Chen and Powell studied the model of distributed plasticity to determine whether it produced results in agreement with the experimental results for the inelastic response of braced structures. The analytical results were compared with the test conducted by Zayas, Mahin, and Popov (1981). Even though the overall response was similar, it was found that the analysis predicted substantially less stiffness and strength degradation.

Lumped plasticity modeling is particularly suitable for the analysis of building frames under seismic loads because plastic action in such a structure is usually confined to small regions at the beam and column ends; the distributed plasticity model is preferable for structures in which the plastic zone locations are not known in advance. The advantage of the lumped plasticity model is the efficiency in computation. The disadvantages are that the local effect of the analysis cannot be monitored, the strength degradation due to crushing and spalling of the concrete cover cannot be considered, and the debonding behavior is not addressed.

7.3 FIBER MODEL

In this model, and in its commonly used version for the flexural analysis of a prismatic or cylindrical member, the fundamental assumption of plane remaining plane is employed. The Zeris and Mahin model (1991), already described in Section 7.1, may also be considered as a kind of fiber model. In the fiber model, the section is divided into some small elements, which may be considered as the cross section of the fibers making the column. Figure 7.6 shows a sample case where the cross section of a rectangular RC concrete member has been divided into steel and concrete fibers. For a force-deflection analysis, the fiber can then be divided along the member, so that the member is divided into fiber elements with a specific length. Afterwards, the axial deformation of each fiber is formulated, which in turn provides the axial-flexural behavior of the section. The finer the mesh, the more precise the results. The fiber model is in fact a finite element method in which some constraints have been applied. The main condition is the assumption of plane remaining plane, the other is the linear approximation of deformation along each fiber element. There are some other versions of the fiber model in which the aforesaid constraints are not strictly applied. This methodology is actually more finite element than fiber model, but may be categorized as the latter considering the fiber elements employed.

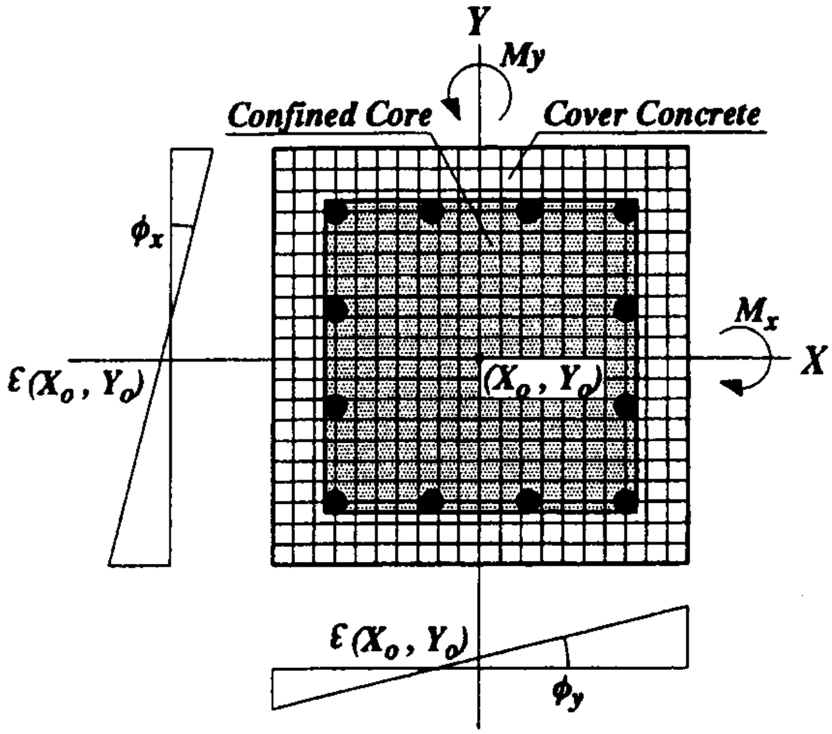

Figure 7.6 A section divided into longitudinal fibers along the member, as in fiber model

Chang et al. (1994) proposed a fiber-element modeling of the cyclic biaxial behavior of RC columns to examine the computational aspects of simulating the moment-curvature and force-displacement behavior of RC columns subjected to cyclic biaxial bending and axial load. Starting from first principles the basic equations of biaxial behavior are derived. Advanced constitutive models for normal and high-strength concrete, and for the cyclic and low-cycle fatigue behavior of reinforcing and prestressing steel bars are integrated in a fiber-element procedure for the simulation of the cyclic and fatigue behavior of columns subjected to biaxial loading. Chang et al. presented two different implementations of the fiber-element modeling procedure. The first uses a five-node rectangular element using a quadratic interpolation function, the second a five-node circular-trapezoidal element more appropriate for circular columns. The use of quadratic interpolation functions in both elements improves convergence, and thus fewer elements are needed in the discretization process.

7.4 MULTISPRING MODELS

Lai et al. (1984) developed an analytical model to simulate the hysteretic and stiffness degrading behavior of RC members subjected to axial load and biaxial bending interaction. The model separates the member into two inelastic elements. Each inelastic element, composed of individual spring elements simulates the inelastic effects of the member as well as the cumulative slip of the anchored bars in the beam-column joint. The formulation of the spring model is based only on the static equilibrium of the cross section according to the current ACI code. The model does not provide any information about the moment-curvature of the section and works only for modeling the end parts of the element. The area of the concrete springs is assigned based on the current axial force and bending moment, and evaluated according to the ACI stress block concept, and is variable in each step. Therefore, in each time increment during the analysis, the spring area should be updated in addition to the material property. If the section is not symmetric, an approximation is applied by averaging the scaled values for the concrete springs in the x and y directions. The model cannot be applied for moment-curvature.

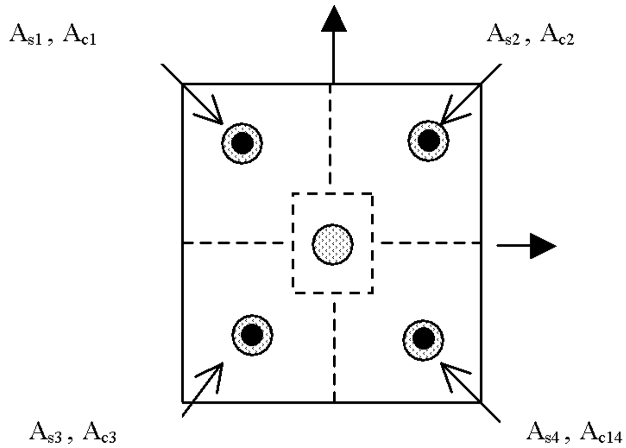

Figure 7.7 A cross section divided into steel and concrete springs, as proposed by Lai et al.

Li (1988) proposed a practical multispring model to simulate the behavior of a section subjected to varying axial load and bilateral bending moment. The model is used mainly to model the nonlinear behavior of the end parts but can still be used to model the moment-curvature of the section. Getting a reasonable result requires a large number of springs, which are usually located at the center of the corresponding parts of the section they replace. This model is actually a kind of the aforesaid fiber model with the same computational deficiency.

A refinement of this model by Lai, Will, and Otani (1984) was provided by Ghusn and Saiidi, (1986) and Jiang and Saiidi (1990), who considered four corner composite springs (1, 2, 3, and 4 in Figure 7.8c) instead of separating them into steel and concrete and one concrete spring (5 in Figure 7.8c) at the center of the member as with the original model described above.

Thus, the nine-spring model was reduced to a five-spring model. When the composite springs are subjected to tension, a steel member representing the longitudinal reinforcement resists the force. A compression force on these springs, however, is resisted by the composite action of the concrete and steel. Because of the difference in the tensile and compressive behavior, the stress-strain curve for the composite springs is unsymmetrical.

Furthermore, Saiidi and Jiang improved the model by using only four corner spring elements (1, 2, 3, and 4 in Figure 7.8d), and compared the results with biaxially loaded columns with a constant or variable axial force. Compared with the five-spring model, the major advantage of this model is that only one type of spring is used, the composite spring. Even though the spring number had been reduced, the comparison between analytical results and experimental data was still good and the computation more efficient. It was shown that this model can simulate the stiffness degrading behavior of RC members with ductile flexural behavior. Compared with the fiber model previously discussed, the multispring model is a simplified fiber model with more efficient computation. Shear effects in this model were ignored as in the fiber model.

A very simple multispring model, simulating the moment-curvature behavior of RC circular sections, is developed. This model is presented in Appendix 3.

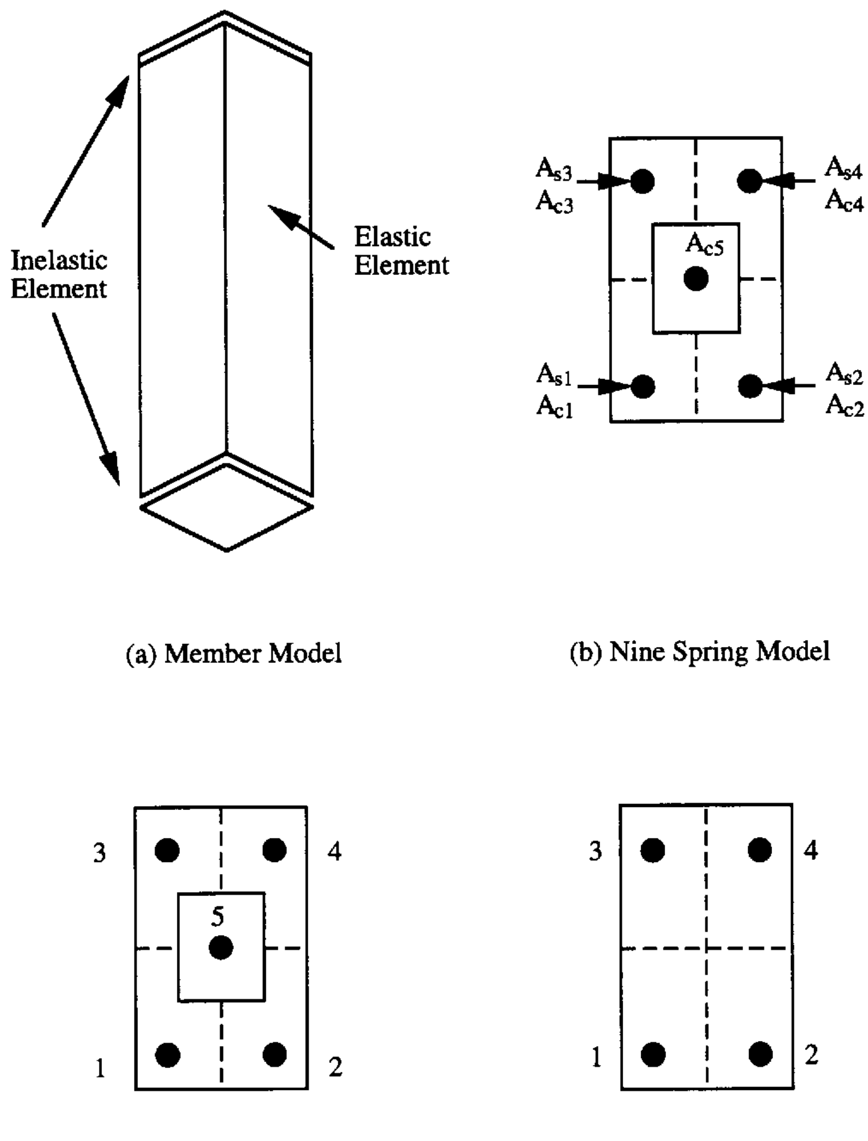

(a) Member Model

(b) Nine Spring Model

(c) Five Spring Model

(d) Four Spring Model

Figure 7.8 Multispring model

7.5 PLASTIC HINGE ASSUMPTION AND METHODS

The calculation of the flexural deflection of an RC member can be carried out by two different main methods. The first uses the finite element approach but needs a huge amount of computational effort, even for the fiber-model-based analysis. When the number of fibers in the cross section and the number of segments, along the member length, are not low, and a hysteretic analysis for a cyclic loading with a variable axial load is needed, the amount of required memory and computation are not comparable with other methods based on the assumption of a plastic hinge. It is evident that in the finite element method, the method of displacement approximation plays a significant role in the accuracy of the results. This is a major issue especially within the "transition length," described later, where elementary assumptions cannot be applied. In other words, in the finite element method, even with a very fine mesh, when the curvature at the critical section falls on the descending branch of the moment-curvature response of the section, the corresponding stiffness matrix is not positively definite anymore, and analytically we cannot go beyond the maximum moment point without resorting to some trial and error or, as called in finite element analysis texts, "adaptive methods." So, the concept of a plastic area, or transition area, where the stress and strain distribution over the cross section becomes normal when the curvature at the critical section falls on the descending branch of the analytical moment curvature, should somehow be employed and a proper curvature (displacement) approximation should be applied to solve the problem. Considering this, one way of reducing the number of the segments along the member is to have some idea about the maximum level of the lateral load that may occur, and then limit the part that falls within the elastic part to just a single element in the longitudinal direction. This will drop the generality of the solution and also divides the element into elastic and plastic regions. The plastic region will not be constant in length and has a variable length depending on many factors, namely the axial load level, and the lateral force and its corresponding moment at different sections. The overall picture of the problem leads us to the most popular approach, the plastic hinge method.

In this method, the deformation is divided into elastic and plastic parts, as is described in the following.

7.5.1 General Description of Plastic Hinge Method

Figure 7.9 is a typical illustration of the plastic hinge method (Priestley and Park, 1987). In this method, the flexural deflection is divided into two main parts:

$$\Delta = \Delta_e + \Delta_p \tag{7.4}$$

where Δ_e is the elastic flexural deflection or contribution of the member flexural deflection excluding the plastic hinge length. This deflection may either be calculated exactly based on the moment-curvature relationship or based on the assumption that the curvature distribution within the yield curvature is linear. Δ_p is the deflection resulting from the plastic hinge and is calculated as follows:

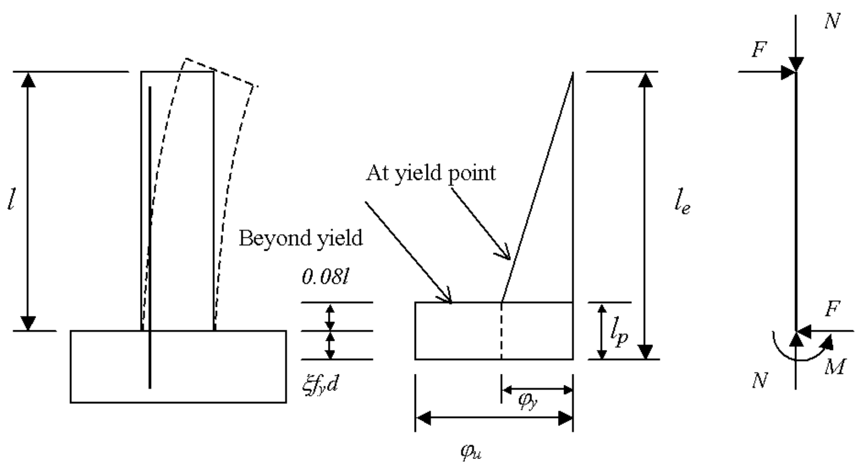

Figure 7.9 Typical plastic hinge method (Priestley and Park)

$$\Delta_p = \phi_p l_p (l_t - \frac{l_p}{2}) \tag{7.5}$$

where l_p is the plastic hinge length, and l_t is the total length (which can be different from the column length as will be mentioned later). If the curvature distribution within the elastic range is assumed to be linearly distributed, Δ_e can be calculated as follows at the yield point:

$$\Delta_e = \frac{1}{3}\phi_y (l_t - l_p)^2 \tag{7.6}$$

It should be noted that several versions of the plastic hinge method have been proposed and that the above is the main framework of the method. In some older versions of this method, the yield curvature is always assumed to be at the interface of the column (or the section of critical moment for a member), and when there is some plastic deformation, the extra curvature is applied within the plastic hinge length. Figure 7.10 shows the way the concept has been used to get the total deformation by Park and Paulay (1975). As shown, the length used to evaluate the elastic deflection is kept as the total length for any length of plastic hinge, while in the previously mentioned method, this length is the total length (total effective length as described) minus the plastic hinge length. It is obvious that the former method fits real situations more than the older versions, especially when a relatively high level of curvature is imposed on the critical section and the situation falls on the descending branch of the moment-curvature curve. In this region the former method also needs some revision, which will be discussed shortly.

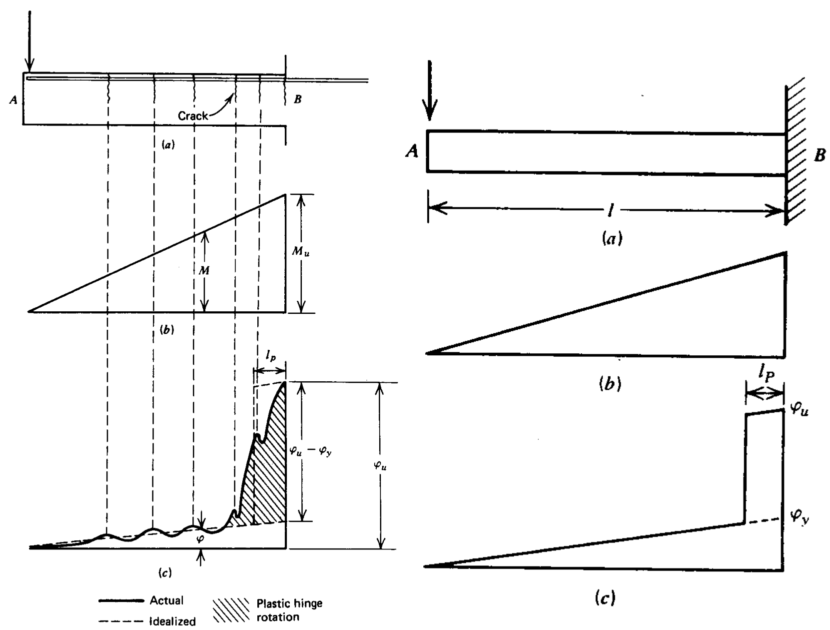

Figure 7.10 Plastic hinge assumption proposed by Park and Paulay (1975).

7.5.2 Empirical Expressions for Plastic Hinge Length

Various empirical expressions have been proposed by investigators for the equivalent length of the plastic hinge l_p and the maximum concrete strain ε_c at ultimate curvature. In all these older methods, the total length is used for evaluating the elastic deflection part of the total deflection. These methods cannot be applied when a relatively high curvature is present at the critical section. As described, the concrete strain must be limited to a certain value, while for a high level of curvature, the strains usually exceed far beyond the values proposed in these methods. Following is a brief review of these methods.

7.5.2.1 Baker

Baker (1956) proposed the following equations for plastic hinge length based on experiments.

For members with unconfined concrete:

$$l_p = k_1 k_2 k_3 \left(\frac{z}{d}\right)^{\frac{1}{4}} d \qquad (7.7)$$

where k_1 = 0.7 for mild steel or 0.9 for cold-worked steel,

$k_2 = 1 + 0.5P_u/P_0,$

where P_u = axial compressive force in a member, and P_0 = axial compressive strength of the member without bending moment

k_3 = 0.6 when f'_c = 5100 psi (35.2 N/mm^2) or 0.9 when f'_c = 1700 psi (11.7 N/mm^2), assuming f'_c = 0.85 cube strength of concrete

z = distance of critical section to the point of contra flexure

d = effective depth of member

Baker indicated that for the range of span/d and z/d ratios normally found in practice, l_p lies in the range between $0.4d$ and $2.4d$.

For members confined by transverse steel

More recent work by Baker (1964) proposes an expression for θ_p implying that for members with tension over part of the section:

$$l_p = 0.8 k_1 k_3 \left(\frac{z}{d}\right) c \qquad (7.8)$$

where c is the neutral axis depth at the ultimate moment and the other symbols have the previous meaning. There are some restrictions stated for the values of the concrete strain, and also for the steel ratio for the aforesaid equations to be valid and applicable.

7.5.2.2 Corley

From the results of tests on simply supported beams, Corley (Corley, 1966) proposed the following expression for the equivalent length of the plastic hinge:

$$l_p = 0.5d + 0.2\sqrt{d}\,(\frac{z}{d}) \tag{7.9}$$

He also suggested the following as a lower bound for the maximum concrete strain:

$$\varepsilon_c = 0.003 + 0.02\frac{b}{z} + (\frac{\rho_s f_y}{20})^2 \tag{7.10}$$

where z = distance from the critical section to the point of contra-flexure, b = width of beam, d = effective depth of beam in inches (1 in. = 25.4 mm), ρ_s = ratio of volume of confining steel (including the compression steel) to volume of concrete core, and f_y = yield strength of the confining steel in kips per square inch (1 kip/in.^{2} = 6.89 N/mm). In discussing Corley's work, other investigators proposed simpler forms of equations that fitted the trend of the data reasonably well, such as:

$$l_p = 0.5d + 0.05z \tag{7.11}$$

$$\varepsilon_c = 0.003 + 0.02\frac{b}{z} + 0.2\rho_s \tag{7.12}$$

This modification to the equation for ε_c makes it more conservative for high values of ρ_s.

7.5.2.3 Priestley and Park

Priestley and Park (1987) proposed a plastic hinge length that considers the strain penetration into the footing for columns, and is dependent on the rebar diameter and column length. The plastic hinge length proposed is:

$$l_p = 0.08l + \xi f_y d \tag{7.13}$$

in which l is the length of the column, ξ is a coefficient that is 0.15 in. (0.022 mm), σ_s is the steel stress in the furthest rebar, and d is the diameter of the main rebar. If the curvature distribution within the elastic range is assumed to be linearly distributed, Δ_e can be calculated as follows at yield point:

$$\Delta_e = \frac{1}{3}\phi_y (l_t - l_p)^2 \tag{7.14}$$

where:

$$l_t = l + \xi f_y d \tag{7.15}$$

The plastic deflection is:

$$\Delta_p = \phi_p l_p (l_t - \frac{l_p}{2}) \tag{7.16}$$

and the total deflection is the sum of the elastic and plastic deflections:

$$\Delta = \Delta_e + \Delta_p \tag{7.17}$$

7.5.3 Discussion of Plastic Hinge Method

As stated earlier, in the oldest versions of the plastic hinge method, it is assumed that for the elastic part of deformation, the curvature at the critical section is equal to the curvature corresponding to the first yield of the longitudinal steel. This is not a realistic assumption because as the moment gets larger (which is usually due to a lateral force), the section where the first yield of the longitudinal steel occurs shifts away from the critical section, which results in a smaller length of elastic deformation calculation. It seems that besides the experimental results, due to this reason analytically all the investigators have somehow related the plastic hinge length to the total length of the member.

For all the proposed methods, the plastic hinge length is constant except for the model proposed by Baker, where it is related to the level of axial load, but for a fixed axial load, the plastic hinge length is constant. This means that for any level of lateral load (or critical moment) the plastic hinge length does not change, having a constant axial load. This is not consistent with the experimental observations and analytical findings. Figure 7.11 compares the required plastic hinge length in the Priestley and Park method based on the experimental data for test 3 where the axial load is 30%$A_g f'_c$ and test 4 where the axial load is equal to zero, and the constant plastic hinge length as proposed by the model. Note that the horizontal axis for both figures is the drift ratio, and that the vertical axis is the plastic hinge length in inches for the length cases and in kips for the horizontal force. These figures are provided based on the experimental data and for comparison purposes. The method used to evaluate the equivalent experimental plastic hinge length for the Priestley and Park method is as follows:

Each test specimen is idealized as a cantilever column. Assuming linear elastic behavior up to the point where yielding occurs at the base of column, the yield displacement at the tip of the column can be computed as:

$$\Delta_y = \frac{\varphi_y L^2}{3} \tag{7.18}$$

where φ_y is the yield curvature at the column base. Byrak and Sheikh (1997), in their method for evaluating the equivalent plastic hinge length, assumed that the plastic hinge rotation at the base is concentrated at the center of the plastic hinge, and decomposed the total displacement $\Delta_{\max}$ into two components Δ_y and Δ_p, the plastic displacement. Δ_p was calculated as:

$$\Delta_p = (\varphi_{\max} - \varphi_y) L_p (L - 0.5 L_p) \tag{7.19}$$

Here they assumed a curvature equal to the yield curvature at the column base for calculating the yield displacement, while the curvature at the top of the plastic hinge will be equal to $\frac{L - L_p}{L}\varphi_y$; this is different from the method proposed by Park and Priestley, where the curvature at the top of plastic hinge is equal to the yield curvature. Byrak and Sheikh concluded that the equivalent plastic hinge length for all their cases is slightly less than the section depth. The method used to evaluate the equivalent plastic hinge here is based on the Park and Priestley method, which yields the following equation for the equivalent plastic hinge length:

$$L_p = \frac{3L\varphi_u - \sqrt{3\varphi_u L^2 - 6\Delta}\sqrt{3\varphi_u - 2\varphi_y} - 2\varphi_y L}{3\varphi_u - 2\varphi_y} \tag{7.20}$$

where L is the column length, in the case of a cantilever case, or the distance between the critical section and the contra-flexure point in the case of a double-curvature member, φ_u is the curvature at the critical section, and φ_y is the curvature corresponding to the first yield of the section, which is defined to be the curvature at the first yield of the longitudinal steel for a specific level of axial load. To evaluate the experimental plastic hinge length, the experimental values for the ultimate and yield curvatures are evaluated based on the experimental data. In other words, the recorded strain on the furthermost bar on the critical section is used to locate the first yield instance. Then the corresponding curvature can be calculated either by using the recorded strains on the furthermost bars at the two opposite sides of the critical section or by using the data recorded by the linear extensometers at the two opposite sides of the column on the segment near the critical section. This process is applicable only for the cases where the level of axial load is constant so that an experimental value for the yield curvature is available; otherwise the experimental yield curvature is valid only for the axial load level corresponding to the instance of the first yield of the longitudinal bar, and cannot be used for other values of the axial load. Figure 7.11 shows that for a constant axial load, the plastic hinge length is not constant and depends on the level of the lateral load, or the critical moment.

None of the models discussed so far proposes a variable plastic hinge length as observed during the tests. Besides the aforesaid experimental evaluation of the plastic hinge length, it was observed during all tests that for the normally used ranges of the axial and lateral loads, as soon as the plastic hinge forms, its length grows to a maximum, and as the deflection is increased, the plastic region shortens very slightly compared to its maximum value, and that the high curvature imposed at the critical section is limited within this length. As a revision of the Priestley and Park method, Xiao et al. (1996) have proposed that the tensile stress in the furthermost rebar at the critical section be used instead of the yield stress of steel in the calculation of the plastic hinge length. Thus, the equation will be changed to:

$$l_p = 0.08l + \xi \sigma_s d \tag{7.21}$$

where σ_s is the tensile stress of the furthermost rebar at the critical section. The elastic part of the deflection is calculated with the same equation:

$$\Delta_e = \frac{1}{3}\phi_y (l_t - l_p)^2 \tag{7.22}$$

and the total deflection is the summation of the plastic deflection and the elastic part. This revision is more realistic from the experimental point of view, since a change in the plastic hinge length is observed for the members with an axial load below the balance value, and especially when the section undergoes strain hardening. For the cases with a high level of axial load, however, this method does not precisely predict the deflection.

All the aforesaid methods cannot be applied when the curvature at the critical section falls on the descending branch of the moment-curvature curve of the section. The method revised by Xiao needs a slight revision to be applicable in this region. The proposed revision is as follows:

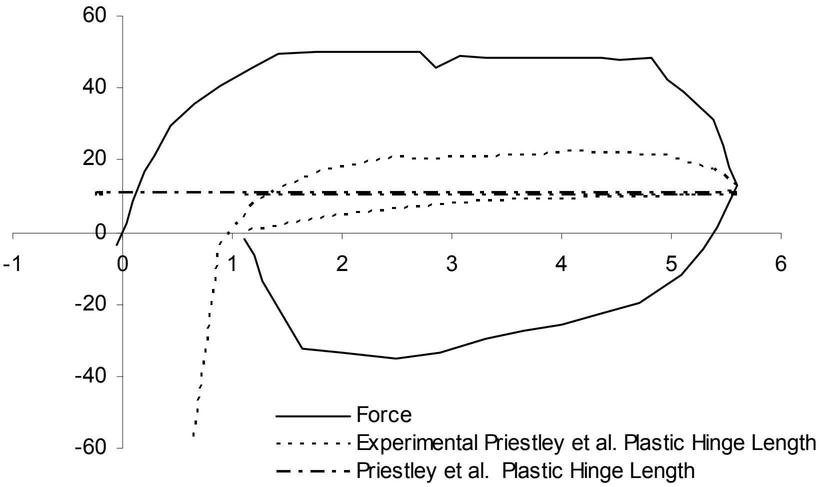

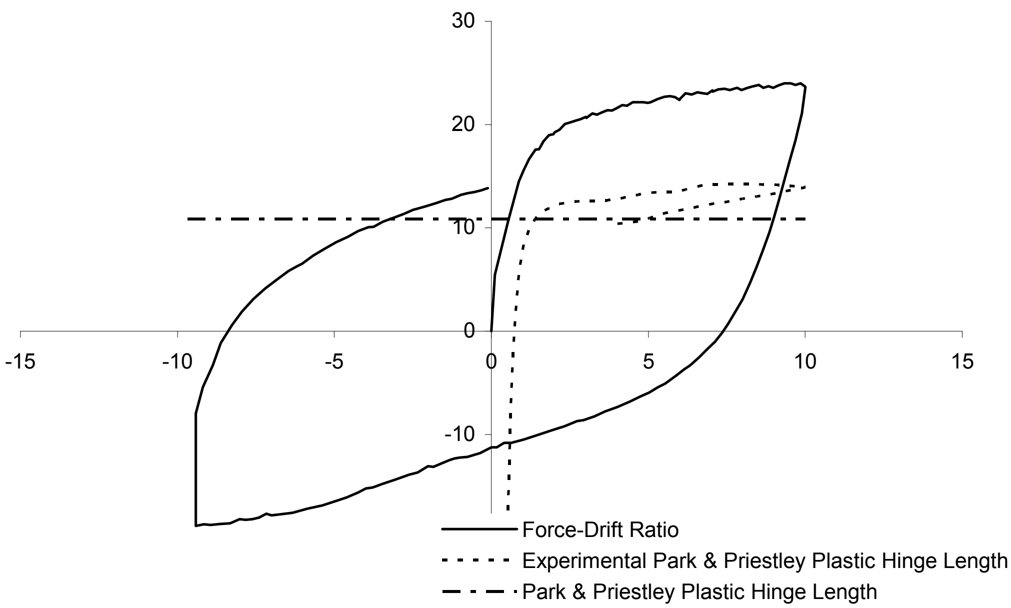

Figure 7.11 Comparison of the required plastic hinge length in the Priestley and Park method based on the experimental data, and the constant value as proposed in the model, on the horizontal-force drift-ratio chart for tests 3 (top) and 4 (bottom). (Note that the vertical axis is length in inches for the plastic hinge cases and force in kips for the horizontal force, serving just for comparison.)

7.5.3.1 Proposed Revision to Priestley and Park Method

For the curvature falling on the ascending branch of the moment curvature, the equations proposed by Priestley and Park with the revision proposed by Xiao can be used, but for the descending part, the elastic part of the deformation will be revised as:

$$\Delta_e = \frac{1}{3}\phi_y\left(\frac{M_{(l_t-l_p)}}{M_y}\right)(l_t-l_p)^2 \tag{7.23}$$

where M_y is the moment at the first tensile yield of the furthermost longitudinal bar on the critical section, and:

$$M_{(l_t-l_p)} = \frac{(l_t-l_p)}{l}M_u \tag{7.24}$$

where l is the length of the member for a cantilever case or the distance between the critical section and the contra-flexure point in a double curvature case, and M_u is the moment at the critical section. Applying this revision will enable the method to be used on the falling branch of the moment-curvature curve, but for a relatively high level of axial load, where the tensile stress of steel is not high and in some cases does not even get close to the yield stress, the method does not conform well to the experimental observations. Here a method is proposed for calculating of the flexural deformation of an RC member with a revised plastic hinge approach. This method is more comparable to the experimental observations than other methods and can be sufficiently verified analytically.

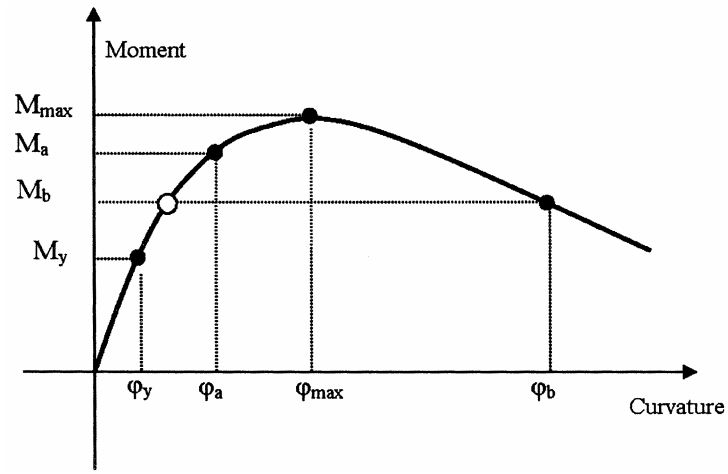

Figure 7.12 A typical moment-curvature curve for a reinforced concrete section

7.5.4 Proposed Plastic Hinge Methods

Figure 7.12 shows a typical analytical moment-curvature response of an RC section. This curve has two branches, an ascending branch and a descending branch, for most cases of loading and material behavior. When a member (here the column) is subjected to a lateral force *F,* as shown in Figure 7.13, the bending moment is linearly increased from zero to *F.L,* where L is the column height, and the distribution of the curvature follows the moment-curvature curve when the moment is mapped to the column height (when the section throughout the column height is the same, with a scale equal to *F*, the concentrated lateral force). As the force increases, the moment and curvature throughout the column increases. As long as the moment at the column toe remains within the yield moment, which corresponds to the first yield of the tensile steel at the section (or for very high axial loads, the yield of the concrete), the curvature distribution is linear, starting from zero at the top and linearly increasing to its value at the column and footing interface. When the force *F* is increased, the moment at the column toe exceeds the yield moment, and there is a nonlinearity in the moment-curvature curve. For an exact solution (like a fiber-based finite element solution), there is no problem while the mesh is fine enough to provide the desired accuracy and the curvature is less than that corresponding to the maximum moment at the critical section, but in the case of a simplified method like what has been the case for the plastic hinge concept, this nonlinearity can be approximated well by assuming a linear distribution of the curvature from the yield point where the curvature is equal to the yield curvature to the toe of the column where the curvature is Φ_u**.** This approximation can be applied up to a force where the moment reaches its maximum value at the column-footing interface. When the curvature exceeds the curvature corresponding to the maximum moment, the force and the moment at the column-footing interface drops as shown in Figure 7.14.

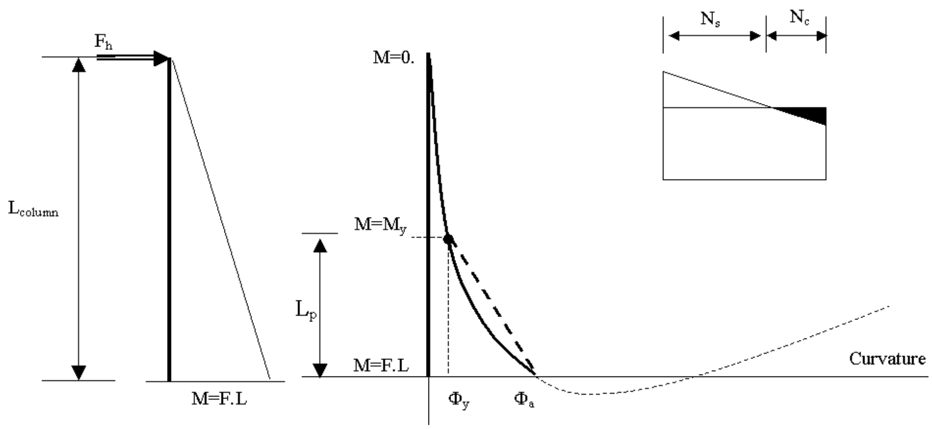

Figure 7.13 Distribution of curvature along a cantilever case column, for a concentrated lateral load, where the moment is linearly distributed along the column height when the curvature at the critical section is less than the curvature corresponding to the maximum moment

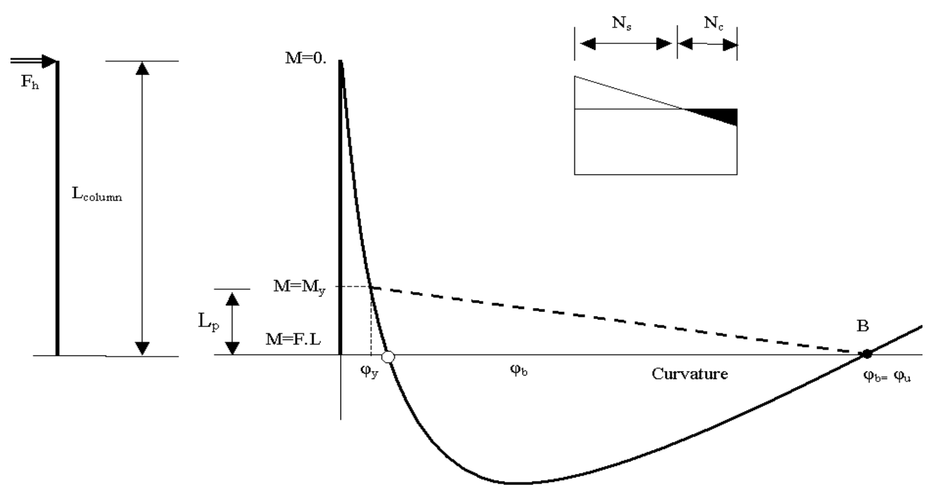

Figure 7.14 Distribution of curvature along a cantilever case column, for a concentrated lateral load, when the curvature at the critical section exceeds the curvature corresponding to the maximum moment

Analytically, in this situation this lateral force and the corresponding moment at the critical section can exist for two curvatures, one before reaching the maximum moment, the other after passing it. Therefore, two states of stress distribution at the column-footing interface can represent the situations for the two different cases. In other words, consider a section very close to the column-footing interface but above it. Analytically, approaching from the top of the column to this section the curvature is close to the curvature at the point marked by the hollow circle in Figure 7.12, while it jumps to Φ_u (or Φ_b as in the figure) at the critical section. If we look at these two very close adjacent sections analytically, the stress distribution is completely different. Since in reality this cannot happen, there is an ambiguous distribution of stress within a distance between two sections on the two different sides of the maximum point. According to the well-known and accepted "Sant Vennan's rule," in a case like this the stress distribution becomes normal within a reasonable distance. Figure 7.12 shows these two points: the point where the curvature is equal to $\Phi_b = \Phi_u$, and the point marked by the hollow circle. There is a transition length within which the curvature is changed from Φ_u to a curvature that falls on the left branch of the moment-curvature curve. It should be noted that the curvature at the point marked by the hollow circle is never present in reality, and the curvature will change within the transition distance so that the curvature at the top of the transition length is equal to what is analytically expected approaching from the top. This transition length is the area where the plastic deformation is present, and is treated as the plastic hinge length. This change of curvature from Φ_u to the curvature at the end of the transition length, considered as the plastic hinge length, which corresponds to the change of stress distribution configuration over the cross section to a stress distribution on the left branch on the curve, follows a pattern that can be approximated well by a line. Since the method proposed here should handle cases with a variable axial load, or a cyclic lateral load, the plastic hinge method cannot be as straightforward as the previous methods. Considering this fact, the definition of plastic hinge, i.e., defining the pattern of curvature distribution over the column height, has to be addressed for different loading and displacement cases. The basics of the proposed method will be explained here, and the algorithm applied in USC_RC for load displacement analysis will be summarized later.

It is obvious that when the curvature in a section exceeds the yield curvature, the section undergoes some plastic curvature, and in reversal of loading the return path does not follow the initial curve and the plastic deformation will not be elastically recovered. In Figure 7.15 the return path at points *A* and *B,* the point corresponding to the maximum moment, and a point within the yield curvature are shown. As long as the return point is within the elastic range, the return path follows the initial elastic curve, while for other points the situation is as illustrated.

Two different methods are proposed here. The first method is a simplified version of the second. Since the idea behind the plastic hinge method is to simplify analysis but still be capable of handling a cyclic loading with a variable axial load condition, the first method is proposed to fulfill the first goal, while the second method is more complicated and needs more computational effort.

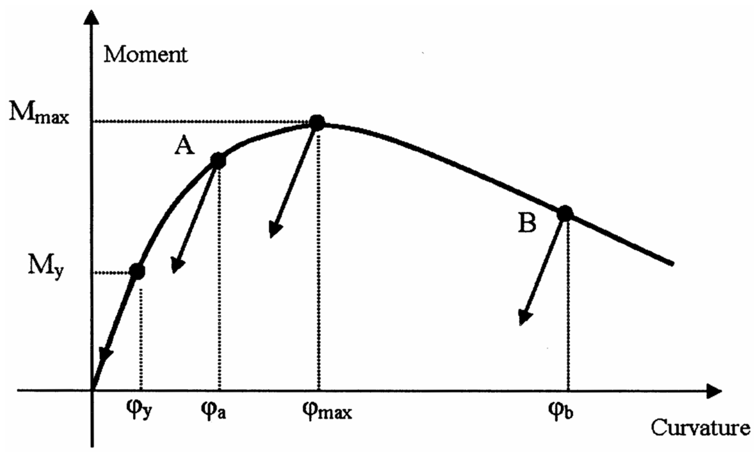

Figure 7.15 Return path on the moment-curvature curve of a section

7.5.4.1 Method One

This method assumes that the curvature between the point of first yield and the critical section is linearly distributed. The first yield point is either due to the first yield of the longitudinal bar on the section or to the first yield of the concrete. The yield of the concrete is defined to be at a strain of 0.002 and when the furthermost fiber of the section undergoes this strain while the steel strain on the opposite side is still less than the yield strain, it is assumed that the section has experienced its yield, which is due to concrete. The distance between the section where the first yield occurs to the critical section is treated as the length on which the transition occurs and will be referred to as l_p. As the lateral force grows for the first time, and while the moment at the critical section is less than the yield moment for the existing axial load, all the length is in a linear elastic state and there is no l_p. The evaluation of the displacement for any situation is straightforward, in this case, a reversal of the loading. As the moment at the critical section reaches the yield moment, this value starts to increase and reaches its maximum when the critical section experiences the maximum moment. l_p is evaluated as:

$$l_p = l.(1 - \frac{M_y}{M_u}) \tag{7.25}$$

where l is the total length, M_y is the yield moment for the existing axial load, and M_u is the moment at the critical section. Let this maximum value be $l_{p\text{-}max}$. Note that in this method it is assumed that when a section experiences a plastic deformation, it cannot be treated as elastic in a different situation, such as reversal of loading as explained earlier. So, the l_p is always either growing or constant with its maximum achieved value so far. When the curvature is less than the curvature corresponding to the maximum moment (for the existing force at the step) and no reversal has occurred, the curvature at the top of the plastic hinge is equal to the actual analytical value corresponding to the moment situation. Analytically, it is equal to the yield curvature, Φ_y, and its corresponding moment is M_y, which is also equal to:

$$M_y = M_{l_p} = \frac{(l - l_p)}{l} M_u \tag{7.26}$$

$$M_y = M_{(l-l_p)} = \frac{(l - l_p)}{l} M_u \tag{7.27}$$

When the curvature on the critical section exceeds the curvature corresponding to the maximum moment or when a reversal of loading happens, the curvature at the top of this l_p drops linearly with the part above it that has been within the elastic-linear range so far. Suppose that the moment at this instance is M_u and the yield curvature and moment corresponding to the existing situation is M_y and Φ_y, respectively. Then the curvature at the top of l_p is equal to:

$$\Phi_{l_p} = \Phi_y \left(\frac{M_{l_p}}{M_y}\right) \tag{7.28}$$

where Φ_{lp} is the curvature at the top of the plastic hinge, Φ_y is the first yield curvature, M_{lp} is the moment at the top of the plastic hinge and is calculated as:

$$M_{l_p} = \frac{(l - l_p)}{l} M_u \tag{7.29}$$

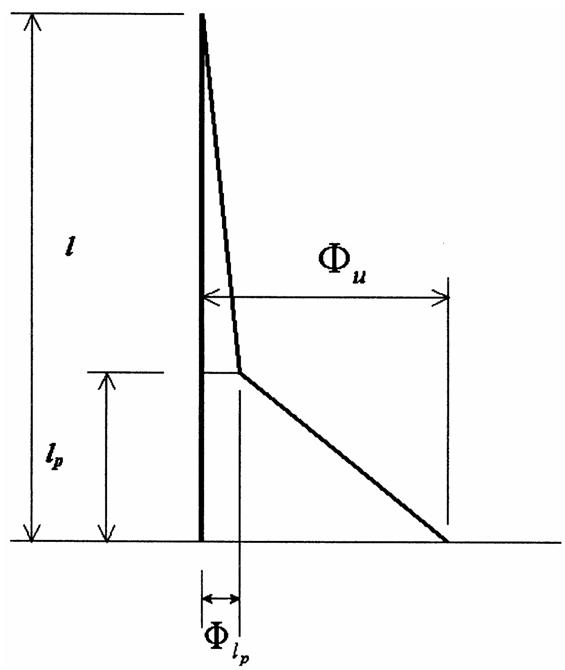

Figure 7.16 USC_RC plastic hinge, method one

therefore:

$$\Phi_{l_p} = \Phi_y(\frac{M_u}{M_y}).\frac{(l-l_p)}{l} \tag{7.30}$$

Then the displacement Δ will be:

$$\Delta = \Delta_e + \Delta_p \tag{7.31}$$

where Δ_p is the plastic flexural deflection and is calculated as:

$$\Delta_p = \int_0^{l_p} [\Phi_{l_p} + \frac{(\Phi_u - \Phi_{l_p})}{l_p} x](l - l_p + x).dx \tag{7.32}$$

or

$$\Delta_p = \Phi_{l_p}.l_p.(l - \frac{l_p}{2}) + \frac{1}{2}.(\Phi_u - \Phi_{l_p}).l_p.(l - \frac{l_p}{3}) \tag{7.33}$$

and Δ_e is the elastic deflection which is evaluated as:

$$\Delta_e = \int_0^{l-l_p} \frac{\Phi_{l_p}}{(l-l_p)}.x.dx \tag{7.34}$$

or

$$\Delta_e = \frac{1}{3}\Phi_{l_p}.(l - l_p)^2 \tag{7.35}$$

The algorithm for the method can be summarized as follows:

Initially l_p is equal to zero. For a given displacement Δ and axial load P, calculate Δ_y as:

$$\Delta_y = \frac{1}{3}\Phi_y.l^2 \tag{7.36}$$

where Φ_y is the yield curvature for the given axial load and l is the total length. If $|\Delta| \leq \Delta_y$, then :

$$\Phi_u = \frac{3\Delta}{l^2} \tag{7.37}$$

where Φ_u is the curvature at the critical section. Use Φ_u to evaluate M_u (moment at the critical section), and then the lateral force would be:

$$F = \frac{M_u}{l} \tag{7.38}$$

during a reversal of loading and while $|\Delta| \leq \Delta_y$ for the case, the problem is linear and the aforesaid process is applied. If $|\Delta| > \Delta_y$ then by trial and error find the proper $\Phi_u > \Phi_y$ for which $l_p = l.(1 - \frac{M_y}{M_u})$ and the curvature at the top of l_p is Φ_y, as can also be calculated using Equation (7.30) so that proper Δ is achieved. Then the corresponding lateral force is simply evaluated as above. During the process keep the record of the maximum and minimum achieved values for lateral force, and displacement, and the maximum achieved value for l_p. When the value of lateral force falls below the maximum lateral load evaluated so far, or when there is a reversal of loading, l_p (as is the maximum evaluated value so far) is used and the same trial and error process is applied to find the proper Φ_u, where the curvature at the top of l_p is calculated using Equation (7.30).

A simplified general flowchart for the method is shown in Figure 7.17. Intermediate algorithms, namely trial and error on the plastic hinge length, or evaluation of the moment curvature, are not shown.

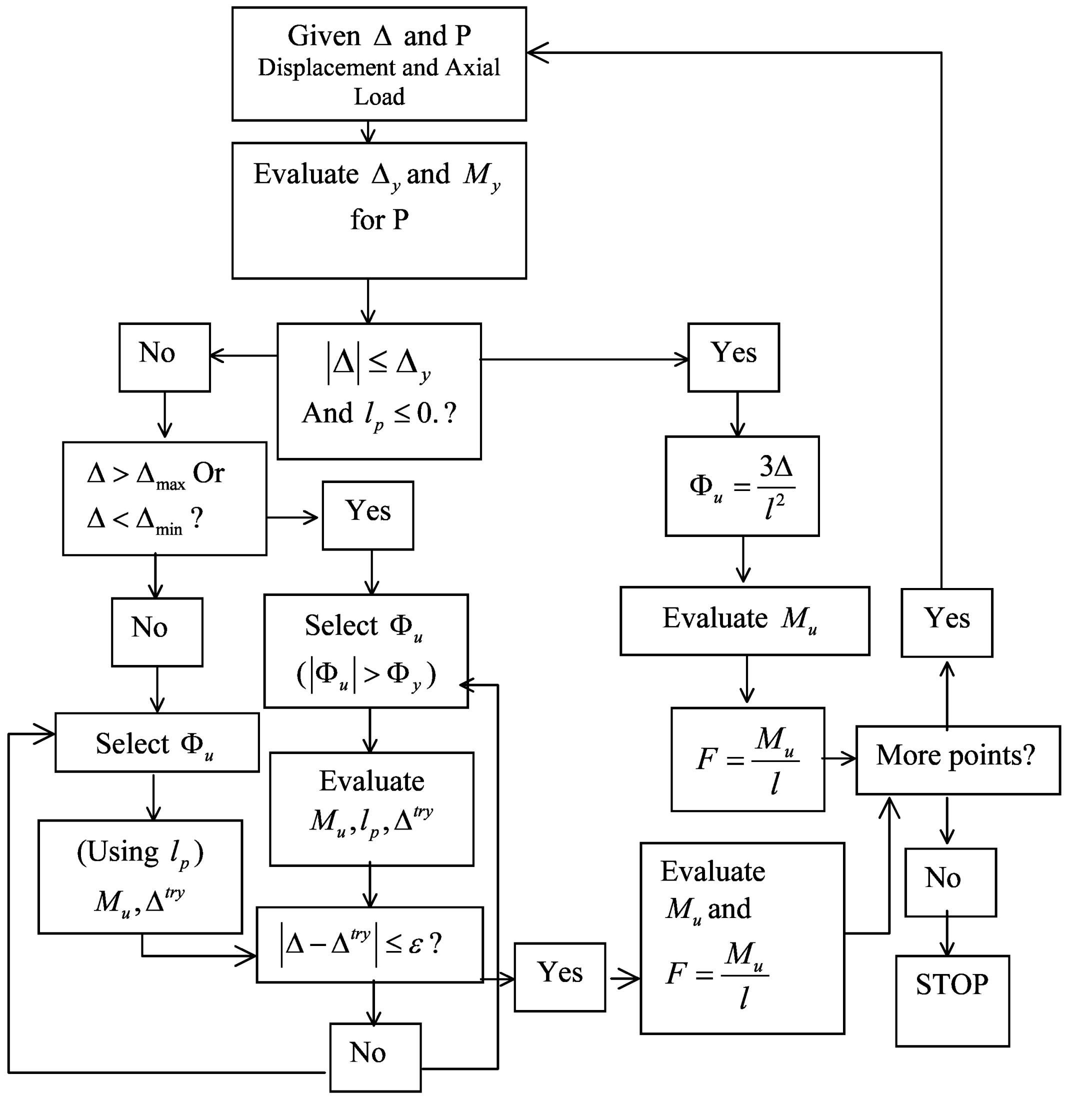

Figure 7.17 Flowchart summarizing the first method for plastic hinge

7.5.4.2 Method Two

As shown by Park and Priestley, a constant plastic hinge length works relatively well for a member under a constant axial load and a monotonic lateral displacement compared to experimental results. Park and Priestley have defined this constant length as $0.08l + 0.15 f_y d$ (or $0.002 f_y d$ in SI). Sheikh et al. also claimed that assuming a plastic hinge length equal to the section depth is a good assumption and yields results comparable to test results. The concept of a fixed plastic hinge length, specifically the Park and Priestley method, was applied by the authors to the cases of pushover analysis under a fixed axial load, and the predictions were satisfactory. The only deficiency of the method in pushover cases under a constant axial load is that the variation of the plastic hinge length, which is evident in the experimental results, is ignored, as shown in Figure 7.11. On the other hand, for a case with a variable axial load and a cyclic lateral displacement or load, these methods are not applicable. The method presented here combines the idea of a constant plastic hinge length and the idea presented in the first method to account for the variation of the plastic hinge length due to both the lateral force and axial load. The total length of the member is divided into three different areas. A constant length (*D*, can be considered as $0.08l + 0.15 f_y d$ or the section depth) close to the critical section, a transition length taken as $0.15 f_y d_b$ (or $0.022 f_y d_b$ [SI]) and the rest of the member length that always stays within the elastic range. The curvature on the part close to the critical section is assumed to be uniform. The curvature on the transition part changes linearly from the curvature on the previous part to a curvature which depends on the level of the first yield curvature for the existing axial load and the level of the lateral force at the moment, as will be discussed. As previously explained, Figure 7.18 shows the assumed distribution of curvature along the column height. At any level of axial load and displacement, depending on the previous conditions for the base curvature, the new curvature at the critical section is found by trial and error so that the desired displacement is achieved. The process needs a trial and error phase because the curvature φ_t (curvature at the top of L_{trans}) is dependent on the level of the base moment and the yield curvature for the existing axial load. The process may be summarized as follows.

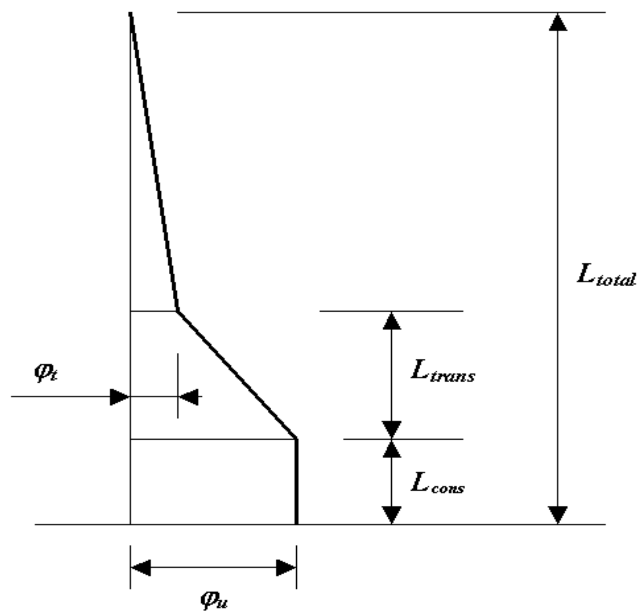

Figure 7.18 Distribution of curvature along the column height as assumed in USC_RC second method

1. Take $l_{cons} = D$, where D is the section depth. For columns with a height to depth ratio of more than 12.5 use $l_{cons} = 0.08l$.
2. For a given axial load and lateral displacement, evaluate the first yield curvature Φ_y and moment M_y. The process is to evaluate the curvature and moment corresponding to the first yield of the longitudinal steel, and also corresponding to a strain of 0.002 for the concrete under the existing axial load. Then, the yield moment and curvature for this level of axial load is the one having the smaller moment.
3. Knowing the previous base curvature and lateral displacement (zero for the first point) and the new target lateral displacement, estimate a new base curvature and evaluate the corresponding moment. Note that the moment is evaluated using the moment-curvature analysis module, where the hysteretic behavior of the section is considered through implementing the hysteretic response of the material on the fiber-modeled section. So, the moment is dependent on the previous history of the curvature experienced by the section.
4. For the base moment, knowing the yield moment and curvature and assuming that the height above the top of the transition length is linearly elastic, evaluate the curvature at the top of transition length Φ_t. The value is evaluated as:

$$\Phi_t = \Phi_y (\frac{M_u}{M_y}).\frac{(l - l_{cons} - l_{trans})}{l} \tag{7.39}$$

where Φ_y is the yield curvature and M_y is the yield moment for the current axial load level, M_u is the base moment, l is the column height, l_{cons} is the length of the segment close to the base, l_{trans} is the transition length, and Φ_{l_t} is the curvature at the top of the transition length.

5. Evaluate the lateral displacement. The lateral displacement consists of two elastic and inelastic parts. The inelastic part is evaluated as:

$$\begin{aligned}\Delta_p = {} & \Phi_t . l_{trans} .(l - l_{cons} - \frac{l_{trans}}{2}) + \frac{1}{2}.(\Phi_u - \Phi_t). l_{trans} .(l - l_{cons} - \frac{l_{trans}}{3}) \\ & + \Phi_u l_{cons} (l - \frac{l_{cons}}{2})\end{aligned} \tag{7.40}$$

and the elastic part is:

$$\Delta_e = \frac{1}{3} \Phi_t (l - l_{cons} - l_{trans})^2 \tag{7.41}$$

and the total deflection is:

$$\Delta = \Delta_e + \Delta_p \tag{7.42}$$

6. Compare the displacement with the desired value and repeat the process from number 2, until the lateral displacement is achieved with the desired accuracy. Then the corresponding lateral force is evaluated as:

$$F = \frac{M_u}{l - \frac{l_{cons}}{2}} \tag{7.43}$$

The second method is implemented in USC_RC as one of the options for the plastic hinge method when analyzing hysteretic cases. For a monotonic loading case under a constant or proportionally variable axial load, the first method applied is the USC_RC method, while the second is that proposed by Park and Priestley for a hysteretic or monotonic loading case.

It should be noted that the pull-out action of the bars or, more precisely, the rotation imposed by the foundation is not explicitly considered in the two aforesaid methods. A third method addresses this effect explicitly by defining a penetration length, as in the Park and Priestley method ($0.022 f_y d$ [SI] or $0.15 f_y d$ [English System]). In this case the length denoted L_{cons} should be revised and the curvature linearly distributed over the penetration length, starting from Φ_u at the column-footing interface to zero at the end of this length.

The second method is summarized in the flowchart of Figure 7.19.

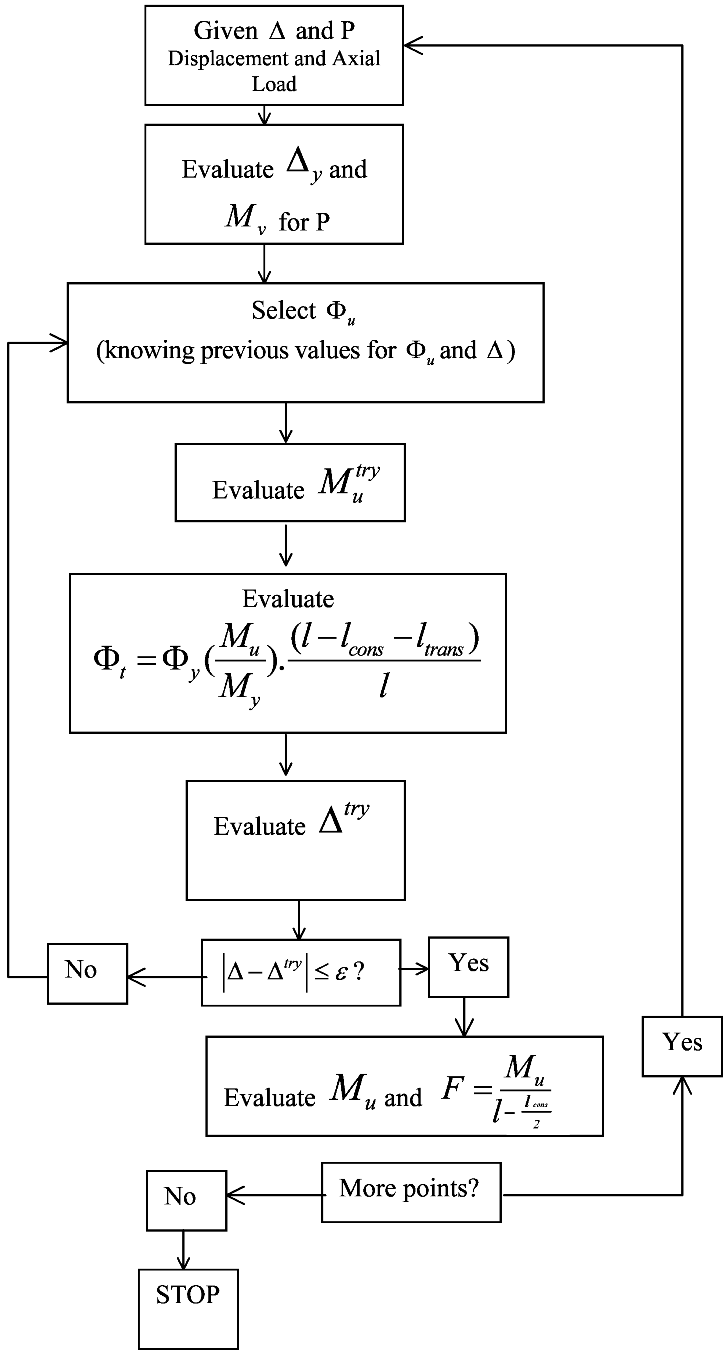

Figure 7.19 Flowchart summarizing the second method for plastic hinge

8 USC_RC Application

8.1 INTRODUCTION

The USC Reinforced Concrete (USC_RC) software program was developed to address the specific analytical needs of the research program described. To the authors' knowledge, none of the commercial or educational software available was suitable for this purpose. The need for the application became apparent during the two phases of the experimental work and when an analytical prediction was required of the behavior of the specimen under a cyclic lateral displacement and variable axial load. Based on test observations and lack of enough experimental support for the loading patterns studied, it was clear that a proper analytical tool with a user-friendly interface would remove these analytical limitations for the authors and other researchers conducting similar research.

The application began as nothing more than a FORTRAN program compiled and used as a console application. Keeping the basic functionality of the console application, a Windows interface was introduced, and more functionality was added later for both the interface and analytical engine.

USC_RC is a user-friendly, Windows-based application that can handle approximately all the needs for analyzing an RC member. Moment curvature, force-deflection, and axial-force bending-moment interaction are the main features. The program can handle both monotonic and hysteretic cases. Most of the models implemented in the program can be customized to fit specific needs. The interface provides enough functionality to view and change the analytical parameters, input data, and to revise and customize sections.

The basic features of the application and the required analytical explanations will be provided in this chapter. The application manual is the basis of the software help file containing the general features of the program and detailed instructions for use. The program can be installed from the installation CD-ROM or downloaded at:

http://www.usc.edu/dept/civil_eng/structural_lab/asad/usc_rc.htm

8.2 BASIC FEATURES

Figure 8.1 shows the main window of the application. The basic input data for the analysis is provided in this window. The input fields provide the selections and data as follows:

Unit System

USC_RC can handle the two different unit systems: All analysis can be carried out in either the SI or English unit system. In SI:

- Force is measured in terms of kilo Newtons
- Length in meters
- Moment in kilo Newton-meters
- Stress in kilo Newtons per square meter
- Force in kips (1000 pound-force)
- Length in inches
- Moment in kip-inches
- Stress in kips per square inch

When an option is clicked, all the quantities change accordingly in the main window and subsequent windows.

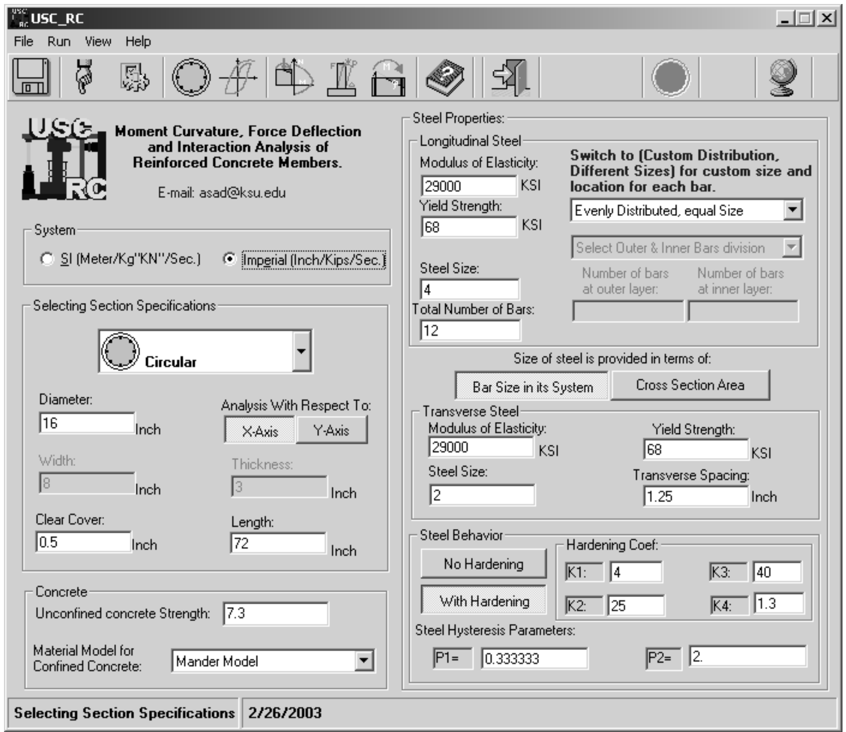

Figure 8.1 The main window interface of USC_RC, the application developed for the analytical part of the research on bridge piers

Cross-section Geometry

At this time four different options are available for the cross-section geometry:

1. rectangular section
2. hollow rectangular
3. circular
4. hollow circular

For a section, there is an options are the two different directions. This is provided for a circular section also because a custom distribution of the bars will make the response of the section different about the two different axes.

- X-Axis: This option conducts the analysis considering the X-axis. Note that depending on the way the height and width are determined in the input data, this axis is not necessarily the strong axis for a rectangular or hollow rectangular section. The user can visually detect it.
- Y-Axis: This option conducts the analysis considering the X-axis. Note that depending on the way the height and width are determined in the input data, this axis is not necessarily the weak axis. The user can visually detect it.

Concrete Properties

Here the strength of the concrete as measured in the lab or as desired for unconfined concrete is provided. The proper model for the confined concrete is also selected. For now, the "Mander model" is the only model available, but other models will be provided later. For the hysteretic behavior of concrete in USC_RC, a specific model is designed and used, which can be regarded as a revised version proposed by Mander et al. for the hysteretic stress-strain response of concrete.

Steel Properties and Arrangement

The steel properties, namely size, behavior, and the number and arrangement of the reinforcement for both the longitudinal and transverse steel are provided. The distribution of the bars for longitudinal reinforcement may be either *evenly distributed* or have a *custom distribution*. For the evenly distributed case and when the section is either *circular or rectangular*, the program will put the bars evenly distributed on the section, and for the evenly distributed case when the section is a *hollow circular or hollow rectangular* section, there are *two options:* (1) determine the number of bars on the outer and inner layers by the program (Automatic option) and (2) select Custom. For the *Automatic* option, the program assigns the proper number of bars to the outer and inner layers based on their respective circumferences. For the *Custom* option, the user provides the number of bars on the outer and inner layers. Obviously, the sum of these two numbers should be equal to the total number of bars; otherwise, the application will ask the user to correct the input values.

Size of Reinforcement

The size of the reinforcement steel, for both the longitudinal and transverse directions, can be given either in terms of the size in the system (e.g., 3 for a #3 bar) or in terms of the area of the cross section of the bars. The user should make sure that proper quantities are used. When the number of the rebar in the system is provided, changing the system will change the bar number so that the selected number in the new system corresponds to the number in the old system. If there is no equivalent number in the new system, the closest number will be selected. (See: *ASTM Soft Metric Reinforcing Bars* for details of the standard)

Table 8.1 ASTM Standard metric reinforcing bars

Bar Size SI [English]	Nominal Dimensions		
	Diameter mm [in.]	Cross-Sectional mm^2 [$in.^2$]	Weight kg/m [lb/ft]
#10 [#3]	9.5 [0.375]	71 [0.11]	0.560 [0.376]
#13 [#4]	12.7 [0.500]	129 [0.20]	0.944 [0.668]
#16 [#5]	15.9 [0.625]	199 [0.31]	1.552 [1.043]
#19 [#6]	19.1 [0.750]	284 [0.44]	2.235 [1.502]
#22 [#7]	22.2 [0.875]	387 [0.60]	3.042 [2.044]
#25 [#8]	25.4 [1.000]	510 [0.79]	3.973 [2.670]
#29 [#9]	28.7 [1.128]	645 [1.00]	5.060 [3.400]
#32 [#10]	32.8 [1.270]	819 [1.27]	6.404 [4.303]
#36 [#11]	35.8 [1.410]	1006 [1.56]	7.907 [5.313]
#43 [#14]	43. [1.693]	1452 [2.25]	11.38 [7.65]
#57 [#18]	57.3 [2.257]	2581 [4.00]	20.24 [13.60]

Also, when the number in a system is provided and the user changes the option to area, the corresponding area is calculated and shown accordingly. Here the user should note that the calculations for switching from the number to area (and vice versa) is done in a way which is completely consistent with the ASTM Standards.

Assume that the user enters #19 in the SI: when switching to the English system it becomes #6, and vice versa. It is important to note that the number gap for the bars in SI corresponding to the bars in the English system is more than one. This means that in some cases when the user provides the rebar number in the SI, and then switches to the English system, the closest English system number will be chosen, and when switching back to SI, the proper SI number will be shown, which may not be exactly the same as the initial number. For example, choosing #22 in SI then switching to the English system will get #7, and then when switching back to SI gets the initial #22. But choosing #24 in SI, then switching to the English system gets #8, and when switching back to SI gets #25, not 24. If the initial input number had been 23, after two switches we would get 22. These are all completely consistent with the standard and are required so that the user is aware of the standard being used. It is also important to note that the area of the cross sections (in either system) is calculated based on the ASTM standards. It means, e.g., that for a #10 rebar (SI), the radius is not assumed to be 5 mm, but is first converted to the equivalent size in the English system (as suggested by the standard); then the area is evaluated and changed to the proper value in the SI. So, the cross-section area for this specific rebar is not $3.14159*(0.01\ m/2)^2=0.00007854\ m^2$, but 0.00007126, as seen in the table.

When the user wants to use a specific size for the bar, regardless of the standard, the size should be entered in terms of the cross-section area. In this case (using this option), changing the system converts only the cross-section area to its new value in the new system without any change considering the standard.

For the custom distribution case, a fully functional interface (Figure 8.2) provides the user with all the functionalities required for the desired custom size and location of the bars on the section. The user accesses this interface by choosing *Custom distribution, different sizes* on the main window. When these are determined by clicking "OK", the main window activates *Show custom distribution and size form* to give the option of revising the custom arrangement and size, if needed.

In this window, the bar location and size can be assigned in different ways. All of these options are properly interrelated and consistent.

1. Clicking on the proper place on the section. Note that the coordinates of the point are always shown in the two X and Y windows below the section. Right-clicking a bar gives the options to resize or delete the bar. The size of the bar is always expressed in terms of the proper value already set according to the selected system or its cross-section area. It should be pointed out that if the size of a bar is not correct in the selected system, it will be switched to the proper value. If the entered size is not appropriate for the corresponding location, the user is notified but the size is not changed.
2. Entering the location and size in the table. Again, if the size or location is not proper, the program does not accept it; if proper, it shows on the section.
3. Reading data from a file. In this case, the file should be in text format and the data should be separated by either a comma or space. X, Y, and the size of bar for each bar is on the same line as the respective bar.

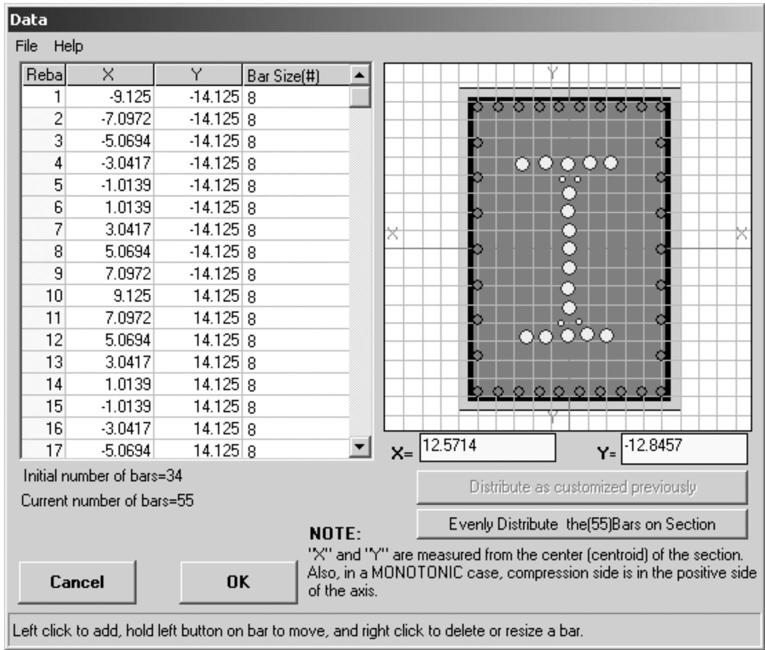

Figure 8.2 The fully functional interface makes it possible to customize a section

To change a bar location or size, the corresponding values can be changed in the table or by dragging the bar to its proper location; the size can be changed by right-clicking the bar. At any time, the bars can be rearranged evenly on the section.

The custom distribution and sizes can be saved for further use. Also the section can be saved in BMP format.

8.2.1 Material Models

The models developed and implemented in USC_RC for the monotonic and hysteretic stress-strain relationship of steel and concrete are as explained in Chapter 1. Here the parameters used in USC_RC are provided. If necessary, the user based on the needs can change these parameters. The parameters have been determined based on the results from material tests carried out in the USC Structural Lab.

For the monotonic stress-strain curve of steel, the input data and parameters are as follows:

$f_y = 469\,MPa\ [68\,ksi]$ and $E = 200000\,MPa\,[29000\,ksi]$

$K_1 = 4.$

$K_2 = 25.$

$K_3 = 40.$

$K_4 = 1.3$

and for the hysteretic behavior the parameters assigned are:

$P_1 = 0.3333$

$P_2 = 2.0$

The unconfined concrete strength was $f_c^{'} = 49.3\,MPa[7.15ksi]$ for the first two tests and $f_c^{'} = 50\,MPa[7.3\,ksi]$ for the last four.. The default value is 50.3 MPa [7.3 ksi] as used for the last four tests. All other specifications for the monotonic and hysteretic curve of confined and unconfined concrete can be found in Chapter 1.

Main Window Command Buttons

There are 10 command buttons in the main window, and one button to show the *Bar Custom Location and Size.* The buttons are active only when the required data are provided. These buttons are as follows:

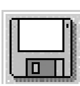 — saves the input data in a text file.

 — restores the default values. The default values match the specifications of the specimens tested in the USC Structural Lab.

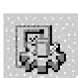 — loads the interface on which the analysis parameters can be adjusted.

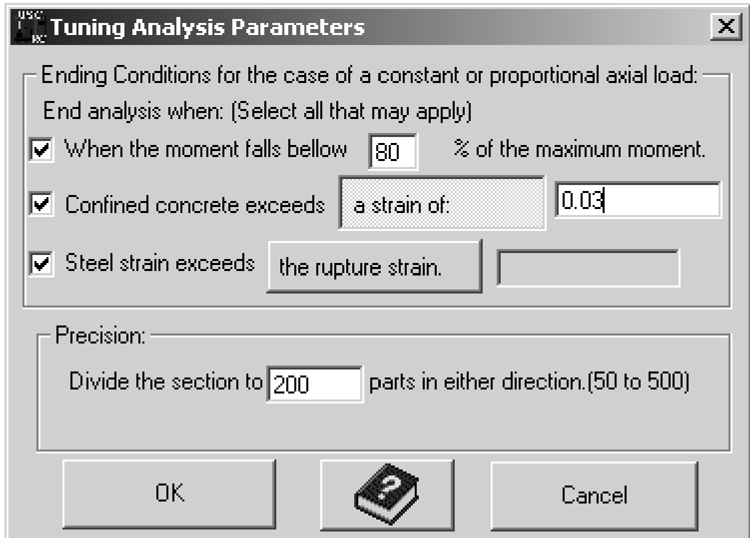

Figure 8.3 Analysis parameters can be tuned based on analytical needs

This interface is different at different instances of the process so that only the adjustable values at the time can be revised. Using this option allows the user to adjust the analysis parameters as desired. All the required information is provided in a dialog box and, if needed, additional information is provided by message boxes as a reaction to user input. The dialog box is shown here. For monotonic analysis in the cases of a constant or proportionally variable axial load, for both moment-curvature and force-deflection analyses, it is essential to have at least one of the second or third conditions in the first part for ending the analysis selected. Although the analysis will be carried out if no condition for ending analysis is selected, if necessary, the user can manually break the process selecting the break button.

This dialog box can be accessed at any stage when the user is concerned about the analysis parameters. The window displays properly when showing only the necessary fields.

The control parameters are:

- Level of bending moment on the critical section of the member that can be used to decide if the analysis should be terminated compared to the maximum level achieved during the analysis.
- Level of confined concrete strain. By using this option, termination can be set at the ultimate strain or a custom strain for confined concrete.

- Level of steel strain. By selecting this parameter, termination can be determined to be either at the ultimate strain of steel (rupture of the first bar) or a custom strain.
- Number of fibers (divisions) on the cross section of the member. This value is recommended for the default value, and cannot be more than 500 in a direction.

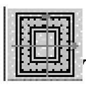This button loads the window showing the section, steel, confined concrete and cover concrete stress-strain relationship based on the data provided by the user.

The following is the window for viewing the selected section and material properties. This window is activated when *View Section and Properties* or the corresponding command from the menu bar is selected.

Here a major part of the input data can be revised where the result is visually available for further judgment. The items that can be revised depend on the option already selected for a custom size and location for bars or even distribution of bars with the same size. The section can be saved in bitmap format. Note that after changing the data as desired, as soon as data are set and the focus is out of the corresponding data field, the section is redrawn accordingly.

The stress-strain relationship for steel and cover and confined concrete can be saved both in terms of the actual calculated numbers and also graphically as shown in the window, but to see the updated curves, the user must push the "*Refresh Plot*" button. This button is active only when an update is required. The selection of the steel behavior is not available in this dialog box, but can be changed in the main dialog box and to revisit the section and material properties. Clicking *View Hysteretic Behavior of Cover and Confined Concrete and Steel* shows the window in which the user can examine the hysteretic response of material and, if necessary, adjust the steel hysteretic parameters.

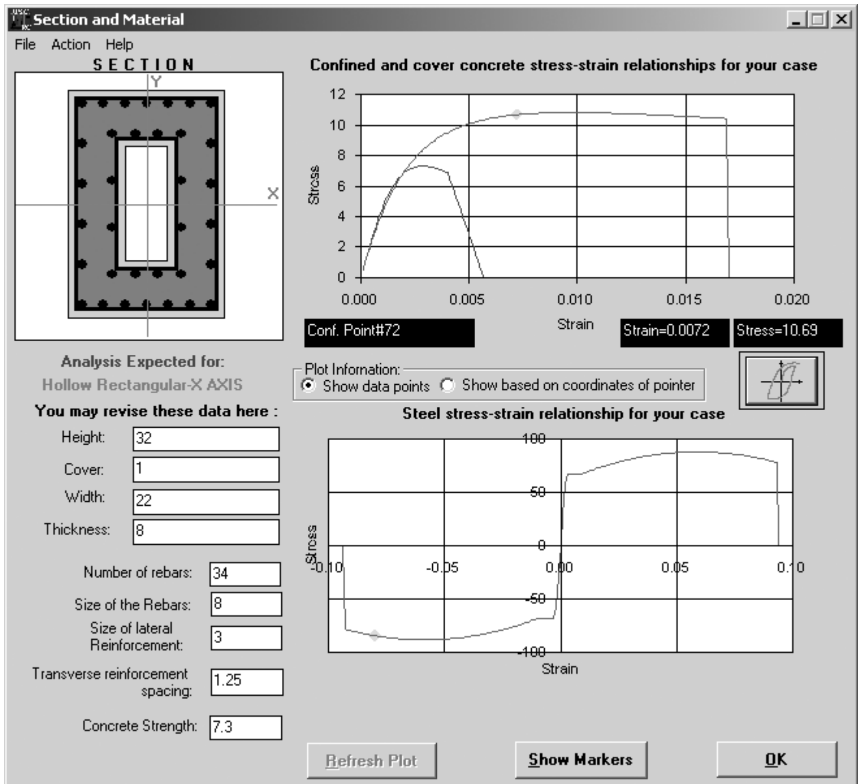

Figure 8.4 Window to view the section, material stress-strain curves, and for revising some of the input data

The two options for viewing the data on the charts are (1) to see the *coordinates* of the mouse moving on the chart and (2) to see the *data points*.

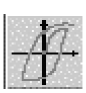 This button loads the window in which the hysteretic response of the material can be viewed and examined. The hysteretic parameters of steel can be adjusted in this window to achieve the desired behavior.

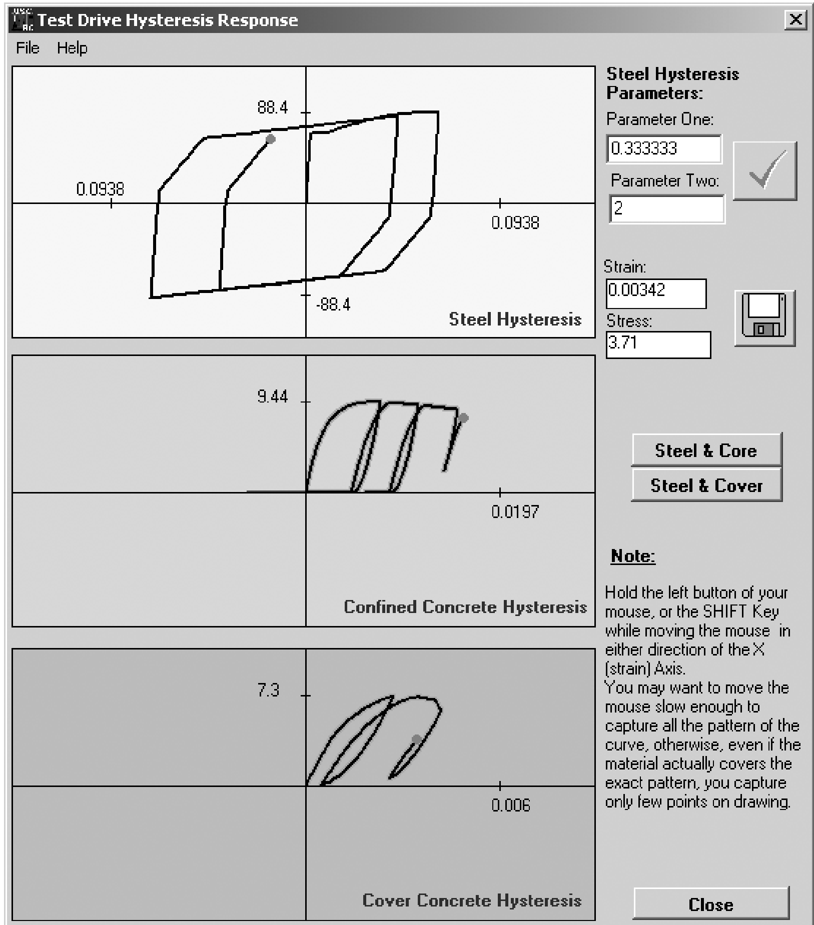

Figure 8.5 The hysteretic response of material can be examined and saved

The user can experiment with either material to explore its hysteretic response. Clicking on each area will put the pointer on the origin, and initializes the curves. Hold down the left-button of the mouse or push SHIFT and move the pointer in either direction of the strain axis to plot the response curve. By moving the mouse properly the hysteretic response of the material for any desired path can be examined. The stress and strain are shown numerically in their respective windows, and the resulting curve can be saved in terms of the produced data, or as a graphic. Note that when a material fails, you will get zero stress even if you return to its allowable range of strain, as in the real world. To capture the detailed response move the mouse slowly; otherwise, the curve will jump from the initial point to the next point and the two points will be connected by a straight line, which is ***not*** the real curve. To see how two materials behave simultaneously, the user has the options of seeing the behavior of steel and confined concrete or the steel and cover concrete at the same time. In these cases, the strains are scaled so that the same scale is used for both materials to provide a proper comparison.

The hysteretic parameters of steel can be adjusted here if needed. Right-clicking any window provides the user with enough tools, such as saving the curve either in a data file or as a picture, starting over the process or getting help.

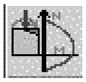 This command button is used for the Axial-Force Bending-Moment Interaction Analysis. The axial-force bending-moment interaction curve can be obtained for any case. The options are as follows:

1. ACI Axial-Force Bending-Moment Interaction Curve for unconfined concrete. The concrete is considered not to be confined, as for most design cases based on the code. For calculation, the concrete strain is kept at the level corresponding to the peak strength (usually 0.002) at one end of the section, while the curvature is changed from zero up to a curvature where the strain at the other end of the confined core of the section reaches the ultimate strain of the longitudinal steel. The steel is assumed to have a bilinear stress-strain relationship curve.
2. ACI Axial-Force Bending-Moment Interaction Curve for confined concrete. The same as above except for the ultimate strength, which will be the strength of the confined concrete based on the model used and the corresponding strain.
3. When the concrete strain corresponds to the peak strength of confined concrete. This value is calculated by the program based on the data provided for the unconfined concrete strength, transverse reinforcement strength and ratio, and also the size and ratio of the longitudinal reinforcement. The strain at one end of the confined core of the section is kept at this strain, while the curvature is started from zero up to a curvature where the strain at the other end of the confined core of the section is equal to the ultimate strain of the longitudinal steel.
4. This option is used when a certain strain is desired for calculation of the axial-force bending-moment interaction curve. Here, if the input strain is negative, it is treated as the steel strain, and if positive, it is treated as the concrete strain. For these two cases the curvature is changed as described in options 2 and 3, depending on the sign of the input strain.
5. Engineering Interaction occurs when the steel strain is limited to the longitudinal steel yield strain, and the confined concrete strain is limited to the confined concrete strain corresponding to the ultimate strength of the confined concrete. The curvature is changed from zero when the strain is the yield strain of steel and is increased up to a curvature when the confined concrete strain is the strain corresponding to the ultimate strength of confined concrete.

Then, the curvature is reversed and decreased to zero where the confined concrete strain is kept at the above-mentioned strain.

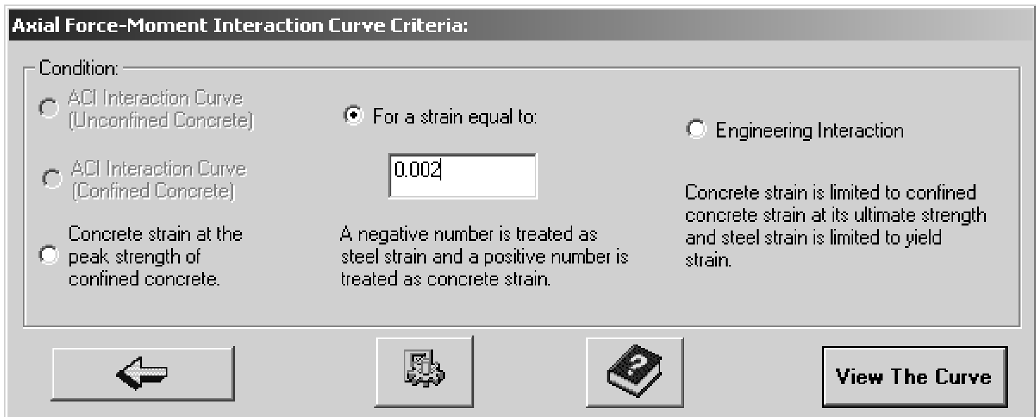

Figure 8.6 Type of interaction analysis is selected through this interface

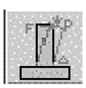 This command button is used for Force-Deflection Analysis. The window prompts the user for further selection. Here the analysis can be done for either a constant axial load, or a nonproportionally or a proportionally variable axial load. All options are similar to the Moment-Curvature Analysis, with curvature replaced by displacement and moment replaced by force; namely, both monotonic and hysteretic analysis can be carried out depending on the axial load condition and selected options. Here the user has the option of different plastic hinge methods.

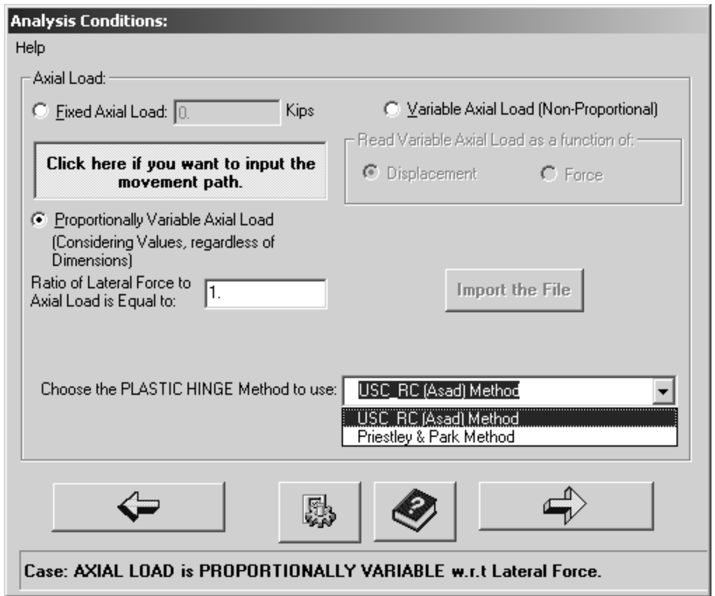

Figure 8.7 Force-deflection analysis can be done for any loading condition, using the desired plastic hinge method

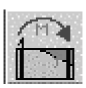 This command button starts the Moment-Curvature Analysis. For a Monotonic Analysis: The analysis can be done either for a fixed axial load case, a nonproportionally variable, or a proportionally variable axial load.

When the axial load is proportionally variable with respect to the bending moment, the program prompts the user for the proportionality value, the minimum (starting) and maximum (ending) values for the curvature, or lets the application set these values. Then, it starts the analysis from the least curvature and goes to the upper value for the curvature, as desired and provided by the user, and provides the analysis results in terms of a chart and a data file that can be saved.

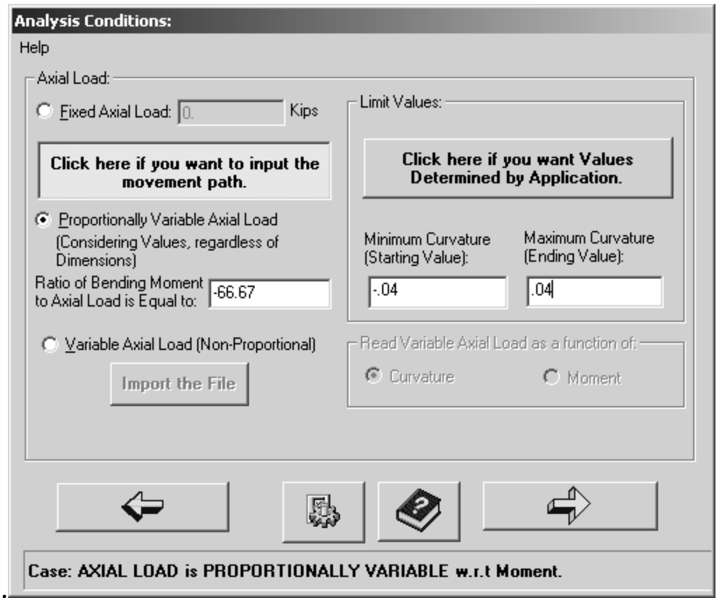

Figure 8.8 Moment-curvature analysis can be done for any loading condition

For a hysteretic analysis, in case of a fixed axial load, the user should provide the level of the axial load. The path of curvature variation (cyclic or any other random movement) should be provided in a text file. Here the only data are curvature, and the data items should be separated by a comma or space.

When a variable axial load case is selected, the axial load can be selected to be either variable with respect to the curvature or the moment. In this case, the data should be provided by the user by reading the data from the corresponding file. Note that the data items should be separated either by comma or space. Also, note that in any case, the application will guide the user through and in case of error, will guide the user with proper messages. Please see the "Axial Load Cases" for more detail on user-provided axial loads, and if it is not within a reasonable range for a case.

Please note that like all other windows in this application (USC_RC Interfaces), a button for further steps is activated only when all the conditions are satisfied. When a single condition fails, the corresponding button is no longer active. Other than these instances the user is provided with enough prompts to get through the analysis properly.

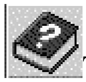This button provides help for the current window. The USC_RC application provides help through a variety of ways at any stage, with different analytical methods.

1. Help contents
   (a) *Contents* in the Help menu.
   (b) *Contents* on the Help window.
2. Help on the current window
   (a) *Help On This Window*, in the Help menu of the Main Window.
   (b) *Help* on Help Menu.
   (c) F1 on other windows (except the Main Window)
3. Context-sensitive Help
   (a) *What's This?*
      - Right-click on any place and choose *What's This?* from the popup Help Menu.
      - *What's This?* In the Help Menu.
   (b) Using *F1 Key*
      - In the Main Window brings up context-sensitive help in a popup box.
      - In other windows brings up that window's help.
4. Tool Tip Texts
   (a) Place the mouse on an object where information is needed. The most convenient method is the *Tool Tip Text.* The required information is briefly provided in a popup box. It is obvious that all other helps are also available, so that the user will always have access to the required help information.

   Help is readily available, especially in the Main Window of the USC_RC Application.

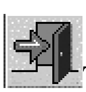This button is used to exit the application.

Main Window Menu Bar:

The main window menu bar consists of the *File, Run, and Help* main menus. All the command buttons are available through the menu bar, including a *Tune Analysis Parameters* command for tuning the analysis parameters for the case. Like the command buttons, each command on the menu bar will be active only if the corresponding action can be done (such as having all the required initial data); otherwise, it is inactive.

8.2.2 Analysis

The analysis, in general, is based on the fiber model. The main analysis types are *Moment-Curvature* under a constant, proportionally or non-proportionally variable axial load, and a monotonic or cyclic curvature or moment; *Force-Deflection* analysis under a constant, proportionally or non-proportionally variable axial load, and a monotonic (pushover) or cyclic (hysteretic) lateral load or displacement; and *Axial-Force Bending-Moment* analysis for different conditions.

8.2.2.1 Moment-Curvature Analysis

Moment-Curvature Analysis can be done for three different cases.

Fixed Axial Load

For a fixed level of axial load (zero, positive, or negative), the analysis can be carried out for either for a *monotonic* or *cyclic* curvature case.

Monotonic Analysis

For a monotonic analysis, the starting and ending values for the curvature can either be set by the user or by the program using the default starting and ending values. The default starting value for the curvature is zero, and the analysis will continue up to a point where the steel strain or confined concrete strain exceeds the ultimate allowable strain (default) or the strains determined by the user when adjusting the analysis parameters, or when the moment falls below a certain percentage of the maximum moment as determined by the user when adjusting the analysis parameters. In any case, the analysis can be stopped or interrupted by the user. At the end of monotonic moment-curvature analysis under a constant axial load, some important points can be shown on the resulting curve that are internally evaluated by another module, as discussed later, certifying the validity of the analysis. Also, for any desired strain (either for concrete or steel) the corresponding curvature, moment, neutral axis position and the strains at the furthermost fibers and bars (concrete and steel) can be evaluated, and the corresponding point is marked on the resulting moment-curvature curve. Note that the axial load cannot exceed the section capacity at any instance; namely, a positive axial load is limited to less than $A_gF'_c+A_sF_u$, and the negative axial load is limited to less than A_sF_u for zero curvature. A_g is the gross cross section (including unconfined and confined area, and F'_c is the corresponding strength for each part), A_s is the net area of the longitudinal steel, and F_u is the ultimate strength of the steel. For each curvature the axial load limit is different, and the program compares the level of axial load provided by the user and the allowed level. The allowable ultimate axial load in either the positive or negative direction is evaluated during the analysis and when the input axial load exceeds this level, the maximum allowable axial load is employed and the point is marked to notify the user about the condition. The main concept of plane remaining plane is a basic assumption in analysis.

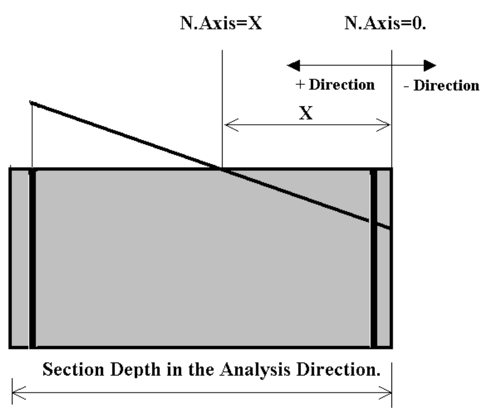

Figure 8.9 Location of the neutral axis on the section and the assumed sign convention

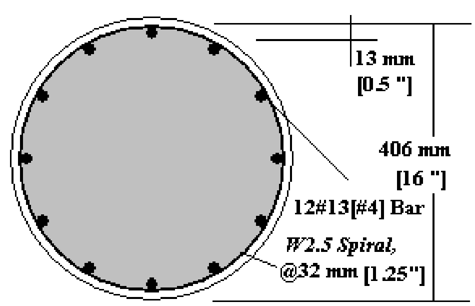

Figure 8.10 Typical section of the specimens tested

The algorithm for evaluating the moment for a given axial load and *curvature* in a direction is as follows:

1. The section is divided into the required number of fibers in the analysis direction.
2. For a specific curvature, a location for the neutral axis is estimated and the corresponding axial load is evaluated by integrating the forces of individual fibers on the section.
3. If the evaluated axial load is equal to the axial load within a predetermined margin, the neutral axis has been found and then the corresponding moment is evaluated and will continue to the next point, if any. If the evaluated axial load is not equal to the axial load, the process will be repeated from step 2, and trial and error will continue until the desired level of axial load is achieved.

Employing a proper method for this process is crucial. The variation of axial load for a specific curvature with respect to the neutral axis position is not a regular curve as shown in Figure 8.11, for the section shown in Figure 8.10, especially for high curvatures. That is why commonly used methods will fail to converge at some points. The routine used in USC_RC is such that it can roughly handle all the cases and will converge to the answer, if any, or will converge to the maximum possible value or minimum possible value if the level of the axial load is more or less than that, respectively. Figure 8.11 shows the huge difference between the maximum possible axial load for the same section with the same properties under different curvatures.

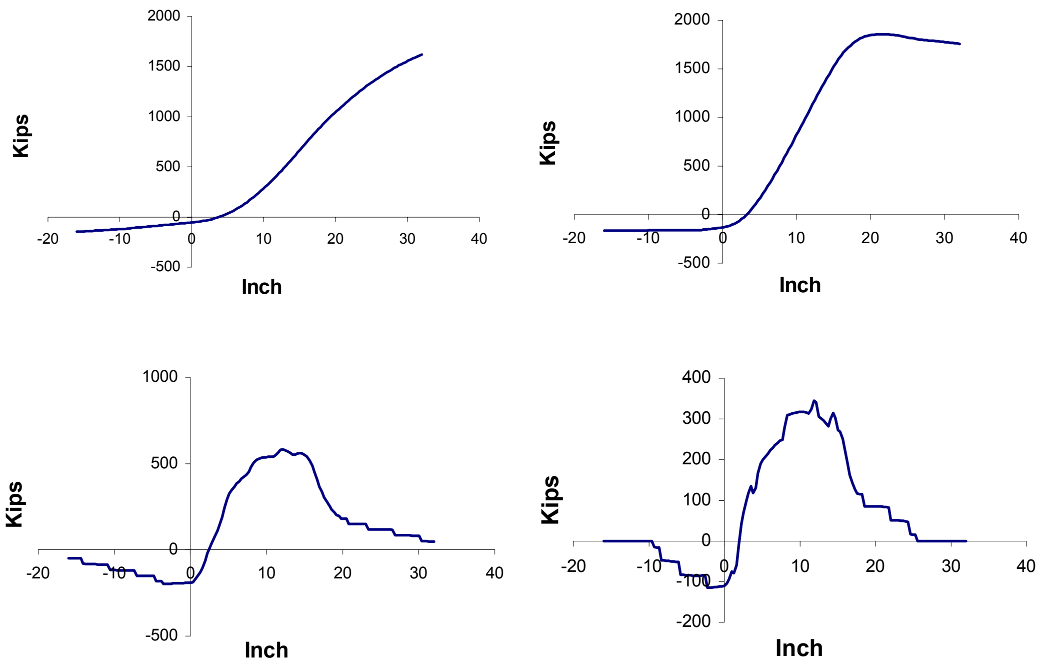

Figure 8.11 Variation of axial load with respect to the neutral axis location on circular section shown in Figure 8.10, for curvatures 0.0001 (top-left), 0.0005 (top-right), 0.005 (bottom-left), and 0.009 (bottom-right)

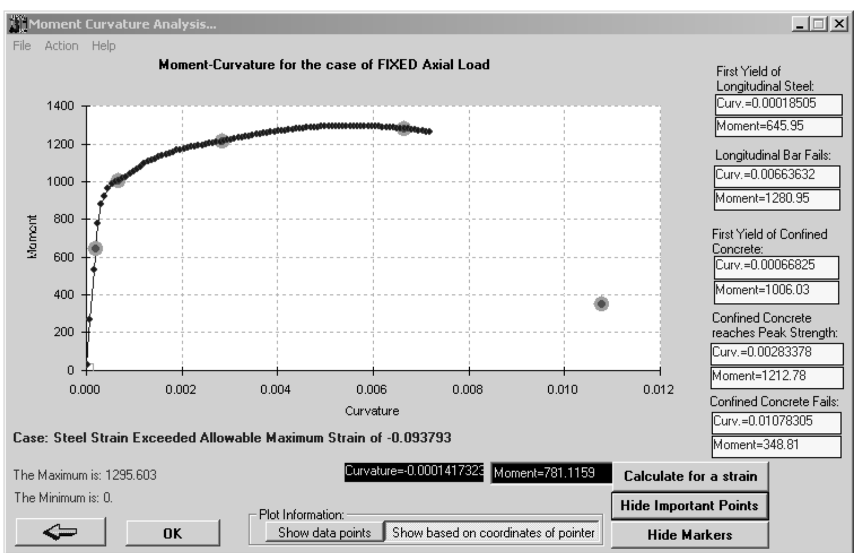

Figure 8.12 Result of a monotonic analysis under a fixed axial load, and the important points

The algorithm to evaluate the moment-curvature results for a specific strain is as follows:

1. For the required strain (concrete when positive or steel when negative), select a position for the neutral axis, and the line connecting the point with the required strain and the neutral axis determines the plane for which the axial force should be evaluated.
2. Evaluate the axial load. If it is equal to the desired level for the step (within the acceptable error margin), the neutral axis is found and the moment will be calculated. Otherwise, the process should be repeated for another location of the neutral axis, until the proper location is achieved.

The module used to find the proper location of the neutral axis in USC_RC can converge to the proper value for all the cases, and when the level of the desired axial load is higher than the maximum possible or less than the minimum possible level, the program does the analysis for the highest or lowest possible level, accordingly, and marks the point to notify the user. In all cases, the data can be saved in a text file, and the actual axial load and the axial load as provided by the user are compared. Since the two methods are different in terms of finding the neutral axis location, in the first the curvature is fixed, in the second the strain at a specific point is fixed, and the curvature varies depending on the neutral axis location; matching the results confirms the accuracy of analysis. The important points that can be shown after a monotonic analysis include the first yield of the longitudinal steel where the confined concrete reaches the strain corresponding to its strength, and where the steel and the confined concrete fail.

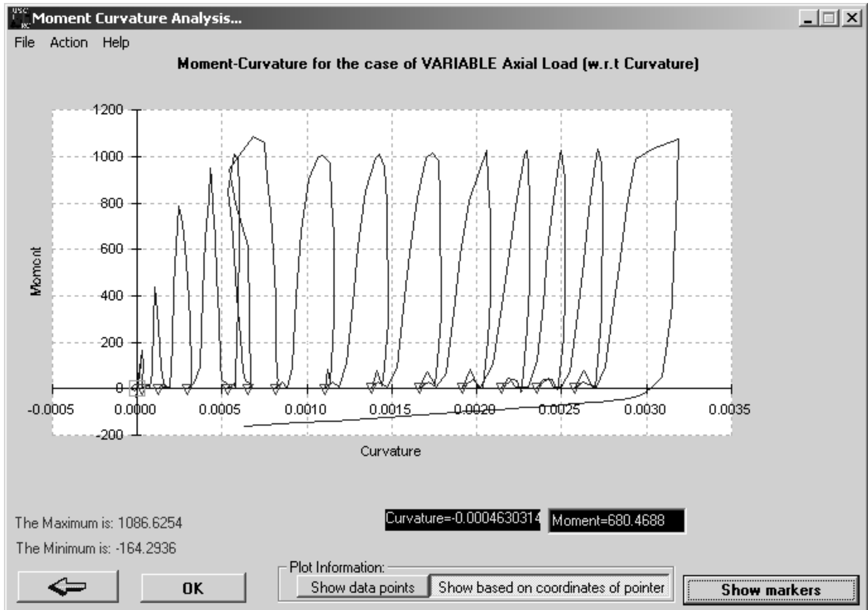

Figure 8.13 Result of a moment-curvature analysis under a variable axial load. Points marked by a small triangle where the input axial load has been less than the minimum allowable axial load.

Hysteretic Analysis

For a hysteretic analysis under a constant axial load, the curvature path should be provided by the user in a text file. The algorithm is similar to that stated for the monotonic case, with the difference being that the curvature path can have reversal points and any arbitrary pattern. For each point (each pair or axial load and curvature) the stress-strain history of each single fiber on the section is recorded is used in evaluating the response for the next point. The hysteretic stress-strain model of the material (steel, confined concrete, and cover concrete) plays the major role here in providing the hysteretic moment-curvature response of the section, but the response depends on the path of the applied curvature. If a monotonic curvature is applied (growing from a starting value to its final value), the result is the monotonic response even if the hysteretic model for the material is employed. The reason is that a monotonic strain in the hysteretic model is always on the monotonic stress-strain curve. A hysteretic (cyclic) curvature will bring up the hysteretic properties of the section as modeled in the hysteretic stress-strain response of the material. It should be added that the level of the axial load is also checked here and if not within the valid range for the curvature, the closest valid value is used and the user is notified by a mark on the curve at the corresponding point; the two values are saved when the data are saved in a text file.

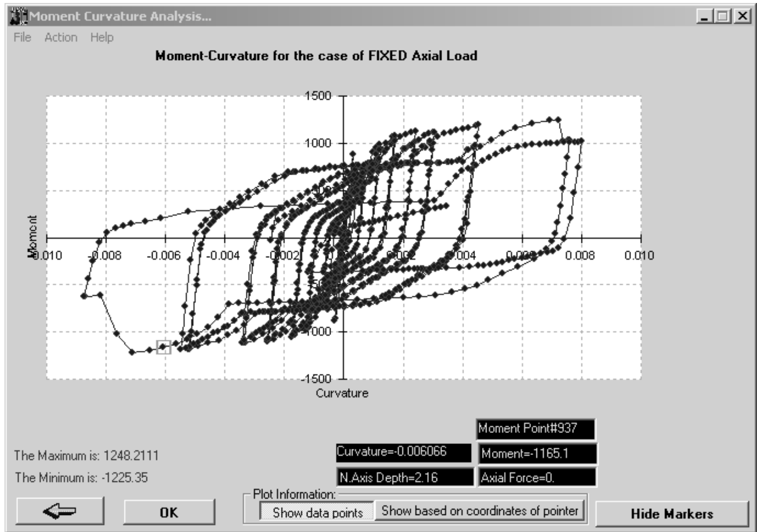

Figure 8.14 Moment-curvature under a zero axial load and cyclic lateral displacement

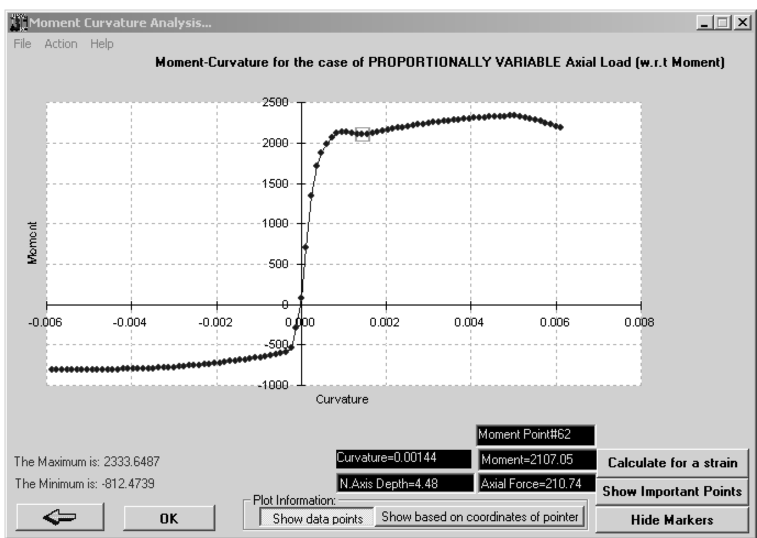

Figure 8.15 Monotonic moment-curvature analysis for a case with the moment to axial load proportionality of 10. Note the axial force and bending moment values for the arbitrary point on the chart.

Proportionally Variable Axial Load

In this case the axial load varies proportionally with respect to the moment. The ratio or $\frac{BendingMoment}{AxialLoad}$ should be provided. During analysis this ratio is a leading parameter, and the neutral axis is determined so that this ratio is satisfied. The options for this case are similar to those for a constant axial load. For a proportionality ratio, the analysis can be done either for a monotonic case or a cyclic (hysteretic) case. For the monotonic case, the starting and ending values can be set by the user by the program. The analysis parameters can be tuned as for the case of a constant axial load. After the monotonic analysis, the important points can be determined by the application, and the moment-curvature specifications for a certain strain can be evaluated, with the same method as was described for a constant axial load. For the hysteretic analysis, the user will provide the curvature path in a text file, and the analysis will be done based on the proportionality ratio already set by the user.

The difference between the cases with a proportionally variable axial load and a constant axial load is the criteria used to find the neutral axis. In the case of a constant axial load, the axial load for each trial neutral axis is compared with the desired level of axial load, and the neutral axis is the point where the difference between the trial value and the desired axial load is less than a predetermined value. For a proportionally variable axial load, for each trial location for the neutral axis, the corresponding moment and axial load are evaluated and then the ratio is compared with the desired ratio. The neutral axis is found when the difference between the trial ratio and the desired ratio is within a predetermined value.

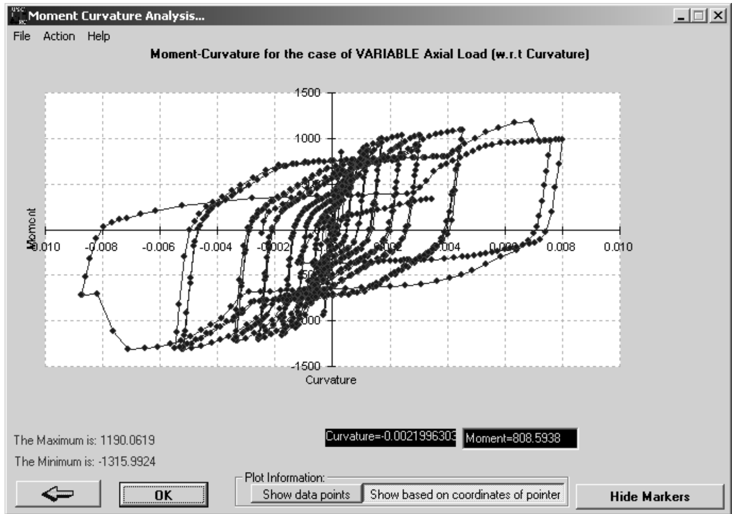

Figure 8.16 Result of the hysteretic analysis of the section, shown in Figure 8.10, under a proportionally variable axial load, with the ratio of –67%

Even if considering the above-mentioned basic rule, the process employed in USC_RC has a more sophisticated algorithm, so that converging toward the true location of the neutral axis is faster and also detects the validity of the user input data. Figure 8.17 to Figure **8.20** show the variation of axial force and bending moment for four different curvatures of 0.0001, 0.0005, 0.005 and 0.009 (1/in.) with respect to the location of the neutral axis on the section shown in Figure 8.9 for the section shown in Figure 8.10. These figures show that the curves are not smooth and regular and that a standard routine may fail in converging to the proper value. As an example, for a certain level of axial force, analytically there may be two or more answers, or in some cases for high curvatures, the maximum axial force that can be achieved may be less than the desired level. The algorithm used in USC_RC is so that, as an example, for the case of a constant axial load, it will be detected if the level of axial load introduced by the user is not within the valid range. This fact has already been addressed. The reader is referred to Appendix II for details of the FORTRAN code for implementing different types of USC_RC analysis.

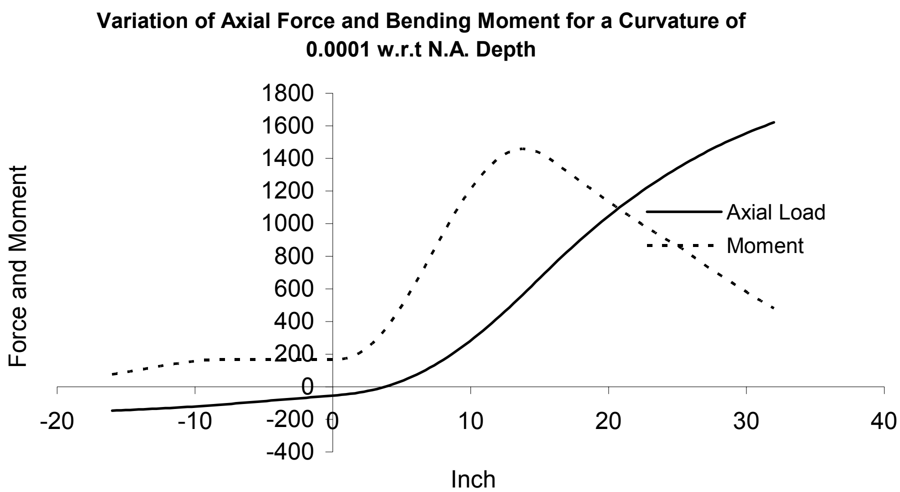

Figure 8.17 Variation of axial force (kips) and bending moment (kip-in.) for a curvature of 0.0001 (1/in.) with respect to the location of neutral axis as shown in Figure 8.9 for the section shown in Figure 8.10

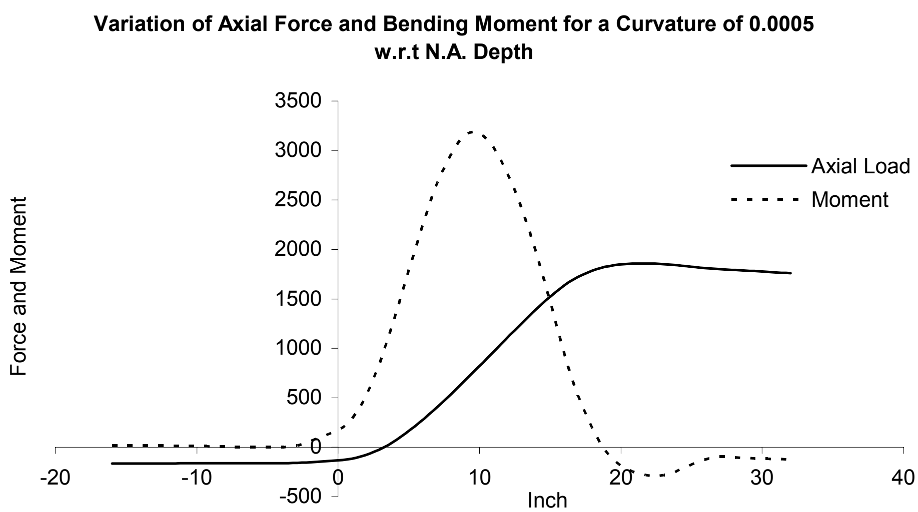

Figure 8.18 Variation of axial force (kips) and bending moment (kip-in.) for a curvature of 0.0005 (1/in.) with respect to the location of neutral axis as shown in Figure 8.9 for the section shown in Figure 8.10

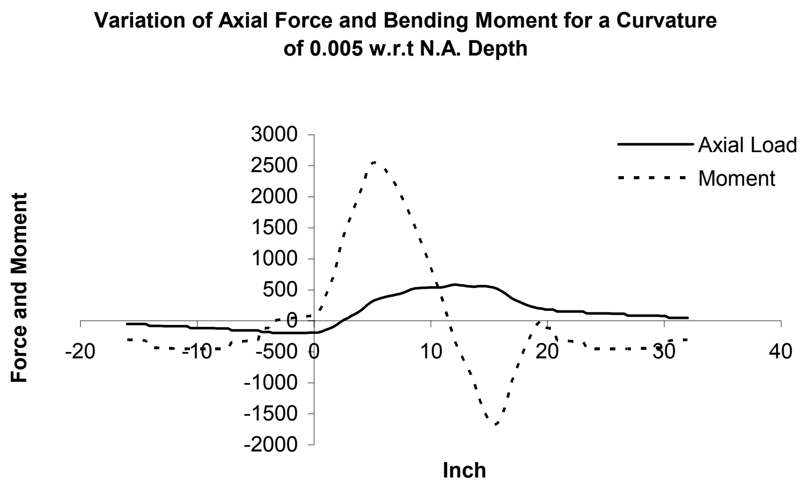

Figure 8.19 Variation of axial force (kips) and bending moment (kip-in.) for a curvature of 0.005 (1/in.) with respect to the location of neutral axis as shown in Figure 8.9 for the section shown in Figure 8.10

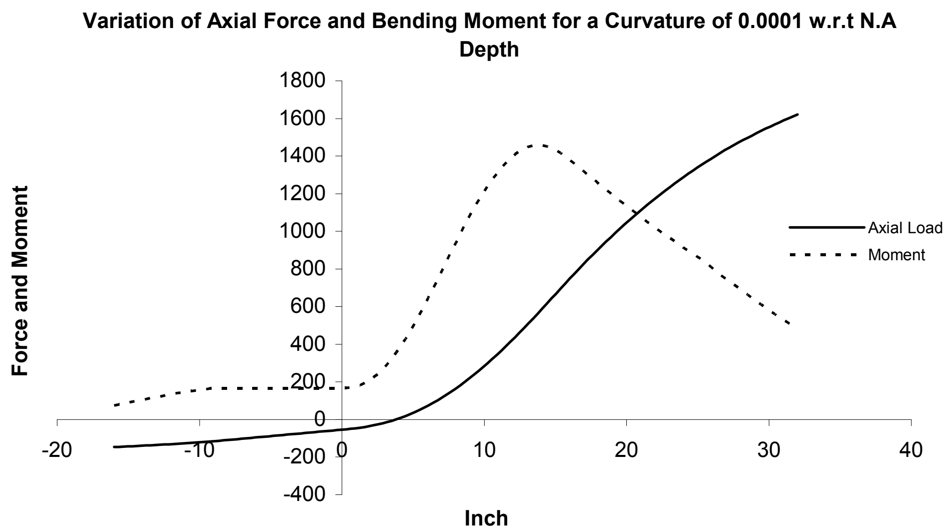

Figure 8.20 Variation of axial force (kips) and bending moment (kip-in.) for a curvature of 0.009 (1/in.) with respect to the location of neutral axis as shown in Figure 8.9 for the section shown in Figure 8.10

Variable Axial Load

In this case the level of the axial load is different for each curvature or bending moment. The variation of the axial load may be in terms of the curvature or the moment. In either case, the data should be provided in a text file, with items separated by a comma or space, as described in the USC_RC help file. Here the axial load should not exceed the allowable maximum value in the positive or negative directions, as described for the case of a fixed axial load earlier.

The process for the case when axial load varies with respect to the curvature or, in other words, when for each curvature an axial load is determined, is similar to the process for a constant axial load and a hysteretic analysis. The difference is that the axial load here is different for different curvatures, while for a constant axial load, the axial load level does not change; however, for a single point, the same process is applied.

When the axial load varies with respect to the moment, for each moment there is an axial load. The process here is to find the proper curvature and the neutral axis location, so two levels of iteration are involved. For a trial curvature, the proper neutral axis location for which the desired axial load is achieved is found. Then the corresponding moment is compared to the desired level of moment and, if necessary, another trial value for the curvature is selected and the process repeated until the desired moment is achieved. It should be noted that for the case where the pair of input data is moment and axial load, when the level of the axial load is more than the maximum, or less than the minimum, possible value for a curvature, or if the moment is more than the moment that can be tolerated under its axial load, the closest proper values to the input values are found and used in the process, and the user is notified. The data points are marked at these locations and the analytical proper values and the values provided by the user are saved in the file when the analysis results are saved.

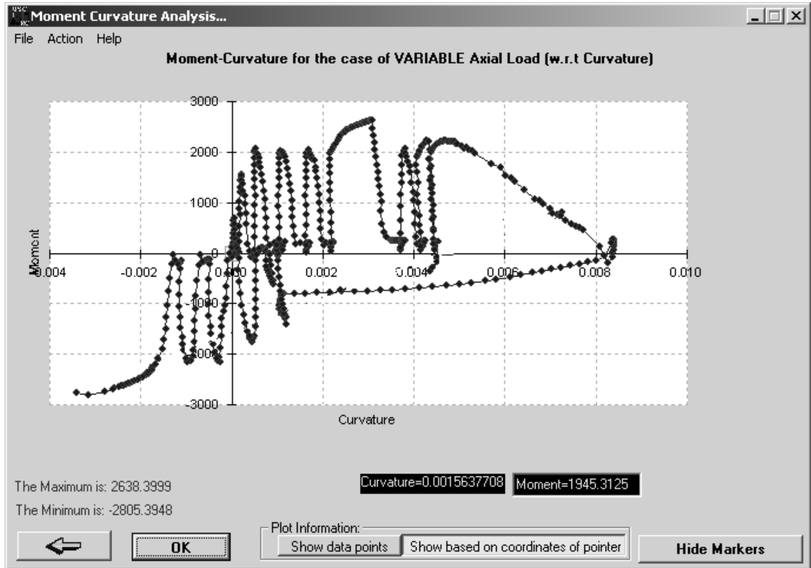

Figure 8.21 Analysis result for a case with a nonproportionally variable axial load. (Test 6, "see experimental program")

8.2.2.2 Force-Deflection Analysis

Force-deflection analysis is carried out for a cantilever case where one end of the member is fixed, without any degree of freedom, and the other end is completely free. Since the direction of the lateral force or displacement is not dynamic, or in other words, the direction of the applied lateral force or displacement remains in one plane, the free end has three degrees of freedom: lateral displacement, vertical displacement, and rotation around the axis normal to the force plane. The cross section of the member is assumed to be uniform throughout the member. Therefore, in a case of a double-curvature member where the two ends are fixed and the force is exerted on the midpoint of the member, using half of the total length in the application and doubling the result gives the desired answer. Figure 8.22 compares these two cases. In this figure, F is the lateral force, δ is the lateral displacement, N is the axial load, η is the axial deformation, α is the rotation, and L is the effective height of the column. Note that in the cantilever case (left), the bottom of the column (column-footing interface) is fixed, and no rotation or translation are allowed. The double-curvature column (right) is fixed at both ends.

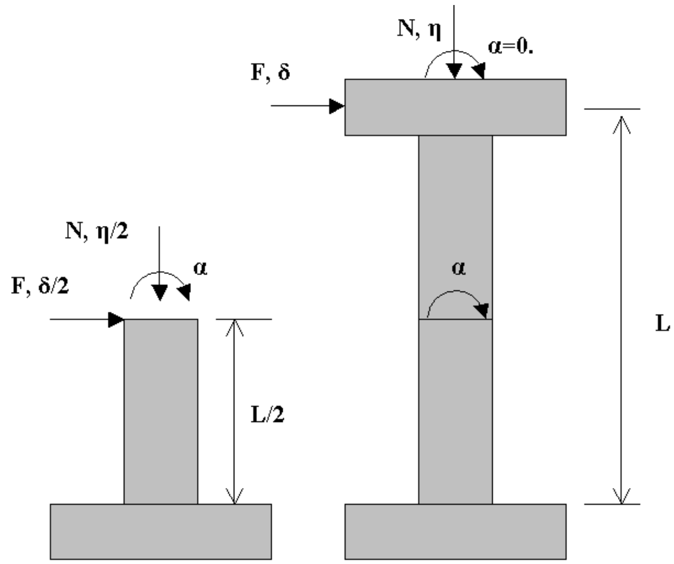

Figure 8.22 Comparison of a cantilever and double-curvature column case

Force-deflection analysis is similar to moment-curvature analysis in terms of its different types. It can be done under a fixed, proportionally variable or nonproportionally variable axial load, and a monotonic or cyclic lateral displacement or force. The nonproportional axial load may be defined in terms of lateral displacement or force.

Fixed Axial Load

For a fixed axial load case, the analysis is either monotonic or hysteretic. Before any kind of force-deflection analysis, a plastic hinge method should be selected. The existing plastic hinge methods in USC_RC are Park and Priestley's, and the author's method proposed in Chapter 2. The analysis is based on moment-curvature analysis. For each deflection and axial load, the corresponding lateral force is calculated as was described for different models of plastic hinge.

For a cyclic analysis under a fixed axial load, the history of force and deflection, and the moment curvature at the proper sections, which in turn is dependent on the stress-strain history of the fibers on the section, is employed. Since a detail of the process has been explained in moment-curvature analysis and the plastic hinge methods, it will not be restated here.

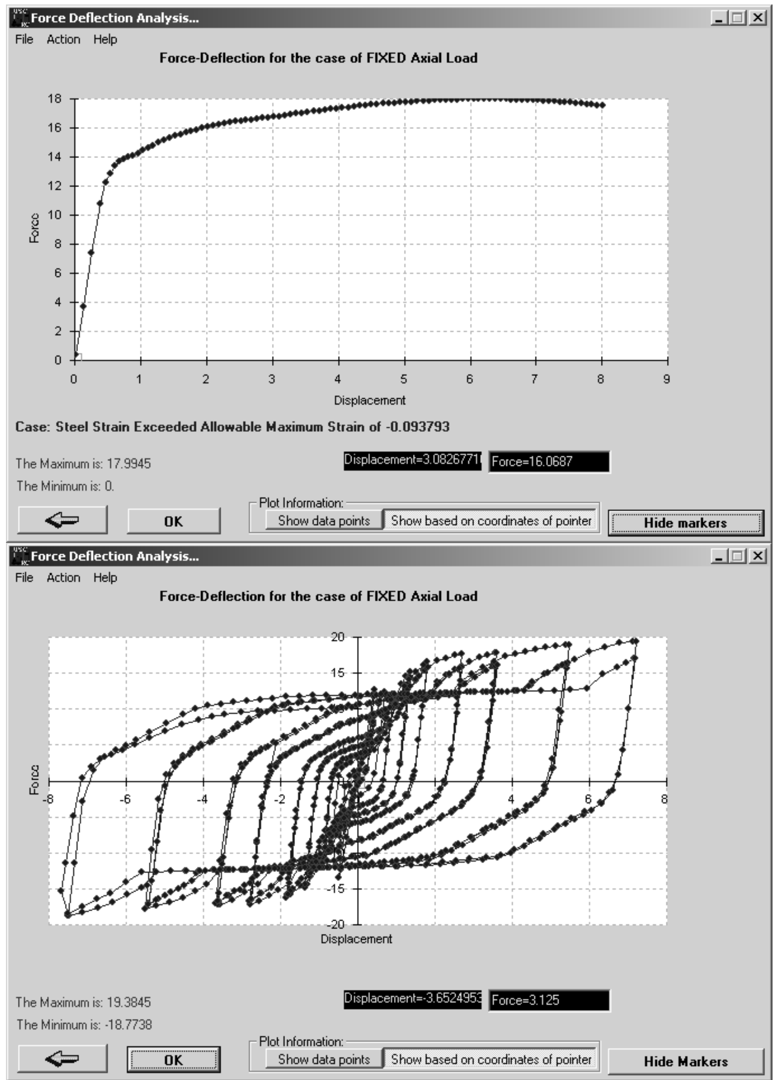

Figure 8.23 Force-deflection analysis for a case with zero axial load, and monotonic (top) and cyclic (bottom) lateral displacement

Proportionally Variable Axial Load

In this case, the axial load changes proportionally with respect to the lateral load. Since the axial load is constant throughout the column for a specific instance, the proportionality is implemented at the critical section (column-footing interface) in terms of moment. So, for a proportionality of $\frac{F}{N}$, where F is the lateral force and N is the axial load, the moment at the critical section would be FL for a cantilever column where L is the height of the column, or in other words the distance between the point of application of the lateral force and critical section. During analysis and based on the plastic hinge method under use, the curvature at the critical section determines the level of lateral force and axial load. For each curvature, the moment and axial load corresponding to this curvature are evaluated by the module used for moment-curvature analysis for a proportionally variable axial load, and then this axial load is used for moment-curvature analysis of other sections on the column at the instance.

For a cyclic lateral displacement, the history of displacement, lateral force, moment, and curvature at the proper sections on the column, based on the plastic hinge method, are used for evaluating the next step. The algorithm is similar to the algorithm used for cyclic analysis under a constant axial load, and the difference is the moment-curvature analysis algorithm implemented in each case. The moment-curvature algorithm for a force-deflection analysis under a constant axial load case is the same algorithm as used for moment-curvature analysis under a constant axial load, while for a force-deflection analysis under a proportionally variable axial load, the moment-curvature algorithm in which the axial load is proportionally variable with respect to moment is employed.

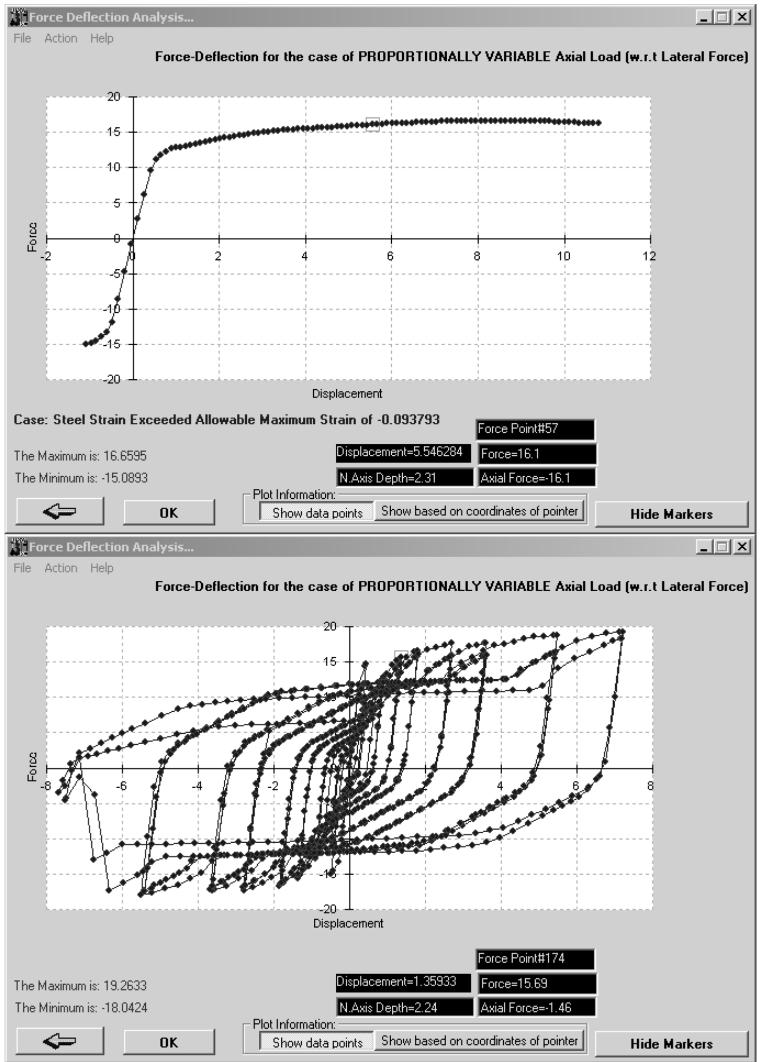

Figure 8.24 Force-deflection analysis results for a case with a lateral force to axial load proportionality ratio of –1, and a monotonic lateral displacement (top), and a ratio of –9.3 and a cyclic lateral displacement. Note the level of force and axial load for the arbitrary point on the curves.

Variable Axial Load

The variation of the axial load can be in terms of the lateral displacement or lateral force. When defined in terms of displacement, the variation for each single lateral displacement an axial load is defined and the corresponding lateral force should be evaluated. If the variation of the axial load is defined in terms of lateral force, for each single lateral force an axial load is defined and the corresponding lateral displacement should be evaluated through analysis.

The process for evaluating the lateral force for a given lateral displacement and axial load is similar to the case of cyclic analysis under a fixed axial load. The lateral force for each step is evaluated based on the previous history of displacement, force, moment, and curvature at the critical and other pertinent sections. The distinction between this case and a cyclic analysis for a fixed axial load is that the first-yield curvature and moment for each step are different from other steps due to the level of axial load. So, the plastic hinge effect for each step is different from others, while for a constant axial load, this effect is similar in terms of the level of the axial load, and the corresponding first-yield moment and curvature.

When the variation of the axial load is defined with respect to the lateral force, for each step, the corresponding moment at the critical section ($M_u = F.L$, F=Lateral Force, L=Column Height) is used to find the curvature at this section, using the moment-curvature analysis for the case of a variable axial load with respect to moment. Then, for this curvature and axial load, using previous values for displacement, force, curvature, and moment at pertinent locations on the column, the deflection is evaluated.

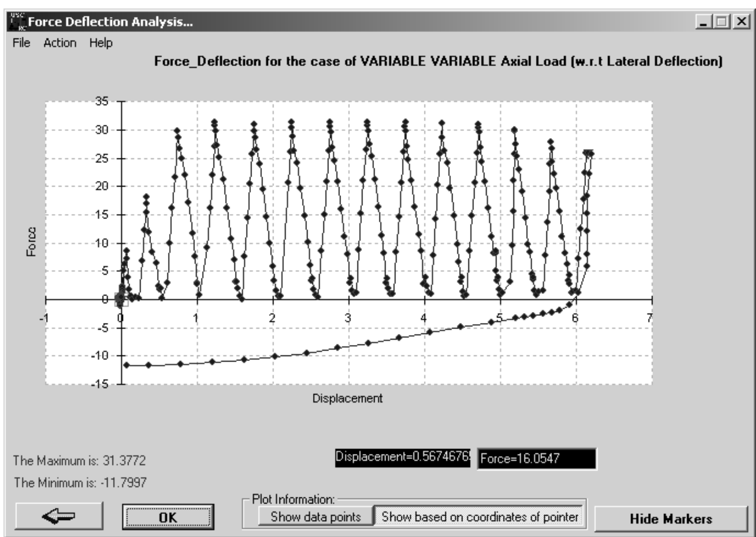

Figure 8.25 Force-deflection analysis result for a case with a variable axial load (analytical result for test 5, see experimental part)

8.2.2.3 Axial-Force Bending-Moment Interaction

The axial-force bending-moment interaction curve is evaluated based on the option selected. The method used in USC_RC is briefly explained here. For all the cases, the axial load and bending moment for each curvature are evaluated by adding the corresponding values for individual confined concrete, cover concrete, and steel fibers. For the bending moment, the force in each fiber is multiplied by the distance between the fiber and the centroid of the section.

Figure 8.26 shows the case for a certain steel strain. The strain at the location of the furthermost bar on the section is set to the steel strain for which the interaction curve is to be evaluated.

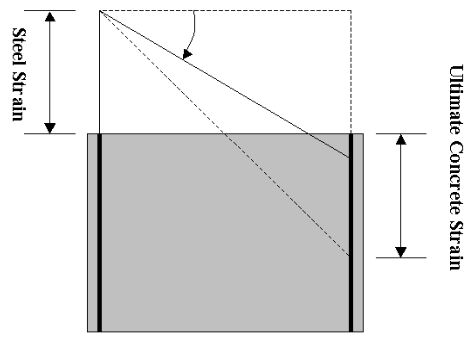

Figure 8.26 Evaluation of axial-force bending-moment interaction for a specific steel strain

Then the axial load and bending moment is evaluated on a section passing through this point. In other words, the strain at the point of the furthermost bar on this section, which serves as the center of rotation, is always kept equal to the strain for which the interaction curve is to be evaluated. Curvature of this section is changed from zero (horizontal) to a curvature where the strain at the furthermost fiber of the confined concrete on the opposite side reaches its ultimate state. So, the curvature range of variation would be:

$$0. \leq \Phi \leq \frac{\varepsilon_{steel} + \varepsilon_{u-Confined}}{D - 2C}$$

where ε_{steel} is the steel strain, $\varepsilon_{u-Confined}$ is the ultimate confined concrete strain, D is the section depth in the direction of analysis, and C is the cover thickness.

When the axial-force bending-moment interaction curve is to be evaluated for a specific strain of confined concrete, the strain at the furthermost fiber on the section is set to that strain, as shown in Figure 8.27, and then the axial force and bending moment are calculated on a section passing through this point as the center of rotation, for different curvatures. The curvature in this case varies as follows:

$$0. \leq \Phi \leq \frac{\varepsilon_{u-steel} + \varepsilon_{Confined}}{D - 2C}$$

where $\varepsilon_{u-steel}$ is the ultimate steel strain, (equal to $K_3\varepsilon_y$ in USC_RC), $\varepsilon_{Confined}$ is the confined concrete strain for which the interaction curve is to be evaluated, D is the section depth, and C the cover concrete thickness.

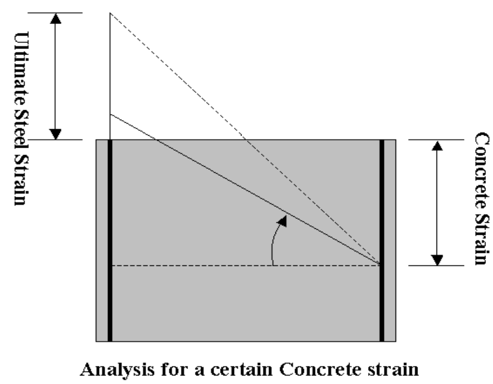

Figure 8.27 Evaluation of axial-force bending-moment interaction curve for a certain confined concrete strain

For the "engineering interaction curve," the confined concrete strain is limited to the strain corresponding to the ultimate strength of the confined concrete, and the steel strain is limited to the yield strain. Figure 8.28 shows the variation of curvature for this case. The center of rotation is first on the furthermost bar on the section and a strain equal to the yield strain of steel. The curvature of the section is then varied from zero that where the strain on the furthermost confined concrete fiber on the opposite side reaches a strain corresponding to the ultimate strength of confined concrete. Then the center of rotation is switched to this point, and the strain on the fiber is kept at this strain and the section curvature is changed from its existing value to zero.

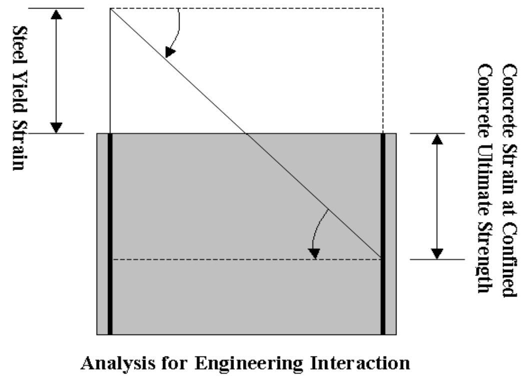

Figure 8.28 Variation of curvature for evaluating the engineering interaction in USC_RC

The variation of curvature in this case is as follows:

$$0. \leq \Phi \leq \frac{\varepsilon_y + \varepsilon_{cc}}{D-2C} \qquad \text{(center of rotation on left side)}$$

$$\frac{\varepsilon_y + \varepsilon_{cc}}{D-2C} \leq \Phi \leq 0. \qquad \text{(center of rotation on right side)}$$

where ε_y is the yield strain of steel and ε_{cc} is the confined concrete strain corresponding to its ultimate strength.

8.2.2.4 USC Viewer, a Byproduct Application

As was stated in viewing the hysteretic response of material, the user of the USC_RC application can examine the hysteretic response of steel, confined and unconfined concrete in an interactive interface where some of the hysteretic parameters for steel can be adjusted. This feature in general can be used to view the response of any system in a two-dimensional space. At the time the USC_RC application was developed, some timber structures were being tested for another project. One of the analytical parts of that research was a hysteretic model developed for the hysteretic response of one of the timber structure. Examining the model for different paths of displacement or strain required providing a data file for a predetermined displacement or strain path, running the program for the model using this pattern, and then viewing the results using other applications such as Excel. Examining the model for every pattern requires all these steps. One of the researchers suggested putting the aforesaid feature of the USC_RC in a separate, small application so that any material model or system response could be viewed for any arbitrary displacement or strain path without the necessity of going through all the steps.

The result, the "USC_Viewer," is actually a fully functional interactive interface for viewing the response of any material or system in a two-dimensional space. The user provides the model for the material or the system, as clearly stated in the help manual. As soon as the model is coded, as should be done anyway, its response can be viewed and examined just by moving the mouse appropriately and the response curve will be plotted. Figure 8.29 shows the main window of the USC_Viewer showing an instance of the default model, provided as a hint for the user.

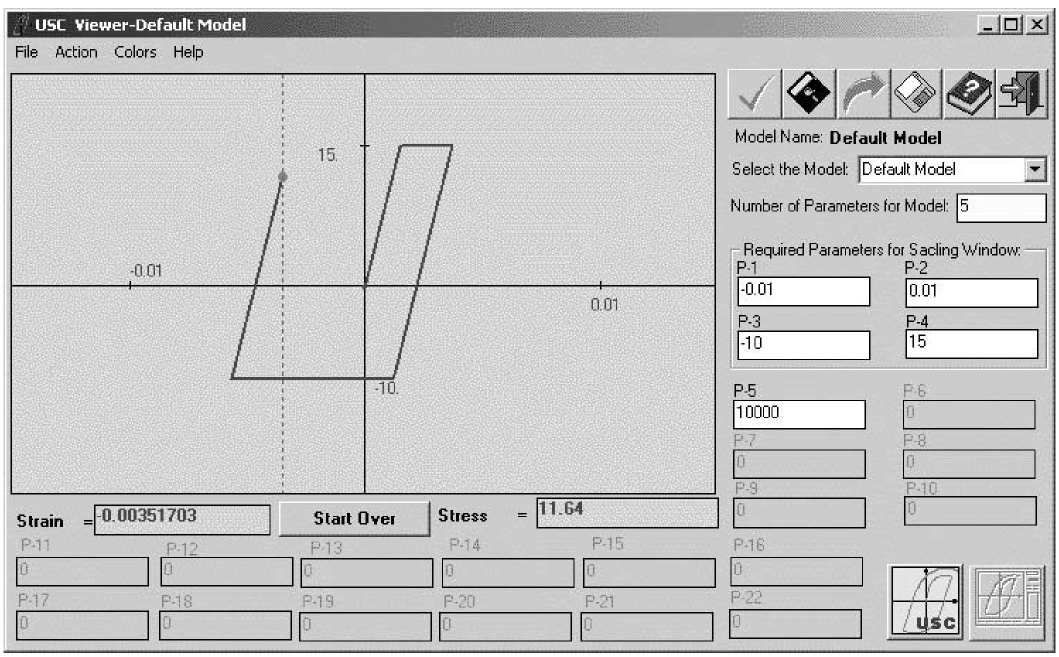

Figure 8.29 Main window of the USC_Viewer, showing an instance of the default model

This small application can be used to examine and view 11 different models at the same time. Each model can have up to 22 different parameters that can be set by the user as needed. Each single model can be saved with the corresponding parameters, and the responses can be saved as a data file or a graph. The last-used parameters for each model are automatically saved for each model and loaded whenever that model is chosen in the future. The names and labels for each model can be change accordingly. These changes will be effective as long as the user changes them again. The application has many other features for a proper interaction and viewing of a model, saving the data and switching between different models. All the features and explanations can be viewed by installing the USC_Viewer from the installation CD or downloading from *http://www-scf.usc.edu/~esmaeily*, running the application, and reading the context-sensitive help whenever needed. In Figure 8.30 the same instance of the default model is viewed in the enlarged viewing window. USC_Viewer is capable of providing a window as large as the screen for a better and detailed examination of the response.

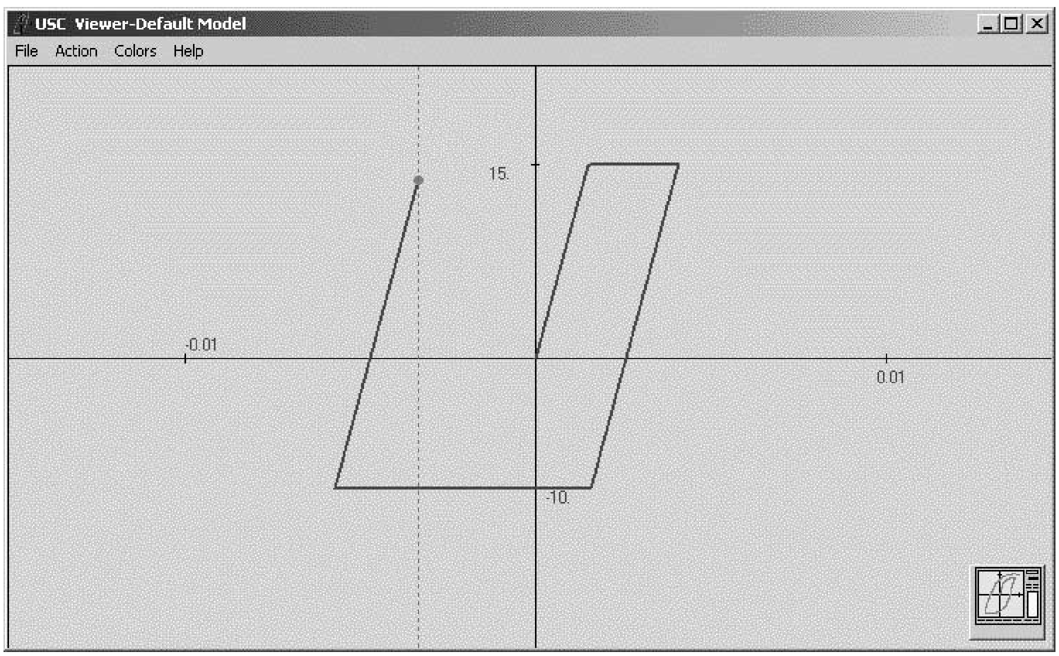

Figure 8.30 The same instance of the default model as in Figure 8.29 in the enlarged viewing window

9 Comparison of Experimental and Analytical Results

In this chapter the test results for the six tests are compared with the analytical results obtained by the USC_RC application. Because of the importance of material models and analytical methods in generating results close to experimental data, the parameters to model the stress-strain response of material have been selected for good compatibility with the test results. The model used for the monotonic stress-strain response of confined and unconfined concrete is the model proposed by Mander et al., as described earlier in detail. The results of material tests on 12 samples of concrete specimens determined the values used in the model for concrete strength. The model developed by the author simulates the monotonic stress-strain response of steel. This model simulates the strain hardening behavior of steel and has the flexibility to be used for roughly modeling any steel monotonic stress-strain curve. Also, models for the hysteretic response of steel, confined, and unconfined concrete were developed by the author and used to simulate the hysteretic response of steel and concrete. The parameters have been adjusted based on the tests of the material in the structural lab at USC.

9.1 MOMENT-CURVATURE RESPONSE

Figure 9.1 shows the moment-curvature response of the first specimen at segment one compared with the analytical curve. Note that the analytical moment-curvature response has been evaluated by USC_RC, the software developed for the analysis of RC members under various loading conditions. Moment-curvature analysis is based on a fiber model, as discussed in a previous chapter, and the section is divided into 100 confined and unconfined concrete fibers in the direction of the applied curvature or moment. The steel fibers on the section are the actual bars in their respective positions and cross-section areas.

The analytical response can be predicted by two approaches. The first approach, for the case in Figure 9.1, does the hysteretic analysis for a variable axial load case, where the curvature pattern and the axial load at any curvature are given as input data for analysis. In such a case, the actual axial load for each single curvature that occurred during testing is provided as input. The second approach considers a fixed axial load and provides it as a constant value for all the curvatures and provides only the curvature path as the input. In this case, the true axial load for each single curvature may be different within a small percentage compared with the fixed level used in the program. The difference in predicted values, however, is negligible as shown in Figure 9.2. The predictions compared to experimental results are conservative, especially for high curvatures, which has been the case for a high level of axial load. This issue will be discussed more when examining the response of other tests under different loading and displacement patterns.

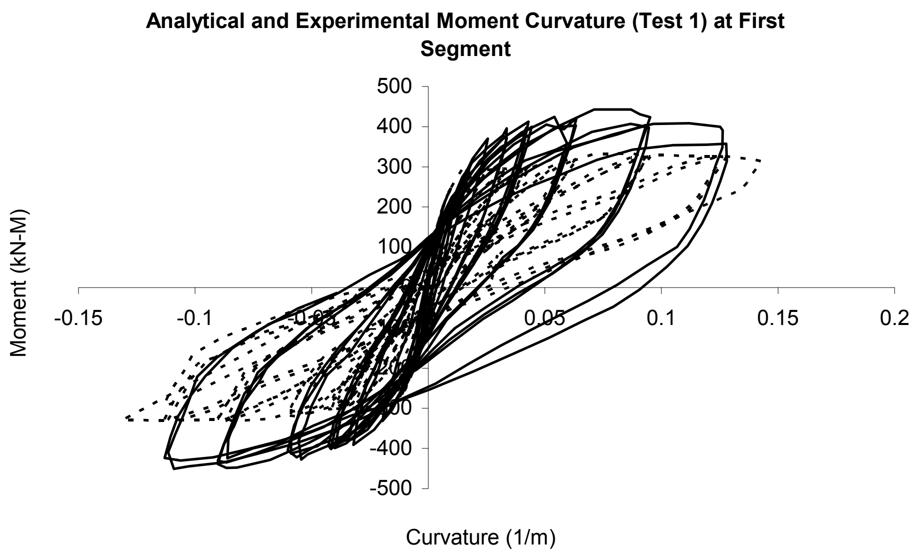

Figure 9.1 Analytical and experimental moment curvature of specimen one

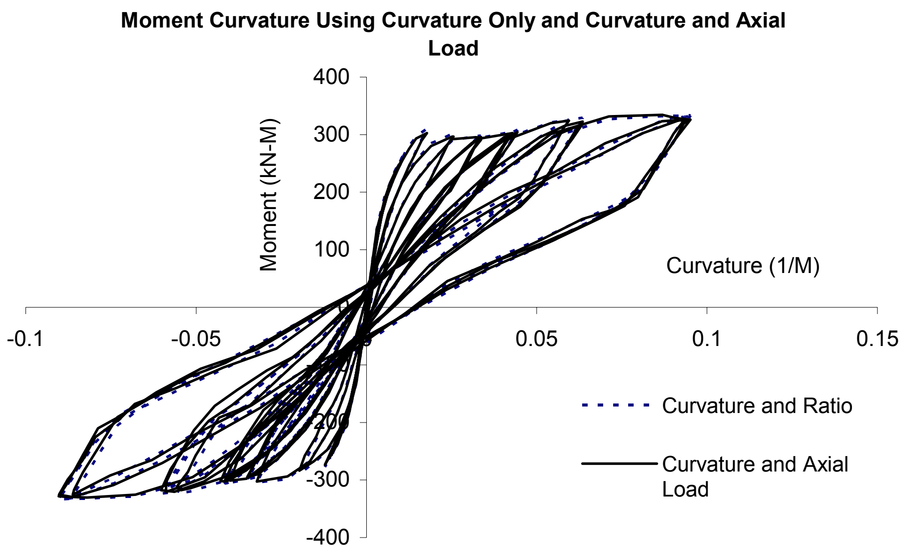

Figure 9.2 Evaluation of analytical response of test one using curvature path and axial load as input data, and using curvature path as input data with a single axial load of 460 kips

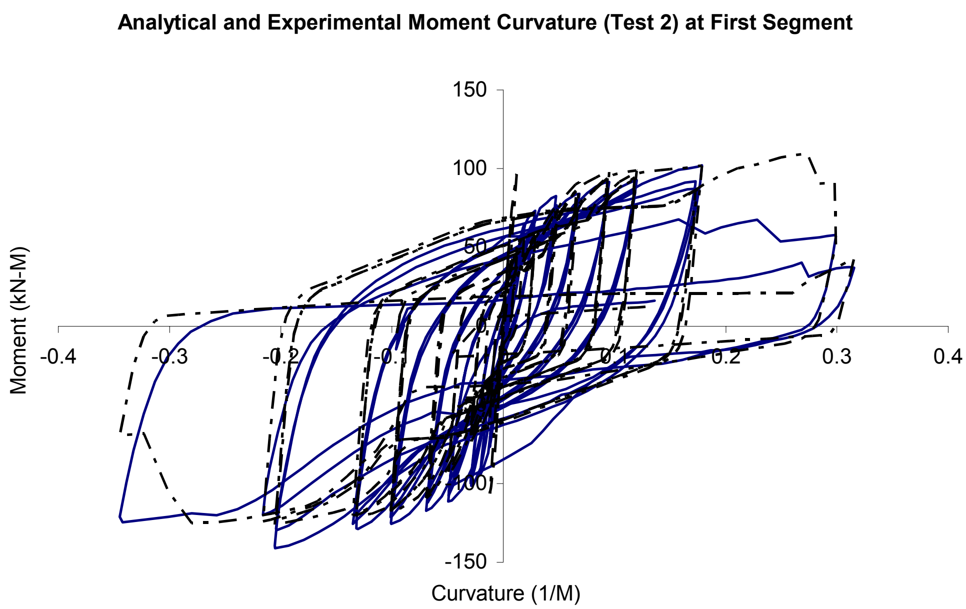

Figure 9.3 Analytical and experimental moment curvature of specimen two

Figure 9.3 shows the experimental moment-curvature curve at the first segment and the analytical output of USC_RC for the case considering a variable axial load proportional to the applied horizontal load. Compared to the experimental results, the analytical results are slightly conservative for the compressive axial load but close for the tensile axial load. The analytical curve has been evaluated by providing the curvature and corresponding axial load for each curvature. Another approach to evaluate the analytical moment curvature is in providing the proportionality ratio and the curvature path. Here the proportionality ratio or moment to axial load is –66.67. Figure 9.4 compares the analytical results for test 2 using the two approaches. The solid curve is for the case where the curvature path and axial load have been provided as input data for analysis, and the dotted curve shows the case when the curvature path has been provided as input data using a single proportionality value.

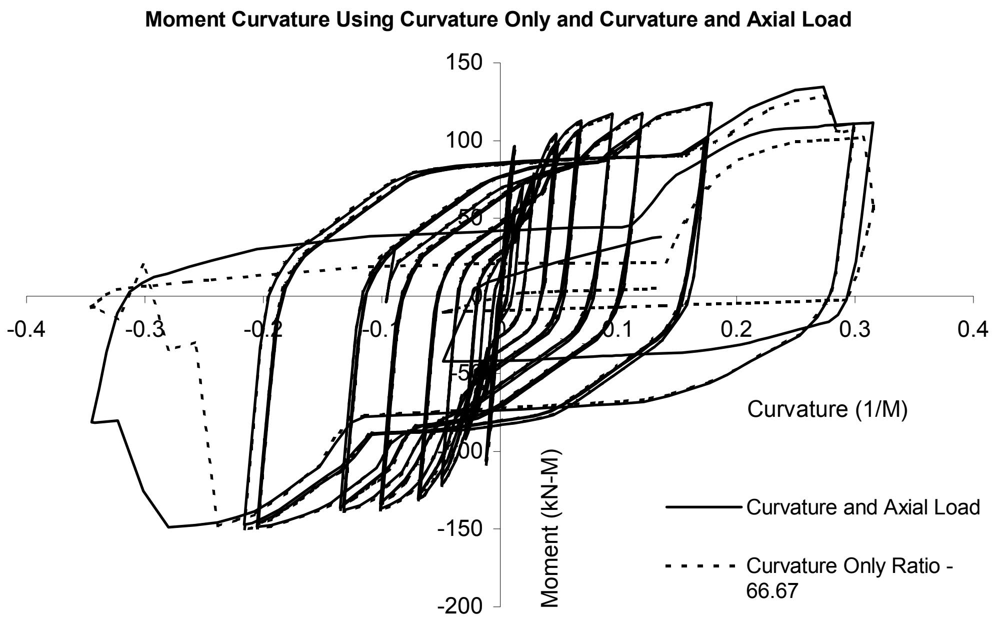

Figure 9.4 Comparing analytical moment curvatures for test 2, using proportionality value and curvature path, and using curvature path and corresponding axial load for each curvature

Figure 9.5 shows the comparison of the moment-curvature response of specimen three at the first segment with the analytical results for the case. The difference between the slope of the two curves at the beginning is because the experimental curve has been plotted based on the data from the measurements at the first segment, which is closest to the column-footing interface and includes the pull-out effect of the bars, while the analytical curve has been evaluated without this effect.

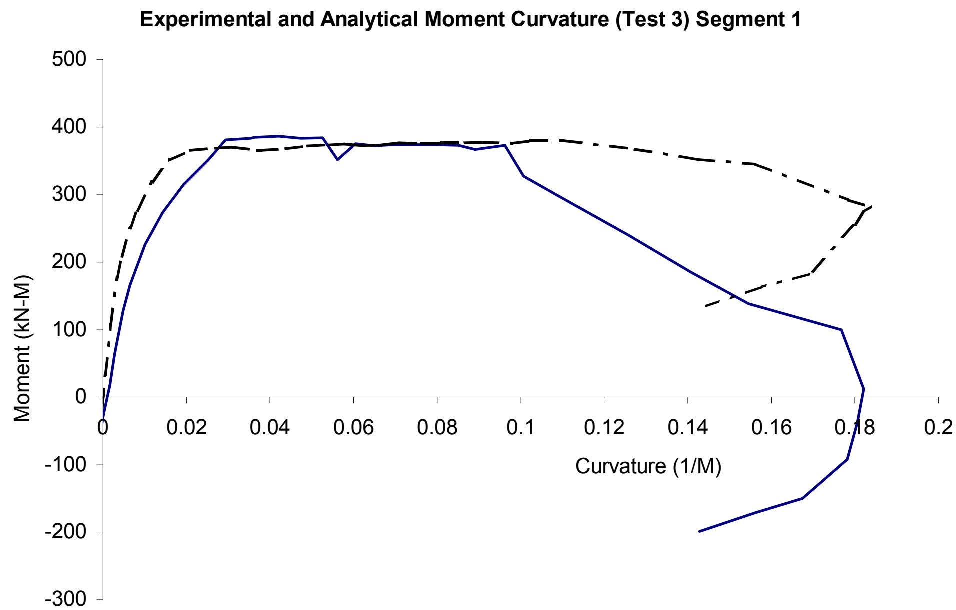

Figure 9.5 Analytical and experimental moment curvature of specimen three

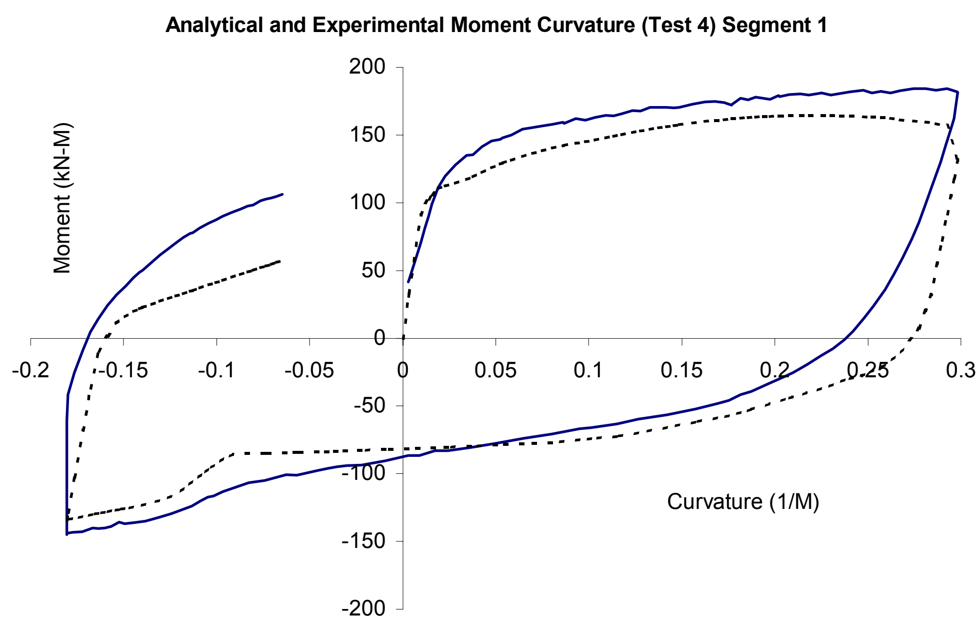

Figure 9.6 Analytical and experimental moment curvature of specimen four

Figure 9.6 shows the moment-curvature response of specimen four at the first segment. The dotted curve is the analytical value for the specimen under the same loading and displacement conditions. The slope of the curve within the first yield is slightly different compared to the analytical results. The reason is the same as for test 3.

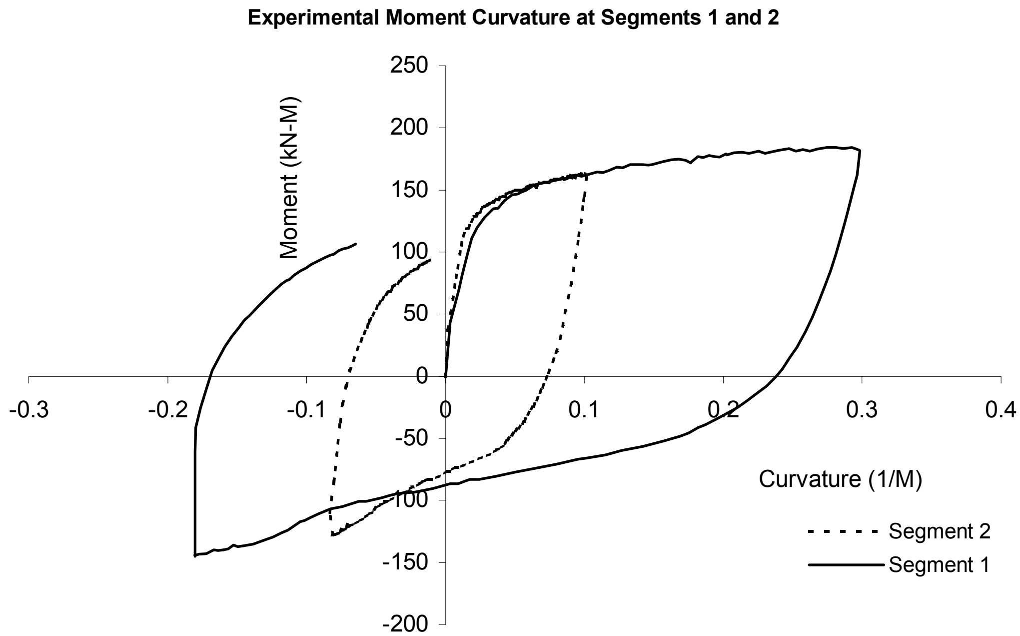

Figure 9.7 Comparison of experimental moment curvature at segments one and two

The experimental curve was plotted based on the data recorded on the first segment of the specimen. This is the segment close to the column-footing interface, and the rotation caused by the pull-out action of the bars is included in the recorded data. So, as the curvature increases, the stress in the furthermost bar increases also, leading to an increase in the rotation caused by the pull-out action of the bars. This difference is zero at the beginning when there is no tensile stress in the bar and increases with tensile stress. Figure 9.7 shows the experimental moment curvature at segments one and two. As expected, the initial difference due to the aforesaid fact is shown for test 4.

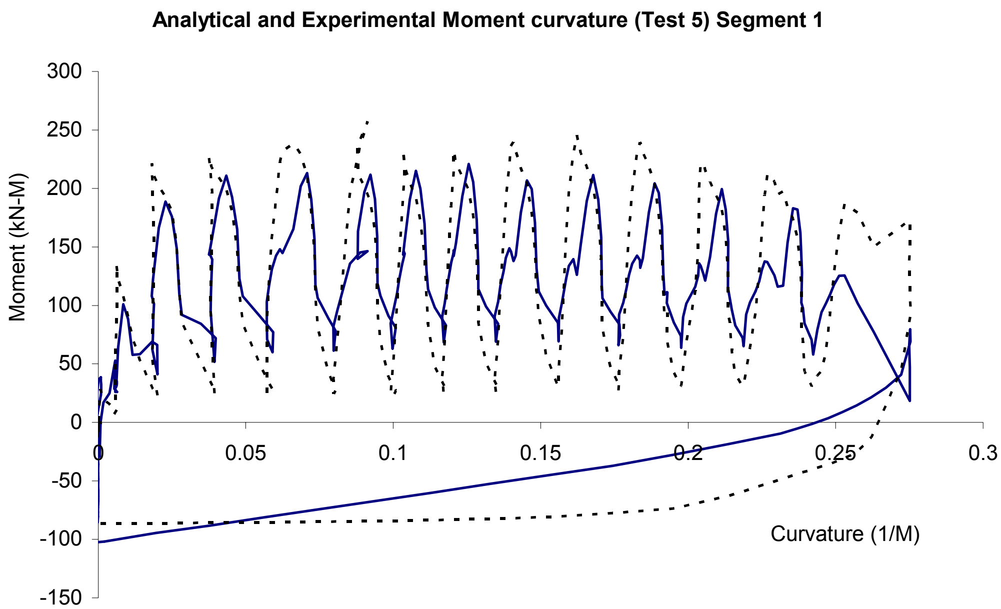

Figure 9.8 Analytical and experimental moment curvature of specimen five

The analytical and experimental moment-curvature responses of specimens five are shown in Figure 9.8. This test was under a variable axial load. The variation of the axial load with respect to the average curvature on the first segment of the specimen is shown in Figure 9.9. The analytical predictions are conservative for a negative (tensile) axial load, while overestimating the flexural strength for a positive (compressive) axial load. This is completely contrary to the observations in previous tests, where the analytical predictions for compressive axial load cases were conservative compared to test results. The reason for this phenomenon may be that in the case of a fixed axial load, the section has already experienced the full level of axial load without any curvature and the confinement is utilized at its highest possible level under this axial load; while in this case, the full axial load is reached at a specific curvature where only a part of the section is under compression. So, it is obvious that the effect of confinement and therefore the capacity will be lower than for the analytical prediction in which no difference is considered between this case and a fixed axial load in terms of the aforesaid condition.

On the other hand, as shown in Figure 9.8, the analysis underestimates the capacity for a tensile axial load, while we have seen for the tests under a relatively constant axial load the predictions are close to test results. The reason for this phenomenon may be similar to what was stated for a compressive axial load. It may be because for a case of constant axial load and at the peak tensile value, the whole steel experiences the same strain when there is no curvature, and then when the curvature is applied, one side has a return strain and the strain at the other side grows, while for a varying axial load there is no reversal strain in any side of the section. This may cause the steel to provide more strength when compared to the constant axial load case.

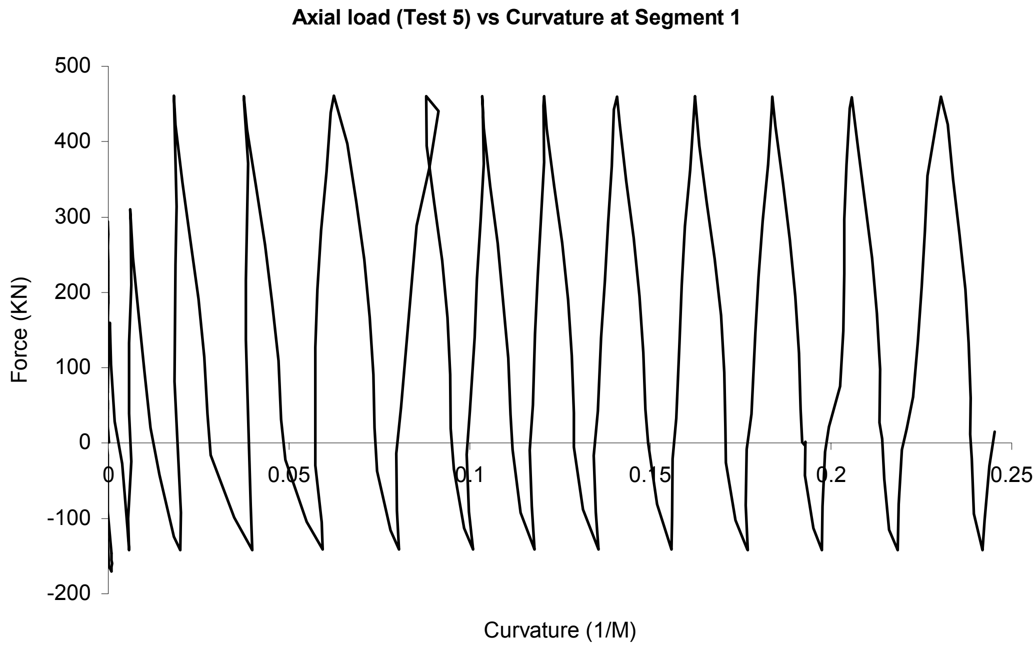

Figure 9.9 Variation of axial load with respect to the average curvature at the first segment for test 5

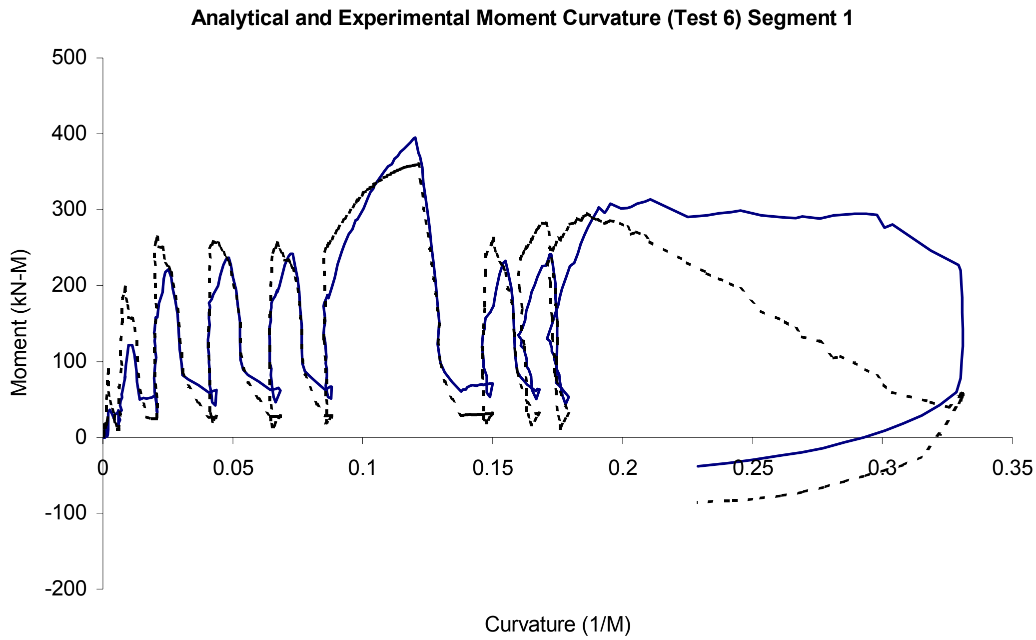

Figure 9.10 Analytical and experimental moment curvature of specimen six

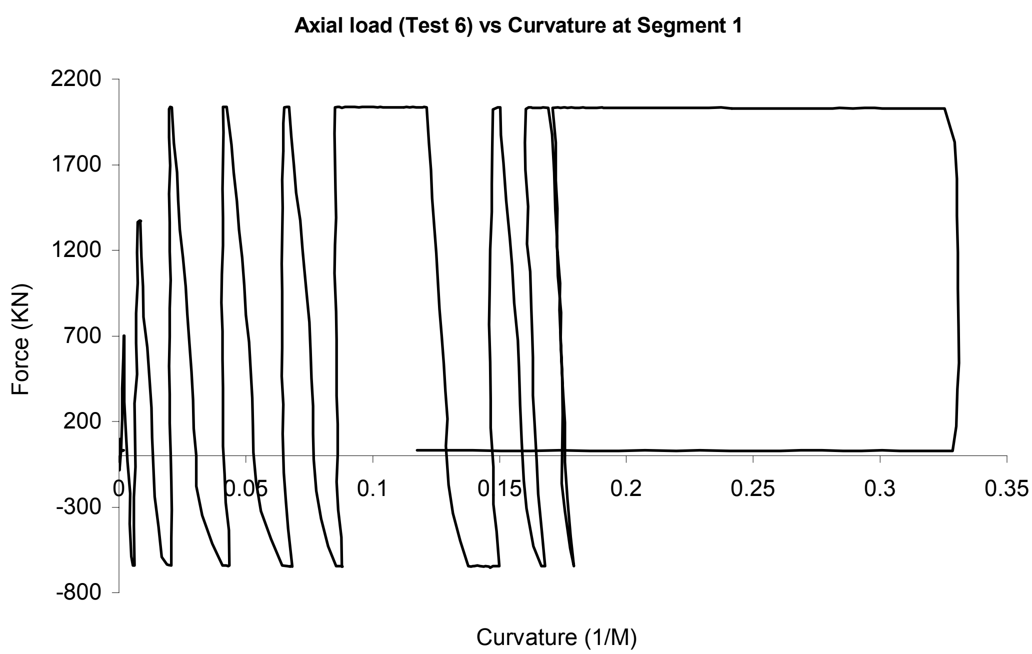

Figure 9.11 Variation of axial load with respect to the average curvature at the first segment for test 6

Figure 9.10 shows the experimental moment-curvature results at the first segment of test 6 compared to the analytical results under the same axial load variation and lateral displacement conditions. Figure 9.11 shows the pattern of axial load with respect to the curvature for this test. The axial load pattern in this test is different from that of in test 5 only in terms of the local stops at peak points, but this difference has caused a relatively significant difference in the response of the two specimens. During the few initial cycles of axial load that are identical for both specimens, the same response pattern is observed for both tests and the analytical and experimental responses are identical, while in test 6 the small difference in the pattern of the axial load caused a completely different response in this test, where the analytical results for the compressive axial load underestimate the capacity.

9.2 HORIZONTAL FORCE-DEFLECTION RESPONSE

The horizontal force-deflection analysis was based on the moment-curvature analysis for the sections as required for each plastic hinge method used in the analysis. Two plastic hinge methods were used for each case to examine the differences. The first is the method developed and used in the USC_RC application, as plastic hinge method 2, and the other method is that method proposed by Park and Priestley as a commonly used plastic hinge method for flexural deflection analysis. The analysis methods and details of the Park and Priestley, and USC_RC plastic hinge methods have been described in previous chapters.

The analytical and experimental horizontal force-deflection responses of specimen one are compared in Figure 9.12 and Figure 9.13. The analytical predictions are conservative compared to the experimental results. The analytical results in Figure 9.12 are evaluated using the plastic hinge method developed and used in the USC_RC application, while in the latter figure the plastic hinge proposed by Park and Priestley has been used. The difference between the analytical predictions using the two different plastic hinge methods is negligible in this case.

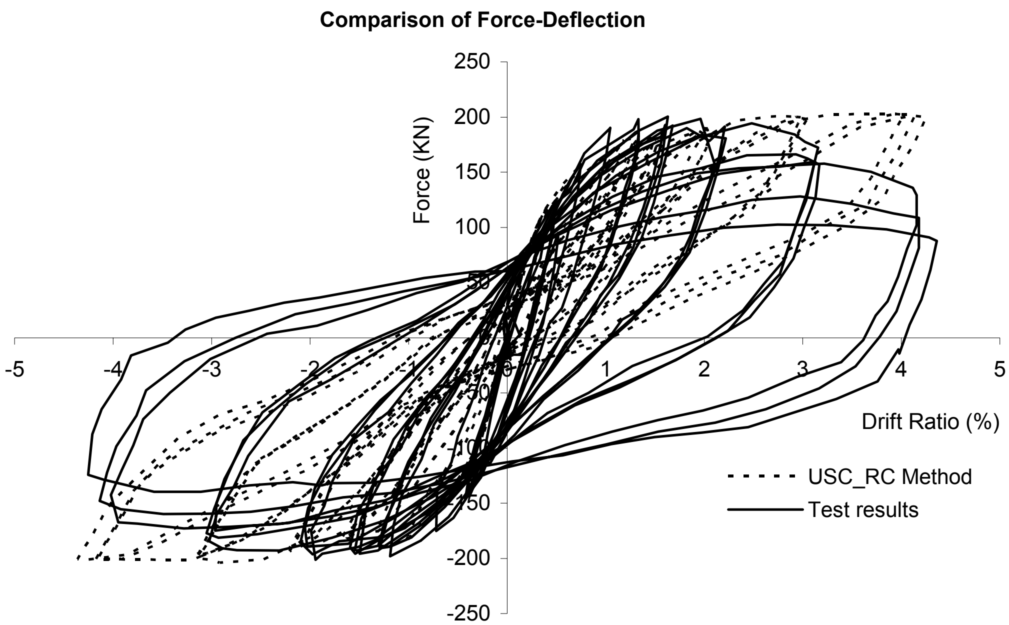

Figure 9.12 Comparison of experimental and analytical force-deflection response of specimen one, using the USC_RC plastic hinge method 2

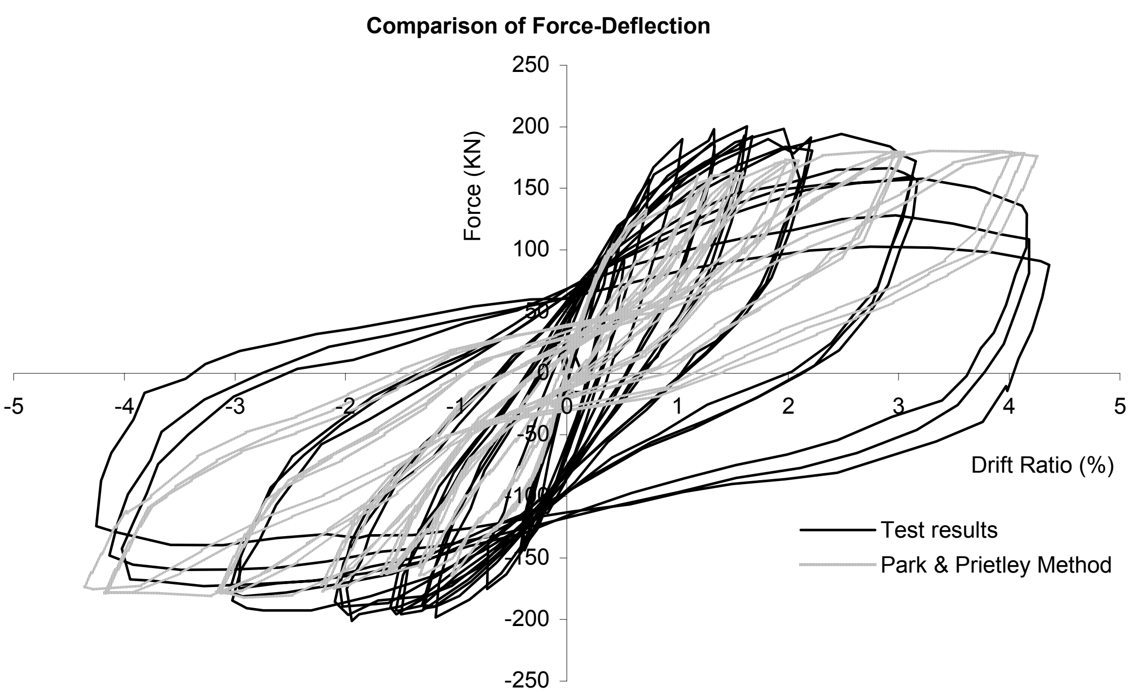

Figure 9.13 Comparison of experimental and analytical force-deflection response of specimen one, using the plastic hinge method proposed by Park and Priestley

Figure 9.14 compares the analytical and experimental results for test two where the axial load was proportionally variable with respect to the lateral force. The plastic hinge method used for the analytical evaluation in Figure 9.14 was the method developed in USC_RC, while for the analytical curve in Figure 9.15, the method proposed by Park and Priestley has been applied. In this case, the difference between the analytical results for these two methods is negligible. The prediction in the pull direction where a compressive axial load was involved is conservative, while in the push direction with a negative or tensile axial load the analytical predictions and experimental results are close.

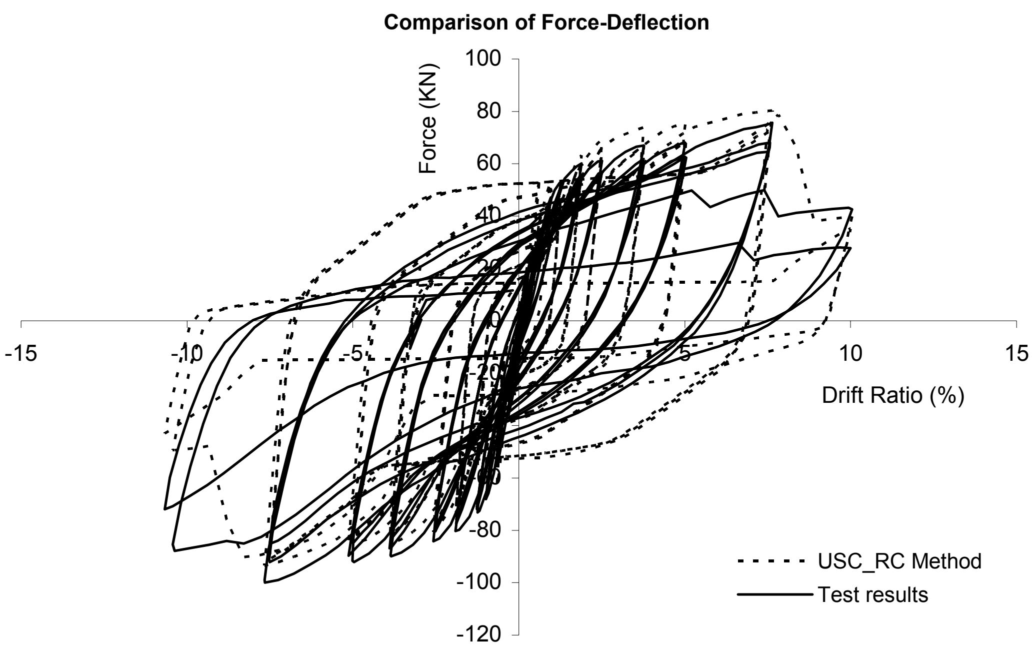

Figure 9.14 Comparison of experimental and analytical force-deflection response of specimen two, using the USC_RC plastic hinge method 2

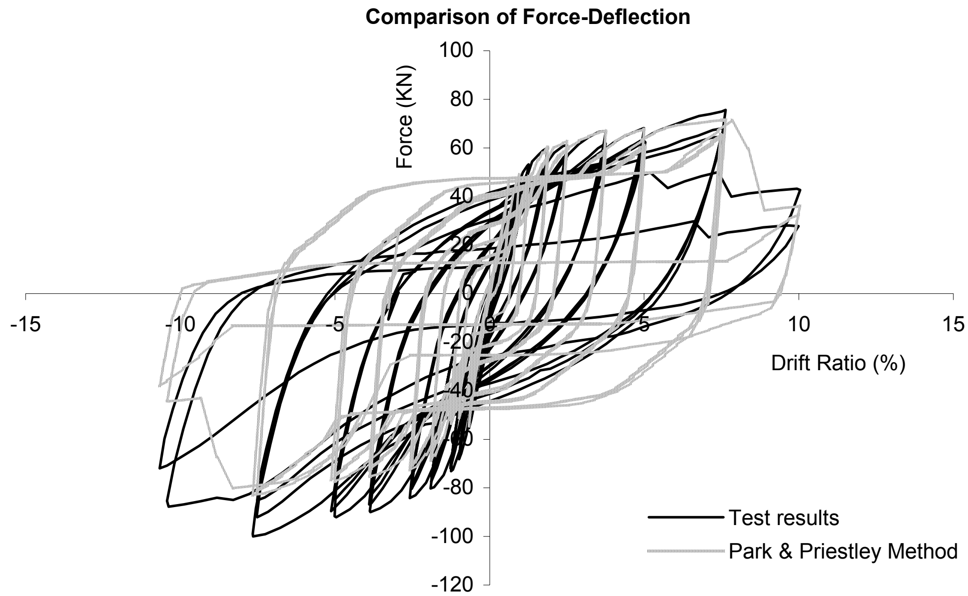

Figure 9.15 Comparison of experimental and analytical force-deflection response of specimen two, using the plastic hinge method proposed by Park and Priestley

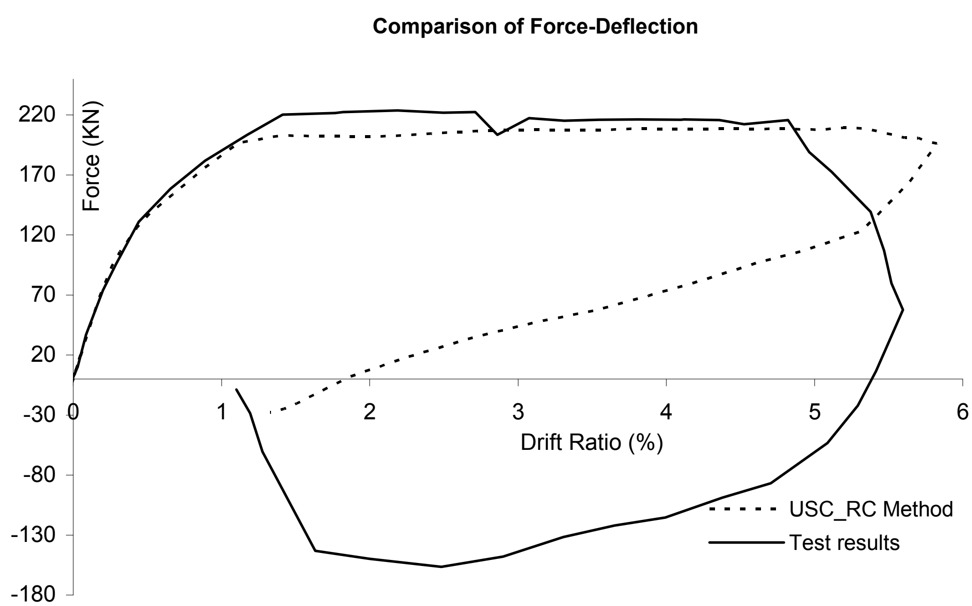

Figure 9.16 Comparison of experimental and analytical force-deflection response of specimen three, using the USC_RC plastic hinge method 2

The experimental results are compared with the analytical results in Figure 9.16 and Figure 9.17 using the two different plastic hinge methods for test 3. The USC_RC plastic hinge method predicts the results better than the Park and Priestley plastic hinge method, but in both cases the analytical results are lower than in the experimental results.

Figure 9.18 compares the experimental force-deflection curve with the analytical results using the USC_RC plastic hinge method for test 4. No axial load has been applied in this case, and a monotonic lateral displacement has been applied up to a drift ratio of 10% and then reversed to a drift ratio close to –10% and then back to zero.

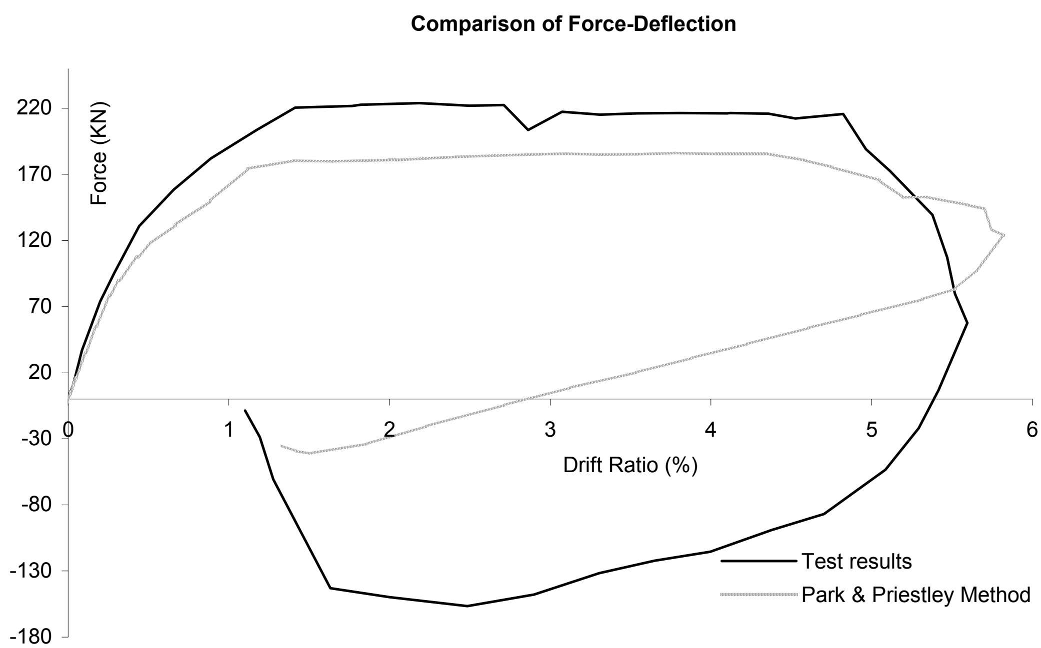

Figure 9.17 Comparison of experimental and analytical force-deflection response of specimen three, using the plastic hinge method proposed by Park and Priestley

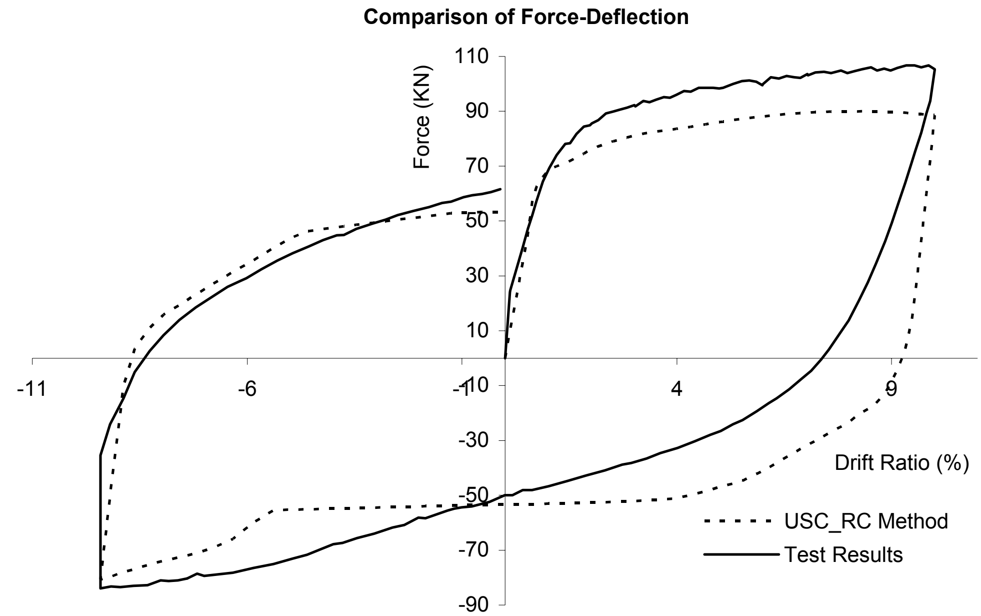

Figure 9.18 Comparison of experimental and analytical force-deflection response of specimen four, using the USC_RC plastic hinge method 2

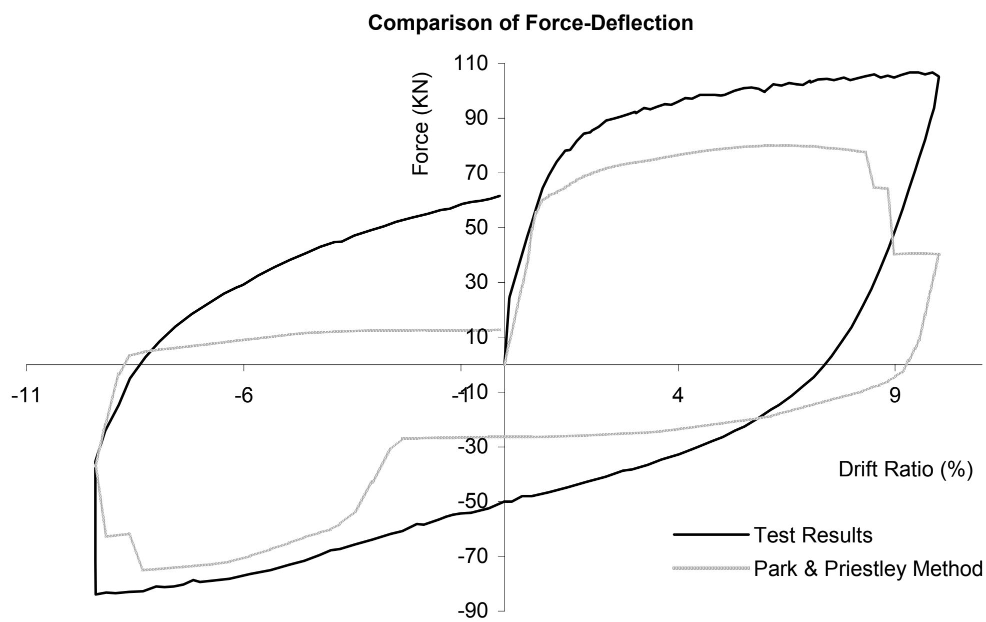

Figure 9.19 Comparison of experimental and analytical force-deflection response of specimen four, using the plastic hinge method proposed by Park and Priestley

In Figure 9.19 the same comparison is made between the experimental and analytical results of test 4, using the plastic hinge method proposed by Park and Priestley. Figures comparing the force-deflections by the two plastic hinge methods show that the USC_RC method provides better prediction than the Park and Priestley method. The reason for this is that in the USC_RC method, the change of the plastic hinge length for various levels of lateral force was considered, while no variation in length was considered in the Park and Priestley method under any loading condition.

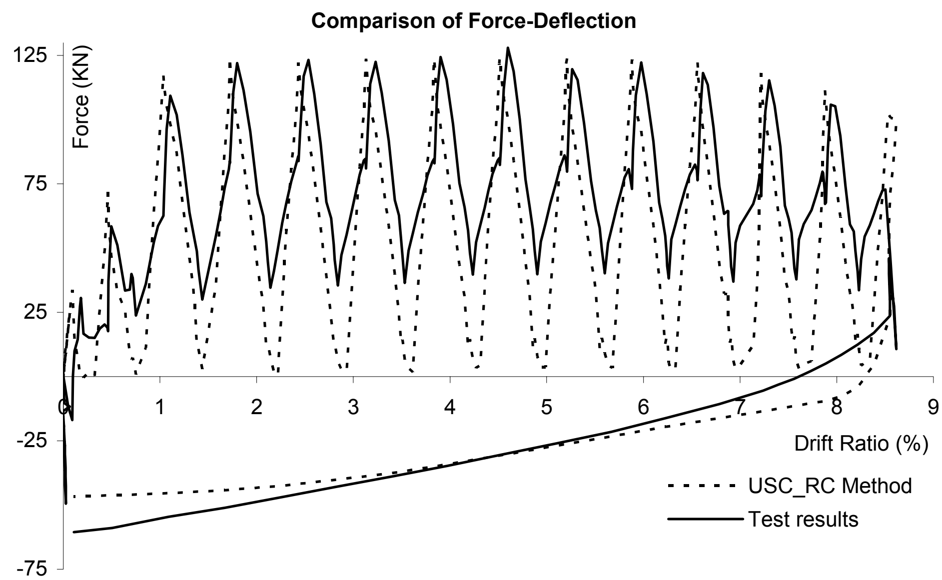

Figure 9.20 Comparison of experimental and analytical force-deflection response of specimen five, using the USC_RC plastic hinge method 2

Figure 9.20 compares the experimental results for test five with the analytical results using the USC_RC plastic hinge method. The analytical results using the Park and Priestley method for this specimen are compared with the experimental results in Figure 9.21.

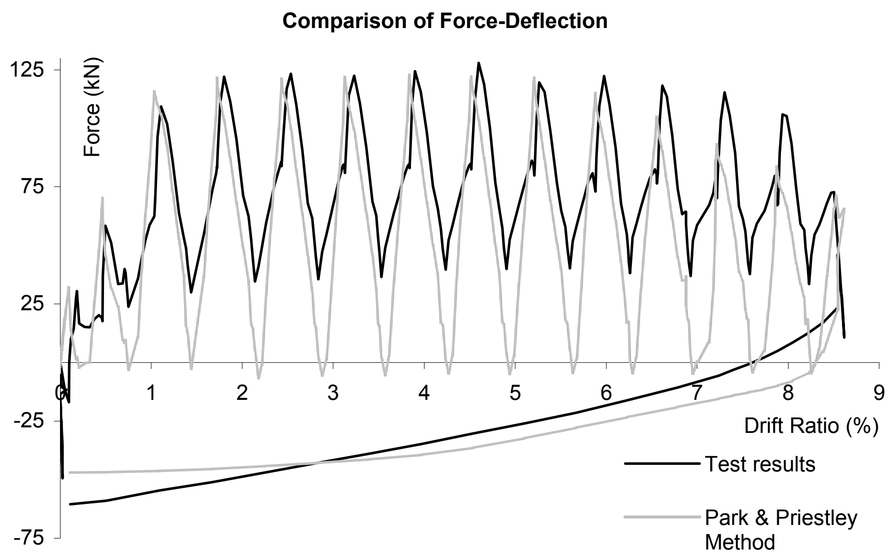

Figure 9.21 Comparison of experimental and analytical force-deflection response of specimen five, using the plastic hinge method proposed by Park and Priestley

Predictions using the USC_RC plastic hinge method seem to be in better agreement with the experimental results. The trend of strength degradation is more consistent with the experimental curve. Also, even if in both methods the strength is underestimated for peak tensile axial loads, the results yielded by the USC_RC method are closer to the experimental values at these points.

The experimental force-deflection response of specimen six is compared with the analytical results using the USC_RC plastic hinge method, in Figure 9.22. Figure 9.23 shows this comparison when the Park and Priestley method for a plastic hinge was used for evaluating the analytical results. Here again, the results from the USC_RC plastic hinge method better agree with the experimental results than those from the Park and Priestley method.

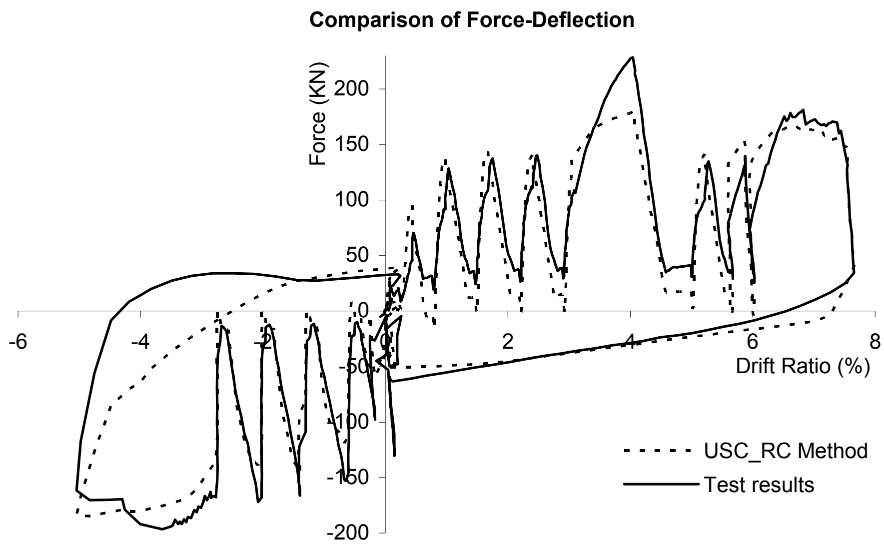

Figure 9.22 Comparison of experimental and analytical force-deflection response of specimen six, using the USC_RC plastic hinge method 2

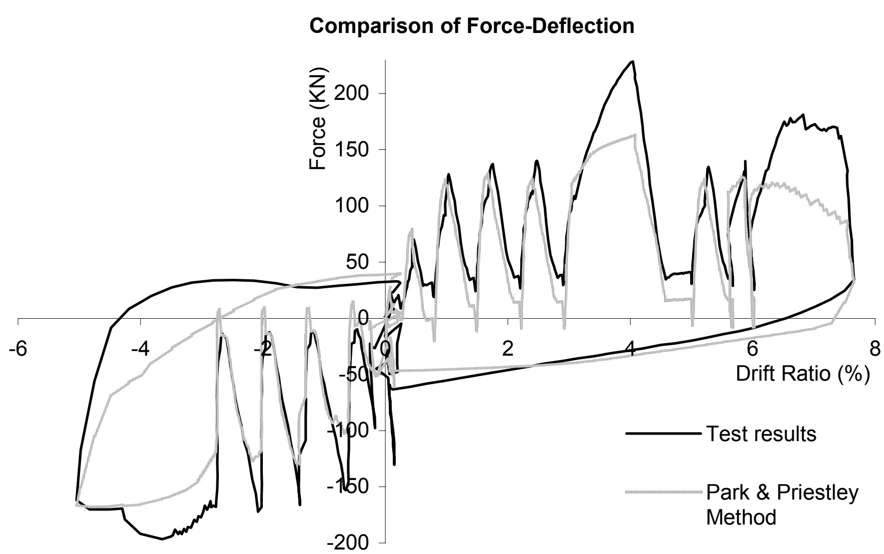

Figure 9.23 Comparison of experimental and analytical force-deflection response of specimen six, using the plastic hinge method proposed by Park and Priestley

10 Summary and Conclusions

Six scaled RC bridge columns with circular sections were tested at the USC Structural Lab as a part of an experimental program investigating the effects of a variable axial load on the seismic behavior of bridge piers. The primary experimental parameters were the axial load and loading pattern. The objectives of the overall research program on the seismic behavior of bridge piers, it required testing several specimens under specific loading patterns, in addition to the cases with a constant axial load, and a proportionally variable axial load. To achieve a predetermined loading pattern in a test, a control system was developed. For any case of the load or displacement control pattern, the actuators were programmed through an interface with the computer so that the desired pattern was achieved.

For the first specimen, the axial load was a constant axial load equal to 30% of column axial load capacity, and for the second specimen a variable axial load proportional to the horizontal force was applied. The horizontal force for the first two tests was a quasi-static cyclic load. The third column was subjected to a constant axial load equal to 30% of the section capacity, and the fourth column was tested without any axial load. The horizontal force for these two tests was a monotonically increasing force starting from zero up to the failure of the column. The fifth specimen was tested under a monotonically increasing lateral displacement with a nonproportionally variable axial load, fluctuating between 30% and –10% of the section capacity. The overall objective of the tests was to study the effects of different quasi-statically loaded displacement paths, the effects of combined, nonproportional cyclic loading inputs for both the axial and lateral directions of columns, and to provide the benchmark data for dynamic and large-scale tests.

The experimental results show that the axial force level and pattern play a significant role in the behavior of the column. An increase in axial load leads to an increase in the flexural capacity but a decrease in the ductility. A relatively high axial load makes the concrete enter the inelastic behavior range before the steel, and more confinement is required to achieve enough ductility in a seismic region. The response is different if the axial load is not constant and is proportional to the horizontal load, as in real situations, and as shown in the experimental results of the second test. In the push direction, where the axial load was decreased to a negative value, the response was more ductile but the capacity was decreased, and in the pull direction, an increase in the axial load slightly increased the capacity without relatively any decrease in ductility. (due to the low level of axial force compared to the first test). A preliminary test with a nonproportional axial load confirmed the significant effect of the axial load on the overall response of the column.

Based on the test results, under a constant axial load, the peak strength and displacement of the column under a cyclic lateral load is close to a monotonic case. The result is different when the axial load is the variable parameter. For the same peak maximum and minimum values, the response will be different under different axial loading patterns. As for tests five and six, reducing the rate of change of the axial load and fixing the level of axial load during the test at some points, resulted in a different response compared to that of test five.

The flexural strength of a column under a variable axial load may be less than the predicted values using the conventional methods, assuming the same level of axial load as for the instance under consideration. This has been shown in the comparison of the analytical and experimental results of the last two tests where the specimens were under a variable axial load and a monotonic lateral displacement. For a variable axial load, the pattern of variation of the axial load with respect to the lateral displacement has a very significant effect on the response of the column. Assessing the flexural strength of a column under seismic excitation when the vertical component cannot be ignored needs special consideration. The column may have a real flexural strength less than that predicted analytically under the same peak level of axial compressive load.

Specimens under a variable axial load demonstrated a better ductility compared to the specimens under a constant axial load as shown by comparing the experimental results of a specimen under a fixed level of compressive axial load and a test under a variable axial load with the same peak value of compression.

The transverse reinforcement when placed as spiral is utilized more than as a noncircular shape. In the first test where the axial load was high enough, the flexural failure of the column was initiated by the yield and rupture of the spiral, so in a case where the axial load is relatively high, increasing the amount of confinement leads to an increase in the strength and ductility, and will delay the failure.

The percentage of the energy absorbed by the column with a high level of axial load with respect to the applied energy to the column is less compared with the percent of the energy absorbed by the column with a proportional but low level axial load.

The length of the plastic hinge is variable in the case of a variable axial load, and the existing plastic hinge model seems to be insufficient to give a realistic estimation for the plastic hinge length in the case of a variable axial load. Also, the location of the plastic hinge may vary if the applied loads are not purely static loads.

One of the objectives of the experimental studies on the seismic behavior of bridge columns under various loading patterns was to investigate the existing analytical tools and models and the way they can address different analytical needs of the problem. First, a relatively good estimation of the behavior of each specimen was needed before each test so that the test setup could be designed properly. After the experimental phase, the models and methods needed to be judged compared to the test results. In this research the existing material models for steel, confined concrete, and unconfined concrete were reviewed, and a stress-strain model for the monotonic response of steel was developed. Also two models for the hysteretic stress-strain response of steel and concrete were developed and used for the hysteretic analysis of the specimens.

Existing analytical methods such as the finite element method, the fiber model, the yield surface method, and the multispring model were briefly reviewed. A simple multispring model for RC circular sections was developed (see Appendix III). The plastic hinge method was discussed and different existing models were compared. To consider the variation of the plastic hinge length due to the level of the lateral force and axial load, a model was proposed for the plastic hinge method and implemented in the application developed for the analytical studies.

The experimental results were compared with the analytical results. This comparison was done for the moment-curvature and lateral force-deflection response of the specimens. It has been shown that while for a constant compressive axial load case the analytical predictions are relatively conservative compared to the test results, for a variable axial load this estimation may be more than the actual response of the specimen at peak compressive values of a nonproportionally variable axial load. On the other hand, for a constant tensile axial load the analytical flexural strength of the specimens was in general slightly more than the experimental values, while in the case of a variable axial load a different situation was observed. These phenomena are very important in the assessment of the seismic behavior of columns, especially where the vertical component of the excitation must be considered.

When test results are compared, the proposed plastic hinge method has been shown to yield better results than the commonly used method.

REFERENCES

Ang B.G., Priestley M.J.N., Park R., "*Ductility of Reinforced Concrete Bridge Piers Under Seismic Loading*", Report No. 81-3, Department of Civil Engineering, University of Canterbury, Christchurch, pp 109 , Feb 1981

Anvar, A., Arya, S.K., Hegemier, G.A.,"*Behaviour of Floor-to-Wall Connections in Concrete Masonry Buildings*", Proceedings of the Second North American Masonry Conference, University of Maryland, College Park, Maryland, 9-11, pp.39.1-39.18, August 1982.

Apostolos Fafitis and Surendra P. Shah, "*Predictions of Ultimate Behavior of Confined Columns Subjected to Large Deformations*", ACI Structural Journal Proceedings, Volume 82, Issue 4, JL82-35, pp. 423-433 , July 1, 1985

Ashraf El-Bahy, Sashi K. Kunnath, William C. Stone, and Andrew W. Taylor; "*Cumulative Seismic Damage of Circular Bridge Columns: Benchmark and Low-Cycle Fatigue Tests*"; ACI Structural Journal, Volume 96, No. 4, 96-S71, July-August 1999, pp. 633-641

Baker A. L. L., *"Ultimate Load Theory Applied to the Design of Reinforced and Prestressed Concrete Frames",* Concrete Publications Ltd., London, pp 91, 1956

Baker, A. L. L. and Amarakone, A. M. N., "*Inelastic Hyperstatic Frames Analysis*", Proceedings of the International Symposium on the Flexural Mechanics of Reinforced Concrete, ASCE-ACI, Miami, pp. 85-142, November 1964.

Balmer, G. G., "*Shearing Strength of Concrete under High Triaxial Stress- Computation of Mohr's Envelope as a Curve*", Structural Research Laboratory, Report SP-23, U.S. Bureau of Reclamation, Denver, 1949.

Beni Assa and Minehiro Nishiyama; "*Prediction of Load-Displacement Curve of High-Strength Concrete Columns Under Simulated Seismic Loading*", ACI Structural Journal, Volume 95, No. 5, pp. 547-557, September 1, 1998

Benzoni, G., Ohtaki, T., Priestley, M.J.N., and Seible, F. "*Seismic Performance of reinforced concrete columns under varying axial load*" Proceedings of the Fourth Caltrans Seismic Research Workshop, California Dept. of Transportation, Sacramento, CA, 1996

Braga, F. Laterza, M., "A *new approach to the confinement of R/C columns*", *11th European Conference on Earthquake Engineering*, Paris 6-11 September 1998

Byrak Oguzhan and Sheikh Shamim, "*High-Strength Concrete Columns under Simulated Earthquake Loading",* ACI Structural Journal, Title No. 94-S65, pp. 708-722, November-December 1997

Chang, G.A. and Mander, J.B., *"Seismic Energy Based Fatigue Damage Analysis of Bridge Columns: Part I, Evaluation of Capacity*", Technical Report NCEER-94-0006, National Center for Earthquake Engineering Research, Buffalo, New York, March 14, 1994

Chen, W.F. and Saleeb, A.F. *"Constitutive equations for engineering materials*", Vol. 1 - elasticity and modeling," Book published by *Wiley Interscience*, New York, pp. 580, 1982

Corley W. G., *"Rotational Capacity of Reinforced Concrete Beams"*, Journal of Structural Division, ASCE, Vol. 92, ST5, October 1966, pp. 121-146.

Cusson, D. and Paultre, P. *"High-strength Concrete Columns Confined by Rectangular Ties"*, ASCE Structural Journal, American Society of Civil Engineers, 120(3), 783-804, 1993

Dutta, A., Mander, J.B. & Kokorina, T., *"Retrofit for control and repairability of damage"*, Earthquake Spectra, Volume 15 No. 4, pp. 657-79, Nov, 1999

Emori, K., and Schnobrich, W. C., *"Analysis of Reinforced Concrete Frame Wall Structures for Strong Motion Earthquakes"*, Civil Engineering Studies, SRS 457, University of Illinois, Urbana, Dec. 1978

Ghee A.B., Priestley M.J.N., Paulay T., *"Seismic Shear Strength of Circular Bridge Piers"*, "Report No. 85-5", Department of Civil Engineering, University of Canterbury, Christchurch, July 1985, pp 480.

Ghee A.B., Priestley M.J.N., Paulay T., "*Seismic Shear Strength of Circular Reinforced Concrete Columns*", ACI Structural Journal, V. 86, No. 1, January-February 1989, pp 45-59.

Ghusn G.E., Saiidi M., "*A Simple Hysteretic Element for Biaxial Bending of R/C Columns and Implementation in NEABS-86*", Report No. CCEER 86-1, University of Nevada, Reno, July 1986.

Gilbersten, N. D., and Moehle, J. P., *"Experimental Study of Small-Scale R/C Columns Subjected to Axial and Shear Force Reversals",* Structural Research Series No. 481, Civil Engineering Studies, University of Illinois, Urbana, 95 pp, July 1980

Golafshani A. A., Beheshti Aval S. B, Sadeghvaziri M. A, *"An Efficient Fiber Element for Analysis of Concrete-Filled Steel Tubes Under Cyclic Loads*", Asian Journal of Civil Engineering, Vol. 1, No. 3, 2000, pp 101, 113.

Hegemier H. E., Murakami G.A., "A *mixture model for unidirectionally fiber reinforced composites*", J. Appl. Mech. 53, pp. 765-773, 1986

Hiroshi Kuramoto, Toshimi Kabeyasawa, Fan-Hao Shen, "*Influence of Axial Deformation on Ductility of High-Strength Reinforced Concrete Columns under Varying Triaxial Force"*, ACI Structural Journal, Title No. 92-S59, September-October 1995, pp 610-618.

Hognestad, E., "*A Study of Combined Bending and Axial Load in Reinforced Concrete Members,*" Univ. of Illinois Eng. Exp. Station, Bulletin No. 1, V. 49, No. 22, November, 128 p., 1951.

Ignatakis C.E., Stavrakakis E.J., Penelis G.G., "*Parametric Analysis of Reinforced Concrete Columns under Axial and Shear Loading Using the Finite Element Method*", ACI Structural Journal, Vol. 86, No. 4, July-August 1989.

Jaradat Omar A., McLean David I., Marsh M. Lee, *"Performance of Existing Bridge Columns Under Cyclic Loading- Part1: Experimental Results and Observed Behavior",* ACI Structural Journal, Title No. 95-S63, November-December 1998, pp 695-704.

Jiang Y., Saiidi M., *"Four Spring Element for Cyclic Response of R/C Columns*", ASCE Journal of Structural Engineering, Vol. 116, No. 4, April 1990.

Kabeyasawa, T.; Shen, F., Kuramoto, H.; and Rubiano, N. R.; *"Experimental Study on Behavior on Ultra High Strength Reinforced Concrete Columns under Triaxial Forces*", Transactions of JCI, Volume 14, pp. 313-320, 1992.

Kent, D. and Park, R. "*Flexural members with confined concrete"*, Journal of Structural Engineering, American Society of Civil Engineers, Vol. 97, No. ST7, July 1971, pp. 1969-1990.

Keshavarzian, M., and Schnobrich, W. C., "*Computed non-linear seismic response of R/C wall-frame structures*", Civil Engineering Studies, SRS 512, University of Illinois at Urbana-Champaign, Urbana, Ill., May 1984.

Kowalsky Mervyn J., Priestley M. J. Nigel, Seible Frieder, *"Shear and Flexural Behavior of Lightweight Concrete Bridge Columns in Seismic Regions",* ACI Structural Journal, Title No. 96-S16, January-February 1999, pp 136-148.

Kreger, M. E., and Linbeck, L., *"Behavior of Reinforced Concrete Columns Subjected to Lateral and Axial Load Reversals"*, Proceeding of the third U.S. National Conference on Earthquake Engineering, Charleston, S.C., August 1986

Kunnath S.K., and Reinhorn A.M., *"Model for Inelastic Biaxial Bending Interaction of Reinforced Concrete Beam-Columns*", ACI Structural Journal, V. 87, No. 3, May-June 1990.

Kuramoto Hiroshi, Kabeyasawa Toshimi, and Shen Fan-Hao; "*Influence of Axial Deformation on Ductility of High-Strength Reinforced Concrete Columns Under Varying Triaxial Forces";* ACI Structural Journal, Vol. 92, No. 5, pp. 610-618, November 1, 1995

Lai Shing-Sham, Will George T., Otani, Shunsuke, *"Model for Inelastic Biaxial Bending of Concrete Members",* Journal of Structural Engineering, ASCE, Vol. 110, No. 11, pp 2563-2583, November 1984

Lehman Dawn E., Moehle Jack P., *"Influence of Longitudinal Reinforcement Ratio on Column Response",* Pacific Earthquake Engineering Research Center, University of California, Berkeley.

Li Bing, R. Park, and H. Tanaka; "*Stress-Strain Behavior of High-Strength Concrete Confined by Ultra-High- and Normal-Strength Transverse Reinforcements*"; ACI Structural Journal, Vol. 98, No. 3, pp. 395-406, May 1, 2001

Li K.N., Aoyama H., Otani S., "*Reinforced Concrete Columns Under Varying Axial Load and Bi-Directional Lateral Load Reversals",* Proceedings, 9th World Conference on Earthquake Engineering, Tokyo, August 1988, Paper No. 5756.

M. J. Nigel Priestley, Frieder Seible, Yan Xiao, and Ravindra Verma; "*Steel Jacket Retrofitting of Reinforced Concrete Bridge Columns for Enhanced Shear Strength-Part 1: Theoretical Considerations and Test Design*"; ACI Structural Journal, Volume 91, No. 4, July 1, 1994, pp. 394-405.

Mander J.B., Priestley M.J.N., Park R., “*Observed Stress Strain Behavior of Confined Concrete*”, ACI Structural Journal, V. 114, No. 8, Aug. 1988, pp 1827-1849.

Mander J.B., Priestley M.J.N., Park R., “*Seismic Design of Bridge Piers*”, Res. Rep. 84-2, Department of Civil Engineering, University of Canterbury, Christchurch, New Zealand, 1984

Mander J.B., Priestley M.J.N., Park R., “*Theoretical Stress Strain Model for Confined Concrete*”, ASCE Journal of Structural Journal, Vol. 114, No. 8, Aug. 1988, pp 1804-1825.

Martirossyan, A. and Xiao, Y.; “*Seismic Performance of High Strength Concrete Columns*”; USC Structural Engineering Research Program, Report No. USC-SERP-96/4, September 1996.

Mitchell D. and Collins M.P., “*Prestressed Concrete Structures”*; Prentice Hall, ISBN 0-13-691635-x, 1991

Nadim I. Wehbe, M. Saiid Saiidi, and David H. Sanders; “*Seismic Performance of Rectangular Bridge Columns with Moderate Confinement*”; ACI Structural Journal, Volume 96, Issue 2, 96-S27, March 1, 1999, pp. 248-258.

Ng K. H., Priestly M.J.N., Park R., *“Seismic Behavior of Circular Reinforced Bridge Piers*”, Report No. 78-14, Department of Civil Engineering, University of Canterbury, Christchurch, 1978, pp 129.

Ngo, D., Scordelis, A. C., “*Finite Element Analysis of Reinforced Concrete Beams*”, Journal of the American Concrete Institute, Vol. 64, No. 3, pp. 152-163, March 1967

Park R., and Blakely R. W. G., “*Seismic Design of Bridges*”, RRU Bulletin No. 33, New Zealand National Road Board, Wellington, 1979, pp 145.

Park R., Paulay T., "*Reinforced Concrete Structures*", John Wiley & Sons, USA, 1975.

Park, R., Kent, D. C., and Sampson, R. A.; “*Reinforced Concrete Members with Cyclic Loading*”, Journal of Structural Division, ASCE, Volume 98, ST7, pp. 1341-1360, July 1972.

Park, Robert and Joen, Pam Hoat, “*Simulated Seismic Load Tests on Prestressed Concrete Piles and Pile-Pile Cap Connections*”, PCI Journal, pp. 42-61, November-December 1990

Powell, G. H., and Chen, P. F., “3D *beam-column element with generalized plastic hinges*”, Journal of Engineering Mechanics, ASCE, 112(7), 627–641, 1986.

Priestley M.J.N., Park R., “*Strength and Ductility of Bridge Substructures*”, RRU Bulletin*,* No. 71, National Roads Board, Wellington, pp. 120, 1984.

Priestley M.J.N., Park R., Potangaroa R.T., “*Ductility of Spirally-Confined Concrete Columns*”, Journal of the Structural Division, ASCE, Vol. 107, No. ST1, pp 181-201, Jan 1981.

Priestley, M. J. N. and Park, R., “*Strength and Ductility of Concrete Bridge Columns under Seismic Loading*”, ACI Structural Journal, Title No. 84-S8, pp. 61-76, Jan.-Feb. 1987

Priestley, M.J. Nigel; Benzoni, Gianmario, “*Seismic Performance of Circular Columns with Low Longitudinal Reinforcement Ratios*”, ACI Structural Journal, vol93, No.4, July-August, 1996, pp. 474-485

Ramberg, W. and Osgood, W. R., *"Description of Stress-Strain Curves by Three Parameters"*, Technical Note 902, National Advisory Committee for Aeronautics, July 1943.

Rashid Y. R., "*Ultimate Strength Analysis of Prestressed Concrete Pressure Vessels*," Nuclear Engineering & Design, 7, pp. 334-344, 1968.

Richart, F.E. and Brown, R.L., *"An Investigation of Reinforced Concrete Columns,"* Univ. of Illinois Eng. Exp. Station, Bulletin No. 267, pp. 1-91, June, 1934

Richart, F.E., *"An Investigation of Web Stresses in Reinforced Concrete Beams,"* Univ. of Illinois Eng. Exp. Sta., Bulletin, No. 166, pp. 1-105. , June, 1927.

Richart, F.E., Brandtzaeg, A., and Brown, R.L., *"A Study of the Failure of Concrete Under Combined Compressive Stresses,"* Univ. of Illinois Eng. Exp. Station, Bulletin No. 185, Vol. 26, No. 12, pp. 1-105 , November, 1928.

Richart, F.E., Brandtzaeg, A., and Brown, R.L., "*The Failure of Plain and Spirally Reinforced Concrete in Compression,*" Univ. of Illinois Eng. Exp. Station, Bulletin, No. 190, V. 26, No. 31, pp. 1-74. , April, 1929

Saatcioglu Murat, Baingo Darek, "*Circular High-Strength Concrete Columns Under Simulated Seismic Loading",* Journal of Structural Engineering, ASCE, March 1999, pp 272-280.

Saatcioglu, M. and Razvi. S.; *"Strength and Ductility of Confined Concrete,"* ASCE Journal of Structural Engineering, Vol. 118, No.6, pp. 590-1607, 1992.

Sadeghvaziri, Ala M., Douglas A. Fouch, *"Behavior of RC Columns under Nonproportionally Varying Axial Load",* Journal of Structural Engineering, ASCE, Vol. 116, No. 7,July,1990, pp 1835-1856.

Scott, B. D., Park, R., and Priestley, M. J. N. (1982), "*Stress-Strain Behavior of Concrete Confined by Overlapping Hoops at Low and High Strain Rates*," American Concrete Institute Journal, Vol. 79, No. 1, pp. 13-27.

Shamim A. Sheikh, Oguzhan Byrak, *"High Strength Concrete Columns under Simulated Earthquake Loading"*, ACI Structural Journal, V. 94, No. 6, November-December 1997.

Sheikh Shamim A., Toklucu Murat T., *"Reinforced Concrete Columns Confined by Circular Spirals and Hoops*", ACI Structural Journal, Title No. 90-S56, September-October 1993, pp 542-553.

Sheikh, S. A. and Uzumeri, S. M., "*Analytical model for concrete confinement in tied columns*," J. Struct., Div., ASCE, Vol. 108, No. ST12, pp. 2703-2722, 1982

Shibata, M., "*Analysis of Elastic-Plastic Behavior of Steel Brace Subjected to Repeated Axial Force.*, International Journal of Solids and Structures, Volume 18, No. 3, pp. 217-228, March 1982

Stevens N.J., Uzmeri S.M., Collins M.P., *"Reinforced Concrete Subjected to Reversed Cyclic Shear- Experiments and Constitutive Model*", ACI Structural Journal, Vol. 88, No. 2, March-April 1991.

Sun Yu-Ping and K. Sakino; "*Experimental study on ductility improvement method for reinforced concrete columns using high-strength materials*", Proceedings, Japan Concrete Institute, Vol. 15, No. 2, pp. 719 – 724, 1993

Sun Z.L., Seible F., Priestley, M.J.N., *"Geometric Filament Model for the Analysis of As-Built & Retrofitted Bridge Columns of Arbitrary Cross-Sections*", The Second Annual Seismic Research Workshop, Division of Structures, Caltrans, March 1993.

Takiguchi, K., Okada, K. and Sakai, M.; "*Ductility capacity of bonded and unbonded reinforced concrete members*", Proc. Architectural Institute of Japan, 249, 1-11, 1976

Takizawa, H. and H. Aoyama, "*Biaxial effects in modeling earthquake response of R/C structures, Earthquake"*, Engineering and Structural Dynamics, v. 4, p. 523-552, 1976

Vecchio, F.J. and Collins, M.P., *"The Modified Compression Field Theory for Reinforced Concrete Elements Subjected to Shear"*, ACI Journal, Proceedings V. 83 No. 2, pp. 219-231, March-April 1986.

Vu, Nganha D.; Priestley, M.J. Nigel; Seible, Frieder; Benzoni, Gianmario, "*Seismic Response of Well Confined Circular Reinforced Concrete Columns with Low Aspect Ratios*", 5th Caltrans Seismic Research Workshop, 1998

Wagner H., "*Ebene Blechwandtrager mit sehr dunnem Stegblech*", Zeitschrift fur Flugtechnik und Motorluftschiffahrt, Berlin, Germany, Vol. 20, Nos. 8-12, 1929.

Xiao, Y.; Yun, H.W., *"Full-Scale Experimental Studies on High-Strength Concrete Columns"*, American Concrete Institute, ACI Structural Journal**,** Vol.99, No.2, pp. 199-207 , March-April issue 2002

Yan Xiao, M. J. Nigel Priestley, and Frieder Seible; "*Seismic Assessment and Retrofit of Bridge Column Footings*"; ACI Structural Journal, Volume 93, No. 1, pp. 79-94, January 1, 1996

Yong, Y-K., Nour, M.G. and Nawy, E.G., *"Behavior of Laterally Confined High-Strength Concrete Under Axial Loads*", Journal of Structural Engineering, ASCE, Vol. 114, No. 2, pp. 332-351 , Feb. 1988.

Youseff Bozorgnia, M.EERI, Mansour Niazi, M.EERI, Kenneth W. Campbell, M.EERI, "*Characteristics of Free-Field Vertical Ground Motion during the Northridge Earthquake*", Earthquake Spectra, Volume 11, No. 4, November 1995, pp 515-525.

Yuk-Lung Wong, T. Paulay, and M. J. Nigel Priestley; "*Response of Circular Reinforced Concrete Columns to Multi-Directional Seismic Attack*"; ACI Structural Journal, Volume 90, Issue 2, 90-S20, pp. 180-191, March 1, 1993

Zahn F.A., Park R., Priestley M.J.N., "*Strength and Ductility of Reinforced Concrete Piers- A Summary Report",* Report No. 83-7, Department of Civil Engineering, University of Canterbury, Christchurch, Dec. 1983, pp 43.

Zayas, V. A., P-S. B. Shing, S. A. Mahin, E. P. Popov, and B. F. Maison, *"Inelastic Structural Modeling of Braced Offshore Platforms for Seismic Loading, Appendix A: Inelastic Brace Element,"* Earthquake Engineering Research Center, Report No. UCB/EERC-81/04, University of California, Berkeley, January 1981

Zeris C. A., Mahin, S. A., "*Behavior of Reinforced Concrete Structures Subjected to Biaxial Excitation*", ASCE Journal of Structural Engineering, Vol. 117, No. 9, pp. 2657-2673 , Sep. 1991

APPENDIX I

TEST GRAPHS BASED ON THE EXPERIMENTAL DATA

ILLUSTRATIVE FIGURES FOR HELPING TO LOCATE PROPER GAGE AND LINEAR POTENTIOMETER AS IS TITLED IN TEST GRAPHS

Example:

R-3-M=R-3-2=Gage on Rebar at Level 3, Location M(or 2)

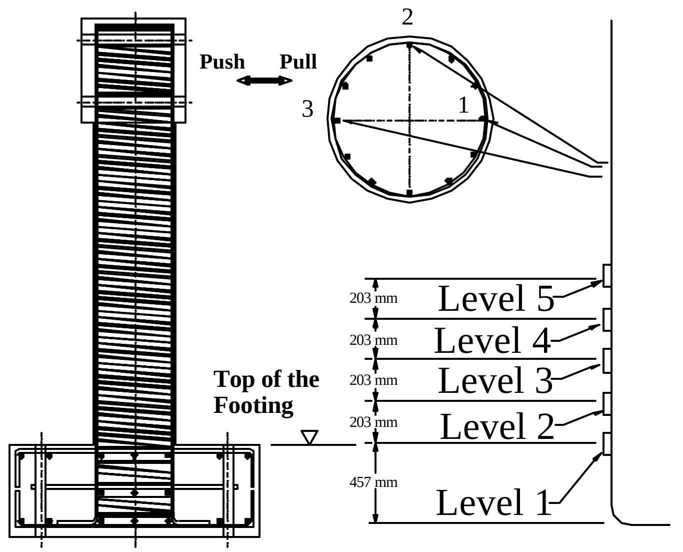

Gages on the Rebars

Example:

S-4-L=S-4-3=Gage on Spiral at Level 4, Location L(or 3)

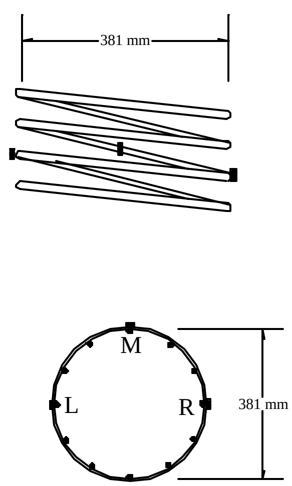

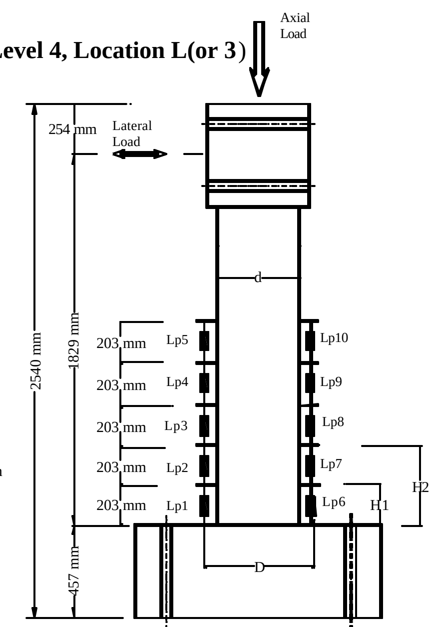

Gages on the Spiral ***Location of linear potentiometers***

TEST GRAPHS BASED ON THE EXPERIMENTAL DATA

TEST ONE

PEER-C1 True-Shear Force vs Drift Ratio

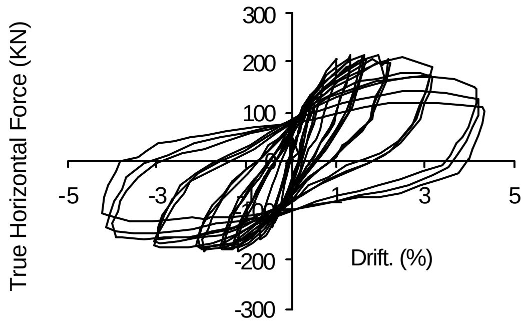

Hysteresis Curve PEER-C1 (raw data)

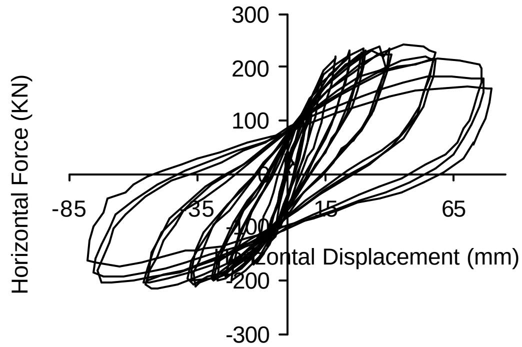

Total Vrtical Deformation vs Drift Ratio

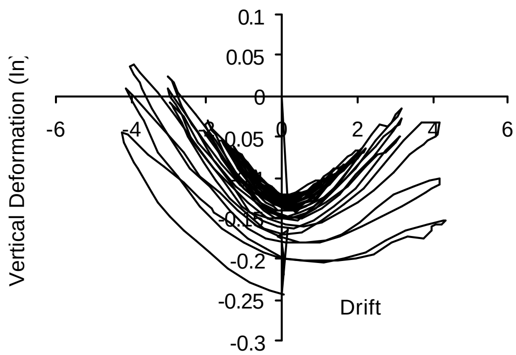

Experimental Horizonta Force-Drift Ratio
(Specimen One) and prediction

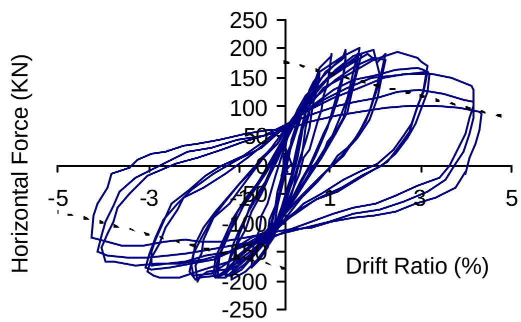

Elongation in the fourth level by the
strain gages on rebars at opposite
sides(specimen one)

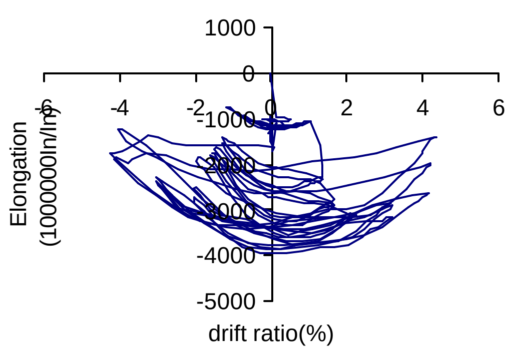

Strain in Long. Rebar(R-1-1) at footing
level vs drift

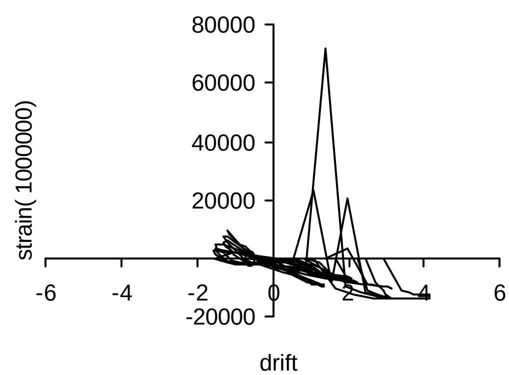

lp1 vs drift ratio

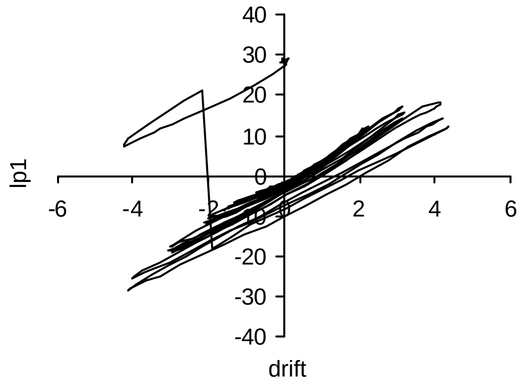

lp6 vs drift ratio

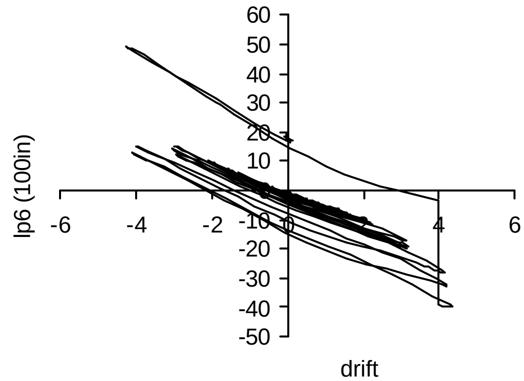

Strain in Longitudinal Rebar on footing (R-1-2)in the middle of section vs drift ratio

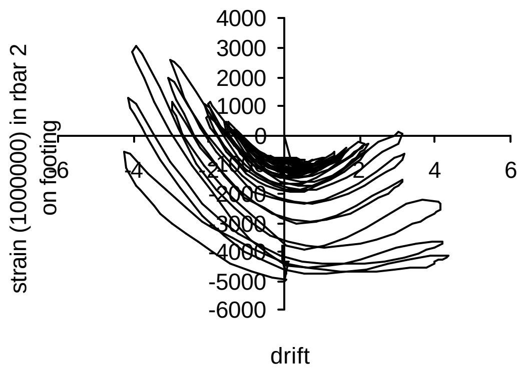

Strain at Spiral at footing level at the side(S-1-L)

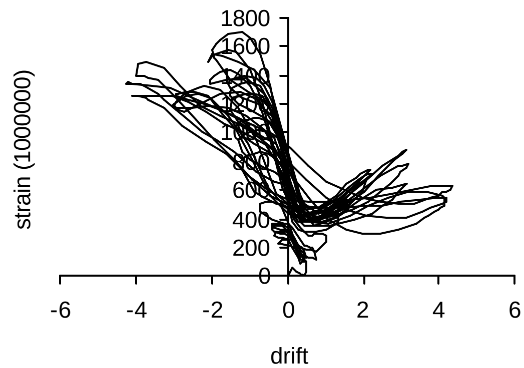

strain on rebar at second level(8") at side outward(R-2-1)

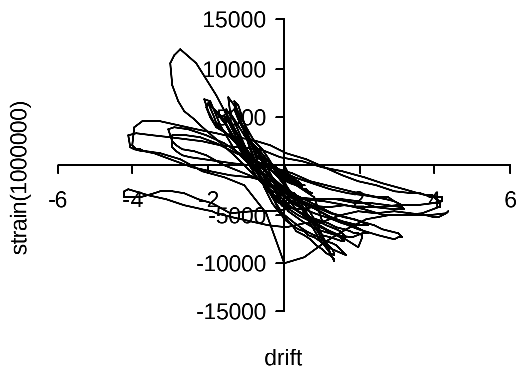

strain in spiral on top of footing in middle(S-1-M)

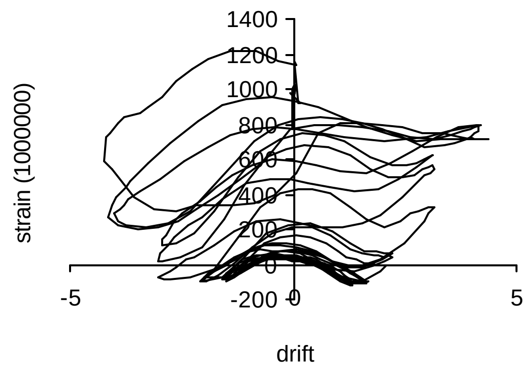

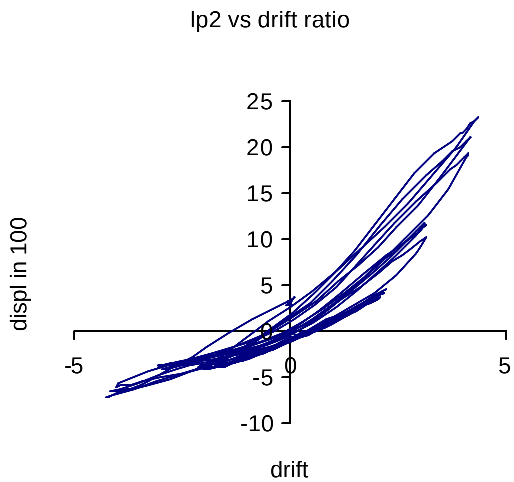
lp2 vs drift ratio
25
20
15
10
5
0
-5
-10
-5
0
5
displ in 100
drift

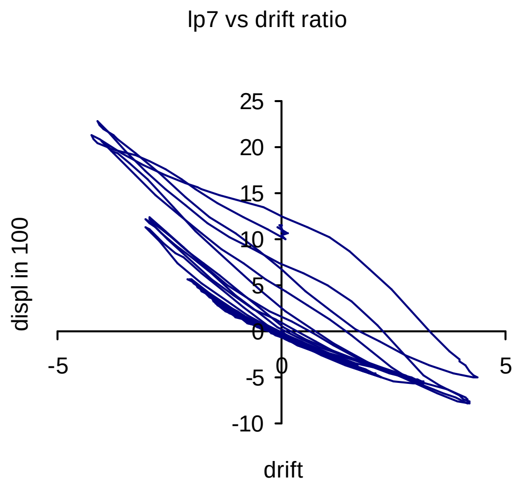
lp7 vs drift ratio
25
20
15
10
5
0
-5
-10
-5
0
5
displ in 100
drift

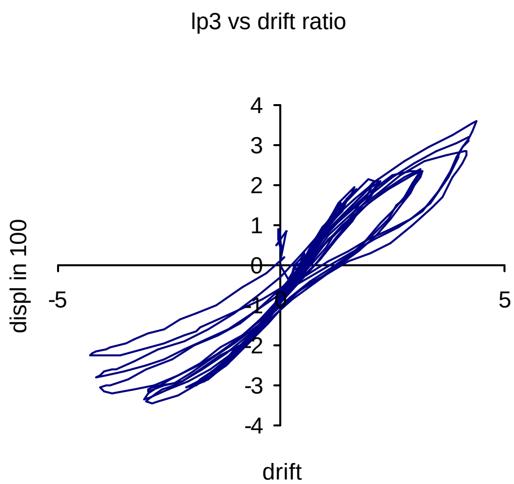
lp3 vs drift ratio
4
3
2
1
0
-1
-2
-3
-4
-5
0
5
displ in 100
drift

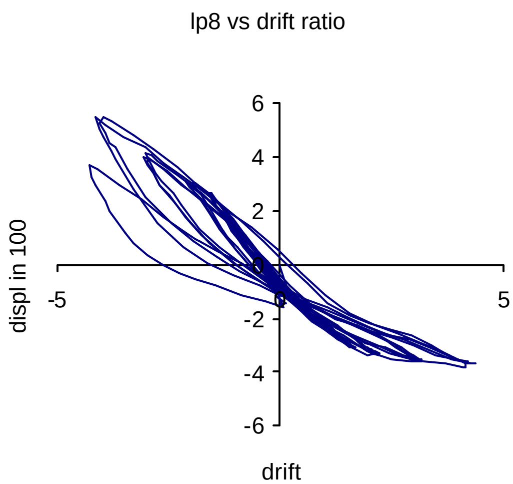
lp8 vs drift ratio
6
4
2
0
-2
-4
-6
-5
0
5
displ in 100
drift

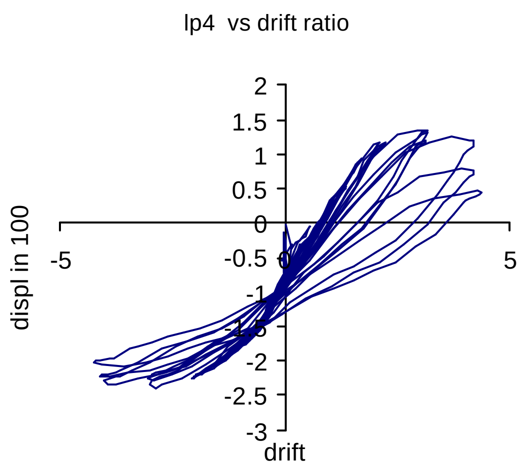
lp4 vs drift ratio
2
1.5
1
0.5
0
-0.5
-1
-1.5
-2
-2.5
-3
-5
0
5
displ in 100
drift

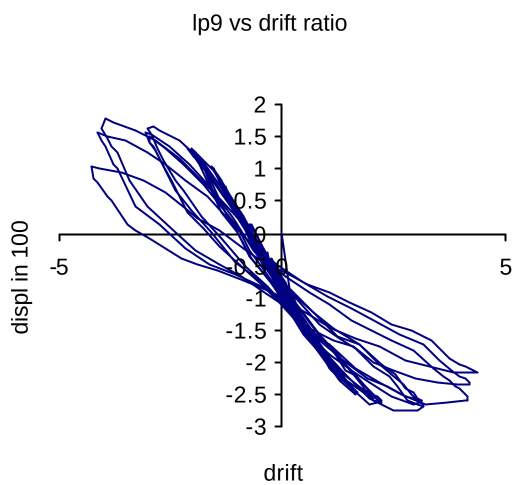
lp9 vs drift ratio
2
1.5
1
0.5
0
-0.5
-1
-1.5
-2
-2.5
-3
-5
0
5
displ in 100
drift

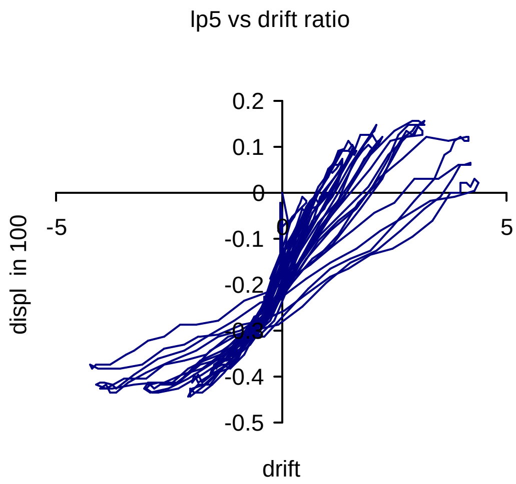
lp5 vs drift ratio
0.2
0.1
0
-0.1
-0.2
-0.3
-0.4
-0.5
-5
0
5
displ in 100
drift

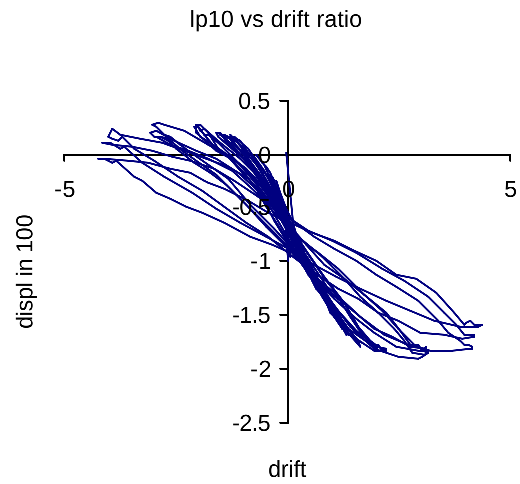
lp10 vs drift ratio
0.5
0
-0.5
-1
-1.5
-2
-2.5
-5
0
5
displ in 100
drift

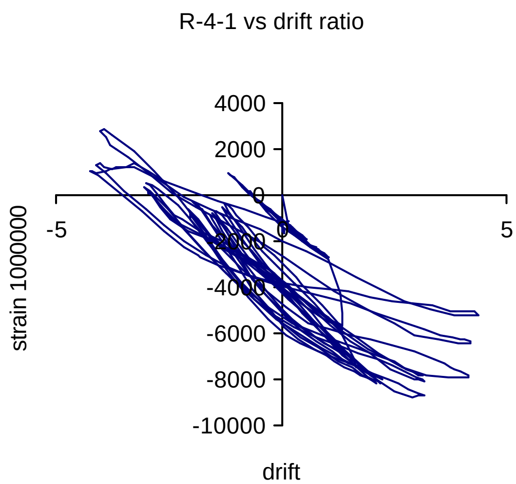
R-4-1 vs drift ratio
4000
2000
0
-2000
-4000
-6000
-8000
-10000
-5
0
5
strain 1000000
drift

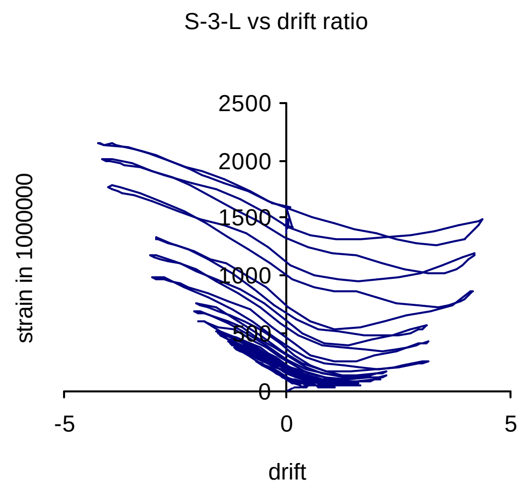
S-3-L vs drift ratio
2500
2000
1500
1000
500
0
-5
0
5
strain in 1000000
drift

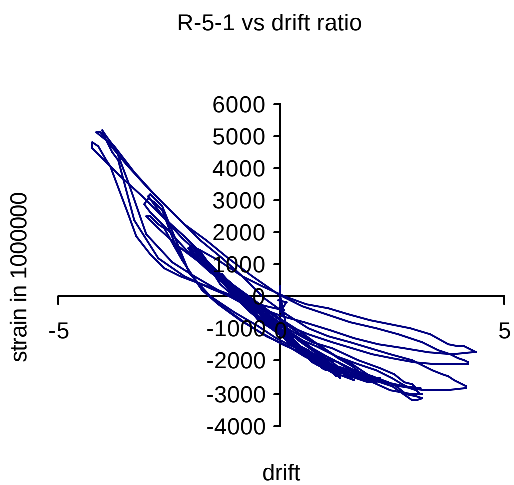
R-5-1 vs drift ratio
6000
5000
4000
3000
2000
1000
0
-1000
-2000
-3000
-4000
-5
0
5
strain in 1000000
drift

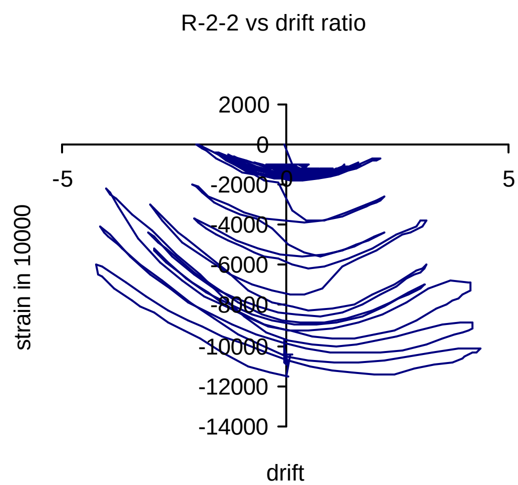
R-2-2 vs drift ratio
2000
0
-2000
-4000
-6000
-8000
-10000
-12000
-14000
-5
0
5
strain in 10000
drift

R-3-2 vs drift ratio

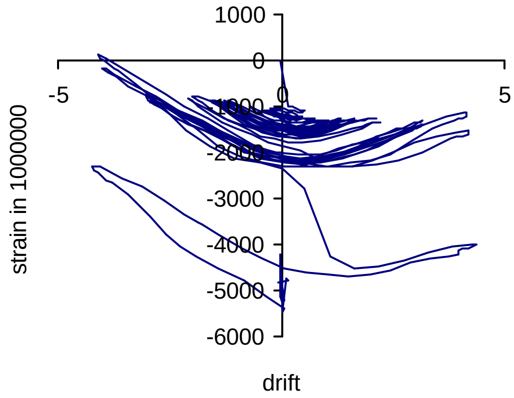

R-4-3 vs drift ratio

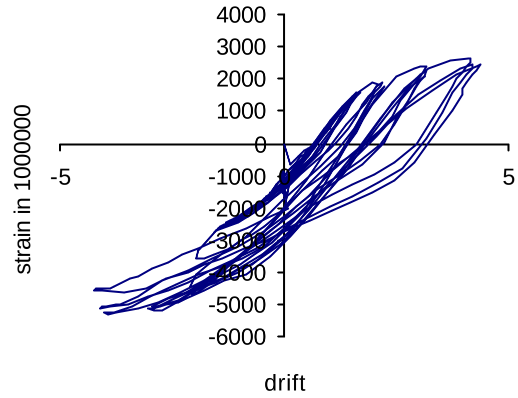

R-3-3 vs drift ratio

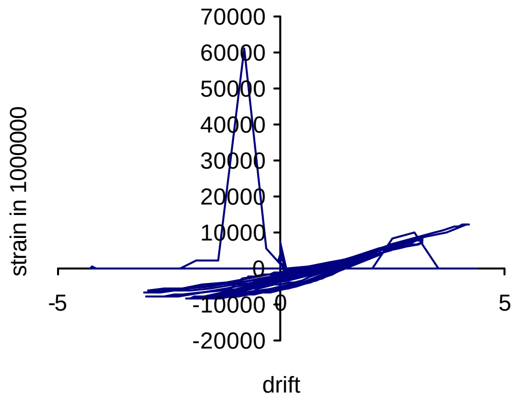

strain at (S-2-L) vs drift ratio

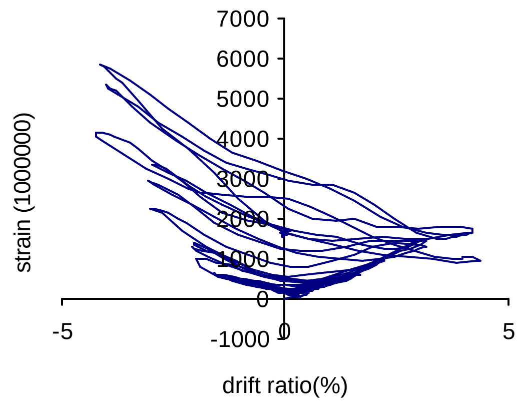

S-2-M vs drift ratio

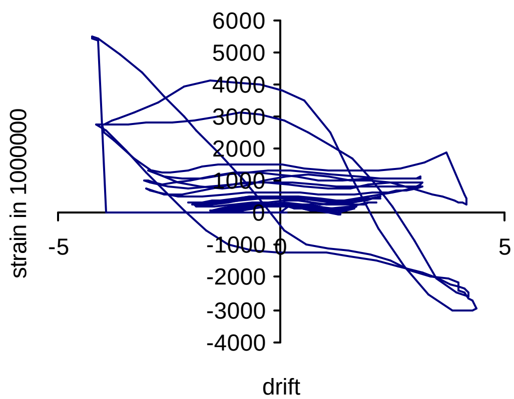

S-1-M vs drift ratio

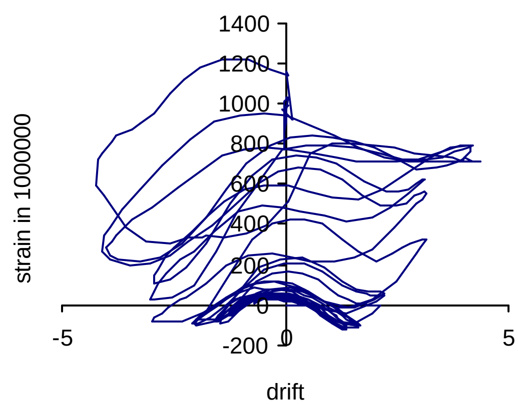

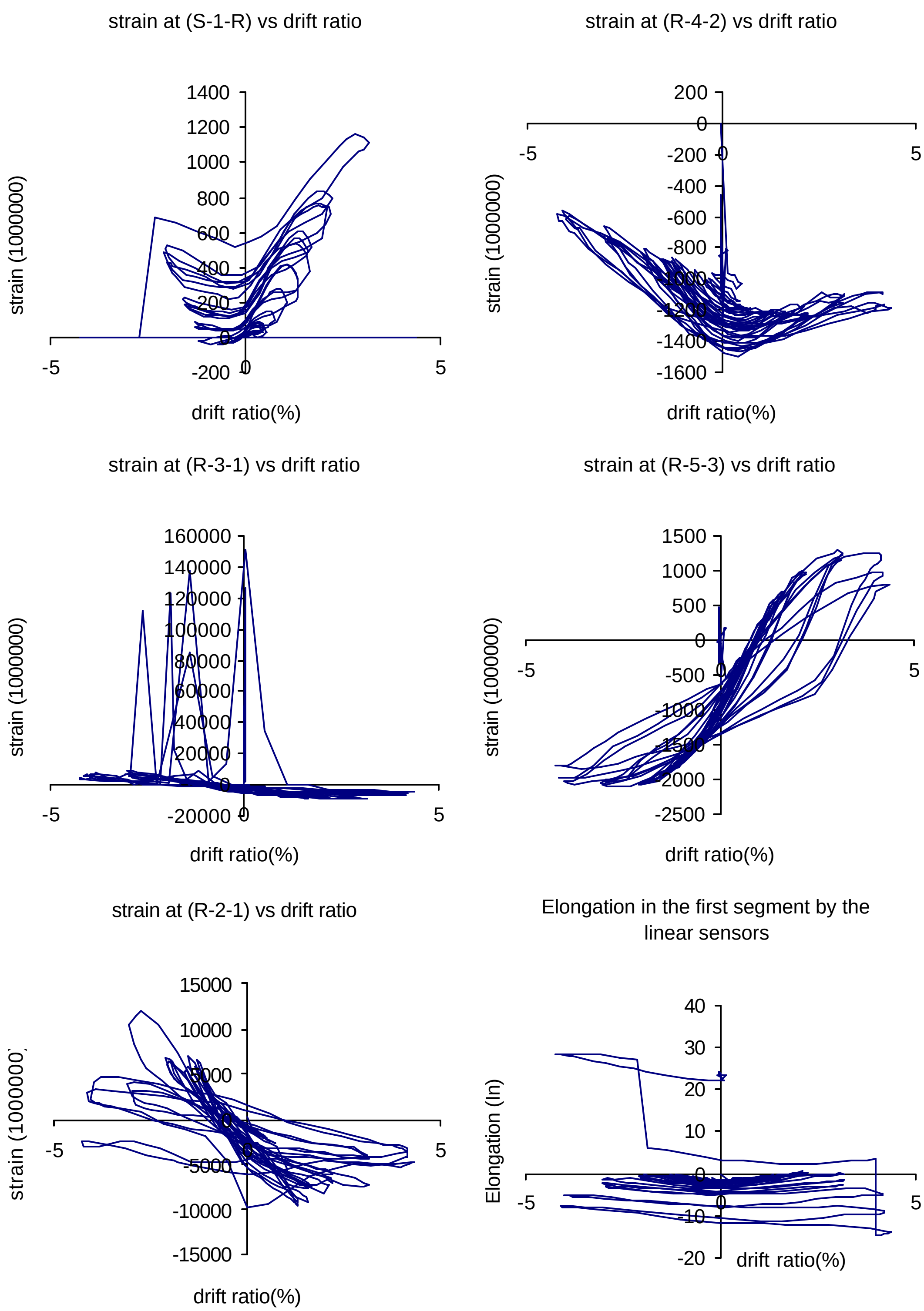
strain at (S-1-R) vs drift ratio
1400
1200
1000
800
600
400
200
0
-200
-5
0
5
strain (1000000)
drift ratio(%)
strain at (R-4-2) vs drift ratio
200
0
-200
-400
-600
-800
-1000
-1200
-1400
-1600
-5
0
5
strain (1000000)
drift ratio(%)
strain at (R-3-1) vs drift ratio
160000
140000
120000
100000
80000
60000
40000
20000
0
-20000
-5
0
5
strain (1000000)
drift ratio(%)
strain at (R-5-3) vs drift ratio
1500
1000
500
0
-500
-1000
-1500
-2000
-2500
-5
0
5
strain (1000000)
drift ratio(%)
strain at (R-2-1) vs drift ratio
15000
10000
5000
0
-5000
-10000
-15000
-5
0
5
drift ratio(%)
Elongation in the first segment by the linear sensors
40
30
20
10
0
-10
-20
-5
0
5
Elongation (In)
drift ratio(%)

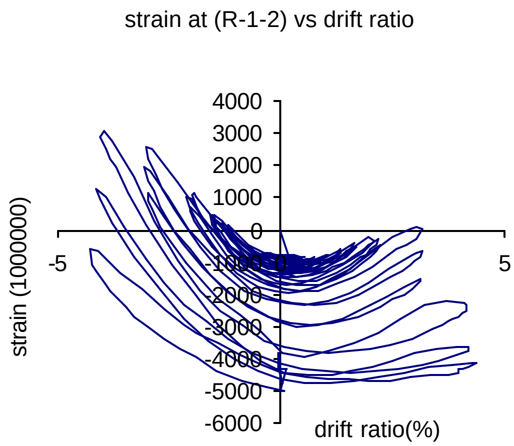
strain at (R-1-2) vs drift ratio
strain (1000000)
drift ratio(%)

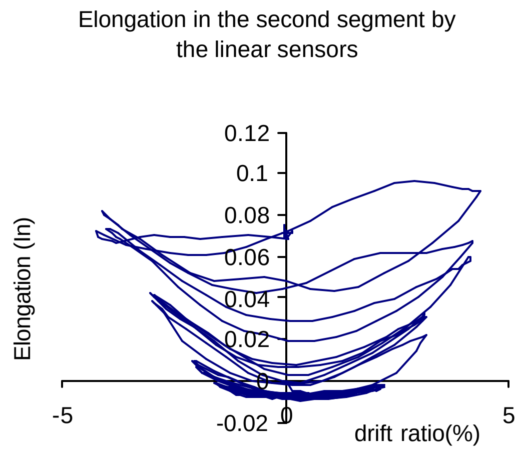
Elongation in the second segment by the linear sensors
Elongation (In)
drift ratio(%)

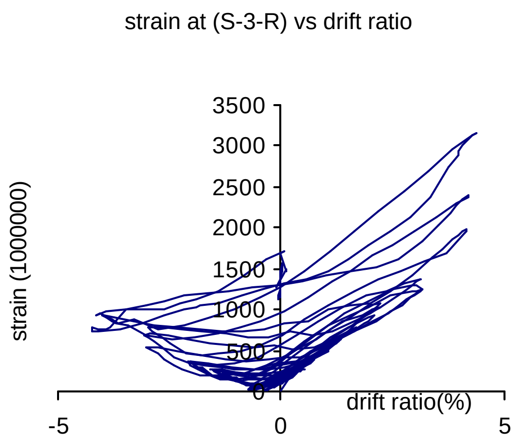
strain at (S-3-R) vs drift ratio
strain (1000000)
drift ratio(%)

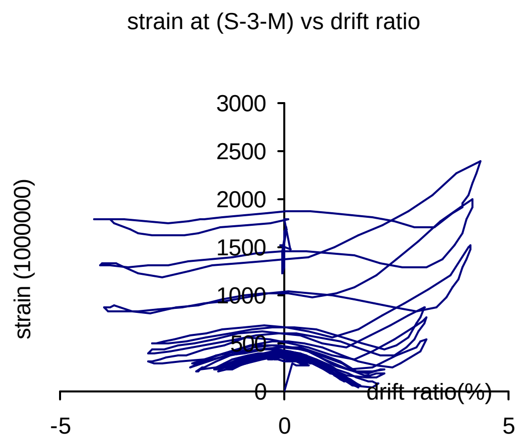
strain at (S-3-M) vs drift ratio
strain (1000000)
drift ratio(%)

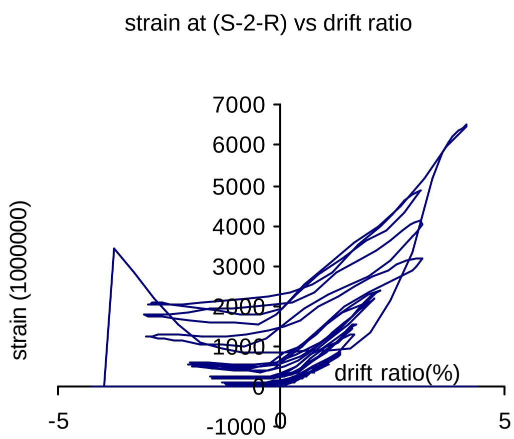
strain at (S-2-R) vs drift ratio
strain (1000000)
drift ratio(%)

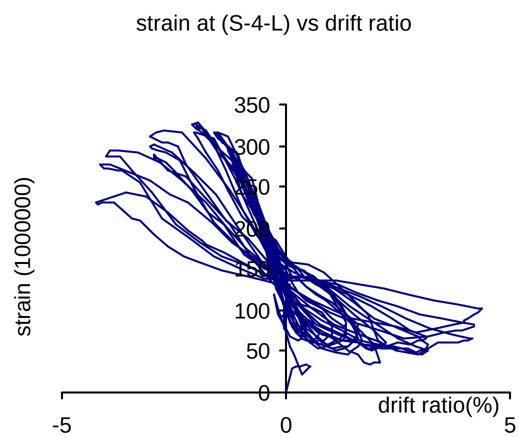
strain at (S-4-L) vs drift ratio
strain (1000000)
drift ratio(%)

Elongation in the third segment by the linear sensors

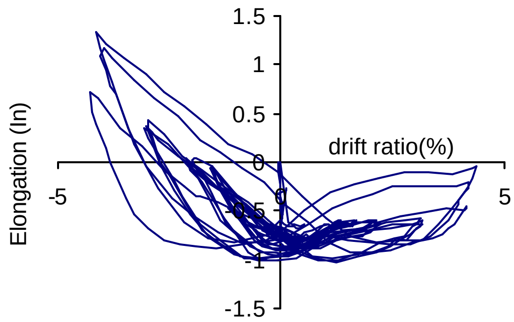

Elongation in the fourth segment by the linear sensors

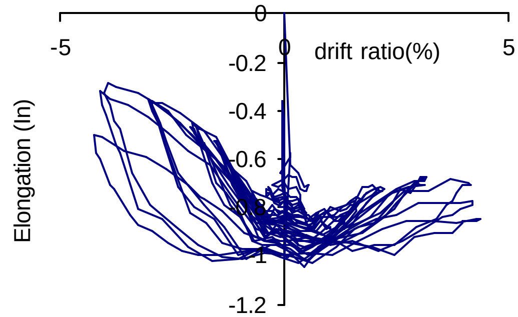

Elongation in the fifth segment by the linear sensors

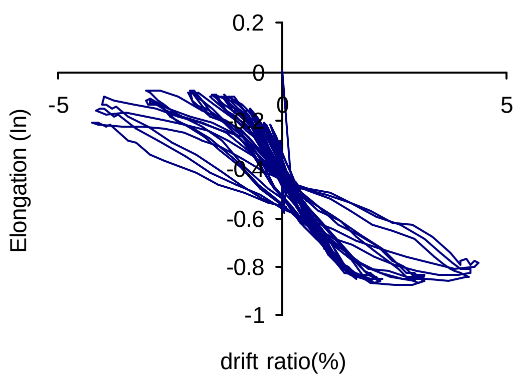

Elongation in the third level by the strain gages on rebars at opposite sides

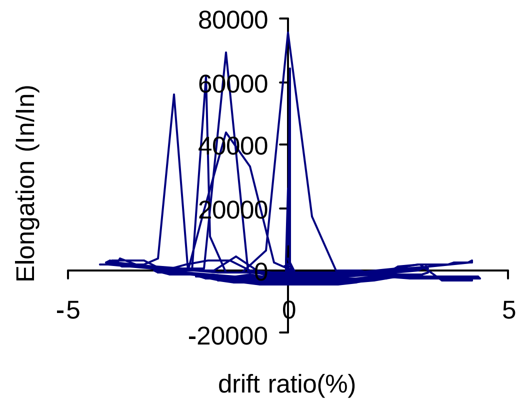

TEST GRAPHS BASED ON THE EXPERIMENTAL DATA

TEST TWO

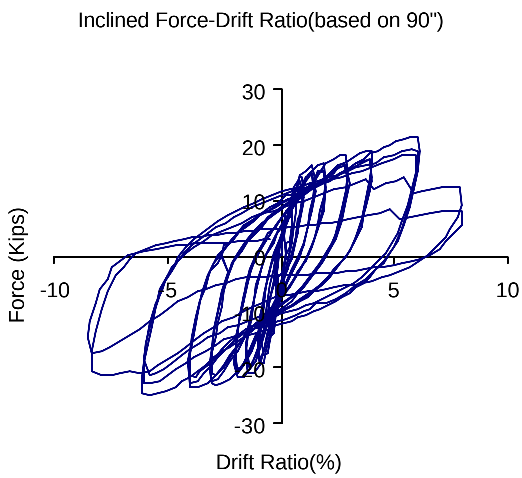
Inclined Force-Drift Ratio(based on 90")
Force (Kips)
Drift Ratio(%)
30
20
10
0
-10
-20
-30
-10
-5
5
10

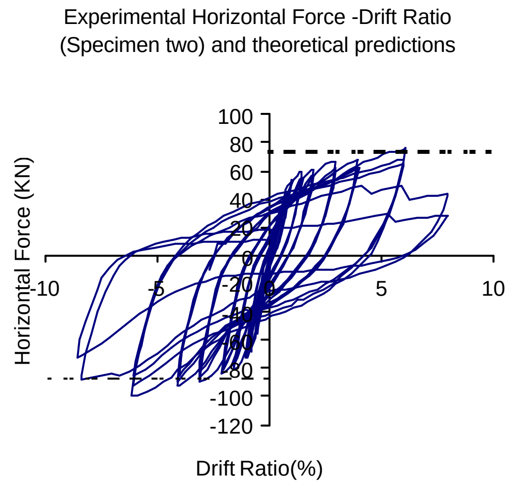
Experimental Horizontal Force -Drift Ratio
(Specimen two) and theoretical predictions
Horizontal Force (KN)
Drift Ratio(%)
100
80
60
40
20
0
-20
-40
-60
-80
-100
-120
-10
-5
0
5
10

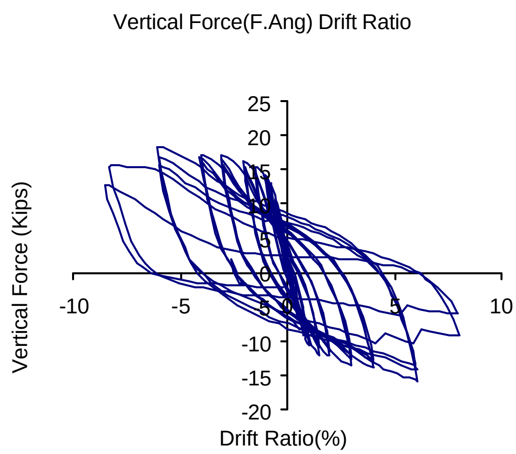
Vertical Force(F.Ang) Drift Ratio
Vertical Force (Kips)
Drift Ratio(%)
25
20
15
10
5
0
-5
-10
-15
-20
-10
-5
0
5
10

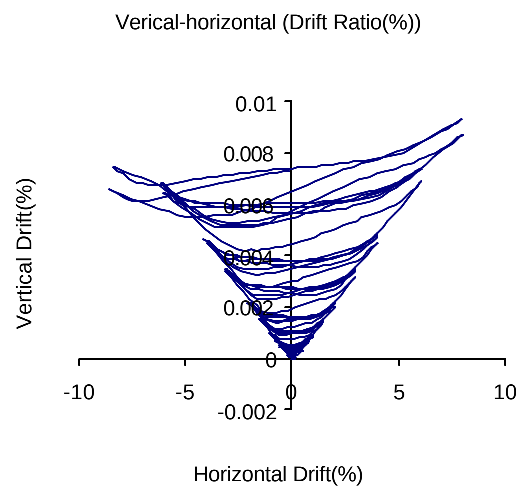
Verical-horizontal (Drift Ratio(%))
Vertical Drift(%)
Horizontal Drift(%)
0.01
0.008
0.006
0.004
0.002
0
-0.002
-10
-5
0
5
10

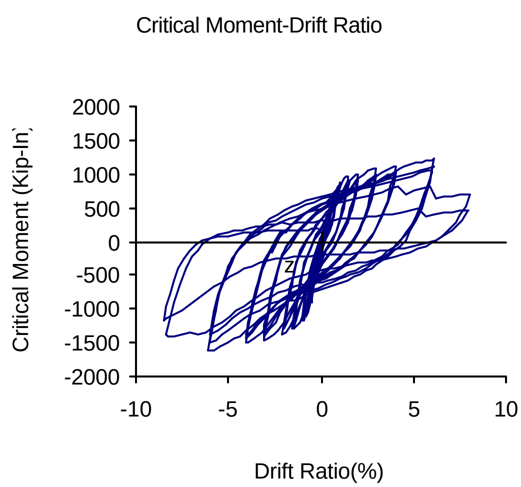
Critical Moment-Drift Ratio
Critical Moment (Kip-In)
Drift Ratio(%)
2000
1500
1000
500
0
-500
-1000
-1500
-2000
-10
-5
0
5
10

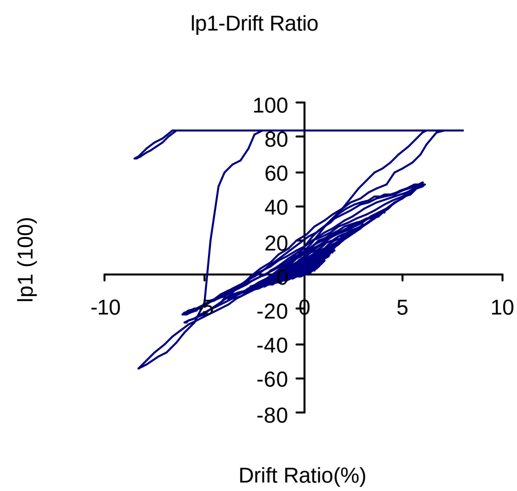
lp1-Drift Ratio
lp1 (100)
Drift Ratio(%)
100
80
60
40
20
0
-20
-40
-60
-80
-10
-5
0
5
10

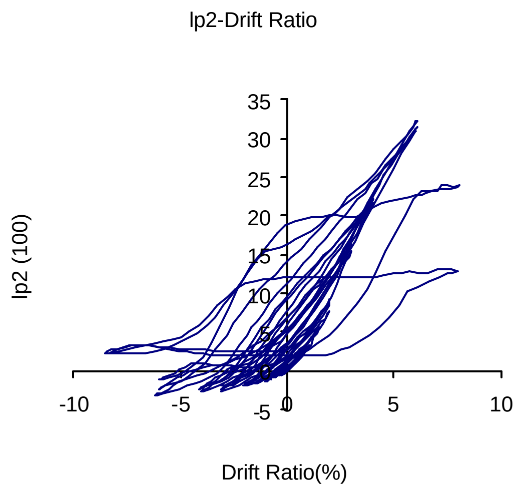
lp2-Drift Ratio
lp2 (100)
Drift Ratio(%)

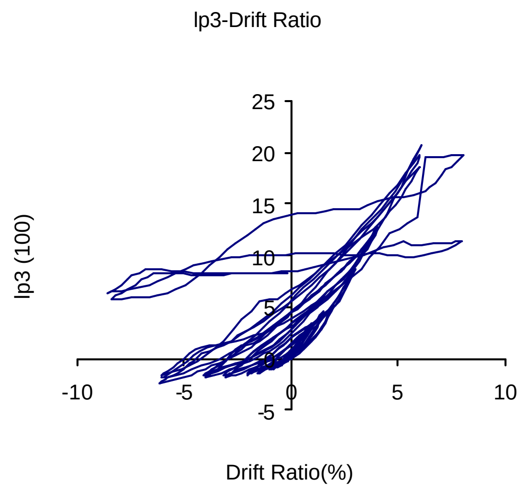
lp3-Drift Ratio
lp3 (100)
Drift Ratio(%)

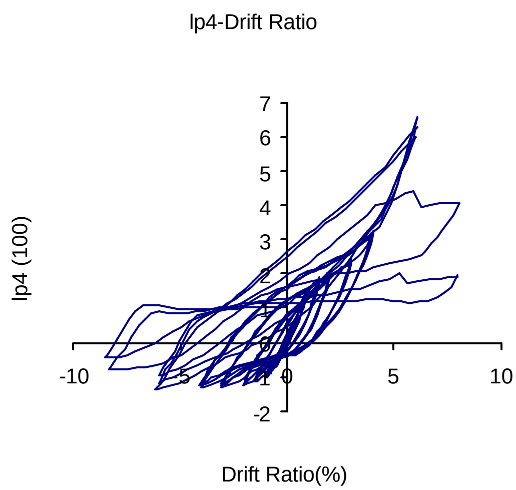
lp4-Drift Ratio
lp4 (100)
Drift Ratio(%)

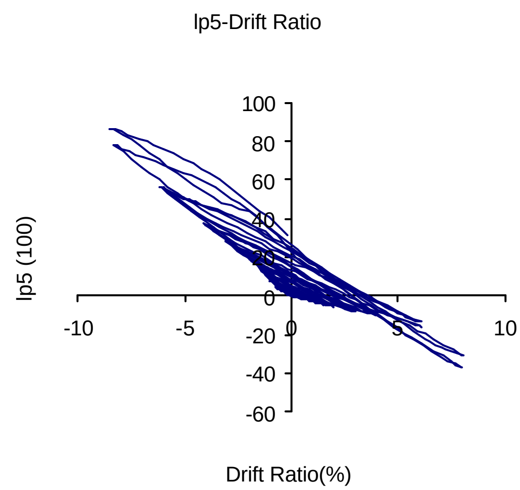
lp5-Drift Ratio
lp5 (100)
Drift Ratio(%)

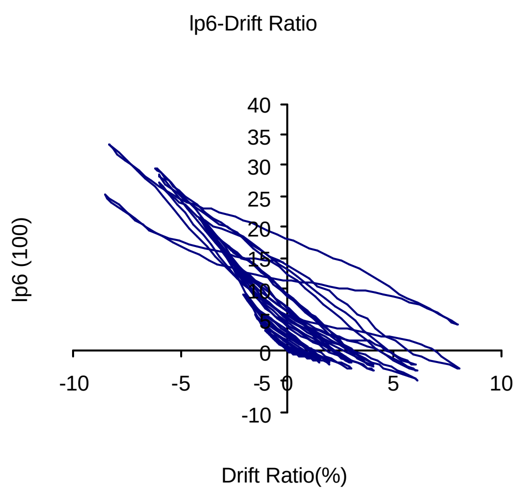
lp6-Drift Ratio
lp6 (100)
Drift Ratio(%)

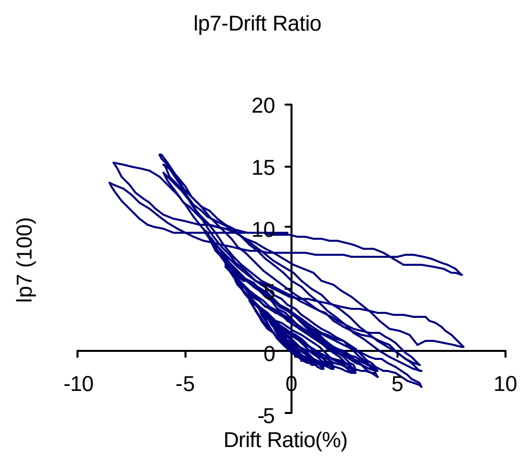
lp7-Drift Ratio
lp7 (100)
Drift Ratio(%)

lp8-Drift Ratio

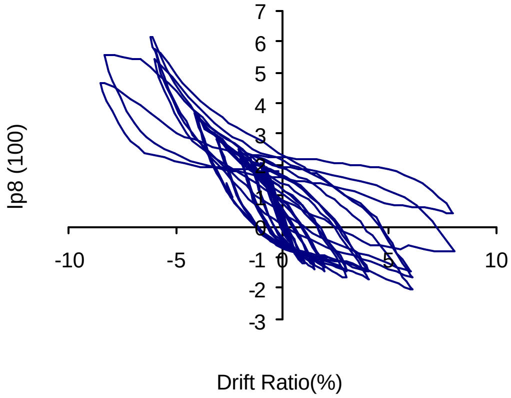

strain at (S-1-R)-Drift Ratio

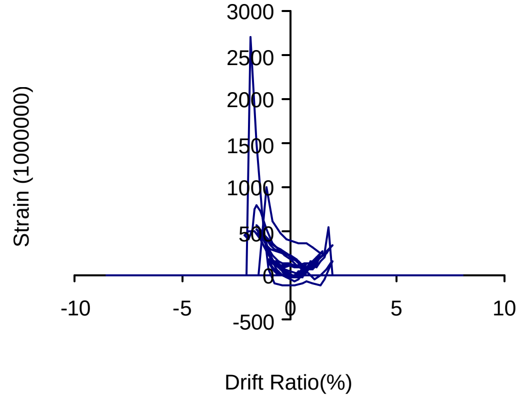

strain at (S-1-M)-Drift Ratio

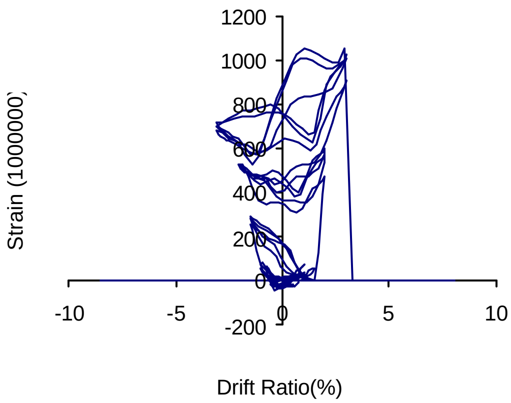

strain at (S-3-L??)-Drift Ratio

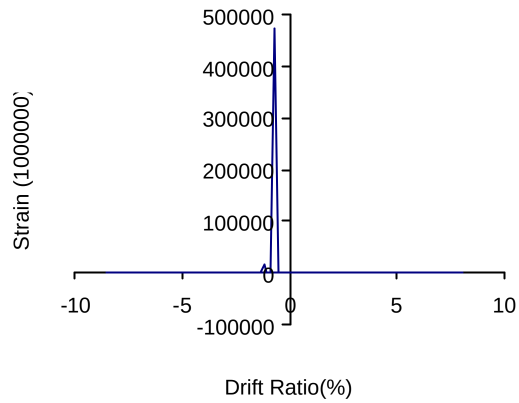

strain at (S-1-L)-Drift Ratio

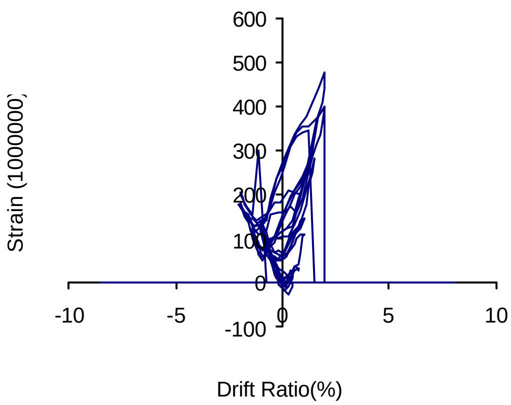

strain at (S-2-R)-Drift Ratio

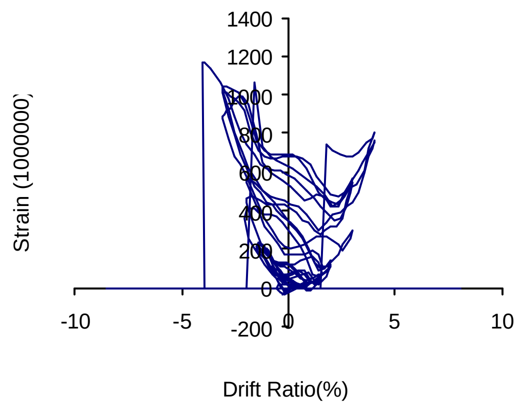

strain at (S-3-M)-Drift Ratio

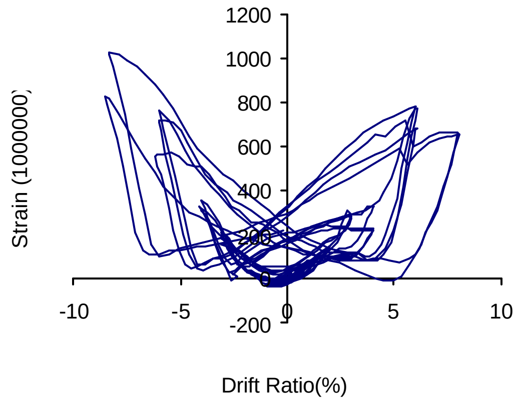

strain at (S-2-M)-Drift Ratio

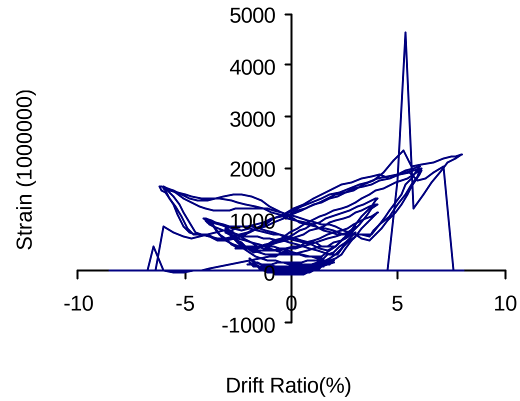

strain at (S-2-L)-Drift Ratio

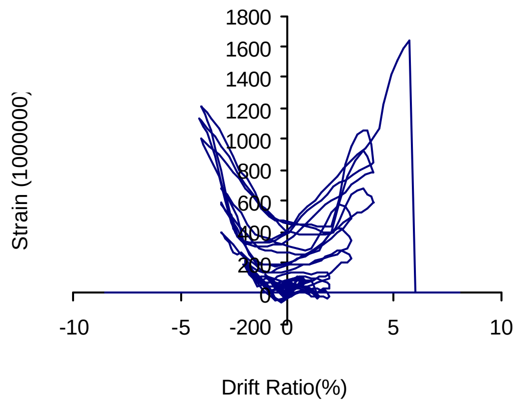

strain at (S-3-R)-Drift Ratio

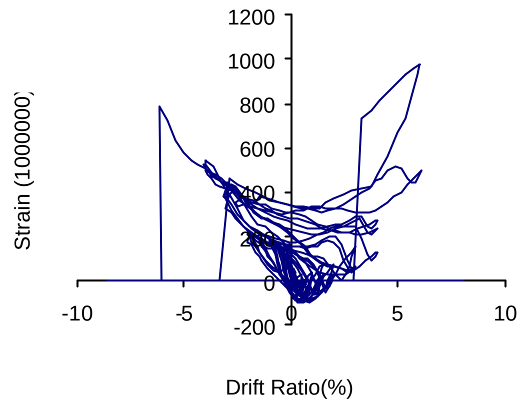

strain at (R-5-3)-Drift Ratio

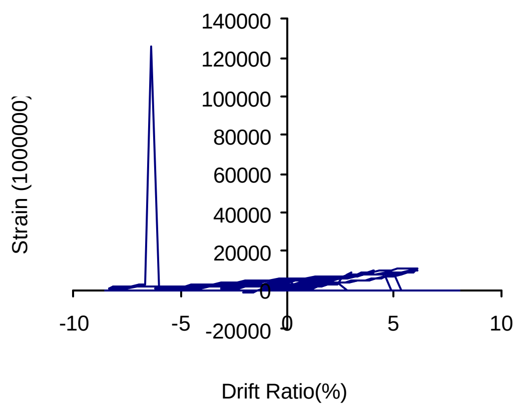

strain at (R-5-2)-Drift Ratio

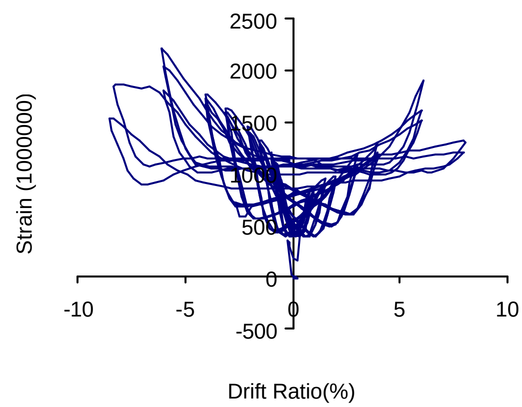

strain at (R-4-1)-Drift Ratio

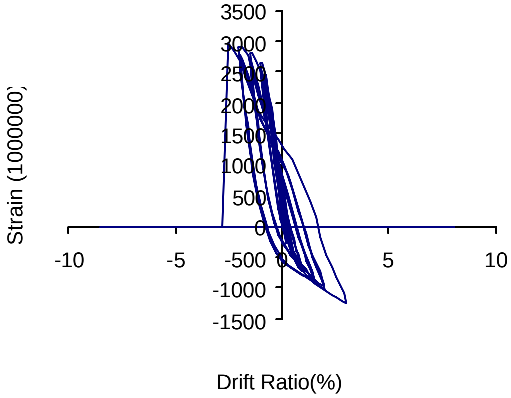

strain at (R-4-2)-Drift Ratio

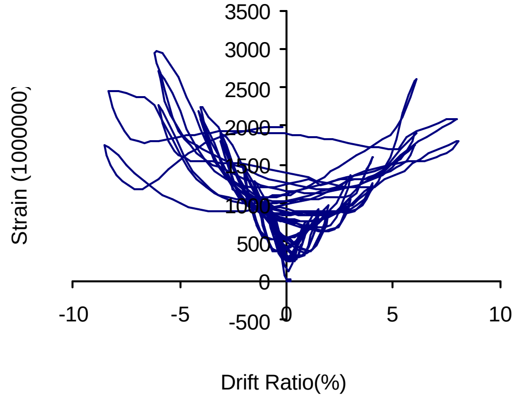

strain at (R-4-3)-Drift Ratio

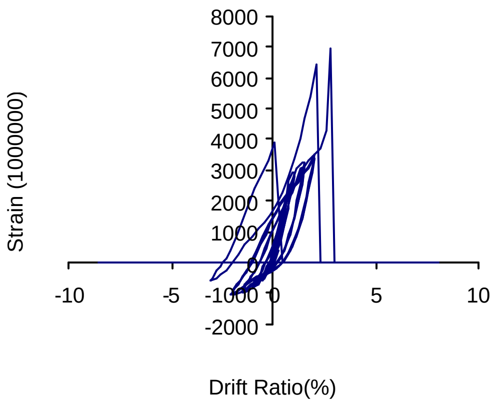

strain at (R-3-3)-Drift Ratio

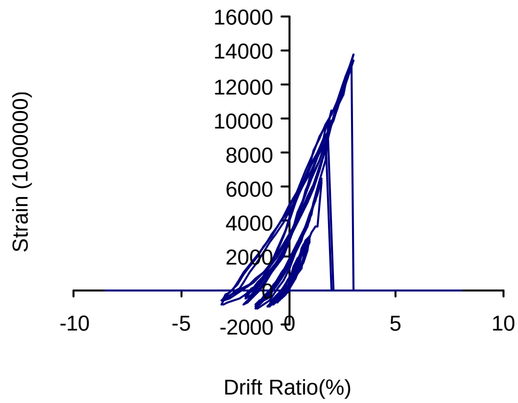

strain at (R-3-2)-Drift Ratio

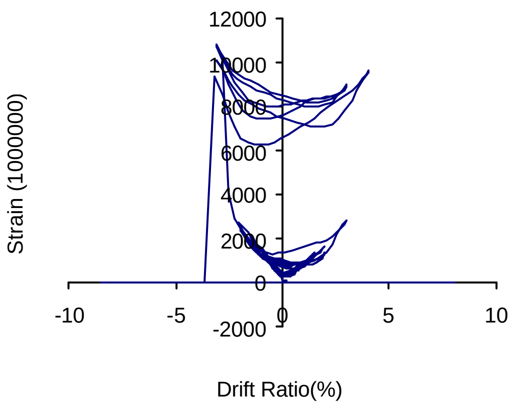

strain at (R-2-2)-Drift Ratio

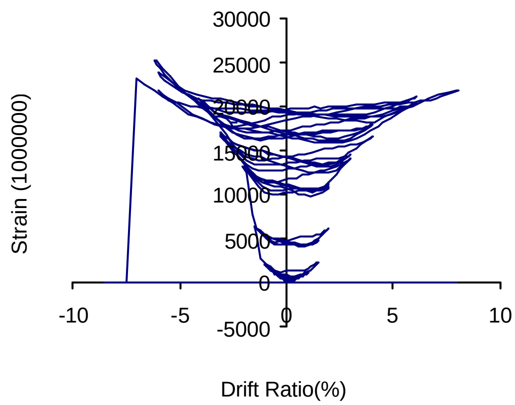

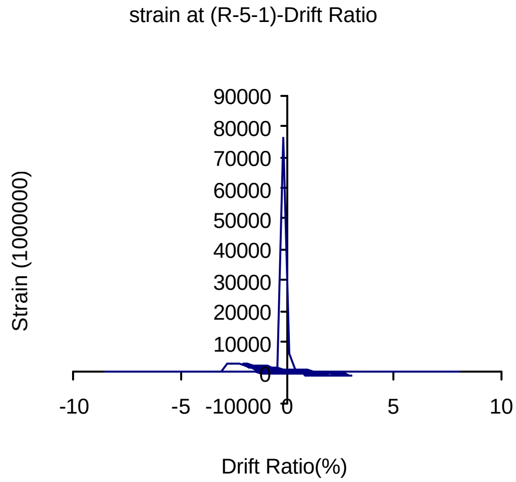
strain at (R-5-1)-Drift Ratio
Strain (1000000)
90000
80000
70000
60000
50000
40000
30000
20000
10000
0
-10000
-10
-5
0
5
10
Drift Ratio(%)

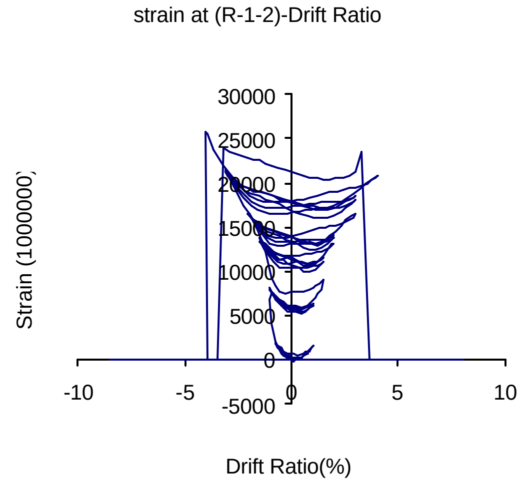
strain at (R-1-2)-Drift Ratio
Strain (1000000)
30000
25000
20000
15000
10000
5000
0
-5000
-10
-5
0
5
10
Drift Ratio(%)

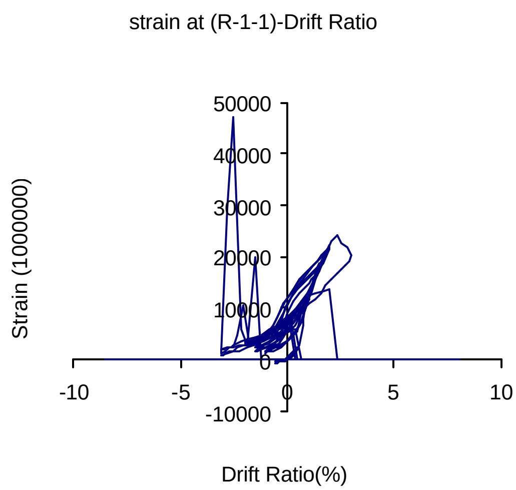
strain at (R-1-1)-Drift Ratio
Strain (1000000)
50000
40000
30000
20000
10000
0
-10000
-10
-5
0
5
10
Drift Ratio(%)

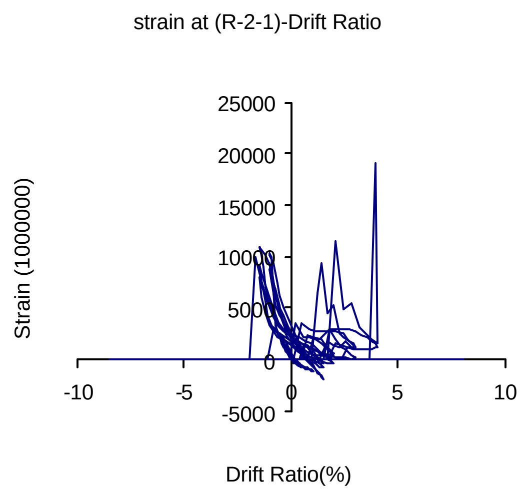
strain at (R-2-1)-Drift Ratio
Strain (1000000)
25000
20000
15000
10000
5000
0
-5000
-10
-5
0
5
10
Drift Ratio(%)

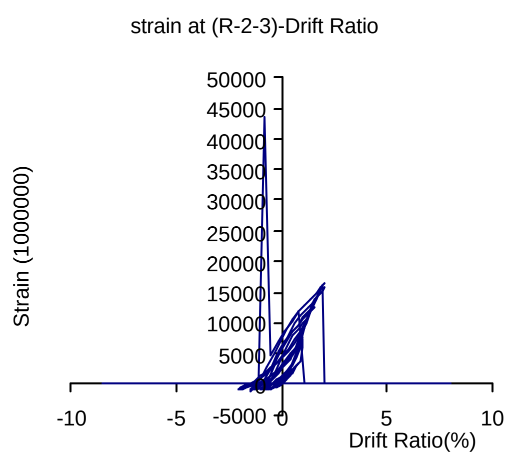
strain at (R-2-3)-Drift Ratio
Strain (1000000)
50000
45000
40000
35000
30000
25000
20000
15000
10000
5000
0
-5000
-10
-5
0
5
10
Drift Ratio(%)

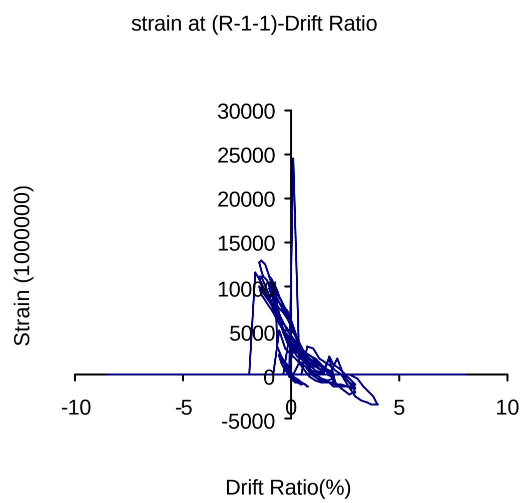
strain at (R-1-1)-Drift Ratio
Strain (1000000)
30000
25000
20000
15000
10000
5000
0
-5000
-10
-5
0
5
10
Drift Ratio(%)

strain at (R-3-1)-Drift Ratio

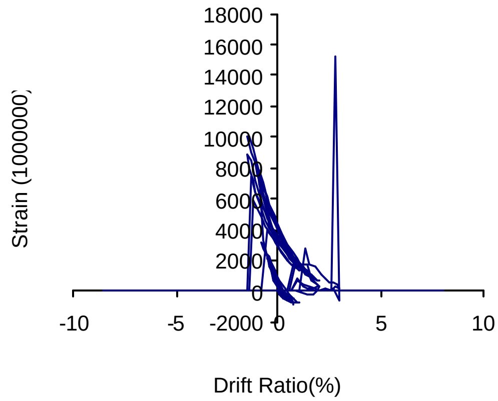

Elongation at fourth level by the gages at opposite sides-Drift Ratio (Specimen two)

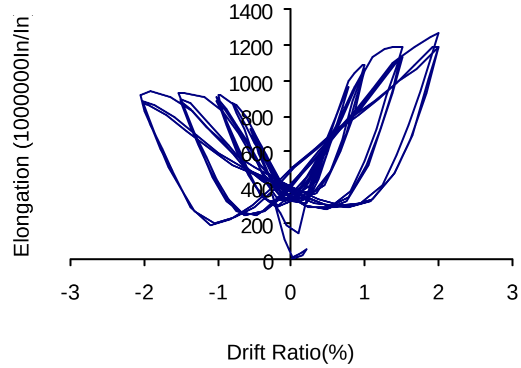

Vertical force-Vertical Displacement(Absorbed energy per one cycle for Vertical force

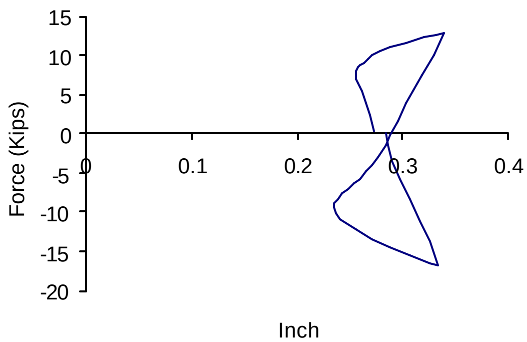

TEST GRAPHS BASED ON THE EXPERIMENTAL DATA

TEST THREE

True Horizontal Force VS Drift Ratio(w/o & w P-D),Test 3

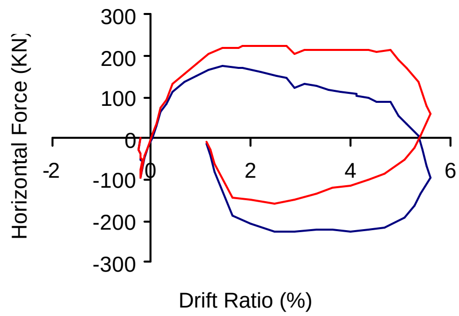

Moment Curvature in Second Segment (By Linear Sensors) and by gages

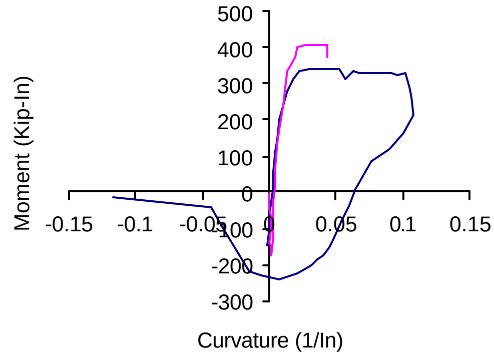

Moment Curvature by using GAGE data at first level, compared with the results from the linear sensors at 5 levels

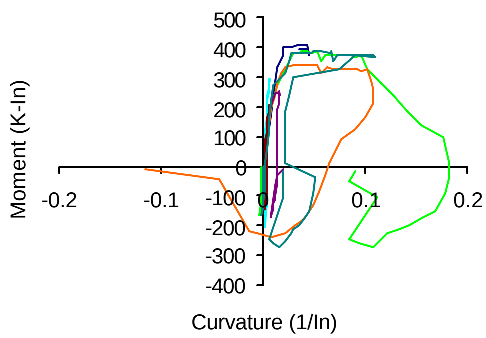

Raw Horizontal Force with and withoutcorrection, vs Drift Ratio

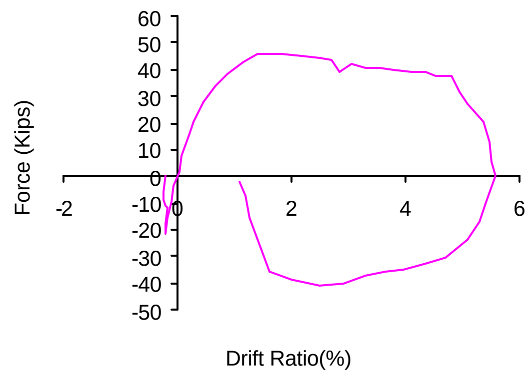

Linear Potensiometer1 vs Drift Ratio

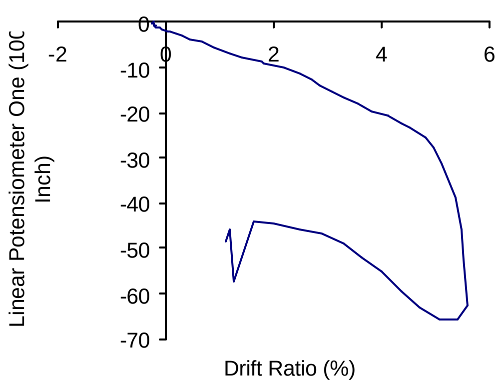

Linear Potensiometer2 vs Drift Ratio

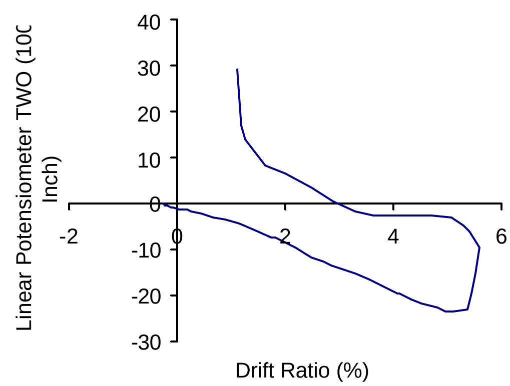

Linear Potensiometer 3 vs Drift Ratio

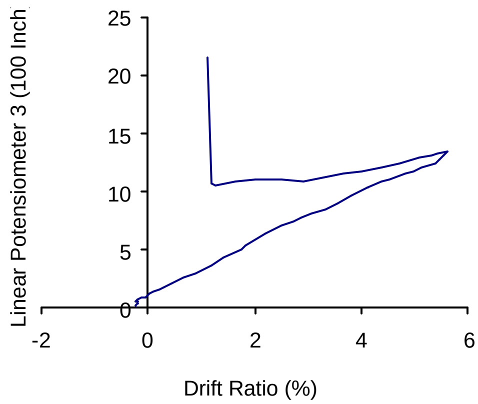

Linear Potensiometer 4 vs Drift Ratio

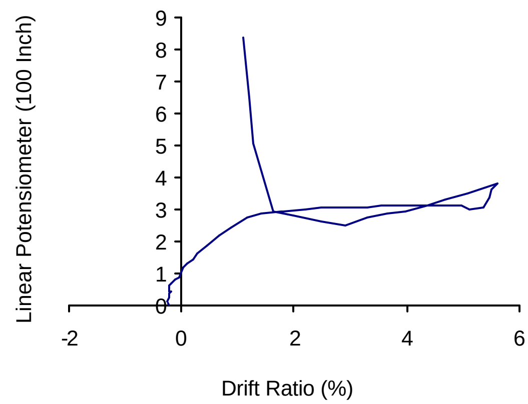

Linear Potensiometer 5 vs Drift Ratio

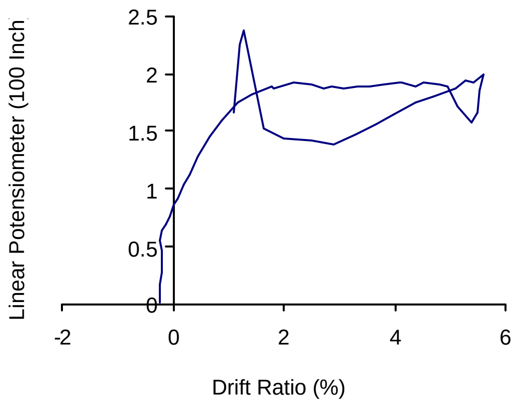

Linear Potensiometer 6 vs Drift Ratio

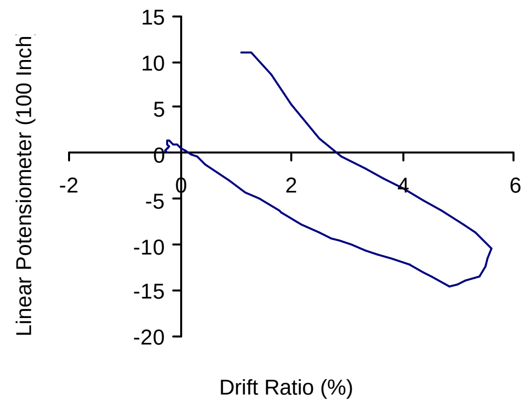

Linear Potensiometer 7 vs Drift Ratio

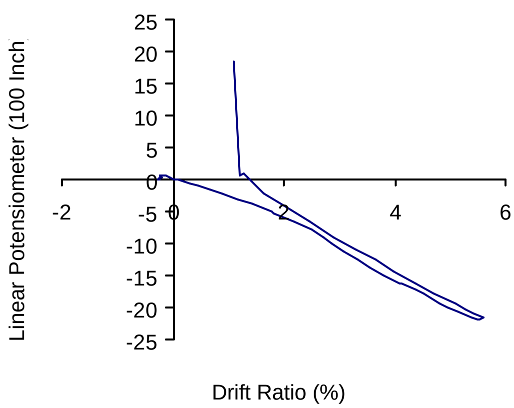

Linear Potensiometer 8 vs Drift Ratio

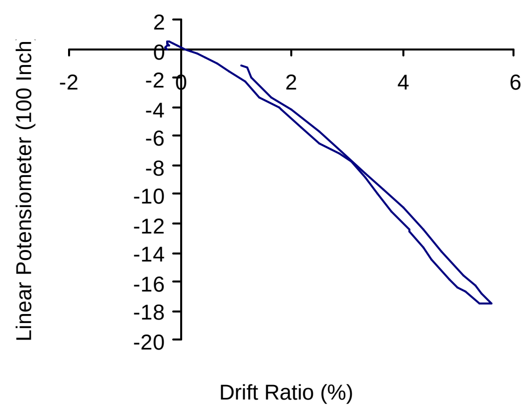

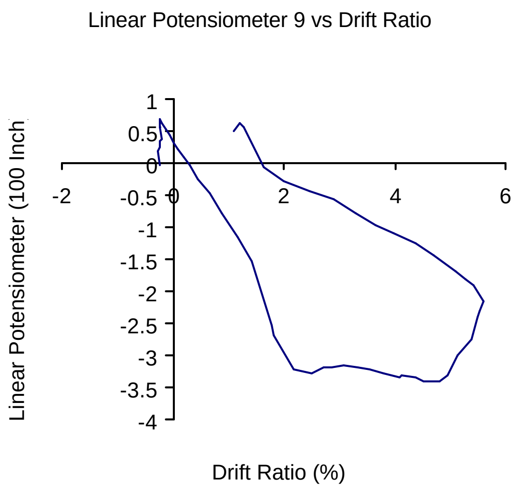
Linear Potensiometer 9 vs Drift Ratio
Linear Potensiometer (100 Inch)
Drift Ratio (%)

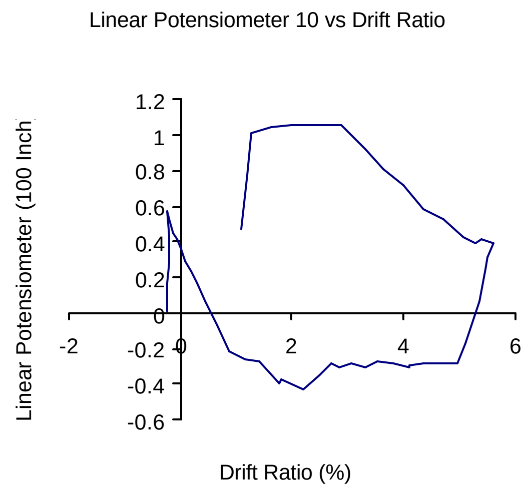
Linear Potensiometer 10 vs Drift Ratio
Linear Potensiometer (100 Inch)
Drift Ratio (%)

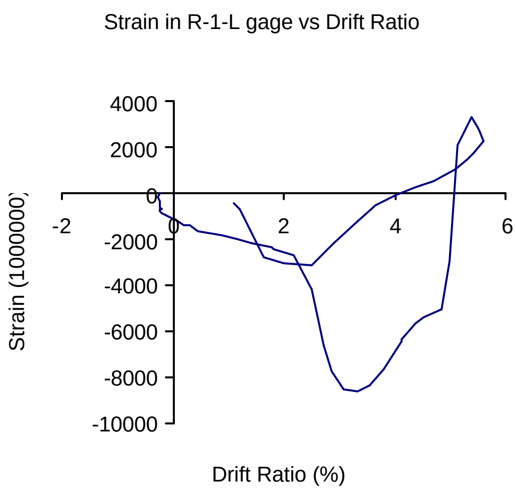
Strain in R-1-L gage vs Drift Ratio
Strain (1000000)
Drift Ratio (%)

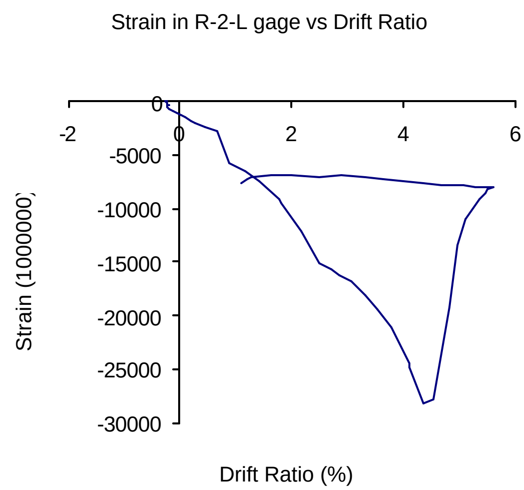
Strain in R-2-L gage vs Drift Ratio
Strain (1000000)
Drift Ratio (%)

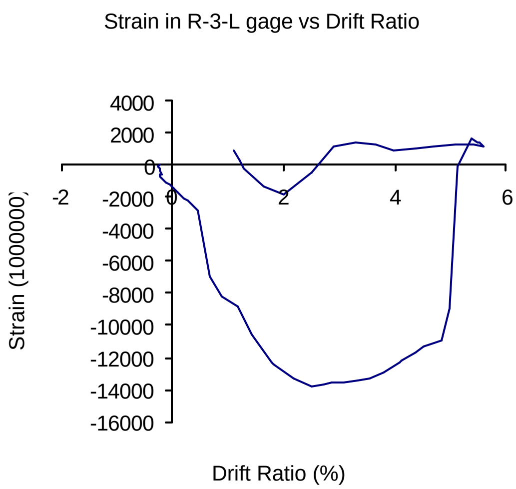
Strain in R-3-L gage vs Drift Ratio
Strain (1000000)
Drift Ratio (%)

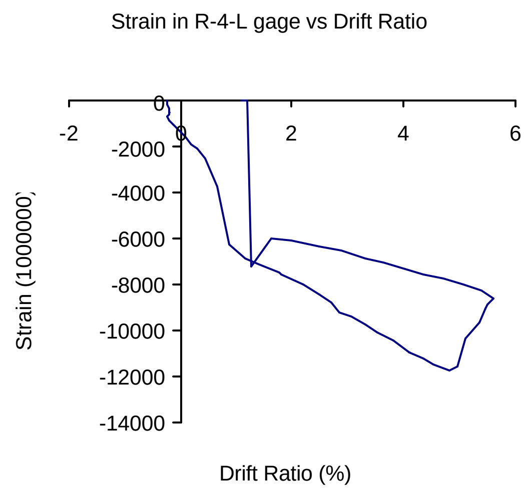
Strain in R-4-L gage vs Drift Ratio
Strain (1000000)
Drift Ratio (%)

Strain in R-5-L gage vs Drift Ratio

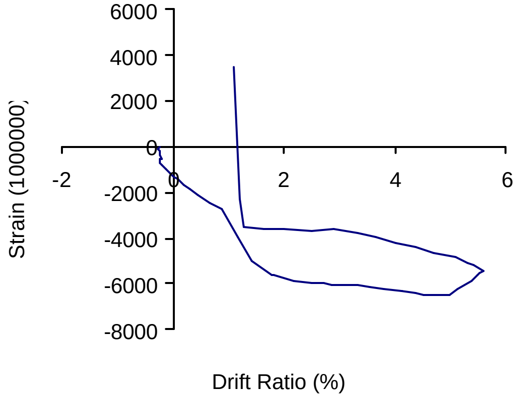

Strain in R-6-L gage vs Drift Ratio

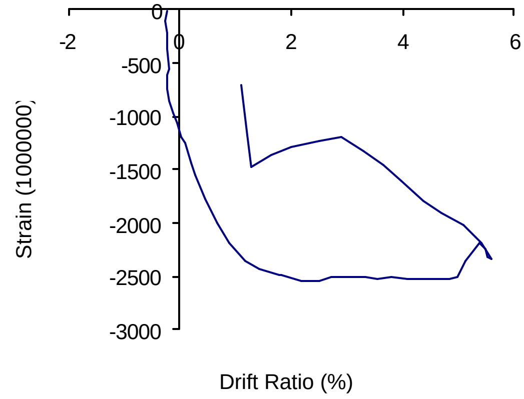

Strain in R-1-M gage vs Drift Ratio

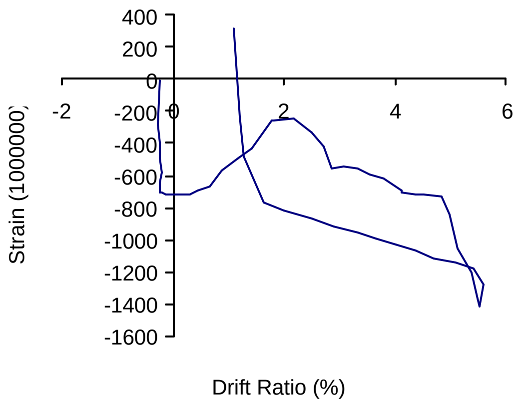

Strain in R-2-M gage vs Drift Ratio

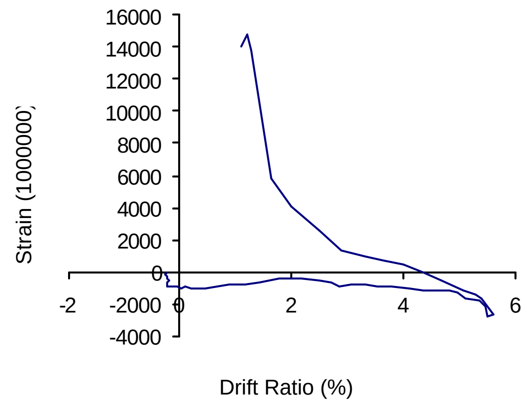

Strain in R-6-M gage vs Drift Ratio

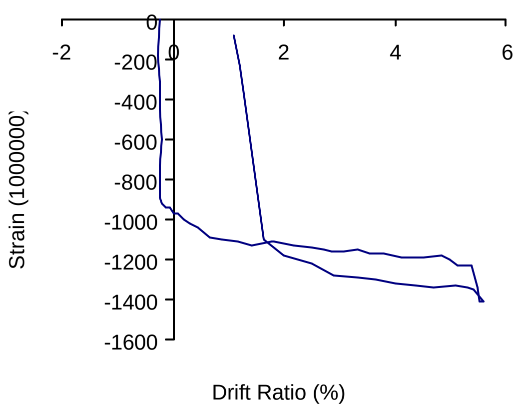

Strain in R-1-R gage vs Drift Ratio

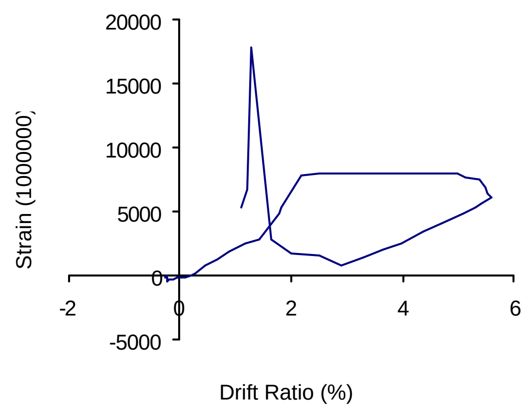

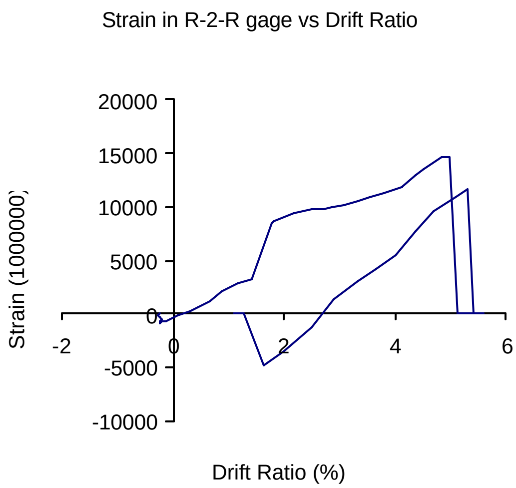
Strain in R-2-R gage vs Drift Ratio
20000
15000
10000
5000
0
-5000
-10000
-2
0
2
4
6
Strain (1000000)
Drift Ratio (%)

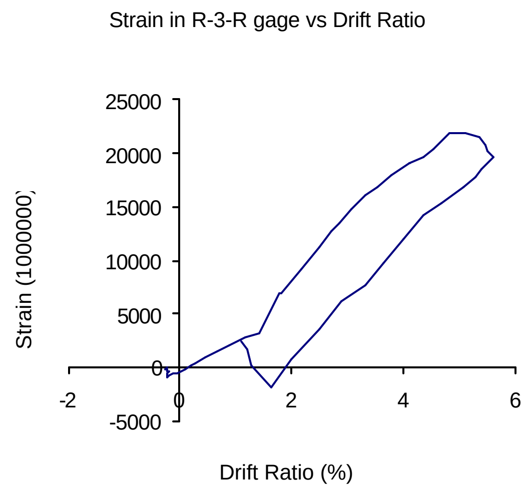
Strain in R-3-R gage vs Drift Ratio
25000
20000
15000
10000
5000
0
-5000
-2
0
2
4
6
Strain (1000000)
Drift Ratio (%)

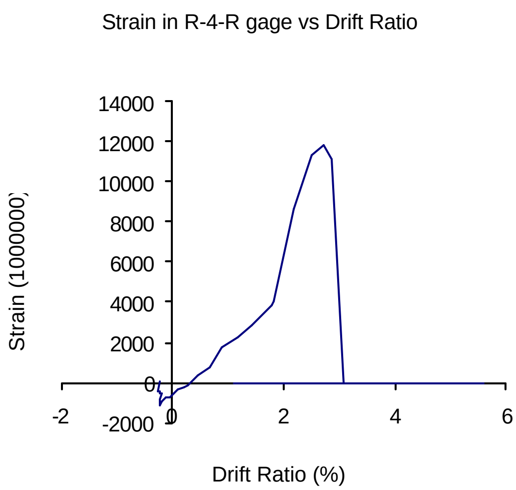
Strain in R-4-R gage vs Drift Ratio
14000
12000
10000
8000
6000
4000
2000
0
-2000
-2
0
2
4
6
Strain (1000000)
Drift Ratio (%)

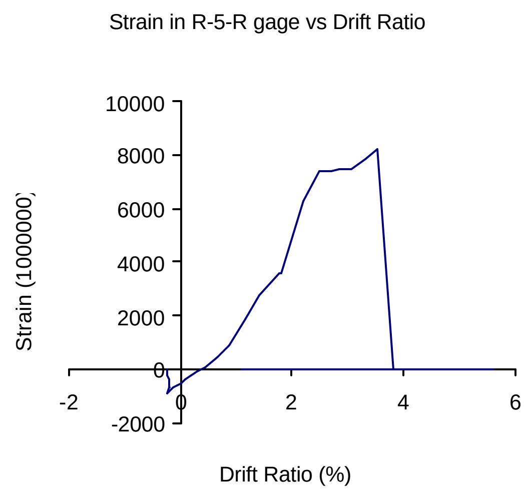
Strain in R-5-R gage vs Drift Ratio
10000
8000
6000
4000
2000
0
-2000
-2
0
2
4
6
Strain (1000000)
Drift Ratio (%)

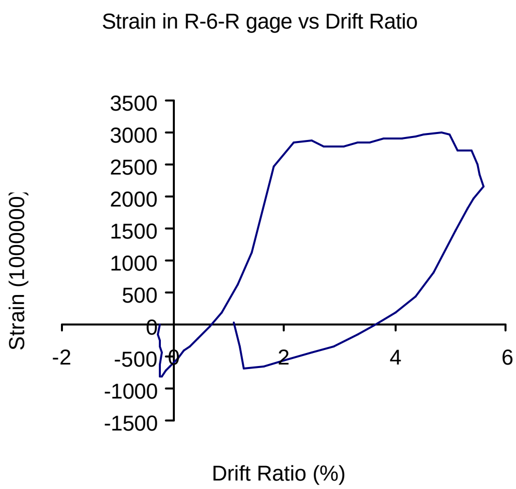
Strain in R-6-R gage vs Drift Ratio
3500
3000
2500
2000
1500
1000
500
0
-500
-1000
-1500
-2
0
2
4
6
Strain (1000000)
Drift Ratio (%)

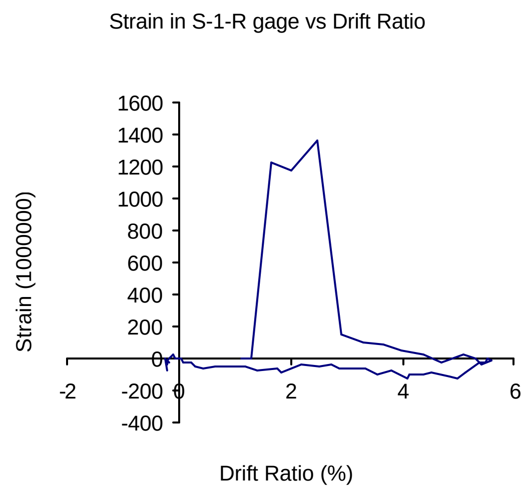
Strain in S-1-R gage vs Drift Ratio
1600
1400
1200
1000
800
600
400
200
0
-200
-400
-2
0
2
4
6
Strain (1000000)
Drift Ratio (%)

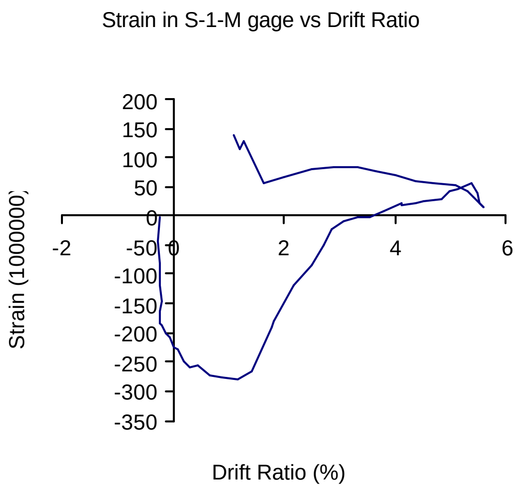
Strain in S-1-M gage vs Drift Ratio
200
150
100
50
0
-50
-100
-150
-200
-250
-300
-350
-2
0
2
4
6
Strain (1000000)
Drift Ratio (%)

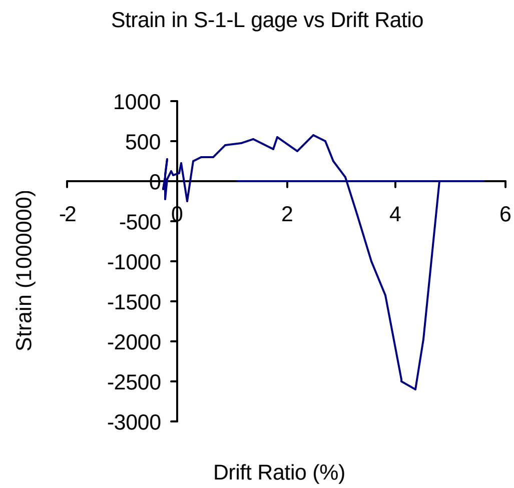
Strain in S-1-L gage vs Drift Ratio
1000
500
0
-500
-1000
-1500
-2000
-2500
-3000
-2
0
2
4
6
Strain (1000000)
Drift Ratio (%)

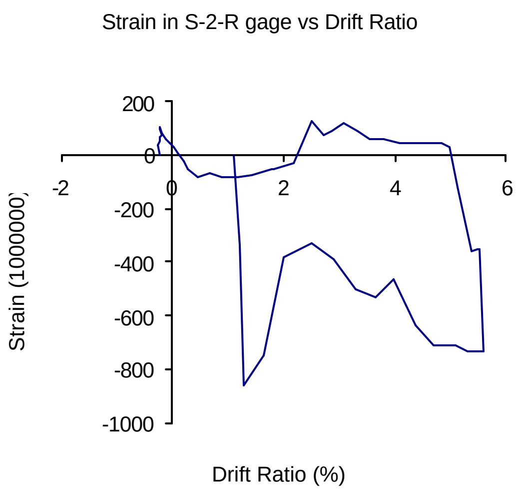
Strain in S-2-R gage vs Drift Ratio
200
0
-200
-400
-600
-800
-1000
-2
0
2
4
6
Strain (1000000)
Drift Ratio (%)

TEST GRAPHS BASED ON THE EXPERIMENTAL DATA

TEST FOUR

Horizontal Force-Drift Ratio

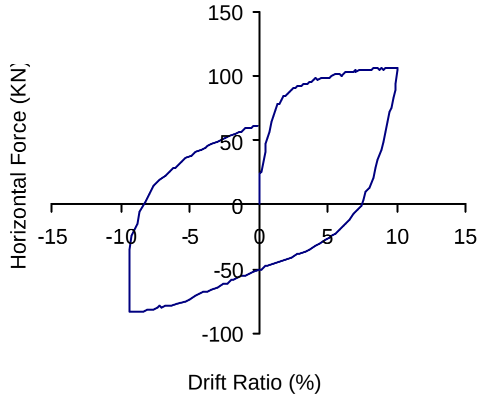

Horizontal Force-Drift Ratio

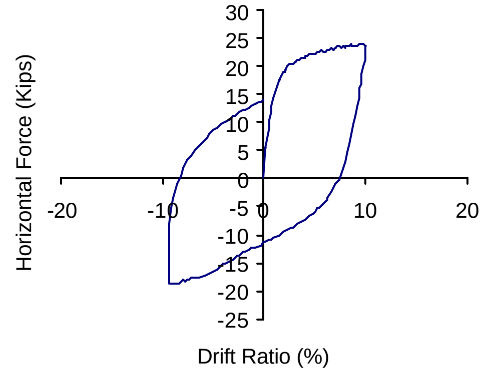

Moment-Curvature at different segments

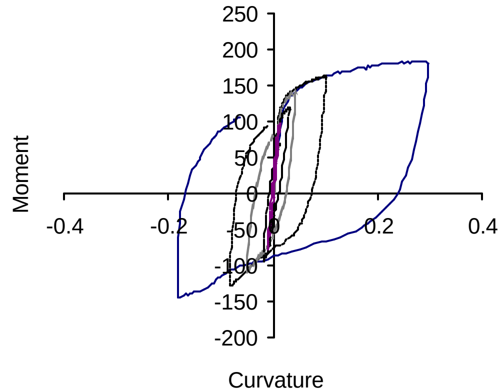

Moment-Curvature at First Segment by linear sensors, compared with the one by gages

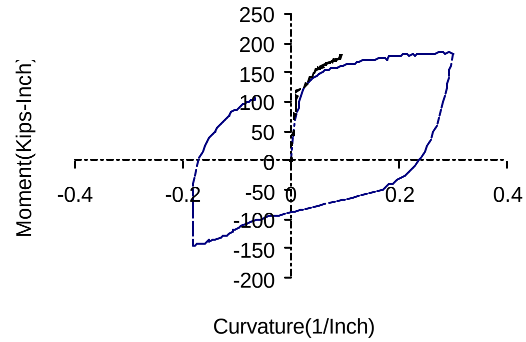

Moment-Curvature at Second Segment

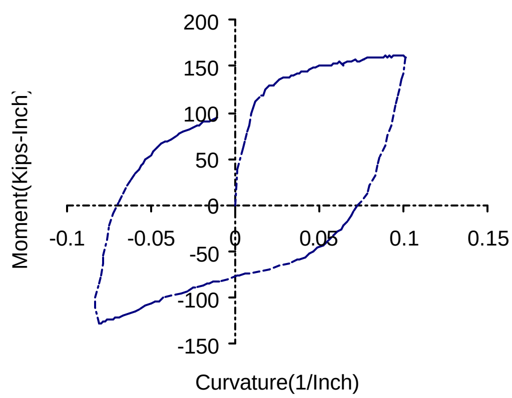

Moment Curvature by the data from Gages

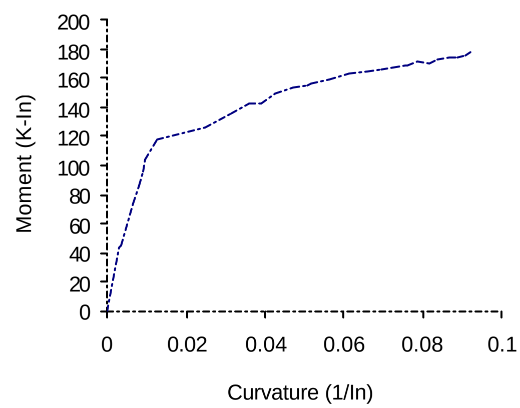

Linear Potensiometer LP-1

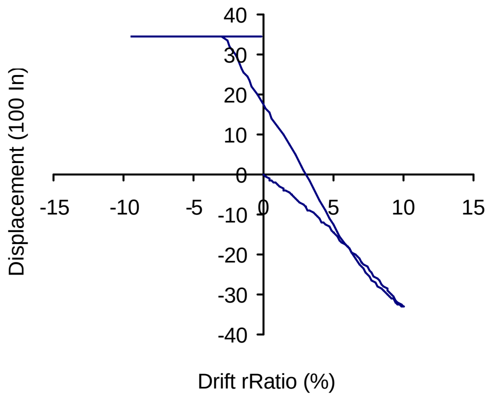

Linear Potensiometer LP-2

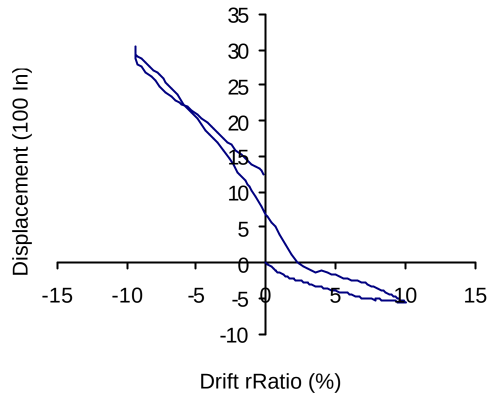

Linear Potensiometer LP-3

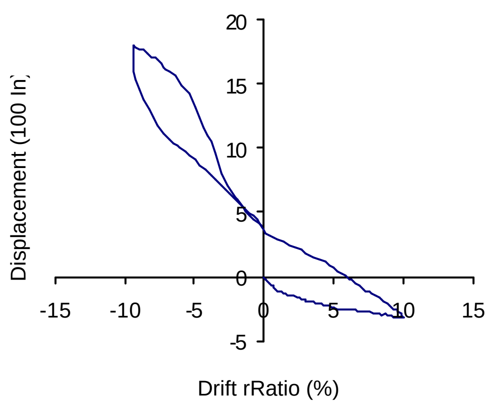

Linear Potensiometer LP-4

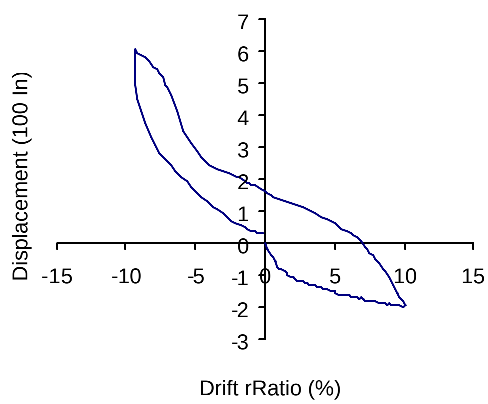

Linear Potensiometer LP-5

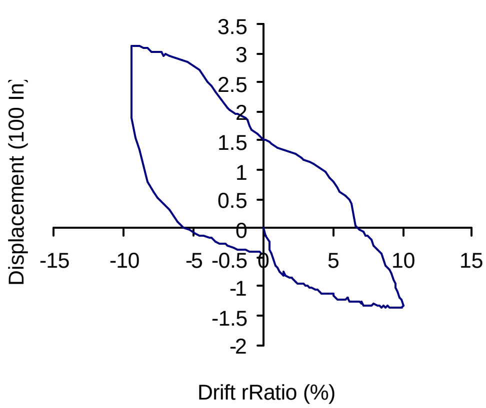

Linear Potensiometer LP-6

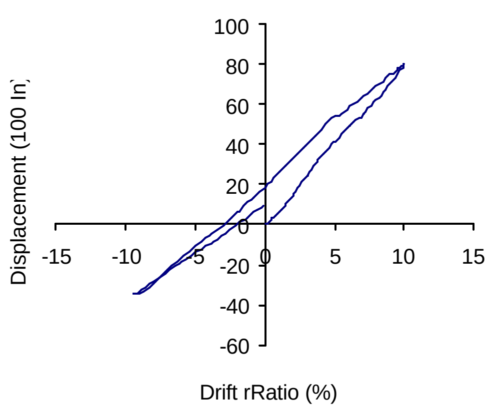

Linear Potensiometer LP-7

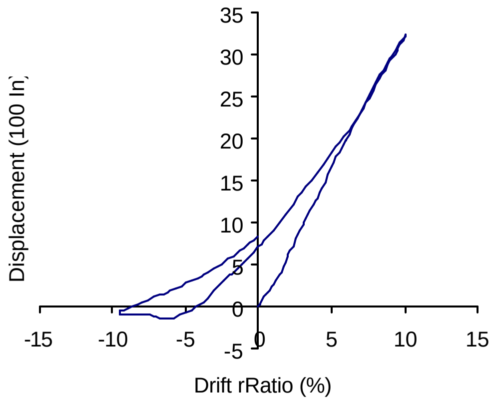

Linear Potensiometer LP-8

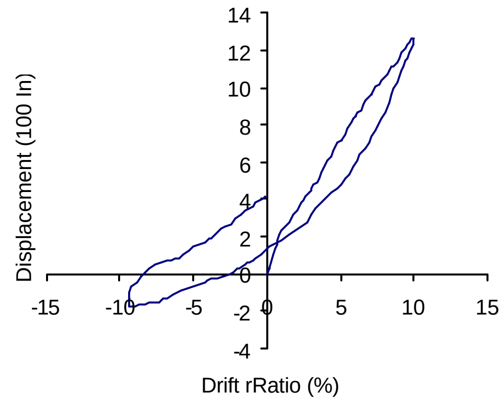

Linear Potensiometer LP-9

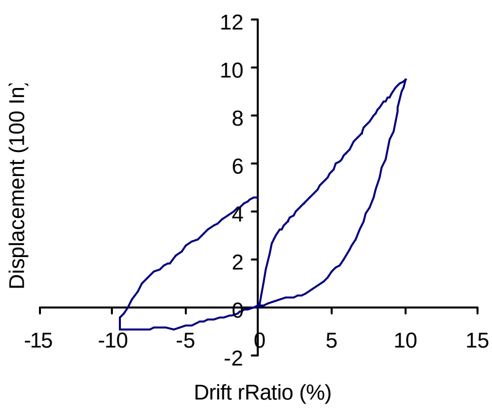

Linear Potensiometer LP-10

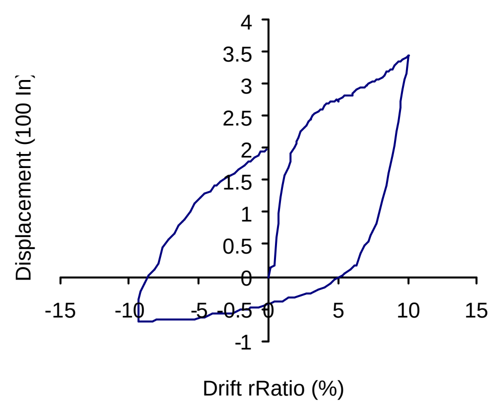

Strain in the Gage R-1-R

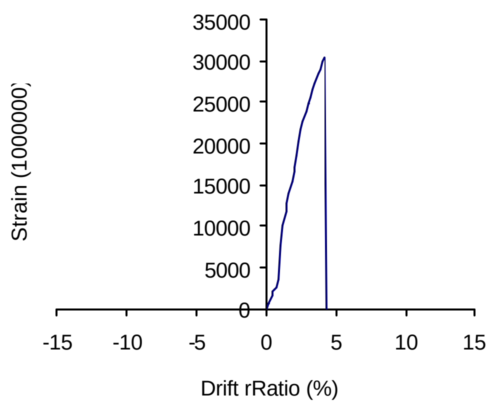

Strain in the Gage R-2-R

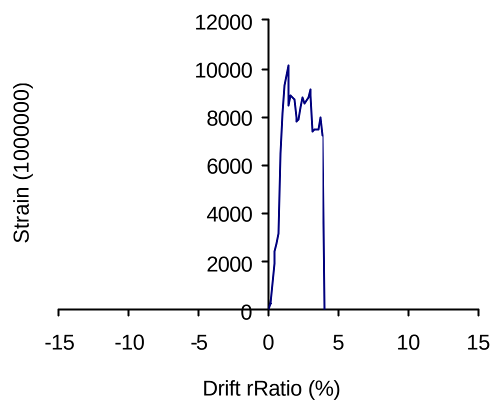

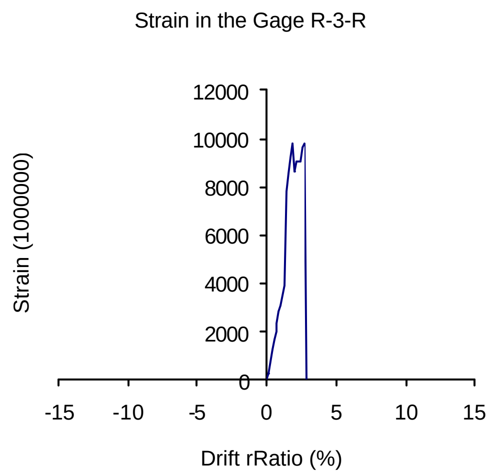
Strain in the Gage R-3-R
Strain (1000000)
12000
10000
8000
6000
4000
2000
0
-15
-10
-5
0
5
10
15
Drift rRatio (%)

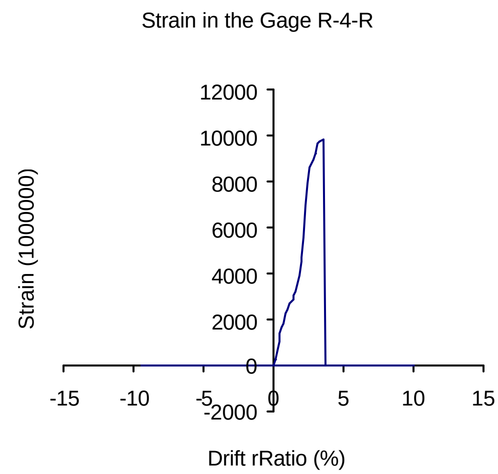
Strain in the Gage R-4-R
Strain (1000000)
12000
10000
8000
6000
4000
2000
0
-2000
-15
-10
-5
0
5
10
15
Drift rRatio (%)

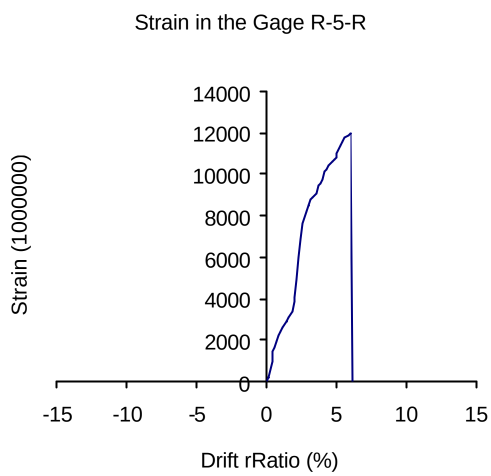
Strain in the Gage R-5-R
Strain (1000000)
14000
12000
10000
8000
6000
4000
2000
0
-15
-10
-5
0
5
10
15
Drift rRatio (%)

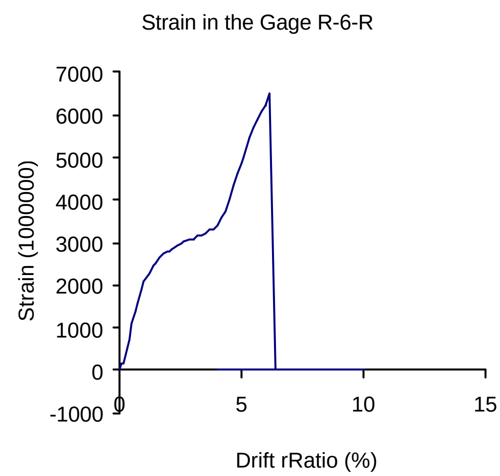
Strain in the Gage R-6-R
Strain (1000000)
7000
6000
5000
4000
3000
2000
1000
0
-1000
0
5
10
15
Drift rRatio (%)

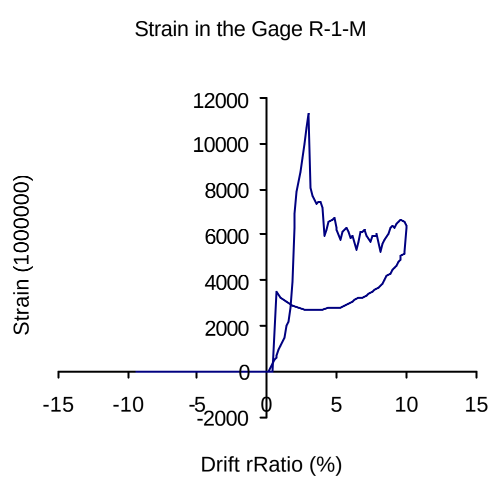
Strain in the Gage R-1-M
Strain (1000000)
12000
10000
8000
6000
4000
2000
0
-2000
-15
-10
-5
0
5
10
15
Drift rRatio (%)

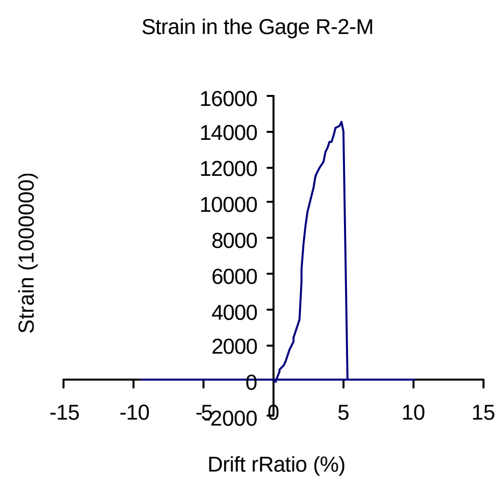
Strain in the Gage R-2-M
Strain (1000000)
16000
14000
12000
10000
8000
6000
4000
2000
0
-2000
-15
-10
-5
0
5
10
15
Drift rRatio (%)

Strain in the Gage S-1_R

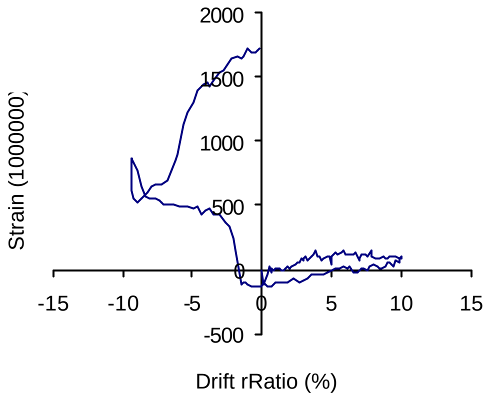

Strain in the Gage S-1-L

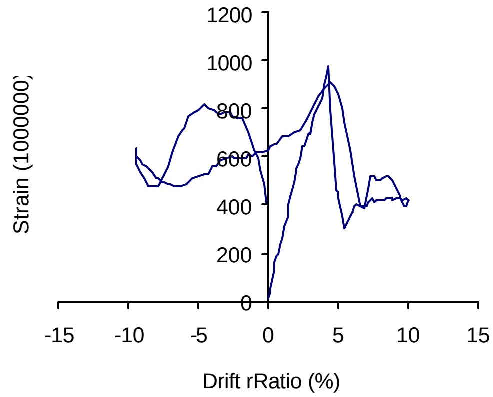

Strain in the Gage S-2-R

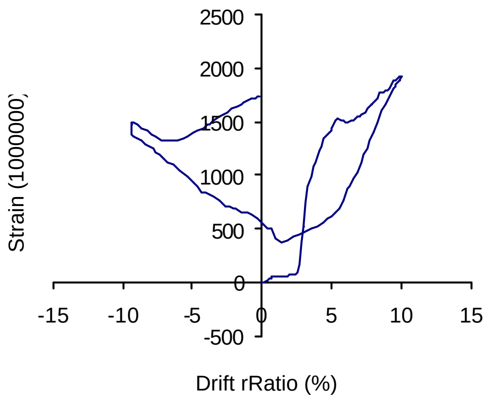

TEST GRAPHS BASED ON THE EXPERIMENTAL DATA

TEST FIVE

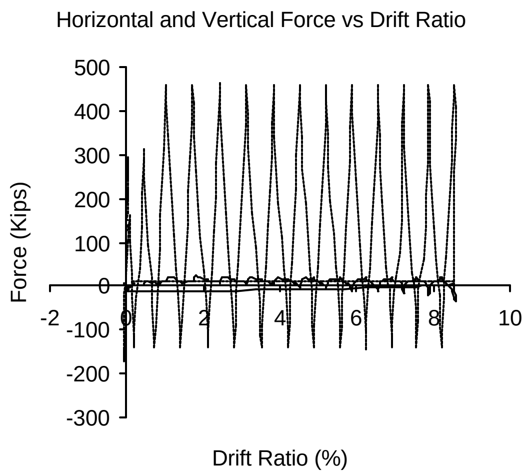
Horizontal and Vertical Force vs Drift Ratio
Force (Kips)
500
400
300
200
100
0
-100
-200
-300
-2
0
2
4
6
8
10
Drift Ratio (%)

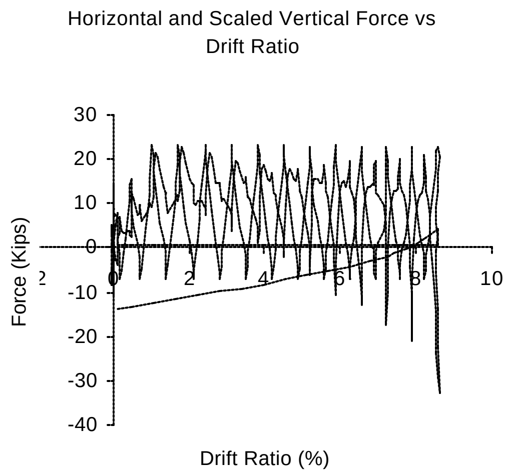
Horizontal and Scaled Vertical Force vs Drift Ratio
Force (Kips)
30
20
10
0
-10
-20
-30
-40
0
2
4
6
8
10
Drift Ratio (%)

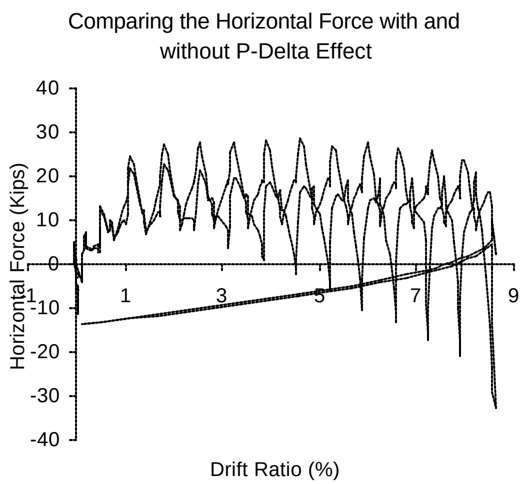
Comparing the Horizontal Force with and without P-Delta Effect
Horizontal Force (Kips)
40
30
20
10
0
-10
-20
-30
-40
1
3
5
7
9
Drift Ratio (%)

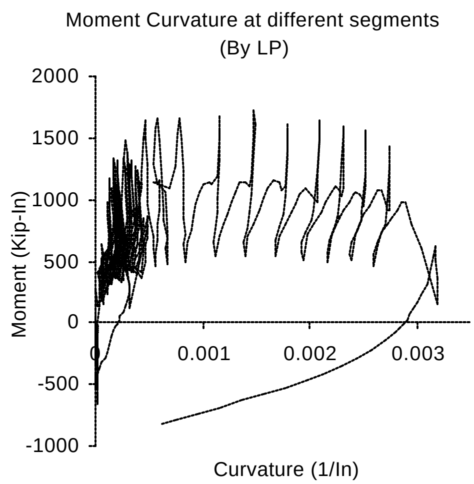
Moment Curvature at different segments (By LP)
Moment (Kip-In)
2000
1500
1000
500
0
-500
-1000
0
0.001
0.002
0.003
Curvature (1/In)

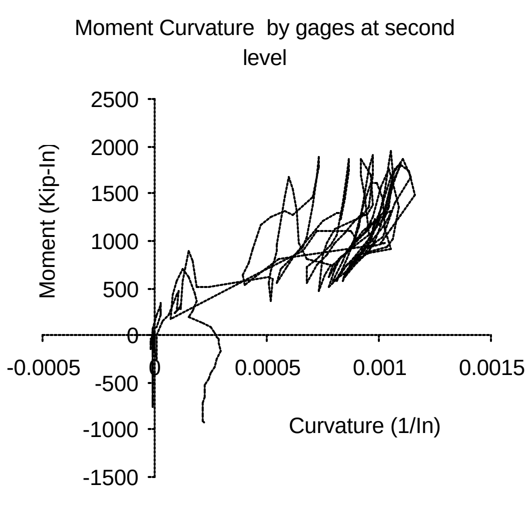
Moment Curvature by gages at second level
Moment (Kip-In)
2500
2000
1500
1000
500
0
-500
-1000
-1500
-0.0005
0
0.0005
0.001
0.0015
Curvature (1/In)

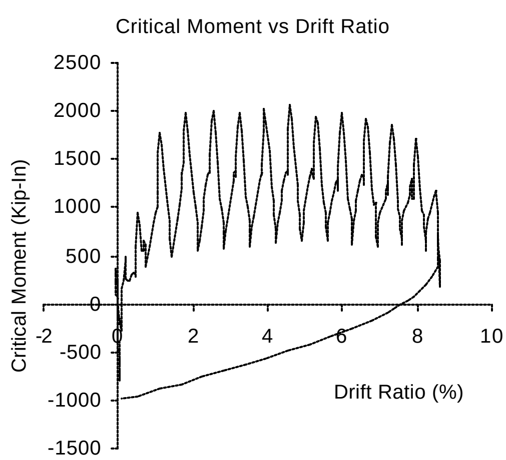
Critical Moment vs Drift Ratio
Critical Moment (Kip-In)
2500
2000
1500
1000
500
0
-500
-1000
-1500
-2
0
2
4
6
8
10
Drift Ratio (%)

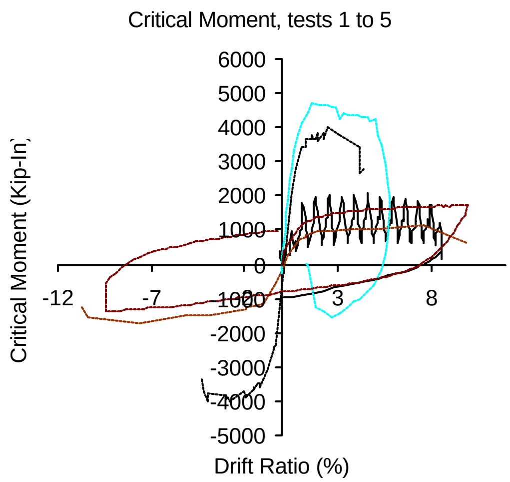
Critical Moment, tests 1 to 5
Critical Moment (Kip-In)
Drift Ratio (%)
6000
5000
4000
3000
2000
1000
0
-1000
-2000
-3000
-4000
-5000
-12
-7
-2
3
8

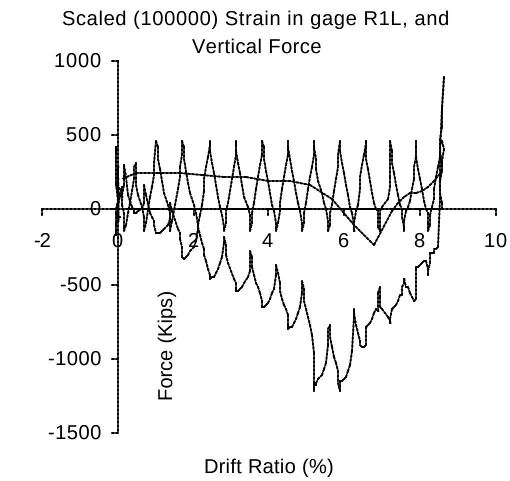
Scaled (100000) Strain in gage R1L, and Vertical Force
Force (Kips)
Drift Ratio (%)
1000
500
0
-500
-1000
-1500
-2
0
2
4
6
8
10

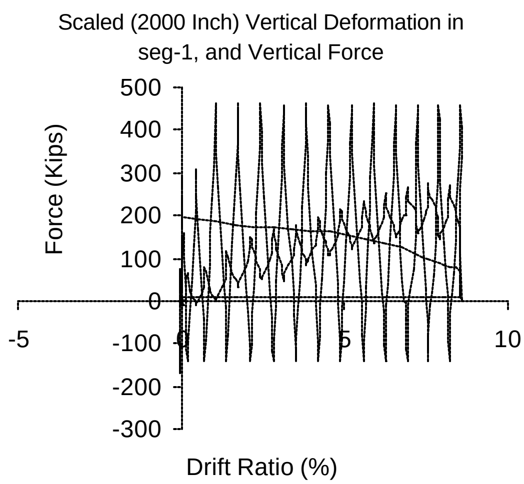
Scaled (2000 Inch) Vertical Deformation in seg-1, and Vertical Force
Force (Kips)
Drift Ratio (%)
500
400
300
200
100
0
-100
-200
-300
-5
0
5
10

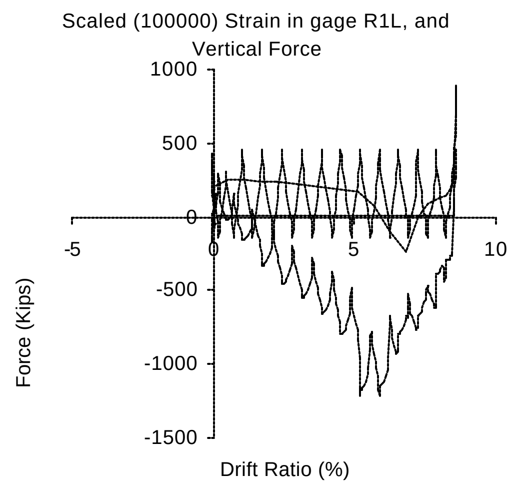
Scaled (100000) Strain in gage R1L, and Vertical Force
Force (Kips)
Drift Ratio (%)
1000
500
0
-500
-1000
-1500
-5
0
5
10

Z

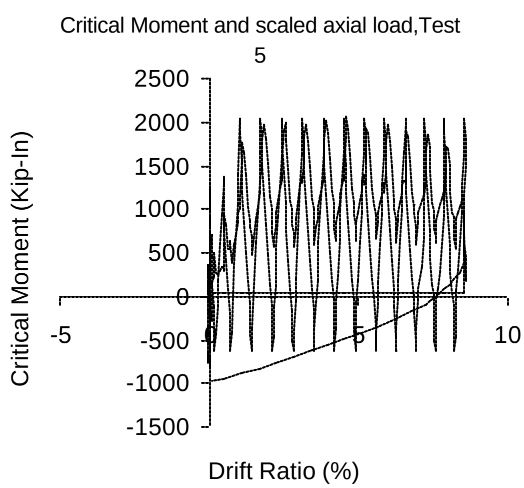
Critical Moment and scaled axial load,Test 5
Critical Moment (Kip-In)
Drift Ratio (%)
2500
2000
1500
1000
500
0
-500
-1000
-1500
-5
0
5
10

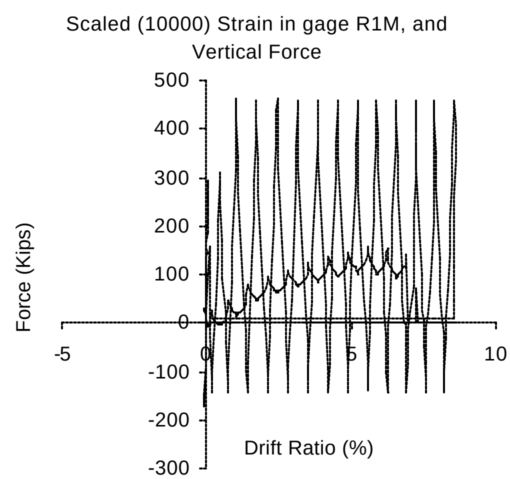
Scaled (10000) Strain in gage R1M, and Vertical Force
Force (Kips)
Drift Ratio (%)
500
400
300
200
100
0
-100
-200
-300
-5
0
5
10

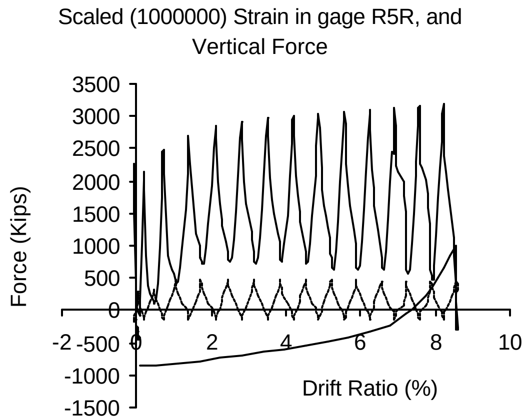
Scaled (1000000) Strain in gage R5R, and Vertical Force
Force (Kips)
Drift Ratio (%)
3500
3000
2500
2000
1500
1000
500
0
-500
-1000
-1500
-2
0
2
4
6
8
10

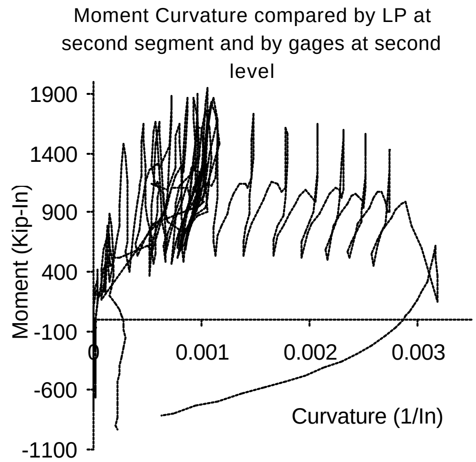
Moment Curvature compared by LP at second segment and by gages at second level
Moment (Kip-In)
Curvature (1/In)
1900
1400
900
400
-100
-600
-1100
0
0.001
0.002
0.003

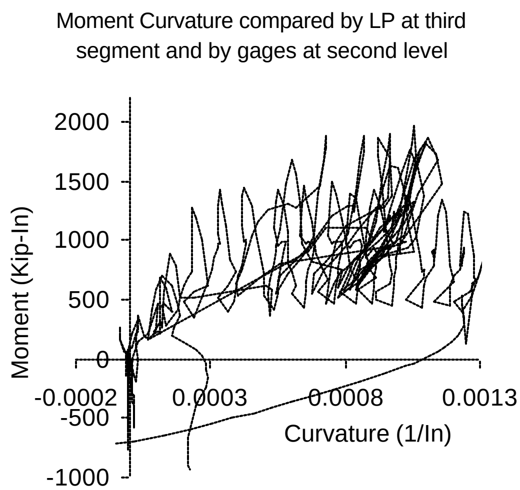
Moment Curvature compared by LP at third segment and by gages at second level
Moment (Kip-In)
Curvature (1/In)
2000
1500
1000
500
0
-500
-1000
-0.0002
0.0003
0.0008
0.0013

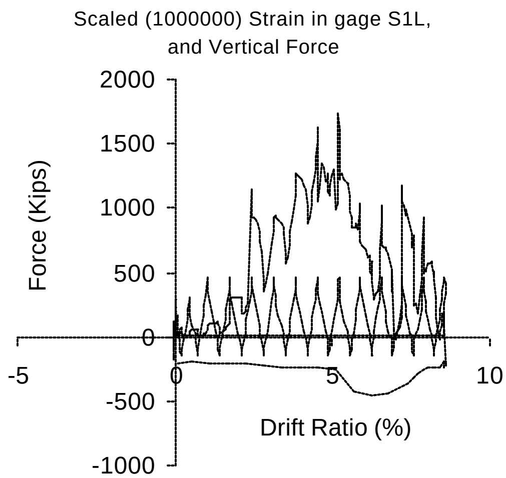
Scaled (1000000) Strain in gage S1L, and Vertical Force
Force (Kips)
Drift Ratio (%)
2000
1500
1000
500
0
-500
-1000
-5
0
5
10

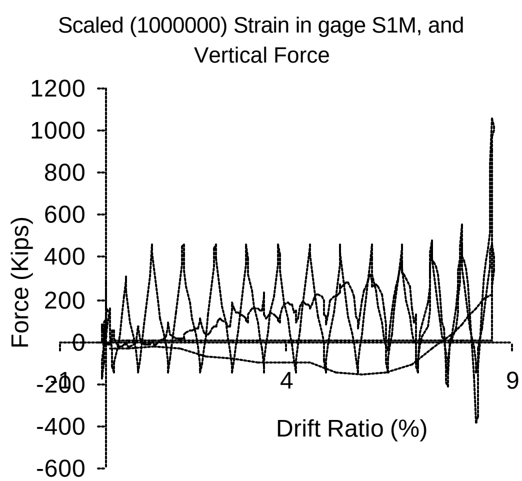
Scaled (1000000) Strain in gage S1M, and Vertical Force
Force (Kips)
Drift Ratio (%)
1200
1000
800
600
400
200
0
-200
-400
-600
-1
4
9

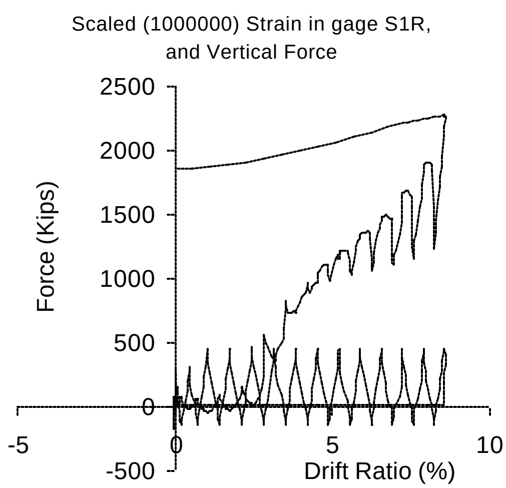
Scaled (1000000) Strain in gage S1R, and Vertical Force
Force (Kips)
Drift Ratio (%)
2500
2000
1500
1000
500
0
-500
-5
0
5
10

TEST GRAPHS BASED ON THE EXPERIMENTAL DATA

TEST SIX

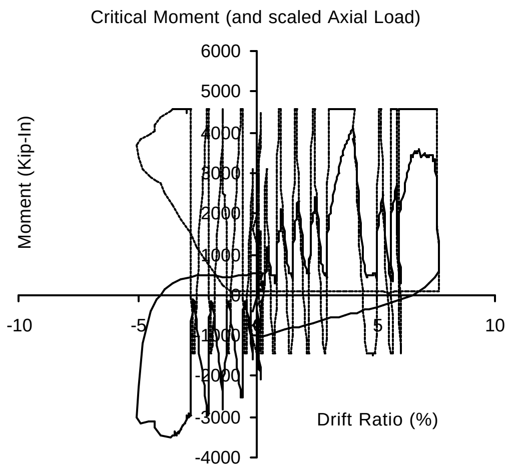
Critical Moment (and scaled Axial Load)
Moment (Kip-In)
6000
5000
4000
3000
2000
1000
0
-1000
-2000
-3000
-4000
-10
-5
5
10
Drift Ratio (%)

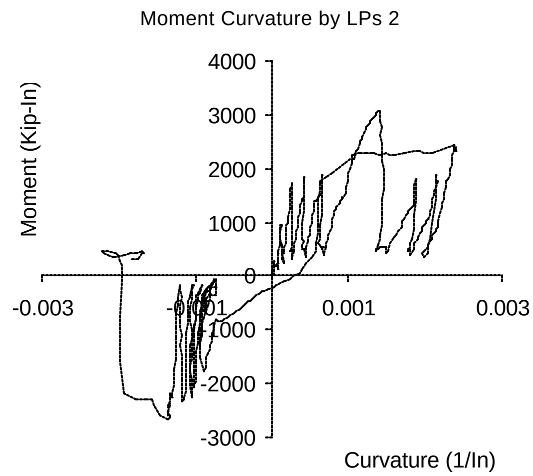
Moment Curvature by LPs 2
Moment (Kip-In)
4000
3000
2000
1000
0
-1000
-2000
-3000
-0.003
-0.001
0.001
0.003
Curvature (1/In)

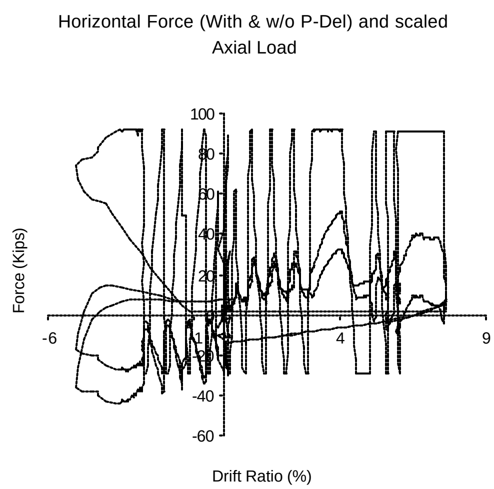
Horizontal Force (With & w/o P-Del) and scaled Axial Load
Force (Kips)
100
80
60
40
20
-20
-40
-60
-6
-1
4
9
Drift Ratio (%)

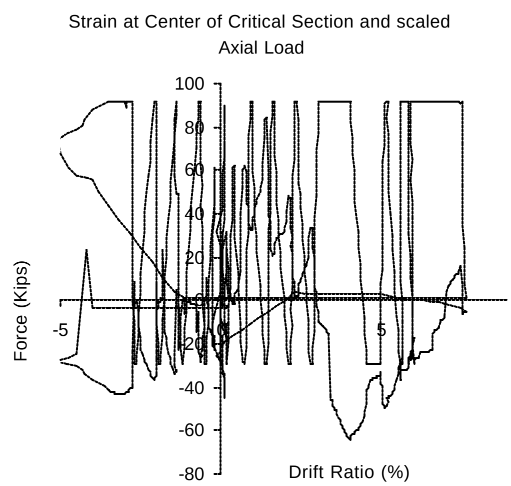
Strain at Center of Critical Section and scaled Axial Load
Force (Kips)
100
80
60
40
20
0
-20
-40
-60
-80
-5
0
5
Drift Ratio (%)

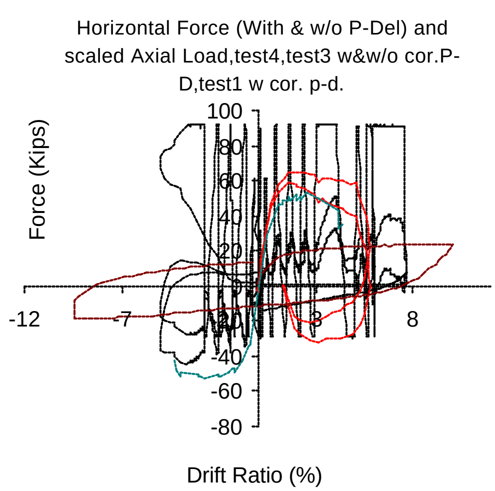
Horizontal Force (With & w/o P-Del) and scaled Axial Load,test4,test3 w&w/o cor.P-D,test1 w cor. p-d.
Force (Kips)
100
80
60
40
20
0
-20
-40
-60
-80
-12
-7
3
8
Drift Ratio (%)

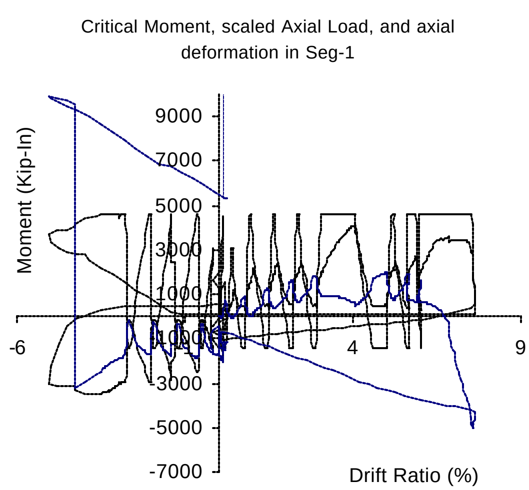
Critical Moment, scaled Axial Load, and axial deformation in Seg-1
Moment (Kip-In)
9000
7000
5000
3000
1000
-1000
-3000
-5000
-7000
-6
4
9
Drift Ratio (%)

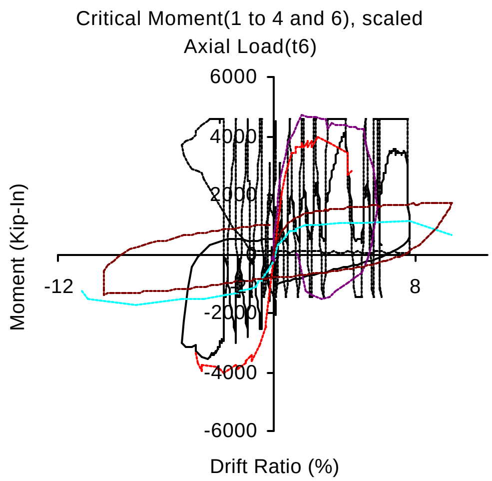
Critical Moment(1 to 4 and 6), scaled Axial Load(t6)
Moment (Kip-In)
Drift Ratio (%)

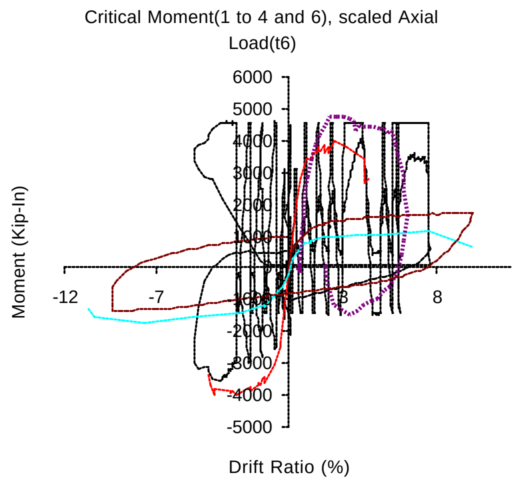
Critical Moment(1 to 4 and 6), scaled Axial Load(t6)
Moment (Kip-In)
Drift Ratio (%)

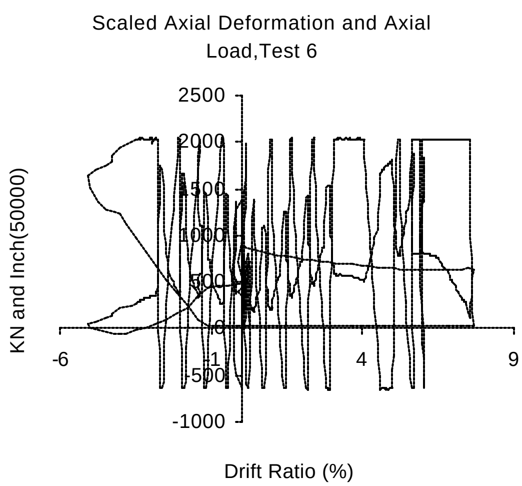
Scaled Axial Deformation and Axial Load,Test 6
KN and Inch(50000)
Drift Ratio (%)

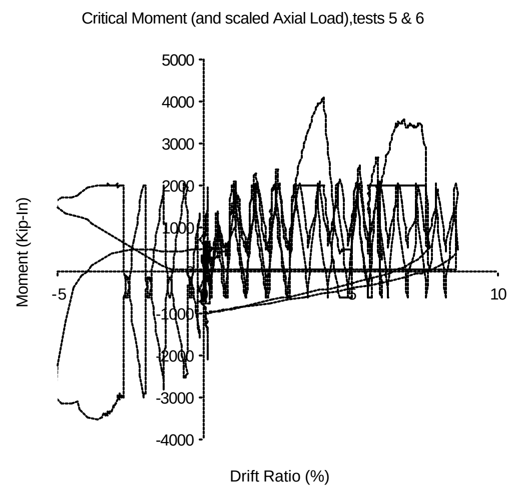
Critical Moment (and scaled Axial Load),tests 5 & 6
Moment (Kip-In)
Drift Ratio (%)

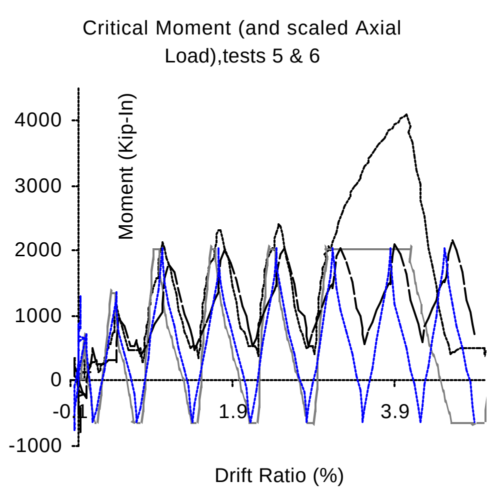
Critical Moment (and scaled Axial Load),tests 5 & 6
Moment (Kip-In)
Drift Ratio (%)

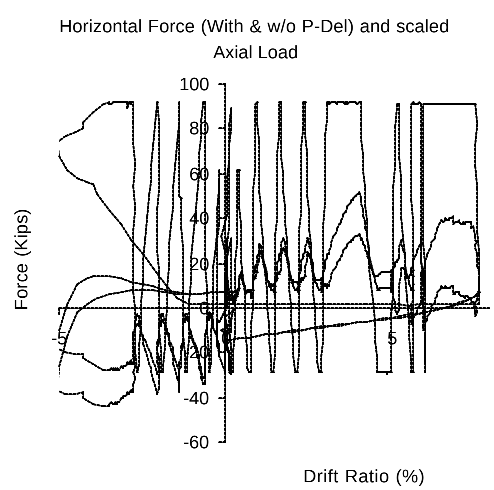
Horizontal Force (With & w/o P-Del) and scaled Axial Load
Force (Kips)
Drift Ratio (%)

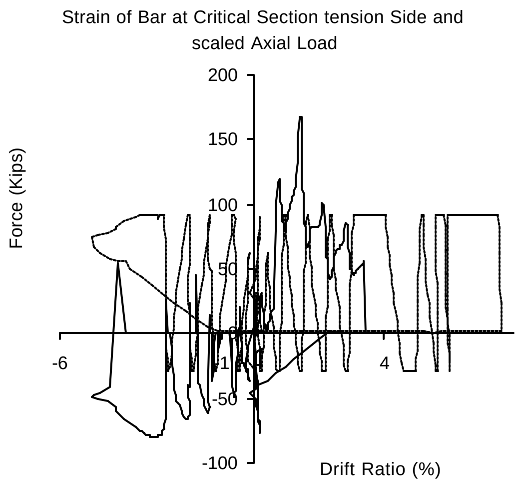
Strain of Bar at Critical Section tension Side and scaled Axial Load
Force (Kips)
200
150
100
50
0
-50
-100
-6
-1
4
Drift Ratio (%)

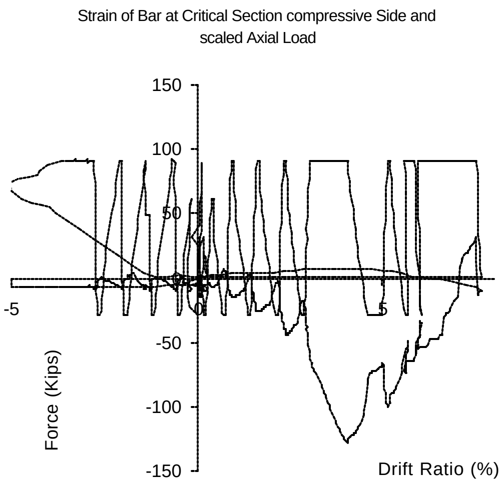
Strain of Bar at Critical Section compressive Side and scaled Axial Load
Force (Kips)
150
100
50
0
-50
-100
-150
-5
0
5
Drift Ratio (%)

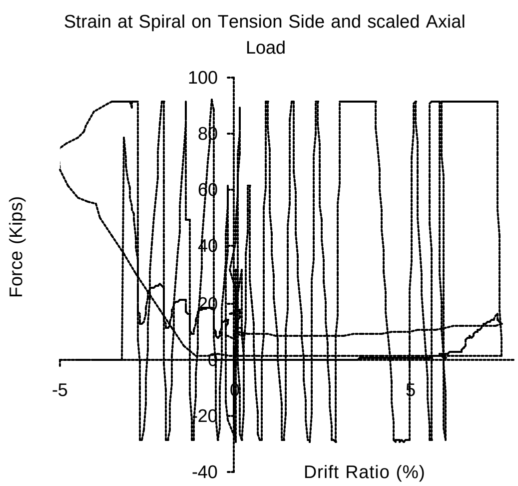
Strain at Spiral on Tension Side and scaled Axial Load
Force (Kips)
100
80
60
40
20
0
-20
-40
-5
0
5
Drift Ratio (%)

APPENDIX II

THE ORIGINAL “FORTRAN 95” CODE USED TO MAKE “DYNAMIC LINK LIBRARY (DLL)” FILE FOR FUNCTIONS AND SUBROUTINES USED IN USC_RC APPLICATION

The Original *"FORTRAN 95"* Code, used to make the *"Dynamic Link Library (dll)" File* for the Functions and Subroutines used in USC_RC Application.

```
!*********************************************************************************
!This subrouine is to exchange the section data between the window
!interface routines and the FORTRAN analysis routines as seen here.
!*********************************************************************************
subroutine sendsection(h,w,t,c,nd,a,nl,xxbb,yybb,mm,ms)
!MS$ATTRIBUTES DLLEXPORT :: SENDSECTION

real*8 h,w,t,c,a(200),xxbb(200),yybb(200)
integer*2 nd,nl,mm,ms

integer*2 ndiv,nlb,m,mstwe
real*8 hdir,wdir,thic,cover,alb(200),xb(200),yb(200)
common /section/hdir,wdir,thic,cover,alb,xb,yb,ndiv,nlb,m,mstwe

hdir=h
wdir=w
thic=t
cover=c
ndiv=nd
alb(1:nlb)=a(1:nlb)
nlb=nl
xb(1:nlb)=xxbb(1:nlb)
yb(1:nlb)=yybb(1:nlb)
m=mm
mstwe=ms
end subroutine

!***********************************************************************************
!This subrouine is to exchange the material data between the window
!interface routines and the FORTRAN analysis routines as seen here.
!***********************************************************************************
subroutine sendmaterial(e,fs,ybbs,kk1,kk2,kk3,kk4,fco,fcc,ybbc,ybbcc,ult,rr,pow,ms)
!MS$ATTRIBUTES DLLEXPORT :: SENDMATERIAL

real*8 e,fs,ybbs,kk1,kk2,kk3,kk4,fco,fcc,ybbc,ybbcc,ult,rr,pow
integer*2 ms

real*8 es,fps,yebs,k1,k2,k3,k4,zarib,zar2,ec,fpco,fpcc,yebc,ebcc,ultebs,r,power
integer*2 mshdg
common/material/es,fps,yebs,k1,k2,k3,k4,zarib,zar2,ec,fpco,fpcc,yebc,ebcc,ultebs,r,
power,mshdg
es=e
fps=fs
yebs=ybbs
```

```
k1=kk1
k2=kk2
k3=kk3
k4=kk4
fpco=fco
fpcc=fcc
yebc=ybbc
ebcc=ybbcc
ultebs=ult
r=rr
power=pow
mshdg=ms
ec=1.7*fco/ybbc
end subroutine

!*****************************************************************************************
!This subrouine is to exchange the steel hysteretic coefficients between
!the window interface routines and the FORTRAN analysis routines as
!seen here.
!*****************************************************************************************
subroutine sendsteelzarib(z1,z2)
!MS$ATTRIBUTES DLLEXPORT :: SENDSTEELZARIB
real*8 z1,z2

real*8 es,fps,yebs,k1,k2,k3,k4,zarib,zar2,ec,fpco,fpcc,yebc,ebcc,ultebs,r,power
integer*2 mshdg
common/material/es,fps,yebs,k1,k2,k3,k4,zarib,zar2,ec,fpco,fpcc,yebc,ebcc,ultebs,r,
power,mshdg

zarib=z1
zar2=z2
end subroutine sendsteelzarib

!*****************************************************************************************
!This subrouine is to exchange some of the required data for hysteretic
!analysis between the window interface routines and the FORTRAN
!analysis routines as seen here.
!*****************************************************************************************
subroutine sendFDInfo(l,d,m,s)
!MS$ATTRIBUTES DLLEXPORT :: SENDFDINFO
real*8 l,d
integer*2 m,s

real*8 leng,dlb,lp
integer*2 method,msys
common/FDInfo/leng,dlb,lp,method,msys

leng=l
```

```
dlb=d
method=m
msys=s
lp=0.
end subroutine sendFDInfo
```

!*
!This subrouine is to initialize the data implemented in the hysteretic
!analysis
!***

```
subroutine initialize(an)
!MS$ATTRIBUTES DLLEXPORT :: INITIALIZE
integer*2 an
real*8 d,aco,acc

integer*2 ndiv,nlb,m,mstwe
real*8 hdir,wdir,thic,cover,alb(200),xb(200),yb(200)
common /section/hdir,wdir,thic,cover,alb,xb,yb,ndiv,nlb,m,mstwe

real*8 es,fps,yebs,k1,k2,k3,k4,zarib,zar2,ec,fpco,fpcc,yebc,ebcc,ultebs,r,power
integer*2 mshdg
common/material/es,fps,yebs,k1,k2,k3,k4,zarib,zar2,ec,fpco,fpcc,yebc,ebcc,ultebs,r,
power,mshdg

real*8 cfiber(500,3),vfiber(500,3),rebar(200,2) !Note 3rd component is the area,
makes faster, steel can be also later
integer*2 cflag(500),vflag(500),sflag(200,2)                    !also distances may be
added to expedite execution
common/hfiber/cfiber,vfiber,rebar,cflag,vflag,sflag

!Added for analysis option used for updating hysteresis
integer*2 anaop
common/updateflag/anaop

!Added for having previous NAxis and Curv. to expedite process
real*8 naxis,pcurv
common/axiscur/naxis,pcurv

naxis=hdir/2.
pcurv=0.

anaop=an

d=hdir/ndiv
cfiber=0.
vfiber=0.
rebar=0.
cflag=0
```

```
vflag=0
sflag=0
do i = 1,ndiv
Select Case (m)
Case (1)
Call arearec((i - 0.5) * d, aco, acc)
Case (2)
Call areahrec((i - 0.5) * d, aco, acc)
Case (3)
Call areace((i - 0.5) * d, aco, acc)
Case (4)
Call areahce((i - 0.5) * d, aco, acc)
End Select
cfiber(i,3)=aco
vfiber(i,3)=acc
end do

end subroutine

!******************************************************************************************
!This is to update the hysteresis record values at the end of each point
!******************************************************************************************
subroutine hupdate(phi,x)
!MS$ATTRIBUTES DLLEXPORT :: HUPDATE

real*8 phi,x,d,tempo

integer*2 ndiv,nlb,m,mstwe
real*8 hdir,wdir,thic,cover,alb(200),xb(200),yb(200)
common /section/hdir,wdir,thic,cover,alb,xb,yb,ndiv,nlb,m,mstwe

real*8 cfiber(500,3),vfiber(500,3),rebar(200,2) !Note 3rd component is the area,
makes faster, steel can be also later
integer*2 cflag(500),vflag(500),sflag(200,2)                    !also distances may be
added to expedite execution
common/hfiber/cfiber,vfiber,rebar,cflag,vflag,sflag

real*8 pstrain,pstress
integer*2 flag,flag2
common/strstate/pstrain,pstress,flag,flag2

d=hdir/ndiv

do i=1,ndiv

pstrain=cfiber(i,1)
pstress=cfiber(i,2)
flag=cflag(i)
```

```
tempo=hconstr((x-(i-0.5)*d)*phi)
cfiber(i,1)=pstrain
cfiber(i,2)=pstress
cflag(i)=flag

pstrain=vfiber(i,1)
pstress=vfiber(i,2)
flag=vflag(i)
tempo=hcovstr((x-(i-0.5)*d)*phi)
vfiber(i,1)=pstrain
vfiber(i,2)=pstress
vflag(i)=flag
end do

do i=1,nlb
pstrain=rebar(i,1)
pstress=rebar(i,2)
flag=sflag(i,1)
flag2=sflag(i,2)
select case (mstwe)
case (2)
tempo=hstrsteel(phi*(x+xb(i)-hdir/2))
case (1)
tempo=hstrsteel(phi*(x+yb(i)-hdir/2))
end select
rebar(i,1)=pstrain
rebar(i,2)=pstress
sflag(i,1)=flag
sflag(i,2)=flag2
end do
end subroutine

!*******************************************************************************
!This is to initialize the demonstration hysteretic curves
!*******************************************************************************
subroutine dinitialize()
!MS$ATTRIBUTES DLLEXPORT :: DINITIALIZE
real*8 es,fps,yebs,k1,k2,k3,k4,zarib,zar2,ec,fpco,fpcc,yebc,ebcc,ultebs,r,power
integer*2 mshdg
common/material/es,fps,yebs,k1,k2,k3,k4,zarib,zar2,ec,fpco,fpcc,yebc,ebcc,ultebs,r,
power,mshdg

integer*2 steelbreak,steelyr,flagccyield,flagcvyield
real*8 pcstrain,imagcstress,pvstrain,imagvstress,psstrain,psstress
common/dhvalues/pcstrain,imagcstress,pvstrain,imagvstress,psstrain,psstress,steel
break,steelyr,flagccyield,flagcvyield
pcstrain=0.
pvstrain=0.
```

```
psstrain=0.
psstress=0.
imagcstress=0.
imagvstress=0.
imagstress=0.
SteelBreak=0
steelyr=0
flagccyield=0
flagcvyield=0
end subroutine
```

!*
!This is to calculate moment curvature of a section under a specific
!axial load and curvature. This subroutine works for all cases even for
!a not allowed axial load. It will get the max possible (either + or -) for
!the curvature and will continue the analysis. The situation is informed
!by the !flag "msit".
!***

```
Subroutine CalMomCur(phi, Axf, xres,msit)
!MS$ATTRIBUTES DLLEXPORT :: CALMOMCUR
real*8 xres(6),trval,trxx, xl,xr,xx,d,dd,ad,p,af,leftval,rigval,b
real*8 phi,Axf
real*8 hdir,wdir,thic,cover,alb(200),xb(200),yb(200)
integer*2 ndiv,nlb,m,mstwe,msit
common /section/hdir,wdir,thic,cover,alb,xb,yb,ndiv,nlb,m,mstwe

!This is added for updating flag
integer*2 analop
common/updateflag/analop

 p = phi
 af = Axf
 xl = hdir/2. !naxis
 trval=af-CalAxf(p, xl)
 xr =xl+ 7.*hdir/ndiv
 d = xr - xl
 dd = d / ndiv
10 leftval = af-CalAxf(p, xl)
 rigval =  af-CalAxf(p, xr)

!This if is added to catch the max during anal. when axial force exceeds allowables
if(abs(leftval)<abs(trval)) then
trval=leftval
trxx=xl
elseif(abs(rigval)<abs(trval)) then
trval=rigval
trxx=xr
endif
```

```
 If(d < dd)Then
  goto 20
endif
If(leftval == 0) Then
        xx = xl
        GoTo 20
        ElseIf(rigval == 0) Then
         xx = xr
         GoTo 20
    ElseIf((leftval * rigval > 0).And.((leftval - rigval).ne.0)) Then
       ad = d * Sign(1.,leftval * p)

       xl = xl + ad
       xr = xr + ad

        ElseIf((leftval * rigval < 0).or.((leftval - rigval).eq.0.)) Then
     xr = (xl + xr) / 2.
        d = xr - xl
end if
   GoTo 10
!here add to pick up the proper xx, msit=0 is the normal and msit=1 is when exceeds
!allowable axial load
20 if((DABS(leftval)<DABS(rigval)).and.(DABS(leftval)<=DABS(trval))) then
      xx = xl
               msit=0
               elseif((DABS(leftval)>DABS(rigval)).and.(DABS(rigval)<=DABS(trval)))
then
               xx=xr
               msit=0

             elseif((DABS(leftval)>=DABS(trval)).and.(DABS(rigval)>=DABS(trval))) then
                        xx=trxx
               !To check that it is actually the case, if statement is added
                        if((dabs(trxx-xl)>dd).and.(dabs(trxx-xr)>dd))then
                                    msit=1
                                    else
                                    msit=0
                                    endif
                        endif
if((msit==0).and.(leftval.ne.rigval)) then
            xx=xr+rigval*(xr-xl)/(leftval-rigval)
endif
xres(1) = p
xres(2) = CalMom(p, xx)
!If added to have the NA compression depth for any case
if(p>0) then
xres(3) = xx
else
```

```
xres(3)=hdir-xx
end if
xres(4) = xx * p
xres(5) = (xx - hdir + cover) * p
xres(6) = CalAxf(p, xx)

!I add this to update based on the analysisop (To be added other options also)
if((analop==12).or.(analop==111)) then
call hupdate(p,xx)
endif
End Subroutine

!*****************************************************************************************
!This is to calculate axial force-bending moment interaction of a section
!for a specific strain of steel or concrete.
!*****************************************************************************************
Subroutine Interaction(ebsilon, xint)
!MS$ATTRIBUTES DLLEXPORT :: INTERACTION
real*8 ebsilon,phim,e,d,p,x,xint(100,4)

real*8 hdir,wdir,thic,cover,alb(200),xb(200),yb(200)
integer ndiv,nlb,m,mstwe
common /section/hdir,wdir,thic,cover,alb,xb,yb,ndiv,nlb,m,mstwe

real*8 es,fps,yebs,k1,k2,k3,k4,zarib,zar2,ec,fpco,fpcc,yebc,ebcc,ultebs,r,power
integer*2 mshdg
common/material/es,fps,yebs,k1,k2,k3,k4,zarib,zar2,ec,fpco,fpcc,yebc,ebcc,ultebs,r,
power,mshdg

e = ebsilon
If(e > 0) Then
phim = (k3 * yebs + e) / (hdir - 2 * cover)
Else
phim = (-e + ultebs) / (hdir - 2 * cover)
End If

d = phim / 99
do i = 1,100
p = sign(1.,e) * (i - 1) * d
If(p == 0) Then
p = 0.00000000001
End If

x = e / p
xint(i, 1) = CalMom(p, x)
xint(i, 2) = CalAxf(p, x)
xint(i, 3) = p
        if(p>0) then
```

```
        xint(i,4) = x
        else
        xint(i,4)=hdir-x
        endif
end do
End Subroutine


!*****************************************************************************
!This is to calculate the engineering axial force-bending moment
!interaction of a section.
!*****************************************************************************
Subroutine EngInteraction(xint)
!MS$ATTRIBUTES DLLEXPORT :: ENGINTERACTION

real*8 phim,d,p,x,xint(100,4)

real*8 hdir,wdir,thic,cover,alb(200),xb(200),yb(200)
integer ndiv,nlb,m,mstwe
common /section/hdir,wdir,thic,cover,alb,xb,yb,ndiv,nlb,m,mstwe

real*8 es,fps,yebs,k1,k2,k3,k4,zarib,zar2,ec,fpco,fpcc,yebc,ebcc,ultebs,r,power
integer*2 mshdg
common/material/es,fps,yebs,k1,k2,k3,k4,zarib,zar2,ec,fpco,fpcc,yebc,ebcc,ultebs,r,
power,mshdg

phim = (yebs + ebcc) / (hdir - 2 * cover)
d = phim / 49
do i = 1,50
p = (i - 1) * d
If(p == 0)Then
p = 0.00000000001
End If
x = ebcc / p
xint(i, 1) = CalMom(p, x)
xint(i, 2) = CalAxf(p, x)
xint(i, 3) = p
xint(i,4)=x
end do

do i = 1,50
p = phim - (i - 1) * d
If(p==0) Then
p = 0.00000000001
End If
x = hdir - cover - yebs / p
xint(i + 50, 1) = CalMom(p, x)
xint(i + 50, 2) = CalAxf(p, x)
```

```
xint(i + 50, 3) = p
xint(i+50,4)=x
end do
End Subroutine
```

!*
!This is the subroutine to calculate the axial load for a specific curvature
!and neutral axis location.
!***
**

```
real*8 Function CalAxf(phi, x)
!MS$ATTRIBUTES DLLEXPORT :: CALAXF

real*8 s,d
real*8 phi,x
real*8 hdir,wdir,thic,cover,alb(200),xb(200),yb(200)
integer*2 ndiv,nlb,m,mstwe
common /section/hdir,wdir,thic,cover,alb,xb,yb,ndiv,nlb,m,mstwe

real*8 cfiber(500,3),vfiber(500,3),rebar(200,2) !Note 3rd component is the area,
makes faster, steel can be also later
integer*2 cflag(500),vflag(500),sflag(200,2)                    !also distances may be
added to expedite execution
common/hfiber/cfiber,vfiber,rebar,cflag,vflag,sflag

real*8 pstrain,pstress
integer*2 flag,flag2
common/strstate/pstrain,pstress,flag,flag2
d = hdir / ndiv
!clockwise phi is positive and x starts from compression side
!compressive strain is positive
s = 0.
do i = 1,ndiv
pstrain=cfiber(i,1)
pstress=cfiber(i,2)
flag=cflag(i)
s = s + cfiber(i,3) * hconstr((x - (i - 0.5) * d) * phi)
end do
do i=1,ndiv
pstrain=vfiber(i,1)
pstress=vfiber(i,2)
flag=vflag(i)
s=s+vfiber(i,3)*hcovstr((x-(i-0.5)*d)*phi)
end do

do i = 1,nlb
pstrain=rebar(i,1)
pstress=rebar(i,2)
flag=sflag(i,1)
```

```
flag2=sflag(i,2)
Select Case (mstwe)
Case (2)
s = s + alb(i) * hstrsteel(phi * (x + xb(i) - hdir / 2))
Case (1)
s = s + alb(i) * hstrsteel(phi * (x + yb(i) - hdir / 2))
End Select
end do
CalAxf = s
End Function

!**************************************************************************************
!This is the subroutine to calculate the bending moment for a specific
!curvature and neutral axis location.
!**************************************************************************************
real*8 Function CalMom(phi, x)
!MS$ATTRIBUTES DLLEXPORT :: CALMOM

real*8 phi,x
real*8 s,d

real*8 hdir,wdir,thic,cover,alb(200),xb(200),yb(200)
integer*2 ndiv,nlb,m,mstwe
common /section/hdir,wdir,thic,cover,alb,xb,yb,ndiv,nlb,m,mstwe

real*8 cfiber(500,3),vfiber(500,3),rebar(200,2) !Note 3rd component is the area,
makes faster, steel can be also later
integer*2 cflag(500),vflag(500),sflag(200,2)                    !also distances may be
added to expedite execution
common/hfiber/cfiber,vfiber,rebar,cflag,vflag,sflag

real*8 pstrain,pstress
integer*2 flag,flag2
common/strstate/pstrain,pstress,flag,flag2

d = hdir / ndiv
s = 0.

do i = 1,ndiv

pstrain=cfiber(i,1)
pstress=cfiber(i,2)
flag=cflag(i)
s = s + (hdir / 2 - (i - 0.5) * d)*cfiber(i,3) * hconstr((x - (i - 0.5) * d) * phi)
end do
do i=1,ndiv
pstrain=vfiber(i,1)
pstress=vfiber(i,2)
```

```
flag=vflag(i)
s=s+(hdir / 2 - (i - 0.5) * d)*vfiber(i,3)*hcovstr((x-(i-0.5)*d)*phi)
end do
do i = 1,nlb
pstrain=rebar(i,1)
pstress=rebar(i,2)
flag=sflag(i,1)
flag2=sflag(i,2)
Select Case (mstwe)
Case (2)
s = s + xb(i) * alb(i) * hstrsteel(phi * (x + xb(i) - hdir / 2))
Case (1)
s = s + yb(i) * alb(i) * hstrsteel(phi * (x + yb(i) - hdir / 2))
End Select
end do
CalMom = s
End Function

!**************************************************************************************
!This is the subroutine for monotonic stress-strain relationship of steel.
!**************************************************************************************
real*8 Function strsteel(strain)
!MS$ATTRIBUTES DLLEXPORT :: STRSTEEL
real*8 strain
real*8 es,fps,yebs,k1,k2,k3,k4,zarib,zar2,ec,fpco,fpcc,yebc,ebcc,ultebs,r,power
integer*2 mshdg
common/material/es,fps,yebs,k1,k2,k3,k4,zarib,zar2,ec,fpco,fpcc,yebc,ebcc,ultebs,r,
power,mshdg

    strsteel = es * strain

      If((Abs(strain) > yebs).And.(Abs(strain) < k3 * yebs)) Then

      Select Case (mshdg)
      Case (0)
       strsteel = fps * sign(1.,strain)
       Case (1)
      If(Abs(strain) < k1 * yebs) Then
       strsteel = fps * sign(1.,strain)
       ElseIf(Abs(strain) > k1 * yebs) Then
      strsteel = ((es * (1 - k4) / yebs) * (Abs(strain)**2) + 2 * k2 * (-es + k4 * es) *
Abs(strain) + es * yebs * (k4 * k1**2 - 2 * k4 * k1 * k2 + k2**2)) * (strain / Abs(strain))
/ (k1**2 - 2 * k1 * k2 + k2**2)
     End If
     End Select

     ElseIf(Abs(strain) > k3 * yebs) Then
        strsteel = 0.
```

```
        End If
End Function

!**********************************************************************************
!This is the subroutine for monotonic stress-strain relationship of
!unconfined concrete. Basic parameters are provided by interface !modules.
!**********************************************************************************
real*8 Function covstr(strain)
!MS$ATTRIBUTES DLLEXPORT :: COVSTR
real*8 strain
real*8 es,fps,yebs,k1,k2,k3,k4,zarib,zar2,ec,fpco,fpcc,yebc,ebcc,ultebs,r,power
integer*2 mshdg
common/material/es,fps,yebs,k1,k2,k3,k4,zarib,zar2,ec,fpco,fpcc,yebc,ebcc,ultebs,r,
power,mshdg
real*8 ss
If((strain > 2 * yebc).Or.(strain < 0)) Then
covstr = 0.
ElseIf(0.004 < 2 * yebc) Then
If(strain < 0.004) Then
covstr = (fpco * power * strain / yebc) / (power - 1 + (strain / yebc)**power)
Else
ss = (fpco * power * 0.004 / yebc) / (power - 1 + (0.004 / yebc)**power)
covstr = ss - (ss / (2 * yebc - 0.004)) * (strain - 0.004)
End If
Else
covstr = (fpco * power * strain / yebc) / (power - 1 + (strain / yebc)**power)
End If
End Function

!**********************************************************************************************
!This is the subroutine for monotonic stress-strain relationship of confined
!concrete.The basic parameters are provided by the interface modules.
!**********************************************************************************************
real*8 Function constr(strain)
!MS$ATTRIBUTES DLLEXPORT :: CONSTR
real*8 strain
real*8 es,fps,yebs,k1,k2,k3,k4,zarib,zar2,ec,fpco,fpcc,yebc,ebcc,ultebs,r,power
integer*2 mshdg
common/material/es,fps,yebs,k1,k2,k3,k4,zarib,zar2,ec,fpco,fpcc,yebc,ebcc,ultebs,r,
power,mshdg

If((strain > ultebs).Or.(strain < 0)) Then
constr = 0
Else
constr = (fpcc * (strain / ebcc) * r) / (r - 1 + (strain / ebcc)**r)
End If
End Function
```

```
!*******************************************************************************************
!This is the internal subroutine for calculating the confined and unconfined
!area of a rectangular cross section. The initial data is provided by the
!interface modules through the common blocks.
!*******************************************************************************************
Subroutine areact(aco, acc)
!MS$ATTRIBUTES DLLEXPORT :: AREACT
real*8 aco,acc
real*8 hdir,wdir,thic,cover,alb(200),xb(200),yb(200)
integer*2 ndiv,nlb,m,mstwe
common /section/hdir,wdir,thic,cover,alb,xb,yb,ndiv,nlb,m,mstwe
if (hdir>wdir) then
aco = 3.14159 * ((hdir - 2 * cover) ** 2) / 4
acc = 3.14159 * hdir ** 2 / 4 - aco
else
aco = 3.14159 * ((wdir - 2 * cover) ** 2) / 4
acc = 3.14159 * wdir ** 2 / 4 - aco
endif
End Subroutine

!*******************************************************************************************
!This is the internal subroutine for calculating the confined and unconfined
!area of a single fiber on a circular cross section. The initial data is
!provided by the interface modules through the common blocks.
!*******************************************************************************************
Subroutine areace(x, aco, acc)
!MS$ATTRIBUTES DLLEXPORT :: AREACE
real*8  c,d,x,aco,acc
real*8 hdir,wdir,thic,cover,alb(200),xb(200),yb(200)
integer*2 ndiv,nlb,m,mstwe
common /section/hdir,wdir,thic,cover,alb,xb,yb,ndiv,nlb,m,mstwe
c = x
d = hdir / ndiv
If ((c <= cover) .or. (c > (hdir - cover))) Then
acc = d * (((hdir / 2) ** 2 - (hdir / 2 - c) ** 2) ** 0.5) * 2
aco = 0
Else
aco = d * (((hdir / 2 - cover) ** 2 - (hdir / 2 - c) ** 2) ** 0.5) * 2
acc = d * (((hdir / 2) ** 2 - (hdir / 2 - c) ** 2) ** 0.5) * 2 - aco
End If
End Subroutine

!*******************************************************************************************
!This is the internal subroutine for calculating the confined and unconfined
!area of a circular cross section. The initial data is provided by the
!interface modules through the common blocks.
!*******************************************************************************************
Subroutine arearect(aco, acc)
```

```
!MS$ATTRIBUTES DLLEXPORT :: AREARECT
real*8 acc,aco
real*8 hdir,wdir,thic,cover,alb(200),xb(200),yb(200)
integer*2 ndiv,nlb,m,mstwe
common /section/hdir,wdir,thic,cover,alb,xb,yb,ndiv,nlb,m,mstwe
aco = (wdir - 2 * cover) * (hdir - 2 * cover)
acc = wdir * hdir - aco
End Subroutine

!*******************************************************************************************
!This is the internal subroutine for calculating the confined and unconfined
!area of a single fiber on a rectangular cross section. The initial data is
!provided by the interface modules through the common blocks.
!*******************************************************************************************
Subroutine arearec(x, aco, acc)
!MS$ATTRIBUTES DLLEXPORT :: AREAREC
real*8 c,d,x,aco,acc

real*8 hdir,wdir,thic,cover,alb(200),xb(200),yb(200)
integer*2 ndiv,nlb,m,mstwe
common /section/hdir,wdir,thic,cover,alb,xb,yb,ndiv,nlb,m,mstwe
c = x
d = hdir / ndiv
If (c <= cover .or. c > (hdir - cover)) Then
acc = d * wdir
aco = 0
ElseIf (c > cover .And. c <= (hdir - cover)) Then
aco = d * (wdir - 2 * cover)
acc = d * wdir - aco
End If
End Subroutine

!*******************************************************************************************
!This is the internal subroutine for calculating the confined and unconfined
!area of a single fiber on a hollow rectangular cross section. The initial
!data is provided by the interface modules through the common blocks.
!*******************************************************************************************
Subroutine areahrec(x, aco, acc)
!MS$ATTRIBUTES DLLEXPORT :: AREAHREC
real*8 c,d,x,aco,acc

real*8 hdir,wdir,thic,cover,alb(200),xb(200),yb(200)
integer*2 ndiv,nlb,m,mstwe
common /section/hdir,wdir,thic,cover,alb,xb,yb,ndiv,nlb,m,mstwe
c = x
d = hdir / ndiv
If((c < cover).Or.(c > (hdir - cover)).And.(c <= hdir)) Then
        acc = wdir * d
```

```
        aco = 0.
        ElseIf((c>cover).And.(c<=(thic - cover)).Or.(c>(hdir-
thic+cover)).And.(c<=(hdir-cover))) Then
          acc = 2 * d * cover
          aco = (wdir - 2 * cover) * d

          ElseIf ((c> (thic - cover)).And.(c <= thic).Or.(c > (hdir - thic)).And.(c <= (hdir
- thic + cover))) Then
            acc = (wdir - 2 * thic + 4 * cover) * d
            aco = (2 * thic - 4 * cover) * d

            Else
              acc = 4 * cover * d
              aco = (2 * thic - 4 * cover) * d

              End If
End Subroutine

!*******************************************************************************************
!This is the subroutine for calculating the confined and unconfined area of
!a single fiber on a hollow circular cross section. The initial data is
!provided by the interface modules through the common blocks.
!*******************************************************************************************
Subroutine areahce(x, aco, acc)
!MS$ATTRIBUTES DLLEXPORT :: AREAHCE

real*8 c,d,x,aco,acc
real*8 hdir,wdir,thic,cover,alb(200),xb(200),yb(200)
integer*2 ndiv,nlb,m,mstwe
common /section/hdir,wdir,thic,cover,alb,xb,yb,ndiv,nlb,m,mstwe
c = x
d = hdir / ndiv
If((c < cover).Or.(c > (hdir - cover))) Then
acc = d * (((hdir / 2) ** 2 - (hdir / 2 - c) ** 2) ** 0.5) * 2.
aco = 0
ElseIf ((c >= cover).And.(c <= (thic - cover)).Or.(c >= (hdir - thic + cover)).And.(c <=
(hdir - cover))) Then
aco = d * (((hdir / 2 - cover) ** 2 - (hdir / 2 - c) ** 2) ** 0.5) * 2.
acc = d * (((hdir / 2) ** 2 - (hdir / 2 - c) ** 2) ** 0.5) * 2.- aco
ElseIf((c > (thic - cover)).Or.(c < (hdir - thic + cover))) Then
aco = d * (((hdir / 2 - cover) ** 2 - (hdir / 2 - c) ** 2) ** 0.5 - ((hdir / 2 - thic + cover) **
2 - (hdir / 2 - c) ** 2) ** 0.5) * 2.
If((c > thic).And.(c < (hdir - thic))) Then
    acc = d * (((hdir / 2) ** 2 - (hdir / 2 - c) ** 2) ** 0.5 - ((hdir / 2 - thic) ** 2 - (hdir / 2 -
c) ** 2) ** 0.5) * 2. - aco
  Else
   acc = d * (((hdir / 2) ** 2 - (hdir / 2 - c) ** 2) ** 0.5) * 2.- aco
 End If
```

```
End If
End Subroutine

!*******************************************************************************************
!This is the subroutine for calculating moment curvature for a given axial
!load and bending moment. This subroutine utilizes the moment curvature
!subroutine which is used for a given axial load and curvature.
!*******************************************************************************************
Subroutine CalCurMom(them, Axf, xres,mist,mmst)
!MS$ATTRIBUTES DLLEXPORT :: CALCURMOM
real*8 xres(6), xl,xr,xx,d,dd,ad,ad1,p,af,leftval,rigval,b
real*8 them,Axf
integer*2 mist,mmst
real*8 hdir,wdir,thic,cover,alb(200),xb(200),yb(200)
integer*2 ndiv,nlb,m,mstwe
common /section/hdir,wdir,thic,cover,alb,xb,yb,ndiv,nlb,m,mstwe

real*8 es,fps,yebs,k1,k2,k3,k4,zarib,zar2,ec,fpco,fpcc,yebc,ebcc,ultebs,r,power
integer*2 mshdg
common/material/es,fps,yebs,k1,k2,k3,k4,zarib,zar2,ec,fpco,fpcc,yebc,ebcc,ultebs,r,
power,mshdg

!added for updating decision
integer*2 analop
common/updateflag/analop

 p = them
 af = Axf
 xl = 0.
xr=(yebs + ebcc) / (hdir - 2 * cover)
 d = xr - xl

 !Here the 10 can be changed to get better results
 dd = d / (ndiv/10.)!* ndiv)
10 call CalMomCur(xl,af,xres,mist)

leftval = p-xres(2)
call CalMomCur(xr,af,xres,mist)

   rigval = p-xres(2)
If(leftval == 0) Then
       xx = xl
       GoTo 20
       ElseIf(rigval == 0) Then
        xx = xr
        GoTo 20
        !added to avoid stucking when reached a constant state
    ElseIf((leftval * rigval > 0).And.((leftval - rigval).ne.0)) Then
```

```
      ad = d * Sign(1.,leftval * (leftval - rigval))
      If(ad1 * ad < 0) Then

  !added for cases when the input moment is more than allowable at the stage
         mmst=1
       xr = (xl + xr) / 2.
      GoTo 15
       End If

      xl = xl + ad
      xr = xr + ad

      Else
      ad1 = 0.
     xl = (xl + xr) / 2.
      End If
15      d = xr - xl
        ad1 = ad
      If (d < dd) Then
      xx = xl
      GoTo 20
      Else
      GoTo 10
    End If

20 if((mmst==0).and.(leftval.ne.rigval)) then
        xx=xr+rigval*(xr-xl)/(leftval-rigval)
endif
call CalMomCur(xx,af,xres,mist)

if(analop==13) then
        if(xres(1)>0.) then
        call hupdate(xres(1),xres(3))
        else
        call hupdate(xres(1),hdir-xres(3))
        endif
endif
 End Subroutine

!*******************************************************************************************
!This is the subroutine for calculating moment curvature for a case when
!the axial load is proportionally variable with respect to the moment.
!*******************************************************************************************
Subroutine ProMomCur(phi, AxfM, xres)
!MS$ATTRIBUTES DLLEXPORT :: PROMOMCUR
real*8 yres,xres(6), xl,xr,xx,d,dd,ad,ad1,p,af,leftval,rigval,b
real*8 phi,AxfM
```

```
real*8 hdir,wdir,thic,cover,alb(200),xb(200),yb(200)
integer*2 ndiv,nlb,m,mstwe
common /section/hdir,wdir,thic,cover,alb,xb,yb,ndiv,nlb,m,mstwe

real*8 es,fps,yebs,k1,k2,k3,k4,zarib,zar2,ec,fpco,fpcc,yebc,ebcc,ultebs,r,power
integer*2 mshdg
common/material/es,fps,yebs,k1,k2,k3,k4,zarib,zar2,ec,fpco,fpcc,yebc,ebcc,ultebs,r,
power,mshdg

integer*2 analop
common/updateflag/analop

 p = phi
 af = AxfM
d=hdir/7.
 if(p>=0.) then
 xl = 0.
 else
 xl=hdir
 endif
  xr=xl+d
 dd = d / (4.* ndiv)
10 leftval = af*CalAxf(p,xl)-CalMom(p,xl)

   rigval =af*CalAxf(p,xr)-CalMom(p,xr)

If(leftval == 0) Then
        xx = xl
        GoTo 20
        ElseIf(rigval == 0) Then
         xx = xr
         GoTo 20
         !added to avoid stucking when reached a constant state
    ElseIf((leftval * rigval > 0).And.((leftval - rigval).ne.0)) Then
       ad = d * Sign(1.,leftval * (leftval - rigval))
       If(ad1 * ad < 0) Then
         xr = (xl + xr) / 2.
       GoTo 15
         End If

       xl = xl + ad
       xr = xr + ad

       Else
       ad1 = 0.
     xl = (xl + xr) / 2.
       End If
15      d = xr - xl
```

```
      ad1 = ad
    If (d < dd) Then
    xx = xl
    GoTo 20
    Else
    GoTo 10
  End If

20 xres(1) = p
xres(2) = CalMom(p, xx)
if(p>0) then
xres(3) = xx
else
xres(3)=hdir-xx
endif

xres(4) = xx * p
xres(5) = (xx - hdir + cover) * p
xres(6) = CalAxf(p, xx)
if(analop==141) then
        if(xres(1)>0.) then
        call hupdate(xres(1),xres(3))
        else
        call hupdate(xres(1),hdir-xres(3))
        endif
endif

End Subroutine


!*****************************************************************************************
!This is the internal subroutine for calculating the hysteretic response of
!confined concrete. The data is updated in update subroutine and the
!initial data is provided by the common blocks of data.
!*****************************************************************************************
real*8 Function hconstr(strain)
!MS$ATTRIBUTES DLLEXPORT :: HCONSTR
real*8 strain,stress,a

real*8 es,fps,yebs,k1,k2,k3,k4,zarib,zar2,ec,fpco,fpcc,yebc,ebcc,ultebs,r,power
integer*2 mshdg
common/material/es,fps,yebs,k1,k2,k3,k4,zarib,zar2,ec,fpco,fpcc,yebc,ebcc,ultebs,r,
power,mshdg

real*8 pstrain,imagstress
integer*2 flagconyield,flag2
common/strstate/pstrain,imagstress,flagconyield,flag2
a=3.
```

```
if((strain>ebcc/a).or.(pstrain>ebcc/a))then
flagconyield=1
endif
stress=imagstress+(strain-pstrain)*ec
imagstress=stress

if(stress<0.) then
stress=0.
elseif(stress>constr(strain))then
        stress=constr(strain)
        imagstress=stress
elseif((strain<ebcc/a).and.flagconyield==0) then
stress=constr(strain)
imagstress=stress
endif
pstrain=strain
hconstr=stress
end function hconstr


!*****************************************************************************************
!This is the internal subroutine for calculating the hysteretic response of
!unconfined concrete. The data is updated in update subroutine and the
!initial data is provided by the common blocks of data.
!*****************************************************************************************
real*8 Function hcovstr(strain)
!MS$ATTRIBUTES DLLEXPORT :: HCOVSTR
real*8 strain,stress,a

real*8 es,fps,yebs,k1,k2,k3,k4,zarib,zar2,ec,fpco,fpcc,yebc,ebcc,ultebs,r,power
integer*2 mshdg
common/material/es,fps,yebs,k1,k2,k3,k4,zarib,zar2,ec,fpco,fpcc,yebc,ebcc,ultebs,r,
power,mshdg

real*8 pstrain,imagstress
integer*2 flagconyield,flag2
common/strstate/pstrain,imagstress,flagconyield,flag2

a=3.
if((strain>yebc/a).or.(pstrain>yebc/a))then
flagconyield=1
endif

stress=imagstress+(strain-pstrain)*ec
imagstress=stress
if(stress<0.) then
stress=0.
elseif(stress>covstr(strain))then
```

```
stress=covstr(strain)
imagstress=stress
elseif((strain<yebc/a).and.flagconyield==0) then
stress=covstr(strain)
imagstress=stress
endif
pstrain=strain
hcovstr=stress
end function hcovstr

!*******************************************************************************************
!This is the internal subroutine for calculating the hysteretic response of
!longitudinal steel. The data is updated in update subroutine and the initial
!data is provided by the common blocks of data.
!*******************************************************************************************
real*8 Function hstrsteel(strain)
!MS$ATTRIBUTES DLLEXPORT :: HSTRSTEEL
real*8 strain,stress,trstr,conver
real*8 es,fps,yebs,k1,k2,k3,k4,zarib,zar2,ec,fpco,fpcc,yebc,ebcc,ultebs,r,power
integer*2 mshdg
common/material/es,fps,yebs,k1,k2,k3,k4,zarib,zar2,ec,fpco,fpcc,yebc,ebcc,ultebs,r,
power,mshdg

real*8 psstrain,psstress
integer*2 steelBreak,steelyr
common/strstate/psstrain,psstress,steelBreak,steelyr

if(abs(strain)>=k3*yebs) then
steelBreak=1
endif
if(steelBreak==1)then
stress=0.
goto 111
endif

if((abs(psstrain)>yebs).and.(abs(strain)<abs(psstrain))) then
steelyr=1
endif
if(steelyr==0) then
stress=strsteel(strain)
goto 111
else
        conver=sign(1.,psstrain)
        psstrain=conver*psstrain
        psstress=conver*psstress
        strain=conver*strain

        if(psstress>zarib*fps) then
```

```
			if(strain>psstrain) then
			stress=psstress+es*(zarib/zar2)*(strain-psstrain)
			elseif(strain<(psstrain-psstress/es-(zarib/2.)*fps/es))  then
			stress=-(zarib/2.)*fps+es*(zarib/(2*zar2))*(strain-
psstrain+psstress/es+(zarib/2.)*fps/es)
			else
			stress=psstress+es*(strain-psstrain)
			endif
		elseif(psstress<-(zarib/2.)*fps) then
			if(strain<psstrain) then
			stress=psstress+es*(zarib/(2*zar2))*(strain-psstrain)
			elseif(strain>(psstrain-psstress/es+zarib*fps/es)) then
			stress=zarib*fps+es*(zarib/zar2)*(strain-psstrain+psstress/es-
zarib*fps/es)
			else
			stress=psstress+es*(strain-psstrain)
			endif
		else
			if(strain>(psstrain-psstress/es+zarib*fps/es)) then
			stress=zarib*fps+es*(zarib/zar2)*(strain-psstrain+psstress/es-
zarib*fps/es)
			elseif(strain<(psstrain-psstress/es-(zarib/2.)*fps/es))  then
			stress=-(zarib/2.)*fps+es*(zarib/(2*zar2))*(strain-
psstrain+psstress/es+(zarib/2.)*fps/es)
			else
			stress=psstress+es*(strain-psstrain)
			endif
		endif

if(stress>0.9*fps) then
		trstr=fps*(0.45+0.5*k4)+fps*(-0.45+0.5*k4)*strain/(k3*yebs)
		if(stress>trstr) then
		stress=trstr
		endif
elseif(stress<(-0.9*fps)) then
		trstr=fps*(-0.45-0.5*k4)+fps*(-0.45+0.5*k4)*strain/(k3*yebs)
		if(stress<trstr) then
		stress=trstr
		endif
endif
stress=conver*stress
strain=conver*strain
endif
111 hstrsteel=stress
psstrain=strain
psstress=stress
end function hstrsteel
```

```
!****************************************************************************************
!This is the internal subroutine for calculating the hysteretic response of
!confined concrete for viewing. The data is updated in update subroutine
!and the initial data is provided by the common blocks of data.
!****************************************************************************************
real*8 Function dhconstr(strain)
!MS$ATTRIBUTES DLLEXPORT :: DHCONSTR
real*8 strain,stress,a,b

real*8 es,fps,yebs,k1,k2,k3,k4,zarib,zar2,ec,fpco,fpcc,yebc,ebcc,ultebs,r,power
integer*2 mshdg
common/material/es,fps,yebs,k1,k2,k3,k4,zarib,zar2,ec,fpco,fpcc,yebc,ebcc,ultebs,r,
power,mshdg

integer*2 steelbreak,steelyr,flagccyield,flagcvyield
real*8 pcstrain,imagcstress,pvstrain,imagvstress,psstrain,psstress
common/dhvalues/pcstrain,imagcstress,pvstrain,imagvstress,psstrain,psstress,steel
break,steelyr,flagccyield,flagcvyield
!These a and b are to adjust the hyst curve
a=3.
b=1.*fpcc
if((strain>ebcc/a).or.(pcstrain>ebcc/a))then
flagccyield=1
endif
if(imagcstress>=0.) then
	if(strain<=pcstrain) then
		if(strain>=(pcstrain-(0.004*imagcstress/ec)**0.5)) then
			stress=(ec/0.004)*(strain-
pcstrain+0.0632456*(imagcstress/ec)**0.5)**2
		else
			stress=(strain-pcstrain+(0.004*imagcstress/ec)**0.5)*ec
		endif

	else
		if(strain<(pcstrain-imagcstress/ec+2*b/ec)) then
		stress=(-(pcstrain**2*ec**2)+4.*imagcstress*b+ec*strain*(4.*(b**2-
b*imagcstress)**0.5-ec*strain)+2.*pcstrain*ec*(-2.*(b**2-
b*imagcstress)**0.5+ec*strain))/(4.*b)
		else
		stress=imagcstress+(strain-pcstrain)*ec
		endif
	endif
else
	if(strain<=(pcstrain-imagcstress/ec)) then
	stress=imagcstress+(strain-pcstrain)*ec
	else
```

```
        stress=(-((pcstrain-imagcstress/ec)**2*ec**2)+ec*strain*(4.*b-
ec*strain)+2.*(pcstrain-imagcstress/ec)*ec*(-2.*b+ec*strain))/(4.*b)
        endif
endif

imagcstress=stress

if(stress<0.) then !if(stress<-0.1*fpcc) then
                stress=0.
elseif(stress>constr(strain))then
        stress=constr(strain)
        imagcstress=stress
elseif((strain<ebcc/a).and.flagccyield==0) then
stress=constr(strain)
imagcstress=stress
endif
pcstrain=strain
pcstress=stress
dhconstr=stress
end function dhconstr
```

```
!*******************************************************************************************
!This is the subroutine for calculating the hysteretic response of
!unconfined concrete for viewing. The data is updated in update
!subroutine and the initial data is provided by the common blocks of data.
!*******************************************************************************************
real*8 Function dhcovstr(strain)
!MS$ATTRIBUTES DLLEXPORT :: DHCOVSTR
real*8 strain,stress,a,b

real*8 es,fps,yebs,k1,k2,k3,k4,zarib,zar2,ec,fpco,fpcc,yebc,ebcc,ultebs,r,power
integer*2 mshdg
common/material/es,fps,yebs,k1,k2,k3,k4,zarib,zar2,ec,fpco,fpcc,yebc,ebcc,ultebs,r,
power,mshdg

integer*2 steelbreak,steelyr,flagccyield,flagcvyield
real*8 pcstrain,imagcstress,pvstrain,imagvstress,psstrain,psstress
common/dhvalues/pcstrain,imagcstress,pvstrain,imagvstress,psstrain,psstress,steel
break,steelyr,flagccyield,flagcvyield

a=3.
b=1.*fpco
if((strain>yebc/a).or.(pvstrain>yebc/a))then
flagcvyield=1
endif
```

```
if(imagvstress>=0.) then
        if(strain<=pvstrain) then
                if(strain>=(pvstrain-(0.004*imagvstress/ec)**0.5)) then
                        stress=(ec/0.004)*(strain-
pvstrain+0.0632456*(imagvstress/ec)**0.5)**2
                else
                        stress=(strain-pvstrain+(0.004*imagvstress/ec)**0.5)*ec
                endif
        else
                if(strain<(pvstrain-imagvstress/ec+2*b/ec)) then
                stress=(-(pvstrain**2*ec**2)+4.*imagvstress*b+ec*strain*(4.*(b**2-
b*imagvstress)**0.5-ec*strain)+2.*pvstrain*ec*(-2.*(b**2-
b*imagvstress)**0.5+ec*strain))/(4.*b)
                else
                stress=imagvstress+(strain-pvstrain)*ec
                endif
        endif
else
        if(strain<=(pvstrain-imagvstress/ec)) then
        stress=imagvstress+(strain-pvstrain)*ec
        else
        stress=(-((pvstrain-imagvstress/ec)**2*ec**2)+ec*strain*(4.*b-
ec*strain)+2.*(pvstrain-imagvstress/ec)*ec*(-2.*b+ec*strain))/(4.*b)
        endif
endif

imagvstress=stress
if(stress<0.) then
stress=0.
elseif(stress>covstr(strain))then
stress=covstr(strain)
imagvstress=stress
elseif((strain<yebc/a).and.flagcvyield==0) then
stress=covstr(strain)
imagvstress=stress
endif
pvstrain=strain
pvstress=stress
dhcovstr=stress
end function dhcovstr

!*******************************************************************************************
!This is the subroutine for calculating the hysteretic response
!oflongitudinal steel for viewing. The data is updated in update subroutine
!and the initial data is provided by the common blocks of data.
!*******************************************************************************************
real*8 Function dhstrsteel(strain)
!MS$ATTRIBUTES DLLEXPORT :: DHSTRSTEEL
```

```
real*8 strain,stress,trstr,conver
real*8 es,fps,yebs,k1,k2,k3,k4,zarib,zar2,ec,fpco,fpcc,yebc,ebcc,ultebs,r,power
integer*2 mshdg
common/material/es,fps,yebs,k1,k2,k3,k4,zarib,zar2,ec,fpco,fpcc,yebc,ebcc,ultebs,r,
power,mshdg

integer*2 steelbreak,steelyr,flagccyield,flagcvyield
real*8 pcstrain,imagcstress,pvstrain,imagvstress,psstrain,psstress
common/dhvalues/pcstrain,imagcstress,pvstrain,imagvstress,psstrain,psstress,steel
break,steelyr,flagccyield,flagcvyield

if(abs(strain)>=k3*yebs) then
steelBreak=1
endif
if(steelBreak==1)then
stress=0.
goto 111
endif

if((abs(psstrain)>yebs).and.(abs(strain)<abs(psstrain))) then
steelyr=1
endif
if(steelyr==0) then
stress=strsteel(strain)
goto 111
else
        conver=sign(1.,psstrain)
        psstrain=conver*psstrain
        psstress=conver*psstress
        strain=conver*strain
        if(psstress>zarib*fps) then
                if(strain>psstrain) then
                stress=psstress+es*(zarib/zar2)*(strain-psstrain)
                elseif(strain<(psstrain-psstress/es-(zarib/2.)*fps/es))  then
                stress=-(zarib/2.)*fps+es*(zarib/(2*zar2))*(strain-
psstrain+psstress/es+(zarib/2.)*fps/es)
                else
                stress=psstress+es*(strain-psstrain)
                endif
        elseif(psstress<-(zarib/2.)*fps) then
                if(strain<psstrain) then
                stress=psstress+es*(zarib/(2*zar2))*(strain-psstrain)
                elseif(strain>(psstrain-psstress/es+zarib*fps/es)) then
                stress=zarib*fps+es*(zarib/zar2)*(strain-psstrain+psstress/es-
zarib*fps/es)
                else
                stress=psstress+es*(strain-psstrain)
                endif
```

```
        else
                if(strain>(psstrain-psstress/es+zarib*fps/es)) then
                stress=zarib*fps+es*(zarib/zar2)*(strain-psstrain+psstress/es-
zarib*fps/es)
                elseif(strain<(psstrain-psstress/es-(zarib/2.)*fps/es))  then
                stress=-(zarib/2.)*fps+es*(zarib/(2*zar2))*(strain-
psstrain+psstress/es+(zarib/2.)*fps/es)
                else
                stress=psstress+es*(strain-psstrain)
                endif
        endif
if(stress>0.9*fps) then
        trstr=fps*(0.45+0.5*k4)+fps*(-0.45+0.5*k4)*strain/(k2*yebs)
        if(stress>trstr) then
        stress=trstr
        endif
elseif(stress<(-0.9*fps)) then
        trstr=fps*(-0.45-0.5*k4)+fps*(-0.45+0.5*k4)*strain/(k2*yebs)
        if(stress<trstr) then
        stress=trstr
        endif
endif
stress=conver*stress
strain=conver*strain
endif
111 dhstrsteel=stress
psstrain=strain
psstress=stress

end function dhstrsteel

!****************************************************************************************
!This is the subroutine for calculating the moment and curvature for a
!specific axial load and steel or concrete strain. This subroutine uses
!monotonic material response through the "CalMonAxF" and
!"CalMonMom", so that the first point of any specific situation can be
!found.
!****************************************************************************************
Subroutine FindPoint(ebsilon, Axf, xres,msit)
!MS$ATTRIBUTES DLLEXPORT :: FINDPOINT
real*8 xres(6),trval,trxx, xl,xr,xx,d,dd,ad,af,leftval,rigval
real*8 ebsilon,Axf
real*8 hdir,wdir,thic,cover,alb(200),xb(200),yb(200)
integer*2 ndiv,nlb,m,mstwe,msit
common /section/hdir,wdir,thic,cover,alb,xb,yb,ndiv,nlb,m,mstwe

integer*2 analop
common/updateflag/analop
```

```
integer*2 ntime
ntime=0

 af = Axf
 xl = hdir/2.

 xr =xl+ 11.*hdir/ndiv !7.*hdir / ndiv
 d = xr - xl
 dd = d / ndiv

select case (analop)

case (14)
101 leftval = af*CalMonAxf(ph(ebsilon,xl),xl)-CalMonMom(ph(ebsilon,xl),xl)

   rigval =af*CalMonAxf(ph(ebsilon,xr),xr)-CalMonMom(ph(ebsilon,xr),xr)

If(leftval == 0) Then
        xx = xl
        goto 30
        ElseIf(rigval == 0) Then
         xx = xr
         goto 30
    ElseIf((leftval * rigval > 0).And.((leftval - rigval).ne.0)) Then
       ad = d * Sign(1.,leftval * (leftval - rigval))
       If(ad1 * ad < 0) Then
         xr = (xl + xr) / 2.
       GoTo 151
         End If

       xl = xl + ad
       xr = xr + ad

       Else
       ad1 = 0.
     xl = (xl + xr) / 2.
       End If
151       d = xr - xl
          ad1 = ad
       If (d < dd) Then
       xx = xl
       goto 30
       Else
       GoTo 101
    End If

case default
```

```
 trval=af-CalMonAxf(ph(ebsilon,xl), xl)
10 leftval = af-CalMonAxf(ph(ebsilon,xl), xl)
   rigval =  af-CalMonAxf(ph(ebsilon,xr), xr)
ntime=ntime+1
!This if is added to catch the maximum during analysis, when
!axial load level exceeds allowable levels.
if(abs(leftval)<abs(trval)) then
trval=leftval
trxx=xl
elseif(abs(rigval)<abs(trval)) then
trval=rigval
trxx=xr
endif
 If(d < dd)Then
  goto 20
endif
if(ntime>ndiv)then
            xx=trxx
            msit=1
            goto 30
endif

If(leftval == 0) Then
        xx = xl
        GoTo 20
        ElseIf(rigval == 0) Then
         xx = xr
         GoTo 20
    ElseIf((leftval * rigval > 0.).And.((leftval - rigval).ne.0.)) Then
       ad = d * Sign(1.,leftval)

       xl = xl + ad
       xr = xr + ad

        ElseIf((leftval * rigval < 0).or.((leftval - rigval).eq.0.)) Then
     xr = (xl + xr) / 2.
        d = xr - xl
end if
   GoTo 10

20 if((DABS(leftval)<DABS(rigval)).and.(DABS(leftval)<=DABS(trval))) then
      xx = xl
               msit=0
               elseif((DABS(leftval)>DABS(rigval)).and.(DABS(rigval)<=DABS(trval)))
then
               xx=xr
               msit=0
```

```
        elseif((DABS(leftval)>=DABS(trval)).and.(DABS(rigval)>=DABS(trval))) then
                xx=trxx
                if((dabs(trxx-xl)>dd).and.(dabs(trxx-xr)>dd))then
                        msit=1
                        else
                        msit=0
                        endif
                endif

end select
30 if((msit==0).and.(leftval.ne.rigval)) then
        xx=xr+rigval*(xr-xl)/(leftval-rigval)
endif

 xres(1) = ph(ebsilon,xx)
xres(2) = CalMonMom(xres(1), xx)
xres(3) = xx
if(ebsilon>0.) then
xres(4) = ebsilon
xres(5) = (xx - hdir + cover) *ebsilon/xx
else
xres(5)=ebsilon
xres(4)=xx*ebsilon/(xx-hdir+cover)
endif
xres(6) = CalMonAxf(xres(1), xx)

contains
real*8 function ph(ebsil,x)
real*8 ebsil,x
if(x==0.) then
ph=1.
goto 11
else
        if(ebsil>0.) then
        ph=ebsil/x
        else
        ph=ebsil/(x-hdir-cover)
        endif
endif
11 end function ph

End Subroutine
```

```
!********************************************************************************
                    !Force Deflection subroutines start from here:
!********************************************************************************

!*****************************************************************************************
!This is the subroutine for calculating the deflection, moment for a specific
!curvature and axial load. This subroutine utilizes different plastic hinge
!methods. The main methods are Park and Priestley method and the
!method proposed by Asad for USC_RC.
!*****************************************************************************************
Subroutine CalDefCur(phi, Axf, dres,msit)
!MS$ATTRIBUTES DLLEXPORT :: CALDEFCUR
real*8 dres(11),sym,syc,trm,trc,trlp,ctlp,mtlp,trstrns
real*8 phi,Axf,lp
integer*2 msit,mt

real*8 ydata(6) !used when FindPoint and CalMomCur

!Note: dres(11) is
(Deflection,Force,PlasticHingelength,cur_top,mom_top,Cur_bot,mom,naxis,s-
strain,c-strain,cal_axf)

real*8 hdir,wdir,thic,cover,alb(200),xb(200),yb(200)
integer*2 ndiv,nlb,m,mstwe
common /section/hdir,wdir,thic,cover,alb,xb,yb,ndiv,nlb,m,mstwe

real*8 es,fps,yebs,k1,k2,k3,k4,zarib,zar2,ec,fpco,fpcc,yebc,ebcc,ultebs,r,power
integer*2 mshdg
common/material/es,fps,yebs,k1,k2,k3,k4,zarib,zar2,ec,fpco,fpcc,yebc,ebcc,ultebs,r,
power,mshdg

real*8 leng,dlb,lpp
integer*2 method,unsys
common/FDInfo/leng,dlb,lpp,method,unsys

integer*2 analop
common/updateflag/analop

call FindPoint(-yebs,axf,ydata,mt)
syc=Abs(ydata(1)) !curvature at steel yeld****All methods
sym=Abs(ydata(2)) !Moment at steel yield******All methods
select case (method)
case (4)
!(Asad Method)
lp=lpp
call FindPoint(yebc/2.,axf,ydata,mt) !I replaced ebcc with yebc !This will consider
propo. or non-prop inside
if(sym<=Abs(ydata(2))) then
```

```
trm=sym
trc=syc
else
trm=Abs(ydata(2))
trc=Abs(ydata(1))
endif
        select case (analop)
                case (21,211,22)
                call CalMomCur(Phi,Axf,ydata,mt)
                case (24,241)
                call ProMomCur(phi, Axf, ydata)
        end select
dres(2)=ydata(2)/leng
if(Abs(ydata(2))>trm) then !When moment at cr.Sec is more than yield
trlp=leng*(1-trm/abs(ydata(2)))
        if(trlp>lp) then
        lp=trlp
        ctlp=sign(trc,phi) !curv. at top of hinge with proper directio
        mtlp=sign(trm,phi) !Mom at top of hinge
        else
        mtlp=dres(2)*(leng-lp)
        ctlp=trc*mtlp/trm
        endif
else
mtlp=(ydata(2))*(leng-lp)/leng
ctlp=trc*mtlp/trm
endif
!Note that pull-out can be added here
dres(1)=ctlp*lp*(leng-lp/2.)+(Phi-ctlp)*lp*(leng-lp/3.)/2.+ctlp*(leng-lp)**2/3.
dres(3)=lp
dres(4)=ctlp
dres(5)=mtlp
case (1)
!(Piestly and Park
        select case (analop)
                case (21,211,22)
                call CalMomCur(Phi,Axf,ydata,mt)
                case (24,241)
                call ProMomCur(phi, Axf, ydata)
        end select
        dres(2)=ydata(2)/leng
        select case (unsys)
        case (1)
        trlp=0.022*fps*dlb
        case (2)
        trlp=0.15*fps*dlb
        end select
        lp=0.08*leng+0.022*fps*dlb
```

```
if(Abs(phi)<Abs(syc)) then
dres(1)=phi*lp*(leng+trlp-lp/2.)+phi*(leng+trlp-lp)**2/3.
else
dres(1)=phi*lp*(leng+trlp-lp/2.)+Sign(syc,phi)*(leng+trlp-lp)**2/3.
endif
dres(3)=lp
dres(4)=sign(syc,phi)
dres(5)=sign(sym,phi)
case (2)
!(Priestly and Park revised by Xiao)
        select case (analop)
                case (21,211,22)
                call CalMomCur(Phi,Axf,ydata,mt)
                case (24,241)
                call ProMomCur(phi, Axf, ydata)
        end select
dres(2)=ydata(2)/leng
        select case (unsys)
        case (1)
        trlp=0.15*Abs(hstrsteel(phi*(hdir-cover-ydata(3)))*dlb)
        case (2)
        trlp=0.022*Abs(hstrsteel(phi*(hdir-cover-ydata(3)))*dlb)
        end select
        lp=0.08*leng+trlp

dres(1)=phi*lp*(leng+trlp-lp/2.)+Sign(syc,phi)*(leng+trlp-lp)**2/3.
dres(3)=lp
dres(4)=sign(syc,phi)
dres(5)=sign(sym,phi)

case (3)
!(Xiao Revised by Asad)
        select case (analop)
                case (21,211,22)
                call CalMomCur(Phi,Axf,ydata,mt)
                case (24,241)
                call ProMomCur(phi, Axf, ydata)
        end select
dres(2)=ydata(2)/leng
                trstrns=phi*(hdir-cover-ydata(3))
                if(abs(trstrns)>k3*yebs) then
                trstrns=k3*yebs
                endif
        select case (unsys)
        case (1)
        trlp=0.15*Abs(strsteel(trstrns)*dlb)
        case (2)
        trlp=0.022*Abs(strsteel(trstrns)*dlb)
```

```
        end select
        lp=0.08*leng+trlp
dres(1)=phi*lp*(leng+trlp-lp/2.)+Sign(syc,phi)*Abs(ydata(2))*(leng-lp)*(leng+trlp-
lp)**2/(3.*leng*sym)
dres(3)=lp
dres(4)=sign(syc,phi)
dres(5)=sign(sym,phi)
end select
dres(6)=ydata(1)
dres(7)=ydata(2)
dres(8)=ydata(3)
dres(9)=ydata(4)
dres(10)=ydata(5)
dres(11)=ydata(6)
msit=mt
select case (analop)
case (21,24)
lpp=lp
end select
end subroutine CalDefCur

!*********************************************************************************************
!This is the subroutine for calculating the moment, curvature and the
!pertinent information for a specific deflection and axial load. This
!subroutine utilizes different plastic hinge methods. The main methods are
!Park and Priestley method and the method proposed by Asad for
!USC_RC.
!*********************************************************************************************
Subroutine CalForDef(def, Axf, dres,mt)
!MS$ATTRIBUTES DLLEXPORT :: CALFORDEF
real*8 dres(11),p,af,phi,trlp,syc,trdefl,d,ad,ad1,leftval,rigval,xl,xr
real*8 def,Axf,lp
integer*2 mt

real*8 hdir,wdir,thic,cover,alb(200),xb(200),yb(200)
integer*2 ndiv,nlb,m,mstwe
common /section/hdir,wdir,thic,cover,alb,xb,yb,ndiv,nlb,m,mstwe

real*8 es,fps,yebs,k1,k2,k3,k4,zarib,zar2,ec,fpco,fpcc,yebc,ebcc,ultebs,r,power
integer*2 mshdg
common/material/es,fps,yebs,k1,k2,k3,k4,zarib,zar2,ec,fpco,fpcc,yebc,ebcc,ultebs,r,
power,mshdg

integer*2 analop
common/updateflag/analop

real*8 leng,dlb,lpp
integer*2 method,unsys
```

```
common/FDInfo/leng,dlb,lpp,method,unsys
real*8 ydata(6)

select case (method)
case(1)
p = def
af = Axf
call FindPoint(-yebs,af,ydata,mt)
syc=Abs(ydata(1))

select case (unsys)
case (1)
        lp=0.08*leng+0.022*fps*dlb
        trlp=0.022*fps*dlb
case (2)
        lp=0.08*leng+0.15*fps*dlb
        trlp=0.15*fps*dlb
end select
trdefl=syc*lp*(leng+trlp-lp/2.)+syc*(leng+trlp-lp)**2/3.
if(Abs(p)<=trdefl) then
phi=syc*p/trdefl
syc=(leng+trlp-lp)*syc/(leng+trlp)
else
phi=(p-sign(syc*(leng+trlp-lp)**2/3.,p))/(lp*(leng+trlp-lp/2.))
endif
        select case (analop)
                case (21,211,22)
                call CalMomCur(Phi,Af,ydata,mt)
                case (24,241)
                call ProMomCur(phi, Af, ydata)
        end select
dres(1)=p
dres(2)=ydata(2)/leng
dres(3)=lp
dres(4)=syc
dres(5)=ydata(2)*(leng+trlp-lp)/(leng+trlp)
dres(6)=phi
dres(7)=ydata(2)
dres(8)=ydata(3)
dres(9)=ydata(4)
dres(10)=ydata(5)
dres(11)=ydata(6)
case default
p = def
af = Axf
d=5*(yebs)/((hdir))
 xl = d
  xr=xl+d
```

```
dd = d / 50.
10 call CalDefCur(xl,af,dres,mt)
leftval =p-dres(1)
call CalDefCur(xr,af,dres,mt)
rigval =p-dres(1)
If(leftval == 0) Then
        xx = xl
        GoTo 20
        ElseIf(rigval == 0) Then
         xx = xr
         GoTo 20
    ElseIf((leftval * rigval > 0).And.((leftval - rigval).ne.0)) Then
       ad = d * Sign(1.,leftval * (leftval - rigval))
       If(ad1 * ad < 0) Then
         xr = (xl + xr) / 2.
       GoTo 15
         End If
       xl = xl + ad
      xr = xr + ad
       Else
       ad1 = 0.
     xl = (xl + xr) / 2.
       End If
15       d = xr - xl
          ad1 = ad
       If (d < dd) Then
       xx = xl
       GoTo 20
       Else
       GoTo 10
    End If
end select
20        if(dres(6)>0.) then
            call hupdate(dres(6),dres(8))
            else
            call hupdate(dres(6),hdir-dres(8))
            endif
lpp=dres(3)
 end subroutine

!******************************************************************************************
!This is the subroutine for calculating the deflection for a specific force
!and axial load. This subroutine utilizes different plastic hinge methods.
!The main methods are Park and Priestley method and the method
!proposed by Asad for USC_RC.
!******************************************************************************************
Subroutine CalDefFor(for, Axf, dres,mt,mst)
!MS$ATTRIBUTES DLLEXPORT :: CALDEFFOR
```

```
real*8 dres(11),p,af,ydata(6)
real*8 for,Axf
integer*2 mt,mst
real*8 hdir,wdir,thic,cover,alb(200),xb(200),yb(200)
integer*2 ndiv,nlb,m,mstwe
common /section/hdir,wdir,thic,cover,alb,xb,yb,ndiv,nlb,m,mstwe
real*8 es,fps,yebs,k1,k2,k3,k4,zarib,zar2,ec,fpco,fpcc,yebc,ebcc,ultebs,r,power
integer*2 mshdg
common/material/es,fps,yebs,k1,k2,k3,k4,zarib,zar2,ec,fpco,fpcc,yebc,ebcc,ultebs,r,
power,mshdg
real*8 leng,dlb,lp
integer*2 method,unsys
common/FDInfo/leng,dlb,lp,method,unsys
integer*2 analop
common/updateflag/analop
for=for*leng
call CalCurMom(for, Axf, ydata,mt,mst)
call CalDefCur(ydata(1), Axf, dres,mt)
20      if(dres(6)>0.) then
        call hupdate(dres(6),dres(8))
        else
        call hupdate(dres(6),hdir-dres(8))
        endif
end subroutine CalDefFor
!This two functions are needed to be used when we want to get stuff without
!hysteresis for plastic hinge purposes, and also FindPoint for Monotonic
real*8 Function CalMonAxf(phi, x)
real*8 s,d
real*8 phi,x
real*8 hdir,wdir,thic,cover,alb(200),xb(200),yb(200)
integer*2 ndiv,nlb,m,mstwe
common /section/hdir,wdir,thic,cover,alb,xb,yb,ndiv,nlb,m,mstwe
real*8 cfiber(500,3),vfiber(500,3),rebar(200,2) !Note 3rd component is the area,
makes faster, steel can be also later
integer*2 cflag(500),vflag(500),sflag(200,2) !also distances may be added to
expedite execution
common/hfiber/cfiber,vfiber,rebar,cflag,vflag,sflag
d = hdir / ndiv
!clockwise phi is positive and x starts from compression side
!compressive strain is positive
s = 0.
do i = 1,ndiv
s = s + cfiber(i,3) * constr((x - (i - 0.5) * d) * phi)
end do
do i=1,ndiv
s=s+vfiber(i,3)*covstr((x-(i-0.5)*d)*phi)
end do
do i = 1,nlb
```

```
Select Case (mstwe)
Case (2)
s = s + alb(i) * strsteel(phi * (x + xb(i) - hdir / 2))
Case (1)
s = s + alb(i) * strsteel(phi * (x + yb(i) - hdir / 2))
End Select
end do
CalMonAxf = s
End Function
real*8 Function CalMonMom(phi, x)
real*8 phi,x
real*8 s,d
real*8 hdir,wdir,thic,cover,alb(200),xb(200),yb(200)
integer*2 ndiv,nlb,m,mstwe
common /section/hdir,wdir,thic,cover,alb,xb,yb,ndiv,nlb,m,mstwe
real*8 cfiber(500,3),vfiber(500,3),rebar(200,2) !Note 3rd component is the area,
makes faster, steel can be also later
integer*2 cflag(500),vflag(500),sflag(200,2)                !also distances may be
added to expedite execution
common/hfiber/cfiber,vfiber,rebar,cflag,vflag,sflag
d = hdir / ndiv
s = 0.
do i = 1,ndiv
s = s + (hdir / 2 - (i - 0.5) * d)*cfiber(i,3) * constr((x - (i - 0.5) * d) * phi)
end do
do i=1,ndiv
s=s+(hdir / 2 - (i - 0.5) * d)*vfiber(i,3)*covstr((x-(i-0.5)*d)*phi)
end do
do i = 1,nlb
Select Case (mstwe)
Case (2)
s = s + xb(i) * alb(i) * strsteel(phi * (x + xb(i) - hdir / 2))
Case (1)
s = s + yb(i) * alb(i) * strsteel(phi * (x + yb(i) - hdir / 2))
End Select
end do
CalMonMom = s
End Function
```

APPENDIX III

MULTISPRING MODEL FOR MOMENT-CURVATURE ANALYSIS OF CIRCULAR REINFORCED CONCRETE COLUMNS

Multispring Model for Moment-Curvature Analysis of Circular Reinforced Concrete Columns

ABSTRACT

A very simple multispring model is to be developed to simulate the nonlinear (elasto-plastic) stiffness- and strength-degrading hysteretic behavior of RC members with circular sections subjected to a combination of dynamic axial force and bilateral dynamic* bending moment. This report is a brief description of the first step of the research, in which a multispring model is proposed to replace a circular RC section. In this step, the model is scaled to have a moment-curvature behavior very close to the results of the fiber model solution of the section, for known material properties (which may be considered as a kind of finite element analysis for the moment-curvature behavior of the RC sections). In subsequent steps, the model will be applied to simulate the nonlinear degrading hysteretic response of an RC circular section subjected to combined axial force bilateral moment, which in turn can be used to predict the flexural deformation of an RC member under the specified conditions. The validity of the model will be investigated by comparing it with the results of a sophisticated analysis and also with experimental data from ongoing tests on RC columns with circular sections subjected to axial force and bending moment.

INTRODUCTION

The moment-curvature characteristics of a section are necessary to obtain the rotational stiffness or, in general, the stiffness matrix of a member, which in turn is essential to analyze the behavior of an RC structure in which the nonlinear degrading property of the materials should be taken into account. This requires a great deal of computational effort and time. Getting precise analytical results for the moment-curvature relationship of an RC circular section with a nonlinear degrading material property requires sophisticated analytical methods. The finite

---

*The bending moment and direction are both dynamic, meaning that the components of the bending moment are independently dynamic.

element method is the most sophisticated but has the deficiency of requiring a great deal of computational effort.

Zeris and Mahin (1991) proposed a kind of finite element model for the analysis of the nonlinear behavior of RC columns under biaxial excitation. Their formulation accounts for most aspects of axial-flexural behavior.

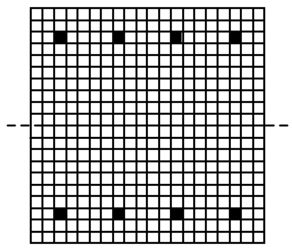

Figure 1 Fiber model example, for division of cross section

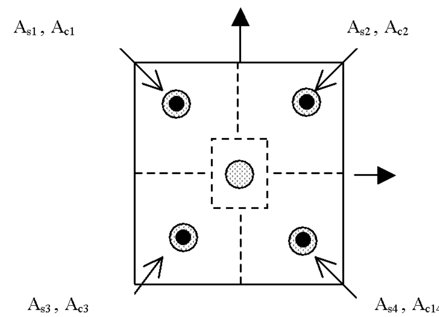

Figure 2 Concrete and steel springs in a multispring model

The section is divided into some small elements, which may be considered as the cross section of the fibers making the column. Under the assumption that plane remains plane, the axial deformation of each fiber is formulated, which in turn provides the axial-flexural behavior of the section. A sample section with the mesh is shown in Figure 1. The finer the mesh, the more precise the results. Again, the amount of computational effort to implement the problem is the main deficiency.

Lai et al. (1984) developed an analytical model to simulate the hysteretic and stiffness degrading behavior of RC members subjected to axial load and biaxial bending interaction. The model separates the member into two inelastic elements. Each inelastic element, composed of individual spring elements, simulates the inelastic effects of the member as well as the cumulative slip of the anchored bars in the beam-column joint. The formulation of the spring model is based only on the static equilibrium of the cross section according to the current ACI Code. The model does not provide any information about the moment-curvature of the section and works only for modeling the end parts of the element. Figure 2 is a sample of the model with the springs. The area of the concrete springs is assigned based on the current axial force and bending moment, evaluated according to the ACI stress block concept, and is variable in each step. Therefore in each time increment during the analysis, the spring area should be updated in addition to the material property. If the section is not symmetric, an approximation is applied by making an average between the scaled values for the concrete springs in the x and y directions. The model cannot be applied for moment-curvature purpose.

Li et al. (1988) proposed a practical multispring model to simulate the behavior of a section subjected to varying axial load and bilateral bending moment. The model is used mainly to model the nonlinear behavior of the end parts, but it still can be used to model the moment-curvature of the section. Getting a reasonable result requires a large number of springs, which are usually located at the center of the corresponding replaced parts of the section. It is actually a kind of the aforesaid fiber model with the same computational deficiency. To overcome this problem, the section is replaced with a comparatively small number of concrete-steel springs. The model is scaled so that the moment-curvature of the section for any axial load is well simulated by the model; therefore, the overall stiffness matrix of the element is more easily computed at any stage compared with other methods.

PROPOSED MODEL

Basic Idea

The main idea is to have a very simple model consisting of a small number of springs for the section so that the moment-curvature curve derived by using the model is close to the one derived by using the fiber model (as a benchmark) for different axial loads. Therefore, the resulting flexural deflection for a beam or column subjected to an axial force and a bilateral moment is the same using either the fiber or multispring models in modeling the section. The moment-curvature curve of a concrete section always passes through a yielding region, the first point of which may be considered to correspond to the yield of the first longitudinal steel bar. If the moment-curvature curves of the fiber and multispring models have the same yield points for a specific axial force, it means that at the same curvature and moment the yielding process starts. Therefore the moment-curvature curves will approximately match in the linear part and will be close beyond the first yield. In addition, if the two curves match in a second or third point, they are more precisely close.

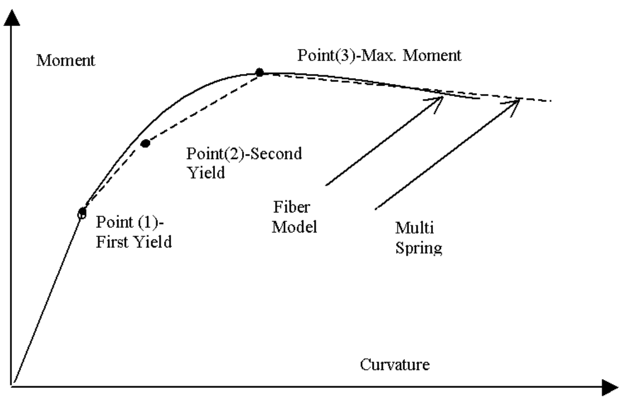

Figure 3 Typical moment-curvature curves, using fiber model and multispring model

Figure 3 shows a typical moment-curvature curve for a section**.** The solid curve represents the fiber model and the dotted curve the multispring model. Points (1) and (2) represent the first yield and the second yield points, respectively, of the multispring model for a certain axial load for which the moment-curvature curves have been evaluated. To have close yield points for the two models, for different axial forces we consider the axial force bending moment interaction curves for the two models at the first yield, and minimize the difference between the axial forces and bending moments for different curvatures. To do this minimization, the parameters are chosen based on the configuration of the multispring model evaluated through the aforesaid minimization. We can apply the same procedure of minimization to another situation, such as having the second yield point of the two moment-curvature curves close, by introducing new parameters, as will be shown in the two-layer model. Having all the parameters, we can construct the model so that the moment-curvature curves for the two models for different axial loads are close. This minimization procedure is done based on the configuration of the multispring model and also the material properties. From a mathematical standpoint, it can be shown that the procedure is practical and realistic considering the continuity of the stress-strain curve of the concrete and its first derivative with respect to strain, at the range where they are defined, and also having a single maximum stress in the stress-strain relationship of confined or unconfined concrete.

General Model

The configuration of the multispring model is different if the concrete and steel springs are combined (except for the concrete spring at the center, which is always only concrete) or separated, and also if we have two parameters (minimizing for the first yield), or four parameters (minimizing for both the first yield and the maximum moment). Each selection has its advantages and disadvantages. Figure 4 and Figure 5 show four possible configurations of the model when concrete and steel springs are combined or separated. Figure 4 shows the case in which the concrete and steel springs are combined. On the left side of the figure one layer of springs and two parameters *a* and *b* are to be determined. However, on the right side two layers of springs and 4 parameters *a, b, c,* and *d,* are to be determined. In both configurations:

N: Number of total springs (a combined spring counts as one spring)

R: Radius of the confined concrete core

A_s: Total area of the longitudinal steel bars in the section

In the first configuration, with 2 parameters:

a is the ratio of the radius of the circle on which the center of the combined concrete-steel springs are located, to *R,* and *b* is the ratio of the radius of the central concrete spring to *R*. Therefore:

$A_{c1} = \pi (bR)^2$ Area of the central pure concrete spring

$A_{c2} = \dfrac{\pi(1-b^2)R^2}{(N-1)}$ Area of all other concrete springs

$A_{ssp} = A_s/(N-1)$ Area of the steel spring

In the second configuration, with 4 parameters:

a is the ratio of the radius of the circle on which the centers of the concrete springs of the outer layer are located to *R*.

b is the ratio of the radius of the circle on which the centers of the concrete springs of the second layer are located to *R*.

c is the ratio of the radius of the central concrete spring to *R*.

d is a number between zero and one, which determines the ratio of the area of the inner layer concrete springs to the total area of the outer and inner layer concrete springs.

Therefore:

$A_{c1} = \pi (cR)^2$ Area of the central concrete spring

$A_{c2} = \dfrac{d\pi(1-c^2)R^2}{[(N-1)/2]}$ Area of the inner layer concrete springs

$$A_{c2} = \frac{(1-d)\pi(1-c^2)R^2}{[(N-1)/2]} \qquad \text{Area of the outer layer concrete springs}$$

$$A_{ssp} = A_s / [(N-1)/2] \qquad \text{Area of the steel springs, which are only on the outer layer}$$

The parameters to be determined are *a* and *b* in the first configuration, and *a, b , c,* and *d* in the second..

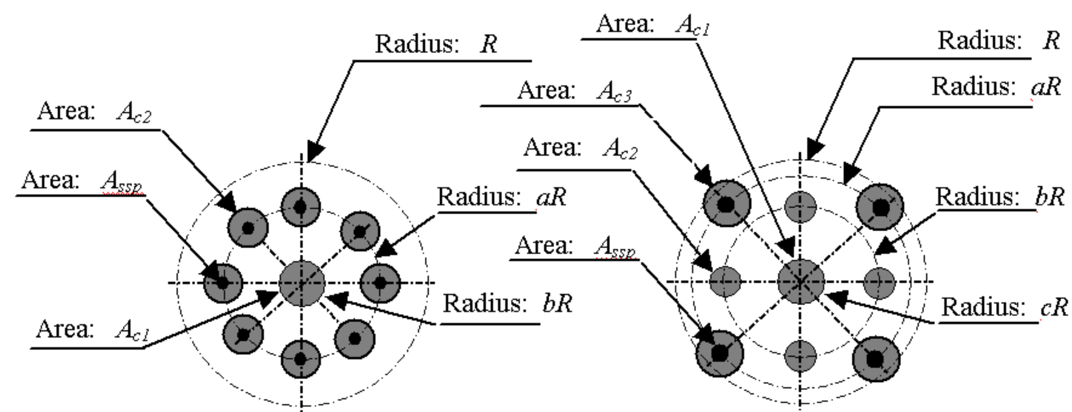

Figure 4 Combined one-layer multispring model, n=9, (left), and two-layer combined multispring model, n=9

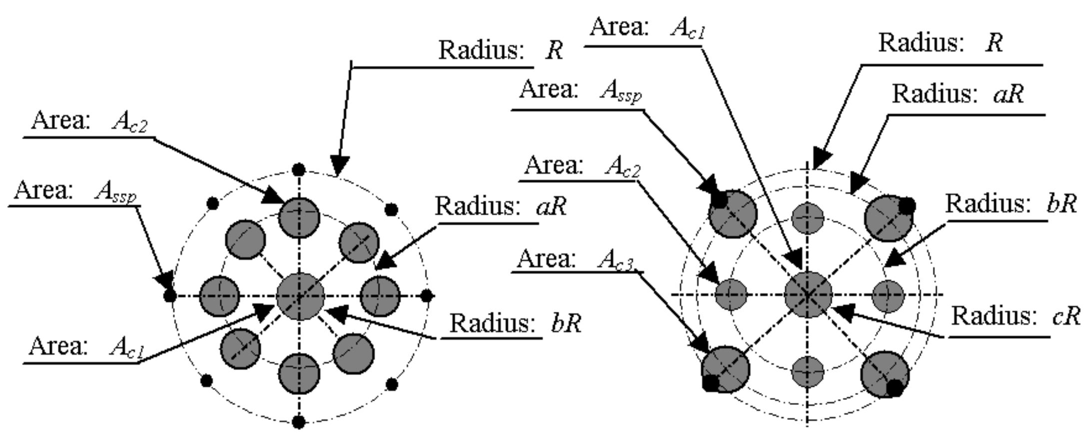

Figure 5 Uncombined one-layer multispring model, n=9 (left), and two-layer multispring model, n=9

The Model Used Here

The multispring model used here to demonstrate the proposed model is of the first configuration type with two parameters, as shown in Figure 4 (left). It consists of 9 concrete-steel springs, which will replace the section. The number of the springs may be chosen according to the problem but, as will be shown, increasing the number of the springs beyond a certain level has a very negligible effect on the results and also may violate the basic purpose of the modeling, which is to simplify the section from the computational standpoint. An incidental fact is that instead of having concrete-steel springs, which means that a specific spring consists of both the designated amount of concrete and steel, steel and concrete springs may be considered in different locations. These two methods have their own advantages and disadvantages, which will be studied during this research. For the illustration purposes of this report, the concrete and steel springs are considered to be at the same location or, in other words, concrete-steel springs, except for the spring, at the center of the section, which is concrete only, in either method. Either way, keeping the model as simple as possible was a main goal so that the method is more efficient compared to others such as the fiber model analysis or other multispring models in which a greater number of springs replace the section.

Material Properties

The procedure is applicable for any reasonable model for material properties. For the purpose of demonstration, the material properties considered here are as follows:

(a) Steel is assumed to have a bilinear stress-strain relationship, with a yield stress = 60 ksi and modulus of elasticity = 29000 ksi.

(b) The confined concrete is assumed to behave according to the model proposed by Mander et al. In this model, $f_c = \dfrac{f'_{cc}\, xr}{r-1+x^r}$, where f'_{cc} is the compressive strength of confined concrete and $x = \dfrac{\varepsilon_c}{\varepsilon_{cc}}$, where ε_c is the longitudinal compressive concrete strain and $\varepsilon_{cc} = \varepsilon_{co}[1+5(\dfrac{f'_{cc}}{f'_{co}}-1)]$, f'_{co} and ε_{co} are the unconfined concrete strength and corresponding strain, which is generally taken as 0.002, and $r = \dfrac{E_c}{E_c - E_{\sec}}$, where $E_c = 5{,}000\sqrt{f'_{co}}MPa$, is the tangent modulus of elasticity of the concrete (1 MPa=145psi) and $E_{\sec} = \dfrac{f'_{cc}}{\varepsilon_{cc}}$. f'_{cc} , is calculated according to the longitudinal and transverse (confinement) reinforcement as described in the corresponding reference.

(c) Regarding material properties, the factors affecting the result may be stated as:

E_s: modulus of elasticity of steel

f'_c: compressive strength of concrete

ρ_{cc}: ratio of area of longitudinal reinforcement to area of core of section

ρ_s: ratio of the volume of transverse confining steel to the volume of confined concrete core

Number of Springs

The number of springs used for the model in this report is taken to be 9, but others may be used as long as the intended simplicity of the model is not violated from the computational standpoint. The number of springs may be considered different in two pre- and post-minimization stages. The number of springs is taken to be a large number, which makes the section to be composed of a ring with radius aR, measured from the center line of the ring as shown in Figure 4 and Figure 5. So the parameters are evaluated independent of the number of springs. The reason is that for any finite number of springs, there are two distinct directions along which the most distinct behaviors are observed, shown in Figure 6. For any reasonable number of springs, the evaluated parameters along these two distinct directions are on the two different sides of the evaluated parameters when using a large number of springs or, i.e., the ring model. As a numeric example, for the section shown in Figure 9, and for N=9, the parameters are evaluated as follows:

Direction 1: a=0.912 b=0.495

Direction 2: a=0.868 b=0.319

While the parameters evaluated by the ring model (for N=100) are:

A=0.882 b=0.399

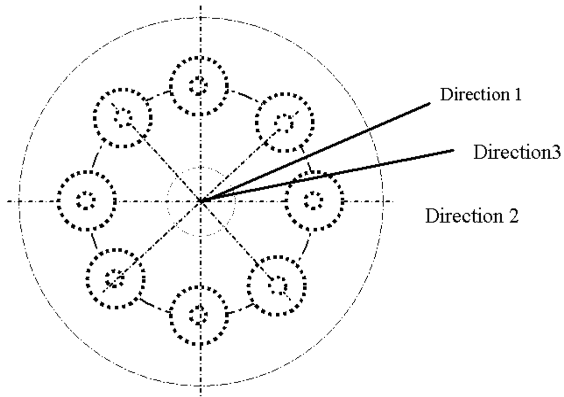

Figure 6 Two distinct directions for multispring model (1 and 2) and the average direction (3)

Therefore, to evaluate the parameters the ring model is used, or a large number for *N* is selected. The evaluated parameters work for any number of springs and the number of springs is thus a matter of precision for the output results. However, *N* has a very small effect beyond a certain number. For simplicity and reasonably precise results, we take *N*=9, as shown by investigations.

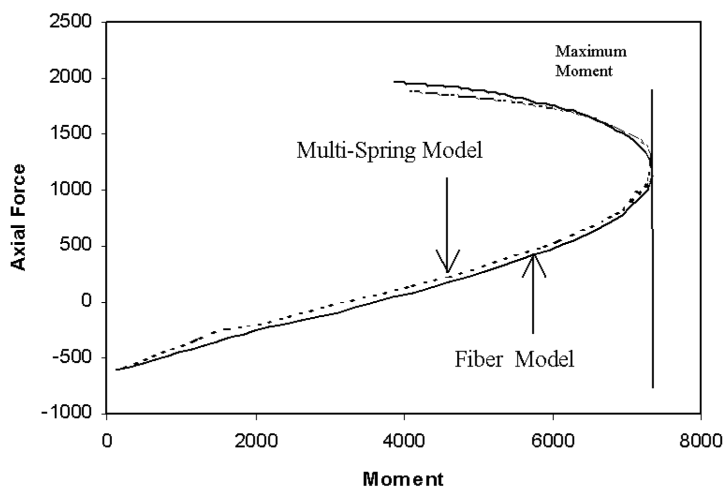

Figure 7 Axial force bending moment interaction curves, at the first tensile yield of steel, for fiber model (solid curve) and multispring model (dotted curve), using the evaluated parameters *a* and *b*

Computation Method

To get the closest result for the moment curvature of the model to that of the fiber model, considered as a benchmark, for different axial forces, the axial force bending moment interaction curve of the section, for the multispring and fiber models at the first yield of the tensile steel, the difference between the axial forces of the two models and also the difference between their bending moments at the first yield for different curvatures has been minimized. This means that for a specific axial force, the two models reach the first yield at the same curvature and moment. The first yield for the fiber model is defined to be the first yield of steel, which in turn is when the strain of the fiber on the circumference of the confined concrete circle reaches the yield strain of steel. The first yield of the spring model is also defined to be when the strain at a point with the same distance from center reaches the yield strain of steel.

Figure 7 shows a portion of the axial force bending moment interaction curve of the section when the tensile strain is fixed at the yield strain of steel. Details of the section used here are shown in Figure 9. The fiber model is used to evaluate the interaction curve shown by the solid curve, while the multispring model is used to evaluate the interaction curve of the section shown by the dotted curve. Parameters *a* and *b* have been determined by the aforesaid minimization procedure. These parameters are evaluated such that the two curves are as close as possible to each other. This may be done through minimizing the mean square error of the axial force and bending moment of the interaction curve of the multispring model compared to the fiber model as a benchmark, within a range of curvatures. The range of curvatures for this process is chosen to be from the point where the axial force is zero to the curvature where we have maximum bending moment for the fiber model. A brief mathematical description of the problem is as follows:

As shown in Figure 8, the strain may be calculated as: $\varepsilon = (2R - x)\phi - \varepsilon_y$ at each point of the section. Then, the axial force and bending moment at the first yield for the fiber model may be computed as follows:

$$P_c = \int_0^{2R} 2 f'_{cc}[(2R - x)\phi - \varepsilon_y].\sqrt{2Rx - x^2}\,dx \qquad \text{(A1.1)}$$

where P_c is the axial force due to concrete.

$$P_{st} = 2\int_0^{\pi} f_{st}[R(1 + Cos(\theta))\phi - \varepsilon_y].R.\frac{A_s}{2\pi R}.d\theta \qquad \text{(A1.2)}$$

where P_{st} is the axial force due to steel.

$$P^f = P_c + P_{st} \tag{A1.3}$$

where P^f is the total axial force for a specific curvature, evaluated for the fiber model.

$$M_c = \int_0^{2R} 2f'_{cc}[(2R-x)\phi - \varepsilon_y].\sqrt{2Rx - x^2}.(R-x)dx \tag{A1.4}$$

$$M_{st} = 2\int_0^{\pi} f_{st}[R(1+Cos(\theta))\phi - \varepsilon_y].R.\frac{A_s}{2\pi R}.R.Cos(\theta).d\theta \tag{A1.5}$$

$M^f = M_c + M_{st}$ is the total moment for the curvature evaluated for the fiber model, where M_c is the moment due to concrete and M_{st} is the moment due to steel, respectively, which are functions of the specific curvature at which each is evaluated. Now, we evaluate the axial force and bending moment for the ring model:

$$\begin{aligned} P^{ms} &= 2\int_0^{\pi} \{f_{cc}[R(1+aCos(\theta))\phi - \varepsilon_y]\frac{(1-b^2)\pi R^2}{2\pi} \\ &+ f_{st}[R(1+aCos(\theta))\phi - \varepsilon_y]\frac{A_s}{2\pi}\}d\theta + f_{cc}[R\phi - \varepsilon_y]\pi b^2 R^2 \end{aligned} \tag{A1.6}$$

$$\begin{aligned} M^{ms} &= 2\int_0^{\pi} aRCos(\theta)\{f_{cc}[R(1+aCos(\theta))\phi - \varepsilon_y]\frac{(1-b^2)\pi R^2}{2\pi} \\ &+ f_{st}[R(1+aCos(\theta))\phi - \varepsilon_y]\frac{A_s}{2\pi}\}d\theta \end{aligned} \tag{A1.7}$$

where P^{ms} and M^{ms} are the axial force and bending moment of the ring model, respectively, and are functions of the curvature. The parameters a and b are present here and will be evaluated during further steps. Now, we define the function:

$$fun(a,b) = \int_{\phi_{\min}}^{\phi_{\max}} \{[P^f(\phi) - P^{ms}(\phi)]^2 + [M^f(\phi) - M^{ms}(\phi)]^2\}d\phi \tag{A1.8}$$

where ϕ_{min} and ϕ_{max} are the lower and upper limits of integration, and correspond to the curvature where we have zero axial force, and where the moment is maximum for the fiber model. Then, solving the equations:

$$\frac{\partial fun(a,b)}{\partial a} = 0, \text{ and } \frac{\partial fun(a,b)}{\partial b} = 0 \tag{A1.9}$$

will give the parameters a and b , which minimize the square difference of the axial forces and bending moments of fiber and ring models, in the range of the aforesaid curvatures. Since the stress-strain relationship curves of steel and concrete are continuous where defined, *fun(a,b),* is a function of the parameters, which can be minimized in terms of the parameters.

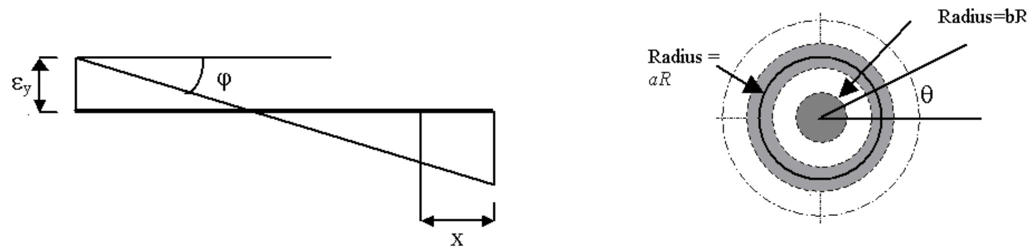

Figure 8 Ring model and corresponding strains for a specific curvature

Section:

The sections used here are shown in Figure 9. For the first section, ρ_{cc} is 0.031 and ρ_s is 0.005. For the given conditions and using Mander's model for confined concrete, the compressive strength of confined concrete, f'_{cc}, is 5.898 ksi (cover concrete strength is 5.0 ksi) and the corresponding strain for concrete, ε_{cc}, is 0.0045. For the second section, which is a typical Caltrans column section, ρ_{cc} is 0.023 and ρ_s is 0.0051. For the given conditions, and using Mander's model for confined concrete, f'_{cc}, is 4.17446 ksi (cover concrete strength is 3.25 ksi).and ε_{cc} is 0.004587.

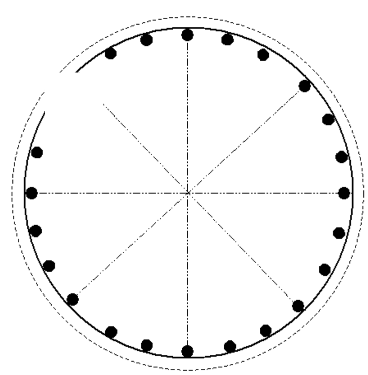

Figure 9 Details of the section used in this report: one, diameter=24″, cover concrete thickness= 1.5″, number of longitudinal bars=24, size=6, size of transverse bars=3, location=4″ c/c, and for two, the corresponding numbers are: 48″, 2″, 23, 11, 4, 3.5″, respectively

Using Model for Engineering Solution

Although the multispring model is provided to simulate the moment-curvature of a RC circular section, as the first step toward simulating the nonlinear stiffness and strength-degrading hysteretic response of an RC element, it may be used to provide engineering solutions for the moment-curvature and axial force bending moment interaction of a circular section. The following briefly describes the steps for getting the required data.

Axial Force Bending Moment Interaction

Having already determined the parameters *a* and *b* by the aforesaid method, or selected parameters a table providing the initial data, the interaction of the axial force and bending moment for a certain condition, e.g., a specific strain in concrete, may easily be evaluated. For example, if the interaction is to be evaluated for a strain of concrete, ε_{cm}, at the surface of the section:

$$P = P_{con} + P_{st} \tag{A1.10}$$

where N_{con} is the axial force due to concrete and N_{st} is the axial force due to steel.
And:

$$P_{con} = \sum_{i=1}^{N} A_{con}^{i} f'_{cc}[\varepsilon_i] \text{, and } P_{st} = \sum_{i=1}^{N-1} A_{st} f_{st}[\varepsilon_i] \tag{A1.11}$$

Where N is the number of springs:

A_{con}^{i} is the area of the i^{th} concrete spring

A_{st} is the area of the i^{th} steel spring

$f_{st}[\varepsilon_i]$ is the steel stress at a strain equal to ε_i based on the material model

$f'_{cc}[\varepsilon_i]$ is the concrete stress at ε_i based on the material model

$\varepsilon_i = \{\varepsilon_{cm} - R\phi\}$ for the central spring and $\varepsilon_i = \{\varepsilon_{cm} - [R - aRCos(\frac{2\pi i}{N-1})]\phi\}$ for all other springs, and ϕ is a curvature for which we calculate the axial force and bending moment. By changing the curvature, we may calculate different points of the axial force bending moment interaction curve. Similarly:

$$M = M_{con} + M_{st} \tag{A1.12}$$

where M_{con} is the bending moment due to concrete and M_{st} is the bending moment due to steel. And:

$$M_{con} = \sum_{i=1}^{N-1} A_{con}^{i} f'_{cc}[\varepsilon_i]\{aRCos(\frac{2\pi i}{N-1})\} \text{ and} \tag{A1.13}$$

$$M_{st} = \sum_{i=1}^{N} A_{st} f_{st}[\varepsilon_i]\{aRCos(\frac{2\pi i}{N-1})\} \tag{A1.14}$$

with the same conditions already stated above.

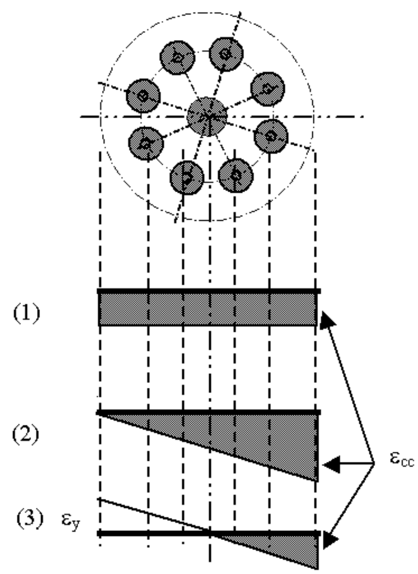

Figure 10 Numerical example

Moment Curvature

To get the moment-curvature curve for a specific axial force, by assuming a bilinear moment-curvature curve with the same procedure as above, we calculate the interaction curve (sample points represent the curve) at the first yield of steel, and then for a specific axial force, we can get the corresponding curvature and moment, and the moment-curvature curve may be plotted. For a trilinear curve, we can get the interaction curve for another situation, such as the second yield of the multispring model, and pick up the corresponding curvature and moment for the axial force, and then plot the moment-curvature curve of the section.

Numerical Example

As a numerical example, we used a typical Caltrans column, with the above details. For this section, the evaluated parameters are: *a=0.875*,and *b=0.3733*, and using the one-layer model with mixed steel and concrete springs. (So the model is composed of 9 springs, of which one is pure concrete at the center.) For calculation, we may choose any direction, e.g., 1,2, or 3 as already shown, but for simplicity, we chose direction 1 and evaluated the interaction curve when the concrete strain was equal to ε_{cc} .The concrete stress-strain relationship curve based on the Mander model and the section specifications is calculated to be:

$$f_{cc}(\varepsilon) = \frac{0.814127281 + \varepsilon}{0.0002372 + \varepsilon^{1.360796}}$$

and the concrete and steel spring areas are:

$A_{c1} = \pi(bR)^2$ Area of the central pure concrete spring

$A_{c1} = \pi(0.37328 \times 21.75)^2 = 207.08$, $A_{c2} = \dfrac{\pi(1-b^2)R^2}{(N-1)}$ Area of other concrete springs

$$A_{c2} = \frac{\pi(1-0.37328^2)21.75^2}{(9-1)} = 159.886$$

$A_{ssp} = A_s/(N-1)$ Area of the steel spring

$A_{ssp} = 34.15255/(9-1) = 4.26907$

Using the aforesaid relations and plugging in the corresponding data, we get the following results:

For case (1): φ=0, *P*=8253.11 kips, *M*=0

For case (2) φ=0.000105455, *P*=6387.46 kips, *M*=25774.86 kip-inch

For case (3) φ=0.000153018, *P*=4018.82 kips, *M*=49857.08 kip-inch

For the case when the axial force is equal to zero, φ=0.000464854, *P*=0 kips, *M*= 40118.46 kip-inch

For a curvature 1.5 times the curvature where axial force is zero, φ=0.00069728, *P*=-39.63 kips, *M*=35332.57 kip-inch

The corresponding axial forces and bending moments for the fiber model are as follows:

For case (1): φ=0, *P*=8253.11 kips, *M*=0

For case (2) φ=0.000105455, *P*=6505.37 kips, *M*=23665.62 kip-inch

For case (3) φ=0.000153018, P=3992.58 kips, M=49136.43 kip-inch

For the case when the axial force is equal to zero, φ=0.000464854, P=0.004 kips, M=36238.11 kip-inch.

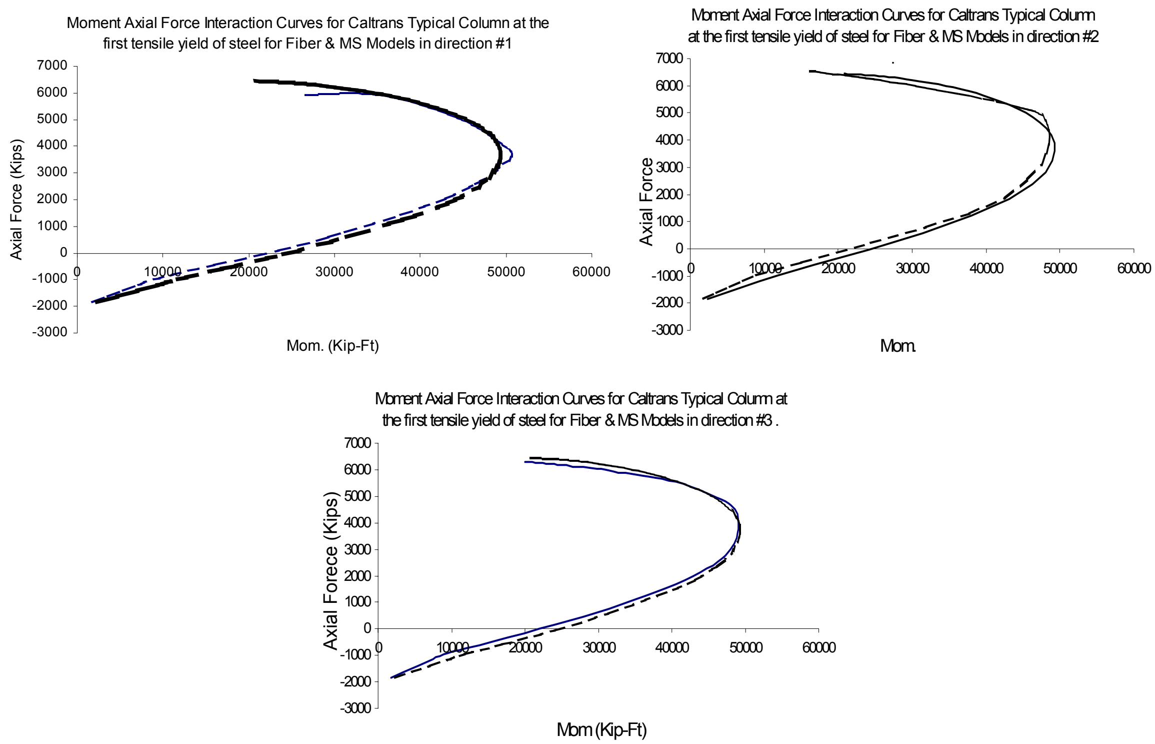

Figure 11 Comparing the results for axial force bending moment interaction from multispring model in three different directions with fiber model

For a curvature 1.5 times the curvature where the axial force is zero, φ=0.00069728, P=-588.82 kips, M=27936.48 kip-inch. We can see the results are close for the multispring model and the fiber model. Figure 11 shows the graphs comparing the results in the three different directions.

Model Verification

To verify the multispring model, the moment-curvature curve of the model and the benchmark fiber model for different axial forces in the two distinct directions and the average direction (see Figure 6) are compared. The axial forces are the ultimate balanced axial force*, half of this force, and zero. The figures starting on the next page show the moment-curvature curves in three different directions for the maximum, half of the maximum, and zero axial force. The dotted curve in each figure represents the multispring model's curve, and the solid curve is the moment-curvature curve of the fiber model. The curves are close for different axial loads and in different directions. Also, when the interaction curves of the multispring model and the fiber model solution in different directions are compared, shown in Figure 11, again the curves are close. The small difference seen between these two curves is because the yield strain is assumed to be at the same distance with respect to the center for both models, which is necessary for the moment-curvature curves to match better. The section used here is a typical Caltrans column.

* The axial force corresponding to the maximum bending moment in the interaction curve for the first yield of steel

Comparing Moment-Curvature of the Caltrans Typical Column, by Fiber Model and MS Model in direction 1 with axial force equal to the Maximum

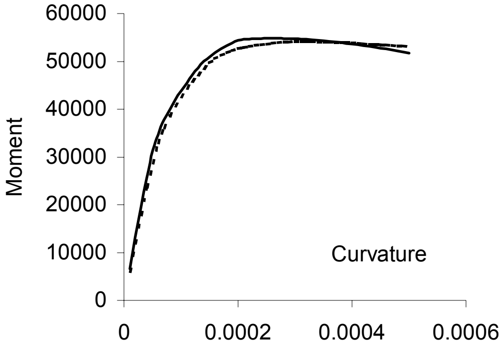

Comparing Moment-Curvature of the Caltrans Typical Column, by Fiber Model and MS Model in direction 2 with axial force equal to the Maximum

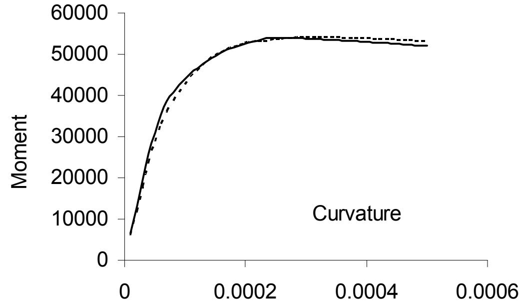

Moment-Curvature of the Caltrans Typical Column, by Fiber Model and MS Model in direction 3 with axial force equal to the Maximum

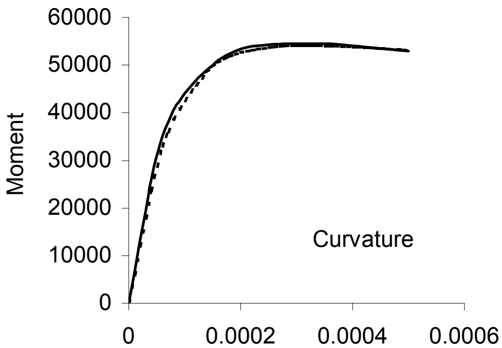

Moment-Curvature of the Caltrans Typical Column, by Fiber Model and MS Model in direction 2 with axial force equal to the half of the Maximum

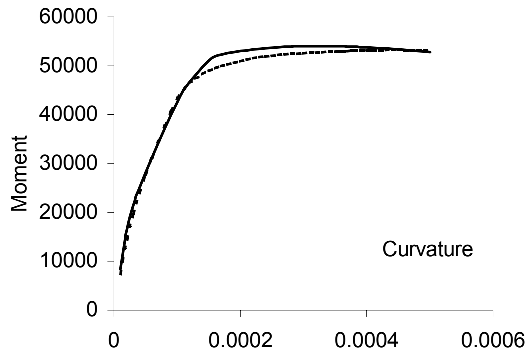

Moment-Curvature of the Caltrans Typical Column, by Fiber Model and MS Model in direction 1 with axial force equal to the half of the Maximum

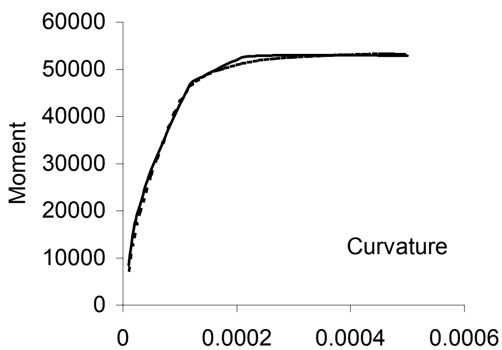

Moment-Curvature of the Caltrans Typical Column, by Fiber Model and MS Model in direction 3 with axial force equal to the half of the Maximum

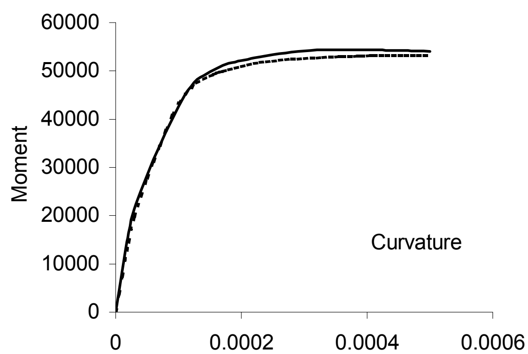

Moment-Curvature of the Caltrans Typical Column, by Fiber Model and MS Model in direction 2 with axial force equal to zero

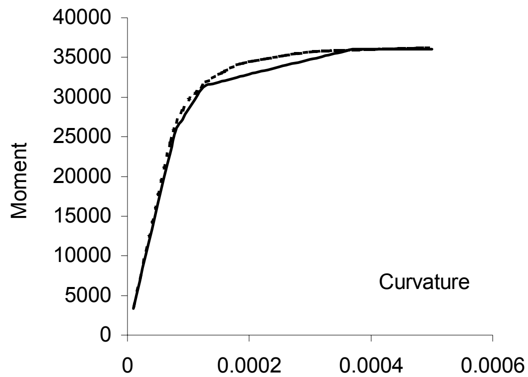

Moment-Curvature of the Caltrans Typical Column, by Fiber Model and MS Model in direction 3 with axial force equal to zero

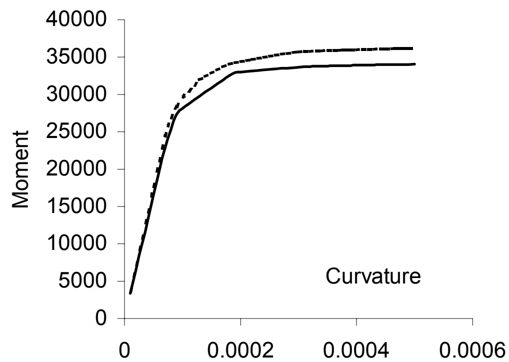

Moment-Curvature of the Caltrans Typical Column, by Fiber Model and MS Model in direction 3 with axial force equal to zero

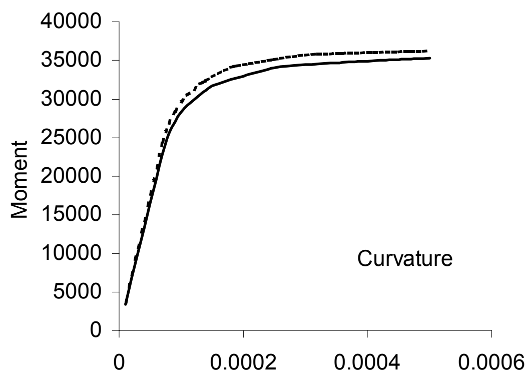

Moment Axial Force Interaction Curves for Caltrans Typical Column at the first tensile yield of steel for Fiber & MS Models in direction #1

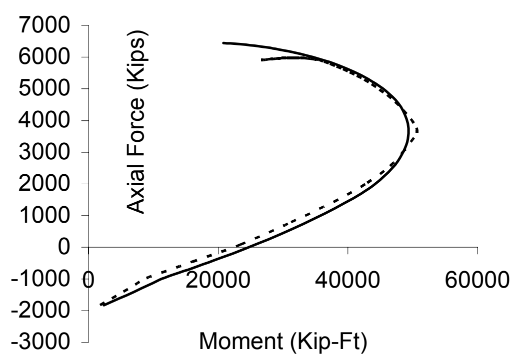

Moment Axial Force Interaction Curves for Caltrans Typical Column at the first tensile yield of steel for Fiber & MS Models in direction #3 .

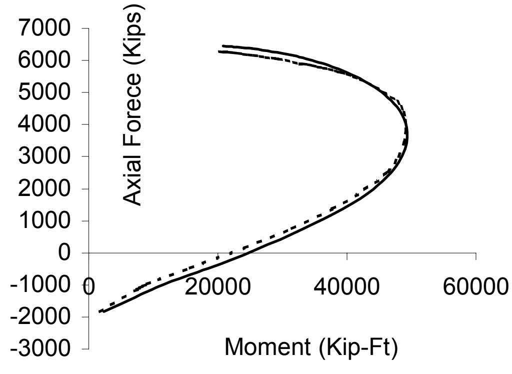

Moment Axial Force Interaction Curves for Caltrans Typical Column at the first tensile yield of steel for Fiber & MS Models in direction #2 .

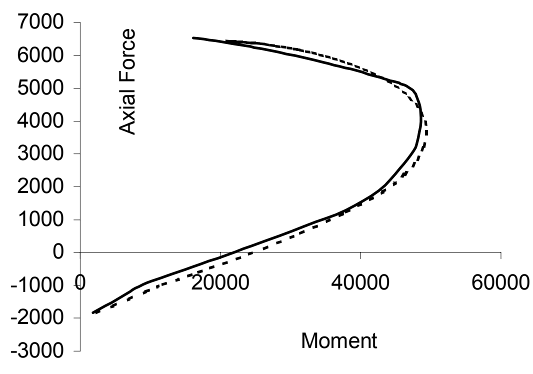

PEER REPORTS

PEER reports are available from the National Information Service for Earthquake Engineering (NISEE). To order PEER reports, please contact the Pacific Earthquake Engineering Research Center, 1301 South 46th Street, Richmond, California 94804-4698. Tel.: (510) 231-9468; Fax: (510) 231-9461.

PEER 2002/17 *Structural Characterization and Seismic Response Analysis of a Highway Overcrossing Equipped with Elastomeric Bearings and Fluid Dampers: A Case Study.* Nicos Makris and Jian Zhang. November 2002.

PEER 2002/16 *Estimation of Uncertainty in Geotechnical Properties for Performance-Based Earthquake Engineering.* Allen L. Jones, Steven L. Kramer, and Pedro Arduino. December 2002.

PEER 2002/15 *Seismic Behavior of Bridge Columns Subjected to Various Loading Patterns.* Asadollah Esmaeily-Gh. and Yan Xiao. December 2002.

PEER 2002/14 *Inelastic Seismic Response of Extended Pile Shaft Supported Bridge Structures.* T.C. Hutchinson, R.W. Boulanger, Y.H. Chai, and I.M. Idriss. December 2002.

PEER 2002/13 *Probabilistic Models and Fragility Estimates for Bridge Components and Systems.* Paolo Gardoni, Armen Der Kiureghian, and Khalid M. Mosalam. June 2002.

PEER 2002/12 *Effects of Fault Dip and Slip Rake on Near-Source Ground Motions: Why Chi-Chi Was a Relatively Mild M7.6 Earthquake.* Brad T. Aagaard, John F. Hall, and Thomas H. Heaton. December 2002.

PEER 2002/11 *Analytical and Experimental Study of Fiber-Reinforced Strip Isolators*. James M. Kelly and Shakhzod M. Takhirov. September 2002.

PEER 2002/10 *Centrifuge Modeling of Settlement and Lateral Spreading with Comparisons to Numerical Analyses***.** Sivapalan Gajan and Bruce L. Kutter. January 2003.

PEER 2002/09 *Documentation and Analysis of Field Case Histories of Seismic Compression during the 1994 Northridge, California, Earthquake.* Jonathan P. Stewart, Patrick M. Smith, Daniel H. Whang, and Jonathan D. Bray. October 2002.

PEER 2002/08 *Component Testing, Stability Analysis and Characterization of Buckling-Restrained Unbonded Braces™.* Cameron Black, Nicos Makris, and Ian Aiken. September 2002.

PEER 2002/07 *Seismic Performance of Pile-Wharf Connections.* Charles W. Roeder, Robert Graff, Jennifer Soderstrom, and Jun Han Yoo. December 2001.

PEER 2002/06 *The Use of Benefit-Cost Analysis for Evaluation of Performance-Based Earthquake Engineering Decisions*. Richard O. Zerbe and Anthony Falit-Baiamonte. September 2001.

PEER 2002/05 *Guidelines, Specifications, and Seismic Performance Characterization of Nonstructural Building Components and Equipment*. André Filiatrault, Constantin Christopoulos, and Christopher Stearns. September 2001.

PEER 2002/03 *Investigation of Sensitivity of Building Loss Estimates to Major Uncertain Variables for the Van Nuys Testbed.* Keith A. Porter, James L. Beck, and Rustem V. Shaikhutdinov. August 2002.

PEER 2002/02 *The Third U.S.-Japan Workshop on Performance-Based Earthquake Engineering Methodology for Reinforced Concrete Building Structures*. July 2002.

PEER 2002/01 *Nonstructural Loss Estimation: The UC Berkeley Case Study. Mary C. Comerio and John C. Stallmeyer.* December 2001.

PEER 2001/16 *Statistics of SDF-System Estimate of Roof Displacement for Pushover Analysis of Buildings.* Anil K. Chopra, Rakesh K. Goel, and Chatpan Chintanapakdee. December 2001.

PEER 2001/15 *Damage to Bridges during the 2001 Nisqually Earthquake.* R. Tyler Ranf, Marc O. Eberhard, and Michael P. Berry. November 2001.

PEER 2001/14 *Rocking Response of Equipment Anchored to a Base Foundation.* Nicos Makris and Cameron J. Black. September 2001.

PEER 2001/13 *Modeling Soil Liquefaction Hazards for Performance-Based Earthquake Engineering.* Steven L. Kramer and Ahmed-W. Elgamal. February 2001.

PEER 2001/12 *Development of Geotechnical Capabilities in OpenSees.* Boris Jeremic. September 2001.

PEER 2001/11 *Analytical and Experimental Study of Fiber-Reinforced Elastomeric Isolators*. James M. Kelly and Shakhzod M. Takhirov. September 2001.

PEER 2001/10 *Amplification Factors for Spectral Acceleration in Active Regions.* Jonathan P. Stewart, Andrew H. Liu, Yoojoong Choi, and Mehmet B. Baturay. December 2001.

PEER 2001/09 *Ground Motion Evaluation Procedures for Performance-Based Design.* Jonathan P. Stewart, Shyh-Jeng Chiou, Jonathan D. Bray, Robert W. Graves, Paul G. Somerville, and Norman A. Abrahamson. September 2001.

PEER 2001/08 *Experimental and Computational Evaluation of Reinforced Concrete Bridge Beam-Column Connections for Seismic Performance*. Clay J. Naito, Jack P. Moehle, and Khalid M. Mosalam. November 2001.

PEER 2001/07 *The Rocking Spectrum and the Shortcomings of Design Guidelines.* Nicos Makris and Dimitrios Konstantinidis. August 2001.

PEER 2001/06 *Development of an Electrical Substation Equipment Performance Database for Evaluation of Equipment Fragilities*. Thalia Agnanos. April 1999.

PEER 2001/05 *Stiffness Analysis of Fiber-Reinforced Elastomeric Isolators.* Hsiang-Chuan Tsai and James M. Kelly. May 2001.

PEER 2001/04 *Organizational and Societal Considerations for Performance-Based Earthquake Engineering.* Peter J. May. April 2001.

PEER 2001/03 *A Modal Pushover Analysis Procedure to Estimate Seismic Demands for Buildings: Theory and Preliminary Evaluation.* Anil K. Chopra and Rakesh K. Goel. January 2001.

PEER 2001/02 *Seismic Response Analysis of Highway Overcrossings Including Soil-Structure Interaction.* Jian Zhang and Nicos Makris. March 2001.

PEER 2001/01 *Experimental Study of Large Seismic Steel Beam-to-Column Connections.* Egor P. Popov and Shakhzod M. Takhirov. November 2000.

PEER 2000/10 *The Second U.S.-Japan Workshop on Performance-Based Earthquake Engineering Methodology for Reinforced Concrete Building Structures.* March 2000.

PEER 2000/09 *Structural Engineering Reconnaissance of the August 17, 1999 Earthquake: Kocaeli (Izmit), Turkey.* Halil Sezen, Kenneth J. Elwood, Andrew S. Whittaker, Khalid Mosalam, John J. Wallace, and John F. Stanton. December 2000.

PEER 2000/08 *Behavior of Reinforced Concrete Bridge Columns Having Varying Aspect Ratios and Varying Lengths of Confinement.* Anthony J. Calderone, Dawn E. Lehman, and Jack P. Moehle. January 2001.

PEER 2000/07 *Cover-Plate and Flange-Plate Reinforced Steel Moment-Resisting Connections.* Taejin Kim, Andrew S. Whittaker, Amir S. Gilani, Vitelmo V. Bertero, and Shakhzod M. Takhirov. September 2000.

PEER 2000/06 *Seismic Evaluation and Analysis of 230-kV Disconnect Switches.* Amir S. J. Gilani, Andrew S. Whittaker, Gregory L. Fenves, Chun-Hao Chen, Henry Ho, and Eric Fujisaki. July 2000.

PEER 2000/05 *Performance-Based Evaluation of Exterior Reinforced Concrete Building Joints for Seismic Excitation.* Chandra Clyde, Chris P. Pantelides, and Lawrence D. Reaveley. July 2000.

PEER 2000/04 *An Evaluation of Seismic Energy Demand: An Attenuation Approach.* Chung-Che Chou and Chia-Ming Uang. July 1999.

PEER 2000/03 *Framing Earthquake Retrofitting Decisions: The Case of Hillside Homes in Los Angeles.* Detlof von Winterfeldt, Nels Roselund, and Alicia Kitsuse. March 2000.

PEER 2000/02 *U.S.-Japan Workshop on the Effects of Near-Field Earthquake Shaking.* Andrew Whittaker, ed. July 2000.

PEER 2000/01 *Further Studies on Seismic Interaction in Interconnected Electrical Substation Equipment.* Armen Der Kiureghian, Kee-Jeung Hong, and Jerome L. Sackman. November 1999.

PEER 1999/14 *Seismic Evaluation and Retrofit of 230-kV Porcelain Transformer Bushings*. Amir S. Gilani, Andrew S. Whittaker, Gregory L. Fenves, and Eric Fujisaki. December 1999.

PEER 1999/13 *Building Vulnerability Studies: Modeling and Evaluation of Tilt-up and Steel Reinforced Concrete Buildings.* John W. Wallace, Jonathan P. Stewart, and Andrew S. Whittaker, editors. December 1999.

PEER 1999/12 *Rehabilitation of Nonductile RC Frame Building Using Encasement Plates and Energy-Dissipating Devices.* Mehrdad Sasani, Vitelmo V. Bertero, James C. Anderson. December 1999.

PEER 1999/11 *Performance Evaluation Database for Concrete Bridge Components and Systems under Simulated Seismic Loads.* Yael D. Hose and Frieder Seible. November 1999.

PEER 1999/10 *U.S.-Japan Workshop on Performance-Based Earthquake Engineering Methodology for Reinforced Concrete Building Structures.* December 1999.

PEER 1999/09 *Performance Improvement of Long Period Building Structures Subjected to Severe Pulse-Type Ground Motions*. James C. Anderson, Vitelmo V. Bertero, and Raul Bertero. October 1999.

PEER 1999/08 *Envelopes for Seismic Response Vectors.* Charles Menun and Armen Der Kiureghian. July 1999.

PEER 1999/07 *Documentation of Strengths and Weaknesses of Current Computer Analysis Methods for Seismic Performance of Reinforced Concrete Members.* William F. Cofer. November 1999.

PEER 1999/06 *Rocking Response and Overturning of Anchored Equipment under Seismic Excitations.* Nicos Makris and Jian Zhang. November 1999.

PEER 1999/05 *Seismic Evaluation of 550 kV Porcelain Transformer Bushings.* Amir S. Gilani, Andrew S. Whittaker, Gregory L. Fenves, and Eric Fujisaki. October 1999.

PEER 1999/04 *Adoption and Enforcement of Earthquake Risk-Reduction Measures.* Peter J. May, Raymond J. Burby, T. Jens Feeley, and Robert Wood.

PEER 1999/03 *Task 3 Characterization of Site Response General Site Categories*. Adrian Rodriguez-Marek, Jonathan D. Bray, and Norman Abrahamson. February 1999.

PEER 1999/02 *Capacity-Demand-Diagram Methods for Estimating Seismic Deformation of Inelastic Structures: SDF Systems*. Anil K. Chopra and Rakesh Goel. April 1999.

PEER 1999/01 *Interaction in Interconnected Electrical Substation Equipment Subjected to Earthquake Ground Motions.* Armen Der Kiureghian, Jerome L. Sackman, and Kee-Jeung Hong. February 1999.

PEER 1998/08 *Behavior and Failure Analysis of a Multiple-Frame Highway Bridge in the 1994 Northridge Earthquake.* Gregory L. Fenves and Michael Ellery. December 1998.

PEER 1998/07 *Empirical Evaluation of Inertial Soil-Structure Interaction Effects.* Jonathan P. Stewart, Raymond B. Seed, and Gregory L. Fenves. November 1998.

PEER 1998/06 *Effect of Damping Mechanisms on the Response of Seismic Isolated Structures.* Nicos Makris and Shih-Po Chang. November 1998.

PEER 1998/05 *Rocking Response and Overturning of Equipment under Horizontal Pulse-Type Motions.* Nicos Makris and Yiannis Roussos. October 1998.

PEER 1998/04 *Pacific Earthquake Engineering Research Invitational Workshop Proceedings, May 14–15, 1998: Defining the Links between Planning, Policy Analysis, Economics and Earthquake Engineering.* Mary Comerio and Peter Gordon. September 1998.

PEER 1998/03 *Repair/Upgrade Procedures for Welded Beam to Column Connections.* James C. Anderson and Xiaojing Duan. May 1998.

PEER 1998/02 *Seismic Evaluation of 196 kV Porcelain Transformer Bushings.* Amir S. Gilani, Juan W. Chavez, Gregory L. Fenves, and Andrew S. Whittaker. May 1998.

PEER 1998/01 *Seismic Performance of Well-Confined Concrete Bridge Columns.* Dawn E. Lehman and Jack P. Moehle. December 2000.